Monte Carlo modelling and radiation measurement with ATAGS, the XArray, and SATURN at CARIBU

Michael Leslie Smith

A thesis submitted for the degree of
Doctor of Philosophy
at The Australian National University

- November, 2019 -

Preface

This work describes an investigation of detector techniques required to measure neutron-rich fission products. Staring in 2008, this project was initially concerned with the β^- feeding intensities of neutron-rich fission products to be measured through the implementation of a large NaI(Tl) detector (ATAGS) at Argonne National Laboratory (ANL). This was to coincide with the CARIBU facility being built. Delays in the commissioning of ATAGS and CARIBU and the fact my PhD candidature was part-time resulted in other groups world-wide building more advanced detectors for these types of measurements, implementing them at other facilities during the analysis and write-up of this work. The project was extended to support three additional measurements using CARIBU at ANL.

Parts of the work presented in this thesis have been or will be published in the following articles:

- **Development of a Total Absorption γ-ray Spectrometer (TAGS) for β-ray studies at Argonne National Laboratory**
  [Chi08]
  C.J. Chiara, F.G. Kondev, C.J. Lister, M.P. Carpenter, T. Lauritsen, E.A. McCutchan, G. Savard, D. Seweryniak, S. Zhu and **M. L. Smith**
  APS 2008 Annual Meeting of the Division of Nuclear Physics, 53:12, 2008

- **TAGS Simulations with GEANT4**
  [Smi10]
  M. L. Smith
  Nuclear Data and Measurement Report, **ANL/NDM-167**, 2010.

- **Methodologies for the application of Total Absorption Gamma-ray Spectroscopy**
  [Col11]
  G. Collin*
  Honours thesis, unpublished, **Australian National University**, 2011.

- **Recent advances in β-decay spectroscopy at CARIBU**
  [Mit16a]
  A.J. Mitchell, P. Copp, G. Savard, C.J. Lister, G.J. Lane, M.P. Carpenter, J.A. Clark, S. Zhu, A.D. Ayangeakaa, S. Bottoni, T.B. Brown, P. Chowdhury, T.W. Chillery, H.M. David, D.J. Hartley, E. Heckmaier, R.V.F. Janssens, K. Kolos, F.G. Kondev, T. Lauritsen, E.A. McCutchan, E.B. Norman, S. Padgett, N.D. Scielzo, D. Seweryniak, **M.L. Smith**, and G.L. Wilson. Heavy Ion Accelerator Symposium 2015: International Nuclear Structure Conference in Remembrance of George Dracoulis EPJ Web of conferences 123:04006, 2016.

- **β-decay half-lives of ^{134,134m}Sb and their isomeric yield ratio produced by the spontaneous fission of ^{252}Cf**

*M.L. Smith - Supervisory role to G. Collin thesis

[Sie18]
K. Siegl, K. Kolos, N.D. Scielzo, A. Aprahamian, G. Savard, M.T. Burkey, M.P. Carpenter, P. Chowdhury J.A. Clark, P. Copp, G.J. Lane, C.J. Lister, S.T. Marley, E. A. McCutchan, A.J. Mitchell, J. Rohrer, **M.L. Smith** and S. Zhu
Physical Review C 98:054307, 2018.

- **Gamma spectroscopy of Rubidium-92 (^{92}Rb) for $\overline{\nu}_e$ flux determination**
  A.C. Gula,..., M.L. Smith,..., *et al.* In preparation for submission to Physical Review C.

- **β-decay and ground-state properties of neutron-rich ^{106}Nb**
  A. J. Mitchell,...., M.L. Smith,..., *et al.* In preparation for submission to Physical Review C.

No part of this thesis has been submitted for a degree at any other university.

Michael Smith
November, 2019

Acknowledgements

This thesis is a significant chunk of my life so far, involving a few major redirections in the project across two countries whilst juggling five job transitions, having lived in 3 different cities whilst keeping a roof over my head and dealing with life in general. There was a more straight-forward path to a PhD given to me as an option way back in the beginning, which I sometimes regret not taking. The length of time of this project has brought me good and bad experiences, and allowed me learning opportunities that only come from time invested and experience gained in taking this longer path. I have met and worked with many people, both experts and novices, whilst on this roller-coaster, many of whom gave me support, encouragement and their time when I needed it.

Firstly to my former colleagues at ANSTO Dr. L. Mo and Dr. D. Alexiev for encouraging me to start this endeavour at the Australian National University (ANU), it feels like a life-time ago. I would like to thank my previous workplaces Club Engadine and the CSIRO at Lucas Heights who allowed me to keep the thesis moving while earning an income. I would like to thank my current employer ANSTO and my extended Nuclear Stewardship family for their support in the final stages of this work. I would like to specifically acknowledge Dr. Freda van Wyngaardt and the late Dr. Mark I. Reinhard for understanding my stresses, providing encouragement and sound advice when I needed it most. Thank you for providing me with a means to complete this thesis whilst juggling my early radionuclide metrology career. Mark, I am sorry you did not get to see the completion of this work- you are missed.

Thank you to the Physics group at Argonne National Laboratory (ANL) for providing access to CARIBU, specifically Prof. G. Savard and Dr. J.A. Clark who orchestrated the building of CARIBU and were available around the clock to tune the beam for these experiments. To Dr. M.P. Carpenter for coordinating and hosting the ATAGS experiment and providing invaluable assistance with the data acquisition system. Thanks go to Prof. C.J. Lister for allowing me to be involved with the ATAGS project and getting me involved in the RIA summer school at ANL in 2008. Thank you to all of the friends I made along the way, both fellow students and staff. I would like to specifically acknowledge Dr. Filip G. Kondev for initially taking a chance and involving me in the project. Thank you for all of the support and mentoring you provided and looking after me in Chicago. I enjoyed our conversations and I learned a great deal from you in those short nine months. I still have so much more to learn.

I would like to acknowledge Dr. Chris Chiara for helping to keep me sane while we overlapped on the ATAGS project and during my time in Chicago. Thank you for looking out for me in Chicago, the many lifts to and from O'Hare, and for the many edits and translations of my gobbledygook drafts leading to this readable thesis. Thank you for being a good friend and helping me see the completion to this ATAGS project.

Thank you Dr K. Kolos and Dr. N.D. Scielzo of Lawrence Livermore National Laboratory (LLNL) for allowing me to contribute to their experiments that make up the latter part of this thesis. Thank you both for your wisdom, patience and finding time to take conference calls via flakey internet connections at odd hours.

Thank you to the Department of Nuclear Physics at the ANU for putting up with me all of these years. I would like to thank Ms. Petra Rickman for all of the support and encouragement you have shown to me over the years. I would like to acknowledge Mr. Gabriel Collins for his Honours work which contributed to this thesis. Thank you to all of the students that I have had the pleasure of meeting and working with along the way. Thank you to Prof. Aidan Byrne and Prof. Tibor Kibedi for being my early supervisors, helping me to start this project and for their encouragement. To Dr. L.J. Bignell, we started our PhD journey together many years ago, thanks for helping to sanity check my Monte Carlo code on the lead up to submission, and for the encouragement throughout. To Mr. Tristan Steele, thank you for putting up with the many venting sessions, providing much needed distractions in Canberra over the years, and sharing in the frustrations of student life. Lindsey and Tristan, thank you for your friendship over these years.

I would like to especially acknowledge the late Prof. George D. Dracoulis for the privilege of being one of his students, although he never got to see the completion of this work. Your questions and conversations scared me, but always taught and challenged my knowledge without any judgement. You provided encouragement, a calm wisdom, a dry sense of humour and inspired a hard work ethic. The department is not the same without you.

Thank you Prof. Andrew Stuchbury for providing advice on this final draft and your support of the project and for keeping the department at ANU healthy for the future. Thank you Dr. A.J. Mitchell for giving me a push across the finish line, and sound advice, whilst juggling your own big life events. Thank you for translating my Australian into legible English and helping to provide fresh eyes and energy on the tail end of this long journey. Thank you for being a good friend.

I am indebted to Prof. Greg J. Lane for his tireless efforts and seemingly endless patience and energy for me and my thesis work. You always found time in your busy schedule, provided constant support, practical discussions and advice in helping to keep up the motivation along this epic journey. Thank you for making time for me at the expense of your own, challenging me, the many fruitful discussions, and your commitment to get me across the line. I have learnt much from you and have enjoyed my time working with you. It has been a privilege to be one of your students. I am looking forward to working on other projects together in the future as a colleague. Thank you for getting me here and looking out for me thoughout these years.

To my Mum, Dad, brothers, sisters and their partners and more recently my partner's family. Thank you for your understanding, the many missed functions and for keeping me distracted and grounded. I couldn't have done this without your support and understanding; I love you guys. A special thanks to Mum and Beth for helping to feed me when times were tough and helping to keep me going financially. To my fur family, thank you for many needed distractions of pats and scratches, sorry about the missed walks while finishing this thing.

And most importantly, to my friend, my partner, the love of my life - Paula (who has her PhD). Thank you for your patience, your understanding and the sacrifice of our limited time together so I could finish this thesis. Thank you for doing the majority of planning of our wedding and honeymoon to allow me to make big pushes towards the completion of this epic journey. I cannot thank you enough for being there and helping me to get this across the finish line, all whilst going on this ride with me and pressing pause on our new life together. I am looking forward to our next chapter together and making up lost time. I love you.

Abstract

The CAlifornium Rare Isotope Breeder Upgrade (CARIBU) at Argonne National Laboratory (ANL), USA allows access to, and measurement of, a broad range of neutron-rich nuclei with high intensities and purity. These nuclei are important test cases to expand our understanding of atomic nuclear structure, nuclear astrophysical processes and nuclear energy application.

The thesis project encompasses the measurement of short-lived radioactive nuclei from CARIBU using various techniques, including Total Absorption Gamma-ray Spectroscopy (TAGS), γ-ray coincidence spectroscopy and β-decay spectroscopy. The two detectors used - the ATAGS spectrometer and the XArray and SATURN decay-spectroscopy station (called XSAT as a combined system) - required complex Monte Carlo radiation transport models in order to interpret the results of recent experiments.

The TAGS technique was implemented at CARIBU by the recommissioning of a large, well-type NaI(Tl) scintillator detector. The detector performance was evaluated through testing of the well-known cases of ^{141}Cs and ^{140}Cs. This experimental program was extended to investigate the less-well-known β^- feeding intensities of ^{141}Xe, ^{140}Xe and ^{104m}Nb/^{104}Nb.

In addition, a Monte Carlo model of XSAT was constructed, validated and applied to the specific cases of ^{134}Sb, ^{134m}Sb, ^{92}Rb, ^{104}Nb and ^{106}Nb in this work. This enabled the determination of the ^{134m}Sb/^{134}Sb branching ratio resulting from ^{252}Cf decay, measurement of ^{92}Rb decay with implications for the so-called 'anti-neutrino anomaly', and the interpretation of the complex spectroscopy following the β-decay of ^{104}Nb$\rightarrow$^{104}Mo and ^{106}Nb$\rightarrow$^{106}Mo. This Monte Carlo modelling was a key element in obtaining and interpreting results from each of these three experiments.

Contents

List of Figures

List of Tables

Chapter 1

Background

Neutron-rich, exotic nuclei offer exciting ground to test our current understanding of atomic nuclei. Many of the current models that describe single-particle behaviour or collective modes of motion were formulated from data collected on energetically stable systems. However, there is growing evidence to show that these models break down, or, at the very least, evolve, as one moves away from the so-called "valley of stability" towards the proton and neutron drip lines. In particular, precise knowledge of the decay properties of nuclei with enhanced neutron-to-proton ratios is critical for a number of applications of nuclear science.

The work of this thesis was initially focused around the re-implementation and testing of a method to measure the β^- feeding intensities of neutron-rich fission products, with applications to our understanding of nucleosynthesis and the behaviour of nuclear fuels. Until recently, these nuclides have been difficult to access experimentally. The commissioning of a new Department of Energy (DOE) facility at Argonne National Laboratory (ANL) - the CAlifornium Rare Isotope Breeder Upgrade (CARIBU) - was a potential game changer, particularly for refractory elements that have low production in other large ISOL facilities*. The CARIBU facility is described further in Section 1.2.2. It experienced initial delays. Hence, this work expanded to encompass a number of experimental studies of neutron-rich nuclei and, in particular, modelling of the bespoke radiation-detection systems used in these studies. The present research was undertaken part-time during a period that overlapped the building and commissioning of CARIBU and uses results from three measurements acquired with collaborators during the first experimental campaign. CARIBU allowed access for the measurement of neutron-rich nuclei with intensities higher than previously achieved (at the time of this work). The thesis describes measurements using two techniques: Total Absorption Gamma-ray Spectroscopy (TAGS, described in Section 2.3) and β - γ spectroscopy using the SATURN decay station in combination with the XArray (XSAT, described in Sections 2.4.1 and 2.4.2). Both of these techniques require accurate transport models for radiation in the detectors in order to interpret the results.

The TAGS technique was implemented at ANL by the recommissioning of a 4π NaI(Tl) detector, ATAGS (see Section 2.3.1), that was initially tested against a well-measured case, ^{141}Cs. These measurements were then extended to include the lesser-known nuclei ^{140}Cs, ^{140}Xe and ^{104}Nb/^{104m}Nb. Initial characterisation of the detector with sources, experimental measurements with CARIBU beams, radiation transport modelling, and analysis of radioactive ion beam measurements, are directly undertaken as part of this

*Isotope Separation On-Line refers to a radioactive ion-beam facility where the radioactive nuclei are created in a target and then extracted from the target for direct use or re-acceleration.

work.

The second technique used the XSAT detector array for $\beta - \gamma$-decay spectroscopy experiments of ^{134m}Sb/^{134}Sb, ^{92}Rb and ^{104,106}Nb. The major contribution to these experiments from the present work consists of radiation transport modelling of these specific cases, allowing the final interpretation of the data to be performed.

1.1 Motivation for studying neutron-rich nuclides

As already noted above, the properties of neutron-rich nuclei are interesting in their own right, due to the novel behaviours that are a consequence of the increased neutron-proton ratio, and must be explained within nuclear models. Some of these interesting phenomena include neutron skins, modification of effective nuclear forces and the changing of shell gaps. Furthermore, the basic nuclear properties such as decay lifetimes, decay branching ratios and the average energy emitted in the form of γ rays and β-particle emissions, can have both practical applications in terms of nuclear design and safety as well as applications in other fields such as nuclear astrophysics where this information is essential input required to understand nucleosynthesis of heavy elements in the rapid-neutron-capture process ("r-process").

1.1.1 Nuclear reactor design and safety

'Decay heat' in nuclear fuel is the heat generated due to the radioactive decay of products resulting from fission. The time behaviour of this quantity is critical in the design and operation of nuclear reactors. It affects fuel removal and reloading processes, safety after accidents (such as a loss of coolant incident), as well as the storage, transport and reprocessing requirements for spent fuel.

In March 2011, the Daiichi Nuclear power plant in Fukushima lost site power and the back-up power from generators due to a tsunami. Cooling pumps are required to circulate water around the fuel elements to remove the heat caused by radioactive decay from fission during operation and from the radioactivity of activated products after control rods are inserted. The decay heat from the fuel without sufficient cooling, resulted in over pressurisation and eventual damage to the reactor containment.

Calculation of the time evolution of the decay heat requires knowledge of the fission yields, β-decay lifetimes, as well as the β-particle and γ-ray decay schemes, for all of the fission products and their subsequent progeny decaying back to the line of stability [Alg10]. The difficulty in getting access to many of these neutron-rich fission fragments, together with the complications of measurement with conventional γ-ray spectroscopy methods, has hindered experimental measurements. As a result, much of the information currently used to determine the decay heat must be complemented with theoretically calculated decay data for nuclei that might suffer from the Pandemonium effect and these data have been shown to be inaccurate in some cases [Dim15]. The result is less-efficient designs to compensate for the large uncertainties in this information to satisfy safety and regulatory compliance.

The International Atomic Energy Agency (IAEA) has noted that there are a number of nuclei for which a lack of experimental information on the β-decay branching ratios has important implications for the design of Gen IV reactors [NEA] and has requested that priority be given to studies of these nuclei.

1.1.2 Astrophysics: Nucleosynthesis models

The astrophysical r-process is a rapid sequence of successive neutron captures, interspersed by beta-decays, that occurs in explosive stellar events such as supernovae and neutron star mergers [Abb17, Kas17]; it is responsible for the formation of most heavy nuclei above iron. The path of the r-process lies through neutron-rich nuclei that are not very well studied and CARIBU promises to be a unique source for a range of r-process nuclei that will not be available elsewhere. While measurements of masses and lifetimes are critical for our general understanding of the r-process, the measurements of beta-decay branching ratios and well-understood level schemes, for which TAGS and XSAT can play an essential role, may be very important for making detailed predictions of the r-process.

1.1.3 Antineutrino anomaly

Thermal neutron-induced fission of ^{235}U is the main process used in nuclear fission power reactors worldwide. Despite the process having been well studied so that the distribution of neutron-rich nuclei is well understood, there has recently been considerable interest in the so-called "antineutrino anomaly". This refers to the observation that the antineutrino spectrum observed at reactors is measured to be of the order of 6% lower than the theoretically predicted spectrum that is based on measurements of the total β^- spectra for the neutron-rich fission products and our understanding of the β-decay process [Men11, Fal12, Son17, Son18]. In addition to this overall deficit, there are differences in the spectral shapes that are not yet understood. While there is considerable excitement about potential new physics explanations for this anomaly, it is also true that there are a range of nuclei which have substantial contributions to the antineutrino spectrum whose decay properties are not well known. The work described in this thesis contributes to experimental measurements that can further refine the predicted antineutrino spectrum and may have an impact on this topic.

1.1.4 Present experiments

Table 1.1 lists the neutron-rich nuclei whose decay has been studied in experiments related to this thesis, as well as the physics interest and the detector system used to study them. All the nuclei have been produced at the CARIBU facility.

^{A}X	Interest	Detector Used
^{141}Cs	Validation experiment	ATAGS
^{140}Cs	Validation plus nuclear decay heat	ATAGS
^{140}Xe	Nuclear decay heat	ATAGS
^{134}Sb/^{134m}Sb	Nuclear models of fission, r-process	XSAT
^{92}Rb	Antineutrino anomaly	XSAT
^{104}Nb/^{106}Nb	Nuclear models (tests of triaxiality)	XSAT

Table 1.1: Radioactive nuclei extracted from CARIBU and studied in this work, including the physics interest and the detector system used in the experiment.

1.2 Access to neutron-rich nuclides

The study of a nuclide's properties is limited by its accessibility. Stable ion-beam accelerators have provided the majority of the access to nuclides that make up the current picture of the nuclear landscape. Traditional fusion-evaporation reactions generated by stable ion-beam accelerators result in nuclides predominantly near stability and to the neutron-deficient side of the valley of stability.

1.2.1 Radioactive-beam facilities

In the last 10+ years, there has been a move away from the traditional stable ion-beam accelerator facilities to rare-isotope or radioactive ion-beam facilities. A major focus of the international nuclear physics community over the last decade has been the development of radioactive beam capabilities for the study of neutron-rich nuclei. While very large scale (billion dollar) facilities such as FRIB in the USA [FRI] and FAIR in Europe [FAI] are being constructed, smaller scale facilities are either in production or being built. The CAlifornium Rare Isotope Breeder Upgrade (CARIBU) is a unique example that was implemented as an upgrade to the Argonne Tandem Linac Accelerator System (ATLAS), as part of building and developing the capability for the much larger FRIB facility, while further providing complimentary exotic beams in the longer term.

1.2.2 CARIBU and ATLAS at Argonne National Laboratory

The Argonne Tandem Linac Accelerator System (ATLAS) is a 20-MV linac accelerator operated as a Department of Energy National Research Facility. Located at Argonne National Laboratory (ANL), ATLAS is capable of delivering ion beams with energies up to 17 MeV per nucleon, of elements from hydrogen to uranium, for nuclear reactions and structure research [ANLa]. The ATLAS laboratory also operates a number of experimental instruments on dedicated beam-lines such as Gammasphere and HELIOS [ANLe, Wuo07].

The CAlifornium Rare Isotope Breeder Upgrade (CARIBU) was designed to provide radioactive ion beams both directly (low energy), and for acceleration by ATLAS, to the existing suite of instruments at ANL. Fission fragments from a ^{252}Cf source are thermalised in a gas catcher and selectively accelerated. Figure 1.1 shows the stages of ion-beam handling with CARIBU:

1. ^{252}Cf source, source degrader and cask;
2. RF gas catcher;
3. RFQ gas cooler;
4. high-resolution isobar separator;
5. switching yard;
6. RFQ buncher;
7. Multi-Reflection Time Of Flight (MR-TOF) separator.

The CARIBU facility is based around a ^{252}Cf source with approximately 37 GBq (1 Ci) in activity [Sav16, Sav05, Sav08]. The half-life is 2.6470(26) years and it decays mainly

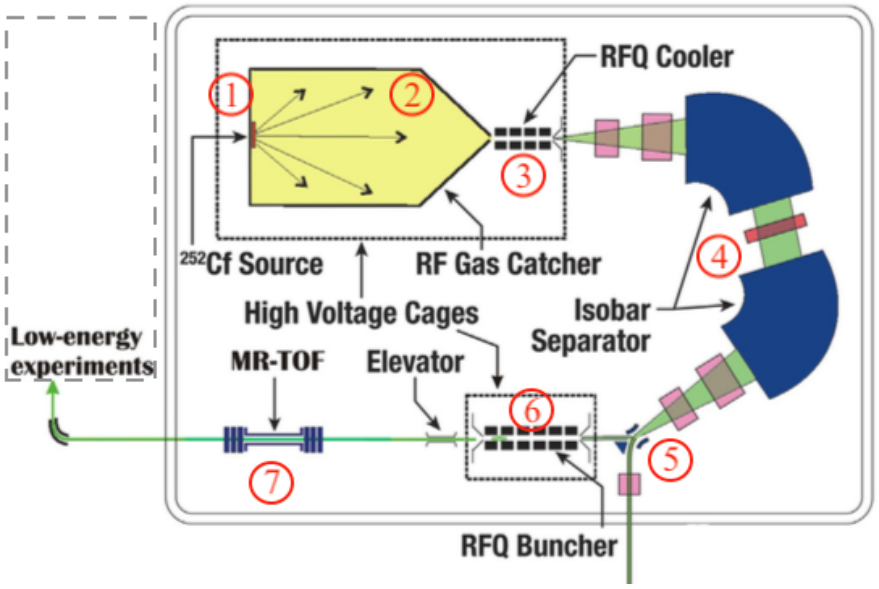

Figure 1.1: Schematic of CARIBU, reproduced from Figure 1 of Savard *et al.* [Sav16]. The main components 1 to 7 are described in the text. The dashed line indicates the floor space utilised for experiments with the low-energy beam line.

via alpha emission to ^{248}Cm, with the remaining 3.086(8)% decaying via spontaneous fission [Be08]. The maximum source strength is constrained by the need to comply with the facility radiation licence at ATLAS. The spontaneous fission of ^{252}Cf produces fragments as shown in Fig. 1.2, that lie mainly in the neutron-rich region that is complementary to nuclides available at typical ISotope On-Line (ISOL) facilities [Sav05, Sav08]. Utilising the capture and re-acceleration of fission fragments, has allowed the building and commissioning of the CARIBU facility at relatively little cost compared to larger scale facilities such as FRIB [FRI]. The development of the CARIBU facility has contributed research towards FRIB design, while producing neutron-rich nuclides to the user community prior to FRIB commissioning.

A source of ^{252}Cf was produced by the High-Flux Isotope Reactor (HFIR) reactor at Oak Ridge National Laboratory (ORNL) [ORN] and a thin, 10 cm^2 deposit was applied to a tantalum disk using electrodeposition. Owing to the high activity required, the handling of the source is done remotely both at the site of production and at CARIBU. A shielded flask is used to minimise the radiation emitted from the source under normal operation at CARIBU. The flask has been designed to dock with a shielded transport container to allow the transfer of the source into CARIBU with minimal handling. The 2π source is covered with 1 mg/cm^2 gold foil 1 mm above the source to confine the radioactivity and protect the down-stream gas systems [Sav16]. While it also acts as an additional confinement layer, an aluminium foil degrader also serves the purpose of reducing the energy of the fission fragments prior to their entry into the gas catcher.

Designed at ANL, the Radio-Frequency (RF) gas catcher uses approximately 45 L of high-purity helium gas at 10 kPa (100 mbar) pressure as a stopping volume for the fission fragments [Sav16]. The gas is used in combination with RF fields to thermalise and contain the ions (minimising their collisions with the wall of the catcher), while a gradient DC

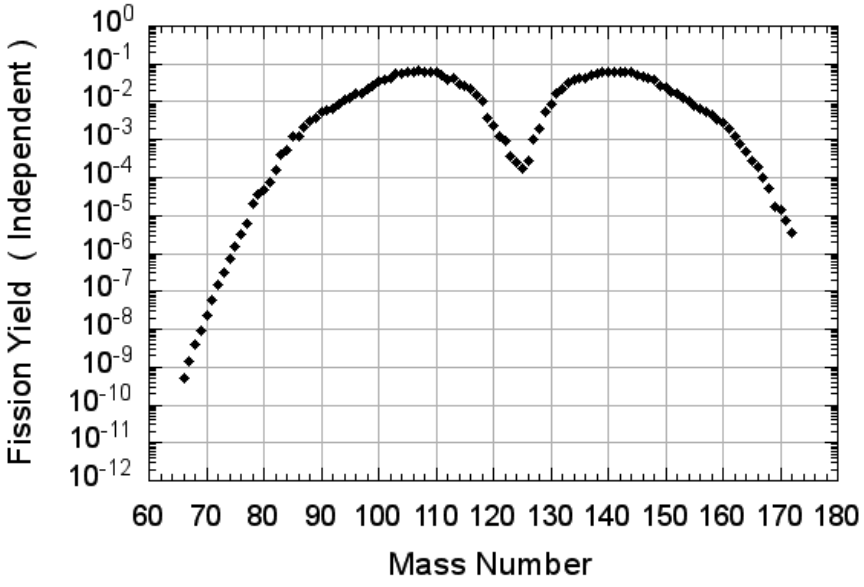

Figure 1.2: The spontaneous fission yields of ^{252}Cf. The plot is from the JAEA Nuclear Data Center website, using JENDL FP Fission Yields Dat File 2011 [JAE].

field directs the captured ions into a tapered nozzle for extraction [Sav16, Sav03]. The resultant ions are in charge states of 1+ or 2+ and are extracted through the catcher nozzle to a Radio-Frequency Quadrupole (RFQ) cooler via gas flow. RFQ structures extract the low-energy ions while differential pumping is applied to remove the helium. Once the pressure is reduced, acceleration of the ions though a 50-kV potential is possible without straggling so that they can be injected into the isobar separator. The time required for the fission fragments to leave the source and arrive at the RFQ cooler is approximately 20 to 30 milliseconds.

The ions pass through the isobar separator with a very high mass resolution of 1 part in 20,000. The separator consists of two 60° magnets with an electrostatic multipole corrector between, and symmetrical optics either side of these magnets, consisting of a quadrupole doublet, a quadrupole singlet and a sextupole singlet [Dav08, Dav09]. The ANL designed isobar separator is based on a scaled down (1/4) version of the isobar separator for FRIB. The reduction in size allows the entire separator to fit on a high-voltage (HV) platform, while still providing the required mass resolution [Sav05]. Silicon detectors covered with foil are used to diagnose and tune the beam, while various slits and beam-stops are used to reduce the buildup of unwanted radiation from the components.

An electrostatic switching yard receives the mass separated ions from the isobar separator and deflects the resulting beam to its end location. At this point, the 30 to 50 keV continuous beam is suitable for acceptance into the ATLAS Electron Cyclotron Resonance (ECR) ion-source[†] for breeding and re-acceleration up to 15 MeV/u through ATLAS to the existing suite of instruments [Sav16, Par16]. The alternative used for the present research is to send the beam to the low-energy beam-line.

[†]This was true at the time of writing and during the research for this thesis. More recently it has been possible to use the Electron Beam Ion Source (EBIS) to couple CARIBU to the ATLAS accelerator.

The present work utilises the low-energy beam-line and this thesis will focus on this part of CARIBU. Additional beam handling is required to further reduce the energy for the low-energy experiments. An RFQ buncher followed by an electrostatic elevator is located on the low-energy beam-line side of the switching yard. The beam is bunched and cooled for 50 to 100 ms producing a variable rate range of 1 to 20 Hz, with beam bunches of approximately 1 μs in length [Par16]. The elevator reduces the energy from the 30 - 50 keV range to an energy below 10 keV, tailored to the requirements of the experiment [Par16].

The mass resolving power can be further improved by the use of a Multi-Reflection Time of Flight (MR-TOF) isobar separator located after the RFQ buncher. Electrostatic mirrors located at either end of the MR-TOF and a lifting pulse are tuned to isochronously trap ions of a selected mass for several cycles before they are released [Hir16]. A mass resolving power of more than 10^5 can be achieved with efficiencies of 30% from initial testing [Hir16]. The MR-TOF was installed at the time of the TAGS experiments at CARIBU in July 2015, but had not been commissioned and so was bypassed. The MR-TOF was used during the subsequent XSAT experiments in November of 2015. The beam is then directed to one of the experimental beam-lines via a double electrostatic kicker that can also function as a beam sweeper [Mit14].

Process	Efficiency	Timing
Gas catcher stopping fraction	50%	
Gas catcher/cooler extraction	45%	20 ms
ECR charge breeding gas (solid)	10% (5%)	30 ms
Bunching	85%	
ATLAS transmission	90%	

Table 1.2: Assumptions made for efficiency and timing when estimating CARIBU ion yields (taken from Savard *et al.* [Sav05]).

The estimated yields of beams produced by CARIBU have been derived by Savard *et al.* in the CARIBU proposal [Sav05]. The spontaneous fission fragment yields from a 1 Ci ^{252}Cf source are used as a starting point to this calculation. The estimated yield of CARIBU uses the known half-lives of the fragments and some assumptions on the timing properties and efficiencies at each stage, as summarised in Table 1.2. The efficiencies of each stage of ion manipulation were determined using stable beams and were observed to be independent of the species. The yields from ^{252}Cf were found to be consistent with intensity data estimations and are used to determine the individual yields in lieu of experiments [Sav16].

1.3 Thesis outline

The remainder of this thesis begins in Chapter 2 with a presentation covering the important features of β decay and some of the relevant detector technologies. Chapter 3 introduces the concept of Monte Carlo modelling, which is the key technique that enables a detailed understanding of the detector response and the extraction of important experimental quantities such as β-feeding intensities. Chapters 4, 5, 6 and 7 present the original work envisaged for this thesis, including ATAGS testing and characterisation, recommissioning on the low-energy beam line at CARIBU, along with analysis and interpretation of the TAGS spectra that give insight into β-feeding intensities in neutron-rich nuclei. The

effort using the XSAT and other detector systems is described in Chapter 8, including the Monte Carlo modelling, validation of these models with experimental and source data, deduction of important detector characterisation properties and the use of these properties for evaluating results from a range of experiments. Lastly, the important conclusions and a description of future work are presented in Chapter 9. The appendices describe in more detail some of the validation work and other related projects that the author was involved in, during the course of the present thesis research.

Chapter 2

β-particle decay and measurement techniques

CARIBU produces neutron-rich nuclei that generally undergo a chain of β^- decays back towards the line of stability. This chapter describes some key aspects of the nuclear theory behind β decay, important limitations and measurement issues when trying to observe and quantify β decay, as well as details of some of the measurement and detector technologies that are used.

2.1 β decay

2.1.1 Types of β decay

Beta decay is caused by the weak interaction and results in the conversion of neutrons into protons or protons into neutrons. There are three types of β decay: two that occur via the spontaneous emission of either electrons (β^-) or positrons (β^+) from the nucleus while the other involves an atomic electron being absorbed by the nucleus (Electron Capture, EC). In all cases, the nucleus undergoes a shift along the isobar towards stability.

When a nuclide is on the neutron-rich side of stability, the predominant process is β^- decay. Given a nuclide X, with atomic number Z, mass number A, and neutron number N, this will decay into nuclide Y by the emission of a β^- particle and an electron anti-neutrino ($\overline{\nu_e}$):

$$ {}^{A}_{Z}X^{N} \rightarrow {}^{A}_{Z+1}Y^{N-1} + \beta^- + \overline{\nu_e} \qquad (\beta^- decay) $$

This is equivalent to a neutron (n) being converted into a proton (p).

$$ n \rightarrow p + \beta^- + \overline{\nu_e} $$

Excluding the effects of recoil, the maximum energy of the emitted electron is given by:

$$ E_{max}(\beta^-) = Q - E_i, $$

where Q is the total energy of the decay as determined by the difference in mass of the parent and daughter and E_i is the energy level populated in the daughter nucleus. This three-body process means the resulting energy is shared between the β^- particle and the anti-neutrino. When the nuclide is on the neutron-deficient side of stability, decay towards stability occurs via β^+ (positron) decay:

$$\begin{aligned} {}^{A}_{Z}X^{N} &\rightarrow {}^{A}_{Z-1}Y^{N+1} + \beta^+ + \nu_e \qquad (\beta^+ decay) \\ p &\rightarrow n + \beta^+ + \nu_e, \end{aligned}$$

or via electron capture (EC):

$$\begin{aligned} {}^{A}_{Z}X^{N} + e^- &\rightarrow {}^{A}_{Z-1}Y^{N+1} + \nu_e \qquad (EC) \\ p + e^- &\rightarrow n + \nu_e \end{aligned}$$

In some cases, these latter two processes can occur in parallel. If the total energy of decay is greater than 1022 keV, which is twice the energy of an electron mass at rest ($2m_0c^2$), the decay can occur via β^+ decay with the energy being shared between the positron and the neutrino. An atomic electron is absorbed by the nucleus in electron capture, resulting in a hole in an atomic shell and a mono-energetic neutrino. The rearrangement of the electrons when the hole is filled can result in the emission of X-rays or Auger electrons.

2.1.2 Kinetic energy of β-particles

The energy from a β decay transition is released in the form of kinetic energy in a 3-body process involving: the recoiling daughter nucleus, the β-particle (electron or positron), and the neutrino (or anti-neutrino). The conservation of linear momentum for the three parts results in a continuous energy distribution for the β spectrum. This is in contrast to α decay that results in a discrete α-particle energy.

The spectrum of emitted β-particles is given by the relation (taken from [Kra88])

$$N(p) \propto p^2(Q - T_e)^2 F(Z', p)|M_{fi}|^2 S(p, q)$$

where: N is the number of β-particles with momentum p, T_e is the kinetic energy of the β-particle, $F(Z', p)$ is the Fermi function with the Coulomb field included, M_{fi} is the nuclear matrix element, and $S(p, q)$ is the shape factor. The shape of the spectrum is dependant upon the type of β decay (β^- or β^+), and also on the atomic number. This is mainly due to the Coulomb field interaction with the daughter nucleus. For example, a positron will be under the influence of a repulsive force from the nucleus giving the β^+ particle additional momentum at low energies compared to an electron. This effect will increase with the atomic number.

2.2 Pandemonium Effect

The direct measurement of β-feeding intensities, by detecting electrons for a decaying nuclide, is difficult owing to the continuous nature of the resulting spectrum. In principle, the β-feeding intensities can be established from discrete γ-ray radiation that follows the

β transitions using high-resolution γ-ray spectroscopy. At the present time, High Purity Germanium (HPGe) is the gold standard for energy resolution and is the most commonly employed detector for high-resolution γ-ray spectroscopy.

In this 'conventional' form of γ-ray spectroscopy, the β-feeding intensity of a level is determined from the difference of the relative intensities of γ rays and conversion electrons populating and de-populating it. This balancing method assumes all of the γ rays that contribute to the decay scheme are detected, which is reasonable for nuclides with few transitions or a low density of daughter states.

Far from stability, where the decay energies (or, equivalently, the Q value) are often large, the daughter nuclei that follow β decay can be populated at high excitation energies where the level densities are high. The result is a fragmented decay, with many weak β decay branches and multiple γ-ray decay pathways from each of the high-lying daughter levels to the ground state. The low-intensity, high-energy γ rays that follow a weak branch are often not distinguishable amongst the background of more prominent γ rays, causing the β transitions feeding these levels to be missed entirely, or underestimated. In addition, there is a reduced sensitivity to higher energy γ-ray transitions as the detection efficiency of HPGe decreases with increasing γ-ray energy. Since the β-decay strengths are calculated from the balance of the total γ ray and conversion-electron intensity populating and de-populating a level, the absence of a low-intensity or high-energy γ-ray transition can significantly effect all of the deduced β-decay feeding intensities. This is commonly referred to as Hardy's "Pandemonium effect" [Har77, Har84].

Hardy *et al.* postulated the losses of β intensity with the use of conventional γ-ray spectroscopy methods and numerically created a fictional nuclide called "Pandemonium" to test it [Har77]. Pandemonium was chosen to have nuclear structure properties resembling the medium-mass nucleus ^{145}Gd, as it has a complicated decay scheme and was of interest at the time of publication. A spin and parity of $1/2^+$ was assumed with Q = 5.0 MeV. Spin, density, level to level distances and transitions were generated using known physics models with assumptions on the γ-ray transitions [Har77]. A γ-ray spectrum of decaying Pandemonium was generated and is shown in Figure 2.1.

Knowledge of the β-feeding intensities of Pandemonium (available in the model) with the simulated γ-ray spectrum, enabled the evaluation of the conventional γ-ray spectroscopy analysis in determining the β-feeding intensities. Hardy deduced that approximately 20% of the γ-ray intensity above 1.7 MeV was un-accounted for [Har77].

Firestone later undertook extensive measurements of ^{145}Gd and criticised Hardy *et al.* for the use of a statistical model over experiment and pointed out several discrepancies between the measured structure of ^{145}Gd and Pandemonium [Fir82]. Hardy *et al.* answered this with another paper stating that Pandemonium is a statistical model to highlight the limitations of conventional γ-ray spectroscopy in determining β intensities of complicated decay schemes [Har84].

To bring some clarity to this argument, TAGS measurements of ^{145}Gd were undertaken by Alkhazov *et al.* in 1985 [Alk85], measuring the β^+(EC) intensities feeding levels of ^{145}Eu. In this work, they conclude that there are inconsistencies of β-decay intensities for ^{145}Gd, in terms of missed transition intensity, as predicted by Hardy. They commented that additional TAGS measurements of 40 other nuclides also showed discrepancies of the β-feeding intensities compared to those determined by conventional γ-ray spectroscopy for both complicated and simple decay schemes. The Pandemonium effect is now generally accepted as a deficiency in nuclear spectroscopy as originally highlighted by Hardy *et al.* [Har77].

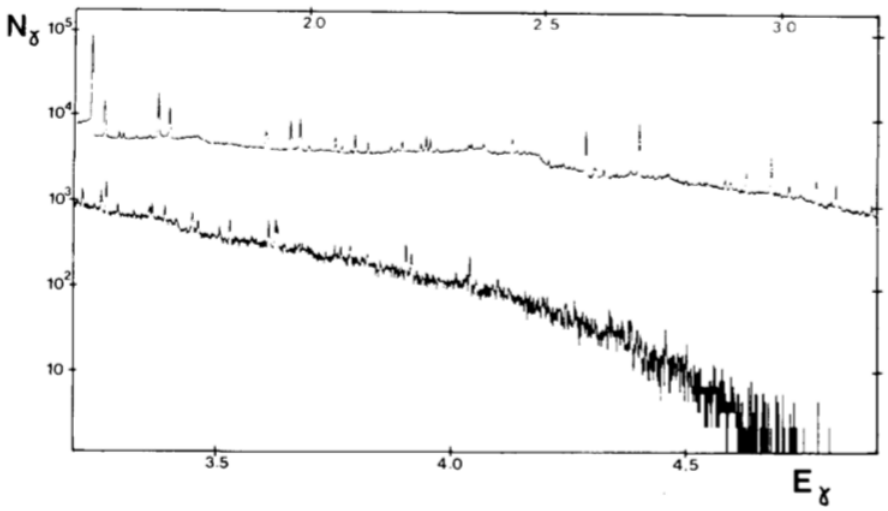

Figure 2.1: Gamma-ray spectrum of the Monte Carlo produced radionuclide, Pandemonium. Reproduced from reference [Har77].

2.3 The Total Absorption Gamma-ray Spectroscopy (TAGS) technique

The Total Absorption Gamma-ray Spectroscopy (TAGS) technique used in this thesis differs from conventional discrete-line γ-ray spectroscopy. A β-decay event often populates an excited state or level that can produce a number of sequential γ-ray emissions in the de-excitation process to the ground state of the daughter nucleus. The TAGS technique utilises a large detector that ideally has an efficiency close to 100%. The γ-ray emissions following a decay are detected simultaneously by the TAGS detector and result in a single response that is the sum of all the detected γ-ray energies from a level. This summed response provides a unique signature of the beta decay feeding to that level.

Figure 2.2 is an example of a partial decay scheme of the β^- decay of ^{A}X, showing levels m to p. The β^- decay that feeds level p (β_p), has low intensity compared to β_o or β_n. This branch β_p, feeds a high-energy level that would result in low-intensity γ-ray emission cascading into the levels below. In conventional spectroscopy, the only indicator for this β_p decay is the single low-intensity $\gamma_{p,o}$ that would likely not be detected. The β feeding intensity would be inappropriately allocated to those βs that are identified below the missed level, in this case β_o. In the TAGS method, the summed response is still of low intensity, but the unique signature ($\gamma_{p,o} + \sum_{L=o}^{g.s.} \gamma_{L,(L-1)}$) is higher in energy than the signature from the adjacent level ($\sum_{L=o}^{g.s.} \gamma_{L,(L-1)}$), and more likely to be detected. In the TAGS method, it doesn't matter how fragmented the decay pathway might be; summing all the γ rays gives you approximately the same signal response independent of the different paths that are followed in the decay to the ground state. Limitations can occur with the presence of internal conversion and metastable states, which can be overcome when the TAGS method is used in conjunction with conventional γ-ray spectroscopy as a complimentary technique.

A requirement of the TAGS method is a $\sim 4\pi$ geometry and related high detection efficiency. The overall cost of a large amount of material with high efficiency often results

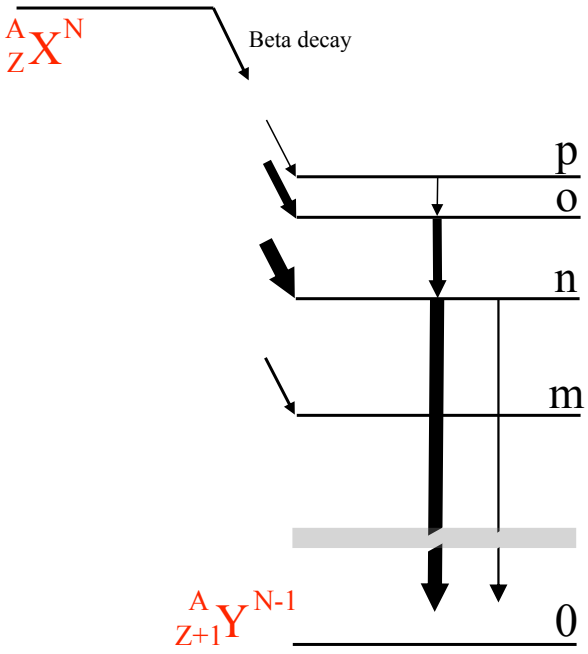

Figure 2.2: Illustrative level scheme showing a cascading decay sequence in ^{A}X. Relative intensities indicated by widths of arrows.

in using detector materials with low energy resolution. These intrinsic detector properties, combined with the large number of β-feeding levels, produces a broad and complex detector response that is difficult to interpret compared with conventional γ-ray spectroscopy. As such, the TAGS method relies heavily on Monte Carlo simulation to characterise the detector response to sequential γ rays in a cascade (see Chapter 3). This response is used to interpret and unfold the individual β-feeding level signatures from the observed spectrum (see Chapter 7). The TAGS method can be limited and provide ambiguity in the results, if used in isolation. For this reason, it is typically used in combination with observations from conventional γ-ray spectroscopy.

2.3.1 ATAGS

During the 1990's, a research group at the Idaho National Engineering Laboratory (INEL) commissioned a detector to undertake TAGS measurements with the INEL on-line isotope separator (ISOL) facility [And87]. The INEL ISOL facility was based on two ~100 μg ^{252}Cf sources located in a hot cell, with fission products transported to an electromagnetic mass separator via a gas-jet technique [And87]. The detector used for these measurements was acquired by Argonne National Laboratory (ANL) in 2007. To distinguish this specific detector from the TAGS (Total Absorption Gamma-ray Spectroscopy) technique, the detector will be referred to hereafter as the Argonne Total Absorption Gamma-ray Spectrometer (ATAGS); a picture is shown in Fig. 2.3.

Greenwood eloquently describes the five design criterion of a TAGS detector applied when building ATAGS in his 1992 article [Gre92b]. These requirements draw upon existing experience of large detectors built around the same time, for example the Karlsruhe 4π BaF_2 detector [Wis90]. The design requirements from Ref. [Gre92b] are:

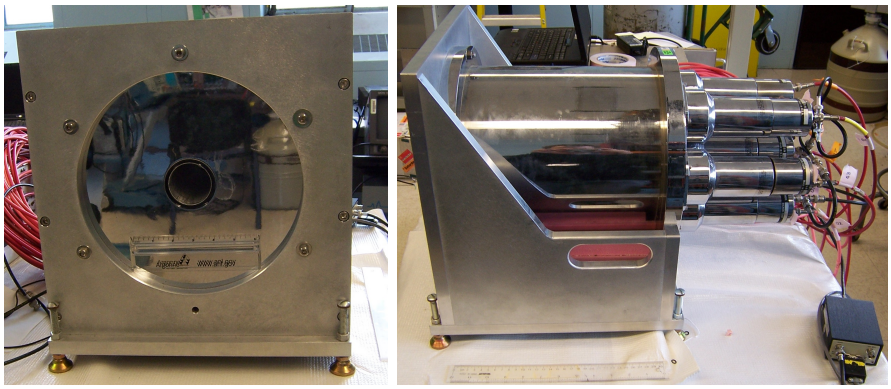

(a) (b)

Figure 2.3: Front and side views of the Argonne Total Absorption Gamma-ray Spectrometer (ATAGS) detector, a large well-type NaI(Tl) detector sitting in a stainless steel stand. Front of the detector with the well opening (left) and side of the detector showing the PhotoMultiplier Tubes (PMTs) (right). Pictures taken at ANL.

1. as close to 4π detection geometry as possible;
2. minimum photon leakage;
3. good energy resolution;
4. minimum photon absorbing material between the source and detector; and
5. minimum detection of β^- or associated bremsstrahlung.

Due to the limitations of budget and material technology of the day, thallium-doped sodium iodide (NaI(Tl)) scintillator provided a good candidate for requirement 1. NaI(Tl) has a high γ-ray detection efficiency, fast detector response, and can be grown in large crystals, but suffers from poor energy resolution (incompatible with requirement 3). The resolution of the 662 keV γ ray from ^{137}Cs was reported to be 7% in 1992 [Gre92b]. The ATAGS was made by Bicron Corporation and was surface compensated using 6.13 MeV γ rays from a ^{244}Cm/^{13}C source in an attempt to improve the resolution [Gre92b]. The technique as described by Sandorfi [San84], is the mapping of the response due to the non-uniformity of intrinsic thallium doping in the scintillator and compensating this by decreasing the amount of the light reflected at the boundary adjacent to more responsive parts of the crystal.

ATAGS is a large cylindrical detector with a hole (well) bored along the symmetry axis (well-type detector). With a radiation source located 2.5 mm from the bottom of the well, a source-to-detector geometry solid angle of close to 4π can be achieved (requirement 1). The NaI(Tl) scintillator crystal has dimension of 254 mm (diameter), 305 mm (length) with a 51 mm (diameter) by 203 mm (depth) well, encased in an 4 mm thick aluminium can; reduced to 2.6 mm in the well. With an almost 4π detection geometry, the ATAGS can simultaneously detect all of the γ-ray decays emitted into the scintillator following a β decay. The summed response from the single decay provides a unique γ-ray signature of the β feeding to that particular level. The TAGS technique using ATAGS enables identification of the β-decay branching ratios that is complimentary to traditional γ-ray

spectroscopy. At INEL, this was provided by a large lithium-drifted germanium [Ge(Li)] detector and a high-purity germanium (HPGe) detector with a beryllium window. These detectors measured both γ rays and X rays at the ISOL detection station, connected via a tape transport system [And87].

Scintillation photons that result from ionisation in the NaI(Tl) material by γ rays interacting within ATAGS are detected by PhotoMultiplier Tubes (PMTs), six symmetrically located around the outside at 60° apart with the seventh located at the centre (Fig. 2.4). These tubes convert the detected light into an electrical signal that is proportional to the energy deposited. ATAGS arrived at ANL with seven 76 mm diameter 10- stage RCA S83021E PMTs installed. Just prior to the first ATAGS experiment, these were replaced with seven Hamamatsu H6559 76 mm diameter, 12-stage PMTs.

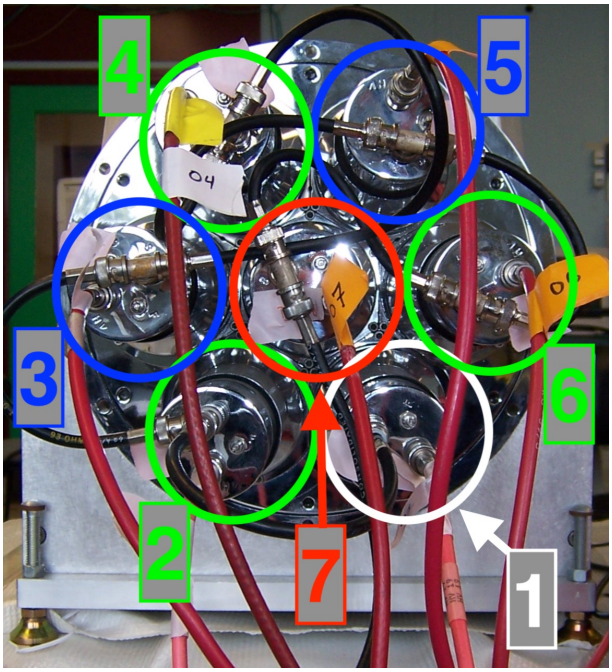

Figure 2.4: Rear view of the Argonne Total Absorption Gamma-ray Spectrometer (ATAGS) detector showing the arrangement of the PhotoMultiplier Tubes (PMTs) and the system of numbering adopted in this work.

Design requirements 4 and 5 are in conflict, such that using material to attenuate the β^- and bremsstrahlung components from a decay will also attenuate the γ rays reaching the detector. Conversely, having thin walls in the well would allow the ATAGS to detect radiation from β components of a decay. This was overcome by Greenwood *et al.* by having thin aluminium walls in the well (2.6 mm) and using auxiliary detectors to measure the β component as a trigger signal for the ATAGS [Gre92b].

During the INEL ISOL measurement campaigns, the seven PMT pre-amplifier signals were passively summed and used in conjunction with one of two thin silicon detectors to measure the associated β-particle. The silicon detectors had a surface area of 300 mm^2 and were 1.0 mm and 1.5 mm thick. Although the solid angle of the silicon detector to the source is limited (5.1 % of 4π), it can be used to determine the contribution of the β component by comparing the singles response (ATAGS only) with the gated response

(ATAGS with silicon detector trigger). The choice of the silicon detector thickness is determined for each experiment to optimise the gated response. The silicon detector was located above the source position on the open side of the well, facing the source.

By design, the large detection efficiency of the detector also makes it more sensitive to background radiation. At INEL, the ATAGS was located at a 90° angle from the ISOL beam-line and inside lead and polyethylene shielding to reduce the background. Both fixed sources and a tape system were used to deliver the implanted radionuclides from the ISOL beam-line, with the total ATAGS count rate being restricted to 4000 Hz to reduce the effects of pile-up.

ATAGS was used at INEL for the measurement of 45 fission products produced using the INEL on-line isotope separator facility by Greenwood, Helmer *et al.* between 1992 and 1997 [Gre92b, Hel94c, Gre92a, Hel94b, Gre95, Gre97]. The neutron-rich fission products measured ranged from Z = 37 to Z = 63 and are shown in Table 2.1.

Z	Isotopes measured at INEL by ATAGS
37	$^{89-91,93}$Rb
38	$^{93-95}$Sr
39	^{94,95}Y
45	^{106}Rh
55	$^{138-141}$Cs
56	$^{141-145}$Ba
57	$^{142-145}$La
58	$^{145-148}$Ce
59	$^{146-149,151}$Pr
60	$^{149,151,153-155}$Nd
61	$^{153-157}$Pm
62	^{157,158}Sm
63	^{158}Eu

Table 2.1: Range of radionuclides measured with ATAGS by Greenwood, Helmer *et al.* at the ISOL facility at Idaho National Engineering Laboratory (INEL) between 1992 and 1997 [Gre92b, Hel94c, Gre92a, Hel94b, Gre95, Gre97].

2.3.2 Other TAGS devices

One of the earliest implementations of the TAGS technique preceding Hardy's Pandemonium, was undertaken by Duke *et al.* in 1970 [Duk70]. Mass separated isotopes of mercury and radon were produced at ISOLDE (CERN) by spallation reactions from 600 MeV protons on the target material [AK70].

The resulting neutron-deficient products, from the Z = 77 to Z = 86 region, were measured in a campaign to determine the average β strength function S_β for positron branches that were known to be weak. Determination of the Q_β values of the weak branches was made possible by using the TAGS technique. This Q_β value, together with half life measurements, enabled the average β strength functions to be calculated.

Duke *et al.* measured the mass-separated radioactive ions implanted on a disc that was relocated and counted off-line by two 15 cm (diameter) x 10 cm (height) NaI(Tl) detectors placed 1.5 cm apart, face to face. There was a limitation of 50 s for short-lived radionuclides due to the physical requirements of transferring the source from the implantation area to the detectors. Chemical separation was undertaken on the longer-lived samples

to improve detection. The Q_β values were deduced by comparing the measured TAGS spectrum with a linear combination of individually calculated responses using the conventional "peeling" method, starting with the higher-energy γ rays. Significant corrections were applied due to the efficiency being less than 100% and comments about the difficulty of the method were made. Duke *et al.* estimated the accuracy of the method as being $\pm$50% and suggested improvements would be achievable by using larger detectors and more accurate response data. In 1972, Erdal *et al.* [Erd72] described an unfolding method using the same detectors by comparison with response functions that were determined by Monte Carlo and a recursion technique.

In 1975, Hornshøj *et al.* undertook measurements of β-strength functions of neutron deficient radionuclides of Hg, Au, Pt, Ir, Xe and I at the CERN ISOLDE facility [Hor75]. This was achieved by using a total γ-ray spectrum as a signature of the average β feeding into high-lying excited states, comparable to Duke *et al.* [Hor75, Duk70]. Horshøj *et al.* extended the method to the medium-mass region with the addition of a plastic scintillator between the (previously mentioned) two NaI(Tl) detectors in order to provide a β^+ veto [Hor75]. The β-strength values of these isobars span the transition of allowed to forbidden β decay, which were compared to shell-model calculations. Further improvements were gained from operating the facility on-line giving access to radionuclides with shorter half-lives.

In parallel to the development of ISOLDE at CERN, a facility capable of producing neutron-rich fission products was developed at the 1 MW R2-0 reactor in Studsvik Sweden, known as the On-line Separation of Isotopes at a Reactor In Studsvik, (OSIRIS) [Bor71]. The facility used ^{235}U located in the neutron flux near the core of the reactor, with separation of the fission products using duplicate equipment manufactured at CERN for ISOLDE, specifically for OSIRIS. In 1976, Lund and Rudstam [Lun76] used OSIRIS with an array of silicon detectors sandwiched between two (7.5 cm diameter x 7.5 cm thick) NaI(Tl) detectors to produce γ-gated β spectra of about 50 neutron-rich nuclides. The Q_β-value of these hard-to-access neutron-rich nuclides with half-lives between 3 seconds and 30 minutes were measured. The radioactive ions were implanted onto a 6 mm width recording tape and moved into the detector for this work with a transport time of approximately 3 seconds. The limitations on the accuracy of these measurements were due to the calibration of the silicon detectors, the extrapolation of the end-point energies, the size of the NaI(Tl) detectors and the background radiation environment.

In 1990, Wisshak *et al.* reported on a large 4π detector array consisting of 42 barium fluoride (BaF_2) crystals for the measurement of neutron capture cross sections [Wis90]. Located at Karlsruhe, Germany, the detector was the largest type of detector of its kind. Although it was not used for TAGS-type measurements, many of the design considerations used for this large scintillator detector influenced the design of ATAGS.

The Total Absorption Spectrometer (TAS) was commissioned by the Lawrence Berkeley National Laboratory (LBNL) after ATAGS was built [Nit95]. The TAS was to be used with the On-line Apparatus for SuperHILAC Isotope Separation (OASIS) facility at LBNL but was moved and installed at the GSI on-line mass separator after the SuperHILAC was shut-down shortly after the detector's construction [Kar97]. The TAS consisted of a similar well-type NaI(Tl) scintillation detector shape, but with larger dimensions than ATAGS (356 mm diameter x 356 mm length, with a well of 51 mm diameter and 203 mm in length). The light is detected by 11 PMTs on the main detector with the signal being passively summed. To improve the solid angle, a NaI(Tl) "plug" detector of dimensions 51 mm diameter x 152 mm long is used to close off the well. There were a number of

design improvements made with this detector compared to ATAGS; the first improvement is a larger sensitive volume. One significant design advantage of TAS is gain control to deal with environmental temperature changes.

Measurements at the GSI on-line separator utilised a tape implantation system to transport the nuclide of interest to the well of TAS. The source position was located at the bottom of the well, surrounded by two 0.5 mm thick silicon wafer detectors allowing the measurement of the energy-loss (ΔE) of electrons and positrons. Adjacent to the outer silicon wafer is a 16 mm diameter x 10 mm long Ge detector for measuring X-rays from electron-capture decays.

Improvements were made by not only the size and design of the TAS, but also in the deconvolution methods and correction used [CO99b] (see Section 7). In combination with the GSI on-line mass separator, the TAS was used for β-decay studies of spherical, rare-earth nuclei and in the decay of neutron-deficient nuclei below ^{100}Sb for the procurement of data relevant to nuclear decay heat applications [Kar98, CO99a, Kar01, Alg04a, Rub05, Rub07].

The Gammasphere array at ANL was also considered for use as a TAGS calorimeter, requiring the removal of the HeavyMets*, and the use of the bismuth germanate suppressors for γ-ray spectroscopy. Gammasphere is an array of 110 HPGe detectors, each with a Compton suppressor in a spherical arrangement around a central target [ANLe]. This suggestion was being tested in this work using Monte Carlo modelling, before efforts were diverted (see Appendix E).

2.3.3 More recent studies

During this thesis work, competing studies and new detectors were developed at other laboratories that superseded aspects of the planned program. Three NaI(Tl) TAGS-type detectors were designed, built and commissioned. These are: DTAS, SuN and MTAS.

DTAS

A Decay Total Absorption Spectrometer (DTAS) [Tai15] was developed in 2015 by a collaboration led by the Universidad de Valencia, Spain. DTAS is an arrangement of sixteen brick-shaped modules made of NaI(Tl), each brick having the dimensions of 15 cm (width) x 15 cm (height) x 25 cm (length). The modules are arranged in two cubes facing each other with a shape that is 3 wide by 3 high, with the centre module missing. Each module has a single large PMT on one end.

DTAS was originally designed for use with the AIDA† assembly at DESPEC‡ [DES]. The choice of design and materials considered detection solid angle, sensitivity to β-delayed neutrons, and cost. DTAS has been used in experiments at the University of Jyväskylä, Finland and will be used at FAIR, Germany (presently under construction).

SuN

A 4π **Su**mming **N**aI(Tl) (SuN) detector [Sim13] was built in 2013 by a collaboration led by the National Superconducting Cyclotron Laboratory (NSCL), located at Michigan State

*HeavyMets - Heavy Metal collimators made of a high-density tungsten alloy.

†Advanced Implantation Detector Array - AIDA.

‡DEcay SPECtroscopy - DESPEC at the Facility for Antiproton and Ion Research in Europe-FAIR.

University, USA. SuN has a cylindrical shape, 41 cm in diameter and 41 cm in length, with a 4.5 cm bore extending the entire length. The detector is split into a top and bottom half allowing the positioning of the detector around a beam line. Each half is segmented into four sections, each section is viewed by three PMTs that are equally spaced around the segments.

MTAS

The Modular Total Absorption Spectrometer (MTAS) [Kar16] was commissioned in 2012 at Oak Ridge National Laboratory (ORNL), USA [WC14]. MTAS consists of 19 modules made of NaI(Tl), each module has a hexagon shaped profile that is 17.6 cm thick 54 cm in length. A central module has the same profile but has a 6.4 cm diameter bore running through the centre extending the entire length. The modules are arranged in a 'honeycomb' shape around the central module. Each module has two PMTs, one attached to each end, with the exception of the central tube, which is viewed by 12 smaller PMTs (6 on either end). The combined detector combines approximately one tonne of NaI(Tl). MTAS is located at the Holifield Radioactive Ion Beam Facility (HRIBF) at ORNL.

2.4 β and $\beta - \gamma$ spectroscopy

The prior discussion about TAGS measurements described the important information that can be provided by observing ALL of the γ rays emitted in a nuclear decay. However, there are important cases where no γ rays will be observed, for example, in direct β-decay transitions between the the ground state of the parent and the ground state of the daughter. Missing these branches can result in serious errors in interpreting the nuclear structure, with implications for understanding nuclear models, or, on a more practical level, may result in obtaining the wrong average energy emitted in a β-decay process and hence an inaccurate estimate of decay heat in nuclear fuel.

This suggests that a high-efficiency spectrometer for observing the β particles emitted in decay could be important. Such a device is the SATURN detector, described further below.

Another scenario to be considered is the case where a sequence of nuclei decay one into another and separation of the information from each decay is required. A TAGS spectrum is relatively featureless and it may not be clear whether the contributions to a spectrum are from one nucleus, or many. In contrast, discrete spectroscopy with high-resolution γ-ray detectors can result in unique energies that enable clear isolation that a particular transition comes from a specific nucleus. Such unique tags can be used to measure nuclear lifetimes for specific nuclei, even in the presence of contaminations from other nuclei, something that may not be possible with a TAGS-type spectrometer.

Discrete line spectroscopy also provides the possibility of measuring spins and parities of the individual levels using techniques such as angular correlations and intensity balances to derive transition multipolarities. In the present work, the XArray was used for high-resolution discrete line spectroscopy.

The work in this thesis also comprises experimental measurements and modelling of the XArray in combination with the SATURN decay station. The combined instrumentation will be referred to as the XSAT. The next sections describe the basic properties of these detector systems.

2.4.1 The XArray

The XArray consists of 5 High-Purity Germanium (HPGe) clover detectors, arranged in close geometry, originally commissioned by ANL to operate at the back of the Fragment Mass Analyser (FMA) with the Gammasphere spectrometer at the front [ANLe, ANLd]. More recently, and in the case of this work, this general purpose high-resolution γ-ray spectrometer has been utilised with the CARIBU low-energy beam line (see Section 1.2.2).

The XArray uses four of the same-sized clovers in the vertical plane, referred to here as "standard" clovers, which are labelled "A", "B", "C", and "D". Each standard clover contains four 60 mm (diameter) x 60 mm (length) coaxial HPGe crystals arranged in a four-leaf clover configuration. A more recent upgrade to the array was undertaken by the addition of a larger clover detector from the same manufacturer, Canberra. The larger clover detector is referred to in this work as the super-clover "S". The super-clover uses four 70 mm (diameter) x 70 mm (length) HPGe crystals, an improvement made possible due to advances in manufacturing at the time of purchase.

Figure 2.5 shows the orientations of the detectors from the side and looking along the beam axis. The vertical and horizontal pairs of detectors are arranged in an X shape.

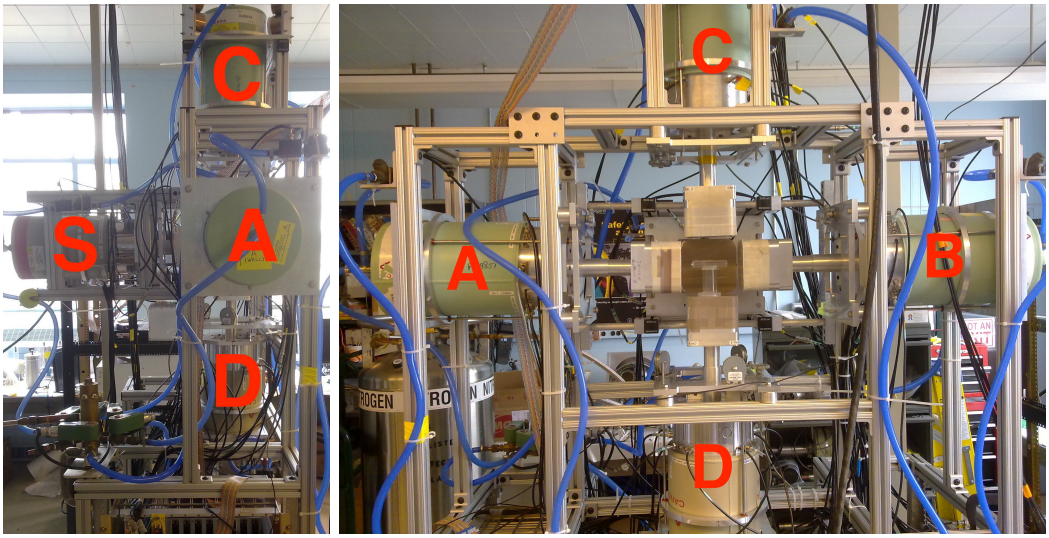

(a) (b)

Figure 2.5: (a) Side and (b) front views of the Argonne XArray showing the orientation of the 4 standard size clovers in horizontal [A,B] and vertical [C,D] pairs. The larger Super Clover [S] is oriented to align with the beam. The pictures also show the support frame and the automatic liquid nitrogen fill system. Pictures taken at ANL during the addition of the Super Clover in 2011.

These detectors are housed in a mobile aluminium frame (T-slot 80/20) that allows for adjustment of the clover positions along the axis in which it is oriented toward and away from the target. The frame also supports the required electronics to operate each detector and includes an automatic liquid nitrogen fill system.

2.4.2 SATURN

Scintillator And Tape Using Radioactive Nuclei (SATURN) is a decay spectroscopy station designed for use with the low energy beamline of CARIBU [Mit14]. It consists of a plastic

β-particle detector and tape transport system.

The SATURN detector

There are two plastic detectors designed for SATURN, both made from polyvinyltoluene (PVT) plastic scintillator (BC-408 from Saint Gobain [SG]). One design uses a paddle-like system surrounding the implantation point with separated detectors (allowing some spatial resolution). The other is a single cylindrical piece of PVT (10 cm [diameter] x 10 cm [length]) with a cut-out slot allowing a tape to reach the centre of the detector volume [Mit14]. The non-segmented PVT design is the β detector of interest in this thesis and is shown in Figure 2.6b.

BC-408 has a density of 1.032 g/cm^3 and is a charged particle detector with fast scintillation properties (0.9 ns rise time). The material is typically selected for its timing properties rather than energy spectroscopy. In the case of this work, the detector acts primarily as a β detector to be used for identifying β-γ coincidences with γ rays detected in the XArray.

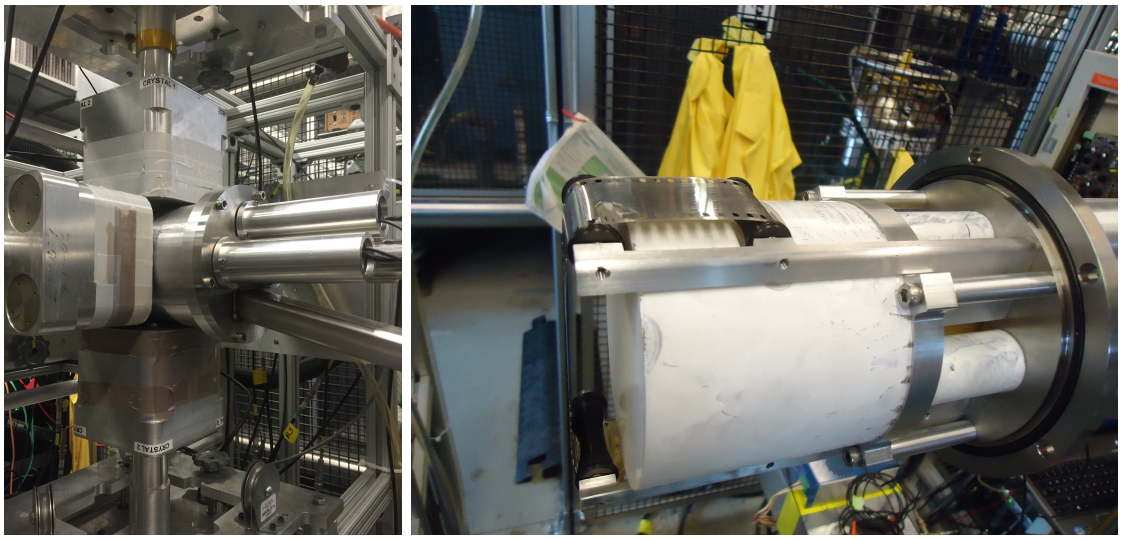

(a) (b)

Figure 2.6: The ANL XSAT and SATURN instruments. (a) The combined XArray and SATURN (XSAT) instrument installed at the CARIBU low-energy beamline. (b) The SATURN detector used in this thesis, shown with the aluminium top-hat removed. The single piece of PVT scintillator and the light guides (see text) are coated in a reflective teflon paint. The low-energy beamline enters SATURN from the right-hand side in each picture.

The plastic detector is housed inside of an aluminium top-hat that provides the vacuum housing coupled to the low energy beamline; it also provides light tightness for the scintillator. The top-hat is designed to sit in the middle of the XArray, minimising the attenuation to γ rays while providing an approximate solid angle of 98% of 4π for β detection [Mit14]. A brass collimator fits into a bore in the plastic detector, directing ions from CARIBU into the central volume of the plastic, where it deposits onto tape from the coupled tape station. Light produced in the plastic scintillator is collected by three PMTs located at the back of the top-hat via light guides. Figure 2.6a shows the combined XSAT

instrument with the SATURN top-hat installed.

The tape station

Two tape stations were commissioned by ANL at the time of CARIBU construction [Ber11] based around a previous design built by Louisiana State University [Mle81]. One tape station was built to be used as a permanent diagnostic tape station attached to the CARIBU low-energy beam line. This tape station is coupled to two HPGe detectors and a β-particle detector. This instrument (of which the tape station is integral), is used to characterise the radioactive ions for both setting up CARIBU and for direct research. The other tape station was built for general-purpose experiments with detectors such as ATAGS and SATURN.

Radioactive ions from CARIBU are implanted onto aluminised mylar tape provided by the tape station in the form of a long, continuous loop. The implantation can occur at the centre of an instrument, as is the case with the SATURN β detector, or the ions can be transported into a detector at some distance from a remote implantation location, such as was done for ATAGS. The tape and the timing of its movement can be utilised to control the source being measured, removing longer-lived progeny that are not of interest from the selected beam.

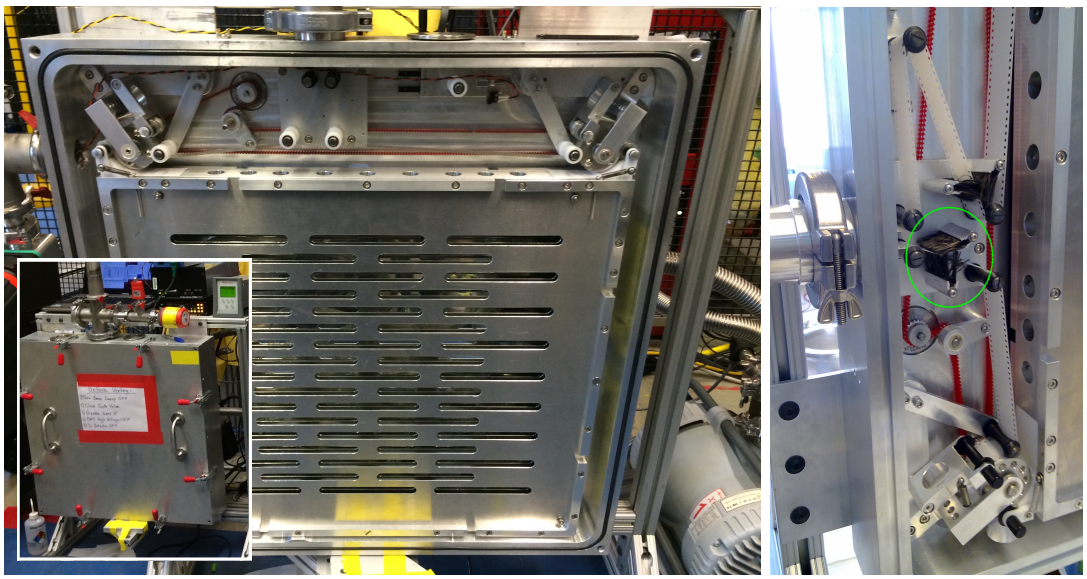

(a) (b)

Figure 2.7: The CARIBU tape station; (a) the general purpose tape station (used with SATURN and ATAGS) with cover removed and closed (inset), and (b) the diagnostic tape station with a close up of the tape. Both pictures show the tape cassette (largest component) and guiding pulleys with drive chain [red]. The diagnostic station is oriented at 90° to the general purpose station and shows the tape grounding brushes (circled).

Figure 2.7 shows (a) the general purpose tape station and (b) the diagnostic tape station, both with the front covers removed to show the components. The tape stations differ in a couple of components and the orientation. Inside the large vacuum box is a continuous loop of tape, with the surplus length stored in a cassette box that has many

machined slots to allow the escape of gas; this is shown as the largest item in Figure 2.7(a). A system of drive and guide cogs can be seen at the top of Fig. 2.7a and the middle of Fig. 2.7b in the tape station box; they move the tape through the system while keeping enough tension. The evacuated beam pipes containing the tape also use free-wheeling guiding pulleys to assist the tape through its intended path and maintain tension. The movement of the tape is done via a computer control program that operates a single drive motor; the mechanical energy is transferred to the drive cogs via the red plastic chain seen in Fig. 2.7b. The entire system is under high vacuum (<13 mPa) achieved via integrated turbo vacuum pumps [Mit14].

A computer control program is used to set up the duty cycle of the tape movement, involving a sequence of beam-on, tape movement and collect sequences. The parameters required for the controller are the timing, speed and length of tape movement for each cycle. The computer also controls an electrostatic kicker trigger that can switch the flow of ions arriving at the low energy beam line from CARIBU in sync with the timing of the tape movement. The resulting triggers from the tape controller are sent to the data acquisition system.

The tape can be replaced so that long-lived radioactivity can be removed and not affect the experiment. The overall length of the tape can also be modified, altering the time before the tape recirculates to be used again. In most cases the tape is coated with a thin layer of conductive metal on one or both sides (often aluminium). For the XSAT experiment in this thesis, 35 mm width aluminised tape was used. Conductive tape is utilised to remove the static charge that can build up over periods of moving the plastic tape through the sequence of teflon pulleys. The charge build up can adversely affect the implantation of the charged ions onto the tape. In the case of the diagnostic tape station, the static charge is grounded by using conductive brushes circled Figure 2.7b. Conductive tape was not used for the ATAGS measurements of Chapter 5.

2.5 Summary

Important aspects of the experimental observations depend on complex phenomena that occur in the detectors and cannot be measured directly. As just one example, β decay from the ground state in the parent to the ground state in the daughter does not emit any γ rays, so that evaluation of the intensity of this branch is not possible using the γ-ray detectors alone, or is only able to be determined by deduction of missing intensity. On the other hand, direct observation of the β branch in a detector like SATURN suffers from the complex nature of the system, so that evaluation of, for example, the β-detection efficiency, is quite difficult from experiment alone. A key outcome of this thesis is recognition of the importance of Monte Carlo simulation of radiation transport in complex nuclear physics detector systems. The next chapter describes the basics of Monte Carlo modelling, especially using the GEANT4 framework, before moving on to describe the details of all the Monte Carlo models that were developed as part of this thesis research.

Chapter 3

Monte Carlo Models

Monte Carlo (MC) simulations are commonly applied to many areas of physics research. Developed around 1940, they were first used to model the transport of nuclear particles and radiation through matter [Met49]. A MC model is essentially a random number generator providing bounded variable inputs to a physics-based model. For example, modelling the path of a γ ray in a detector would use a random number as input to the calculation of the mean free path in the first step. Individually, these steps do not provide much information, nor does the whole scattering path of a single particle, but looking at the statistical distribution of many paths can provide a good basis for comparison with experiment.

3.1 GEANT4

GEometry ANd Tracking 4 (GEANT4) is a MC transportation code that was developed in the late 1990's as a CERN collaboration, initially by the high-energy physics community [Ago03, All06, All16]. Based on the object oriented language C++, GEANT4 is an update of the FORTRAN-based GEANT3. GEANT4 allows for a generic framework within which a number of models covering a range of processes and energies can be applied to many areas from high-energy physics to DNA simulations.

GEANT4 was chosen for the modelling of the ATAGS and XSAT detectors due to the flexibility of the code and the suitability of the physics classes that it employs [CERa]. Many other projects involving the modelling of γ-ray intensities in detectors have used GEANT4 including AGATA [AGA], GRETA [GREa] and other TAGS type detectors [CO99a].

The first major work of this thesis focused on modelling the response of the ATAGS and XSAT detector systems using GEANT4. The ATAGS model will be used to interpret the complex experimental γ-ray response, in order to obtain β decay feeding intensities (I_{β^-}). There has been considerable effort directed towards reproducing many features of the detector as the uncertainties of the derived Q_β values will be limited by the accuracy of the modelling. Many versions of the ATAGS simulation have been developed over the course of this thesis with increasing complexity as more physical properties are included. The other major modelling effort revolves around the prediction of the β-particle detection efficiency for the SATURN detector and the γ-ray detection efficiency of the XArray.

A brief overview of GEANT4 is provided in the following subsections as it pertains to the options included in this thesis. It is not intended as a complete reference guide to GEANT4, since detailed information can be found online [CERa]. In the following overview, examples are given for the ATAGS. Later sections describe both the ATAGS and XSAT models in more detail.

3.1.1 Detector construction

Detector construction is the class* where the elements and materials used in the simulation are described and built. Starting from chemical element building blocks, such as Na and I, the materials or compounds in the detector are described, e.g. NaI(Tl). The materials are then assigned to make up the logical volumes of objects that are constructed using various built-in shapes. These objects are then placed in the "World" volume. In this way, complex geometries and materials can be produced from basic shapes and elements.

A common problem with building models of detectors is the inability to measure internal dimensions of components, particularly when there is no documentation. In the case of ATAGS, all of the dimensions have been taken from references from the group that originally commissioned the detector [Gre92b, Hel94b]. For the XArray, most of the major dimensions have been obtained from the manufacturers specification, but some key details are missing.

The NaI(Tl) material in the ATAGS model makes up the bulk of the detector volume. A nominal thallium doping of 1 x 10^{-3} mole fraction is used in the simulation, corresponding to approximately 0.136% mass fraction. The NaI(Tl) is enclosed in an aluminium can on three sides and a glass SiO_2 window on the rear of the detector. A silicon detector is placed in the well, while a thin section of aluminium plate placed adjacent to the SiO_2 window acts as a simulated photocathode. The DetectorConstruction is also the place where the active detector volumes (SensitiveDetectors) are defined (see Sect. 3.1.3). The OpenGL rendering of this constructed detector is shown in Fig. 3.3.

The models in this work include the possibility to simulate optical photons produced in scintillation processes. To accommodate this, additional properties such as the refractive index as a function of the photon energy are manually defined for each material and boundary interface.

3.1.2 PhysicsList and PrimaryGeneratorAction

The PrimaryGeneratorAction is a mandatory class defining the method by which particles are generated. The base class is a gun that fires mono-energetic particles in a defined direction. The models in this work use the General Particle Source (GPS) class that allows the user to fully define the energy and direction of the emitted particles. The standard particle-gun class is also implemented at times to accomodate externally generated input files where the particles, energies and directions are defined explicitly. The running mode and associated header information that is required for these modes are software selectable.

The PhysicsList class allows the user to define the properties and behaviour of the particles or photons that will be used in the simulation. For example, an electron is first defined using either the provided particle details or a modified version, then the physical behaviour of this particle is associated to physics modules, for example multiple scattering.

There are a wide variety of physics modules available, usually written by groups that focus on a particular energy range. For the ATAGS model, the low energy Penelope or the Livermore physics modules are employed. Various cuts are applied in the model to limit the computation time. Some of these are: the production cuts limiting the modelled

*A class in this context is a C++ class, which is a user-defined declaration that involves data and functions. A specific example for detector construction is the building of shapes, a box would include the dimensions a, b and c (the data) and a function"G4Box(x,y,z)" would create a box of size x, y, and z, where the data a,b,c replaces x,y,z.

energies from 250 eV to 100 GeV, the default cut for the loss table manager is 0.01 μm, and the maximum photons per step is 100. Also implemented in the PhysicsList is the Radioactive Decay Module (RDM). This is a module that allows the creation of a radioactive ion as the source of particles. It uses input files that define the decay paths and intensities (Radioactivedecay file) and an additional file (Photoevaporation file) to handle the subsequent transition(s).

The data in the RDM input files are obtained from Evaluated Nuclear Structure Data Format (ENSDF) database [ens], which is refreshed to the latest data with each new version of GEANT4. The advantage of using the RDM, is that the total response to a decay is treated in a single "event" (see EventAction and SteppingAction in Section 3.1.4 for the description of a "event"), with all of the particles emitted in the decay (γ's, β's, IC e^-'s etc) handled without the need for them to be defined explicitly. Note however, that if the desired nuclide is at the limit of existing measurements, there will be no evaluated information in the ENSDF database and the RDM module will be of little value.

The standard optical photons from GEANT4 were utilised in these models as a way of exploring the effects of photon collection on detector efficiency and other behaviour. It is noteworthy that the use of this standard method to model more complex optical physics requires externally generated models that would incorporate more complete optical processes.

3.1.3 SensitiveDetector

A SensitiveDetector is a specified material or volume in the geometry that is of particular interest. For example with reference to the ATAGS, the NaI(Tl) volume would be defined as a SensitiveDetector, allowing information on the interactions and processes occurring in that volume to be extracted. It is first defined in the DetectorConstruction and usually follows a particular logical volume, such as the silicon detector. When a particle or photon interacts with this volume, the associated SensitiveDetector class will be called. In this class, information about the interaction or hit (for example, energy deposition) can be accumulated.

The ATAGS model contains sensitive volumes for the NaI(Tl), the silicon detector and the aluminium plate that acts as a simulated PMT. The NaI(Tl) SensitiveDetector uses an energy-deposited method from the step class (see below) to determine the detector response to a particle interacting within it.

3.1.4 EventAction and SteppingAction

A "step" in the simulation is a single transport of a particle or photon followed by an interaction. An event consists of the variable number of steps that result from the initial particles or photons. For example, if we take the case of a γ ray of initial energy E_0, then the first step may involve Compton scattering and the production of a Compton electron together with the scattered γ ray. The following step tracking the scattered γ ray could consist of another Compton scatter or a photoelectric absorption, and so on, until there are no more interactions. The simulation will then back track and pick up the first Compton electron and systematically follow this through all of its steps. The resultant total steps from the initial, and subsequent secondary particles are collectively defined as an event.

The EventAction and SteppingAction classes are user classes that are called after each event and step respectively. They allow for the addition or extraction of information at these levels. In the case of the TAGS model, information that is produced by the RDM is

extracted at the step level and passed to the EventAction. The EventAction accumulates all of the relevant information from the SensitiveDetector classes and the SteppingAction, and passes this bundle to the RunAction where it can be written to an output file.

3.1.5 RunAction and Output

RunAction is the final user action class called in this model. Its main purpose is to collate the data and write the results to an output file. In the present simulation, information is written in a binary format to minimise the size of the output file.

The output written for this work consists of three word components of data containing 4 bytes (32 bits) each, designed to align with standard memory boundaries. The first 32 bit word is further broken into fixed smaller sizes of 2, 8, 4, 2 and 16 bits. This allows different information to be passed using the same 12 byte structure (3 x 4), identified by the sub-components in the first 4 bytes.

The format of this structure is shown in Figure 3.1, with the columns representing the different definitions signalled by the value of part 1. Parts 1 to 4a make up the first word and part 5 and 6 make up the second and third words. The types of information include a header marker, a new event marker, the Radioactive Decay Module (RDM) or gun emitted information, the Sensitive Detector (SD) recorded and a time stamp. The header defines the total events expected in an entire data set when using the RDM module, this way the total number of events generated at the beginning of a simulation can be captured. The text of the header follows this marker and by default contains three lines of text (40 characters long) being descriptors and version details of the simulation, and three integers for the number of events intended on being simulated, the number of detectors used and the spectral length. Additional lines of text can be added to the header through the use of part 2 of the header marker, but these text lines are limited to a size of 40 characters each.

The new event marker signals the beginning of a new event and contains the number and type of events that are contained within the event, which is also the number of words that follow. Part 2 indicates the number of optical-photon detectors that were triggered (have hits recorded) in the event, and hence the expected number of lines to follow the event marker. Similarly, part 5 indicates the number of RDM or gun emissions that were generated within the event, for example, the decay of ^{60}Co would generate 3 RDM emissions, 1 β and 2 γ's. Part 6 indicates the number of triggered detectors that had either a standard energy deposition event recorded, or have recorded optical photons.

The RDM or gun information contains the type of particle generated/emitted by the RDM or gun and the energy of that particle. This information has to be extracted from the RDM module in a convoluted way by identifying the original emissions amongst all of the tracks generated. The final event type is a Sensitive Detector (SD) hit record that contains the detector and element numbers for the hit, recorded as an energy or a number of photons. To implement a non-proportionality correction in the data, referred to here as the Cano-Ott correction (see Section 4.4.2), the energy before and after a step is recorded along an entire track. The Cano-Ott flag is used to record all SD hits along each track and is activated in the EventAction include file by hard coded flags. The flags used for the type of information are shown in the new event marker, part4. The result of activating this Cano-Ott flag results in getting an SD word triplet (12 bytes) for every step, significantly increasing the overall output file size.

The event information is recorded sequentially in the order that GEANT4 processes

			Event line information type depending on part 1			
word	data part	size [bits]	header marker	New event marker	RDM/gun emitted	SD hit recorded
1	part 1	2	3 [11]	0 [00]	1 [01]	2 [10]
	part 2	8	number of text lines (40 char length) in the header	number of PMT event lines	emitted: 0 [000] - ion 1 [001] - e^- 2 [010] - e^+ 4 [100] - α 5 [101] - γ 6 [110] - $\bar{\nu}_e$ 7 [111] - ν_e	Detector number
	part 3	4	-	units 0 [00]- MeV 1 [01]- keV	-	Detector element
	part 4	2	-	[x1] optical flag [1x] Cano-Ott flag	-	Energy type: 0 [00]- energy MeV 1 [01]- energy keV 2 [10]- optical photon 3 [11]- time stamp
	part 4a	16	spare	spare	spare	spare
2	part 5	32	-	RDM/gun event lines	-	Intial energy (Cano-Ott flag 1)
3	part 6	32	total events expected	SD hit event lines	Emitted energy	Energy deposited OR optical photon counts

Table 3.1: Data structure used for the Monte Carlo simulation output. A data item or line consists of three binary words of 4 bytes each (32 bits). The first word is sub-divided into 5 parts of fixed lengths (part 1, part 2,..., part 4a). The type of information contained in the event line is determined by part 1 of the first word. Event line information can be collated and written in various ways including a) all SD hit steps along a track (case when the Cano-Ott flag is 1) or b) simply the final summed energy. If the SD hit record part4 includes a time stamp, an additional 2 words follow the existing structure where the entire 64 bits of the 4^{th}+5^{th} word is combined into a time-stamp. In this way, the size of the words are not changed. Complete details in the text.

this information. Figure 3.1 shows the interpreted text output of the binary files produced with the ATAGS model for 10 events, each line represents the 3 words with a) an example of the optical photon output, and b) the output with the Cano-Ott correction active. As an example, after a new event marker we expect to see information from a RDM/gun and all of the resulting SD hit records in each detector associated with that emission. If there is a second emission, then this would repeat in the same way. The relative position of the hit records is associated with the emission that produced the hit, allowing the splitting of components of a decay into parts. For the examples provided in Figure 3.1, the β emission is not detected by any of the detectors as it is low in energy.

To ensure there are no rounding issues, the energies are expanded across the full 32 bits by use of the spectral length parameter given in the header. This is then converted when being read in. The data format can also be used for experimental data and scripts were written to convert experimental data to the format in Table 3.1. Often the events in experimental data include a time stamp which has been implemented by the addition of 2 words that follow the existing structure where the entire 64 bits of the 4^{th}+5^{th} word is combined into a time-stamp. This is triggered when the SD hit record part4 includes a time stamp. In this way, the size of the words are not changed.

3.2 ATAGS model

The ATAGS model was built and updated across many years and incorporates the various versions as GEANT4 code was updated. The current simulation code is written for GEANT4.10.2.p03 on linux and includes optical photons and the ability to change the physics list from a macro file. The options discussed in the previous sections have been incorporated into a basic model which then has the unique detector construction added. The schematic for the ATAGS detector is given in Figure 3.2. The dimensions have been guided by publications from the INEL group who originally commissioned the detector [Gre92b, Hel94b].

The openGL rendering of the resulting simulation of ATAGS in Figure 3.3 shows the various components as the outer materials are made progressively transparent. A section of vacuum pipe is added into the well of ATAGS to match the experimental setup of the commissioning experiment (see sect 5.1.1). Figure 3.3b shows the well of the detector and the aluminium outer can that encloses the NaI(Tl) scintillator crystal.

A dead layer was added to the simulation, consisting of a thin layer of inert NaI(Tl) material in the well (shown as yellow in Fig. 3.3). The thickness of this layer can only be determined through the matching of simulations to experiments for low energy X or γ rays. The dead layer was added to the simulation with a variable thickness, that allowed the adjustment of the layer for comparison with experiment. The dead layer essentially only affects the low energy components, which becomes less significant as additional attenuation material is added from the vacuum pipe housing the implanted tape. As the TAGS method is predominantly used for the measurement of nuclides with large $Q(\beta^-)$ values, the low energy threshold matching in the simulation is not critical to the success of the method.

The optical photons are collected via aluminium disks that act as photocathodes (shown in Fig. 3.3d). The size and location of these pseudo photocathodes match the physical ATAGS as shown in Figure 2.4. When an optical photon touches the pseudo photocathode material, the optical photon is counted and the photon killed. Properties of the photocathode material can be added in the detection process such as the quantum efficiency.

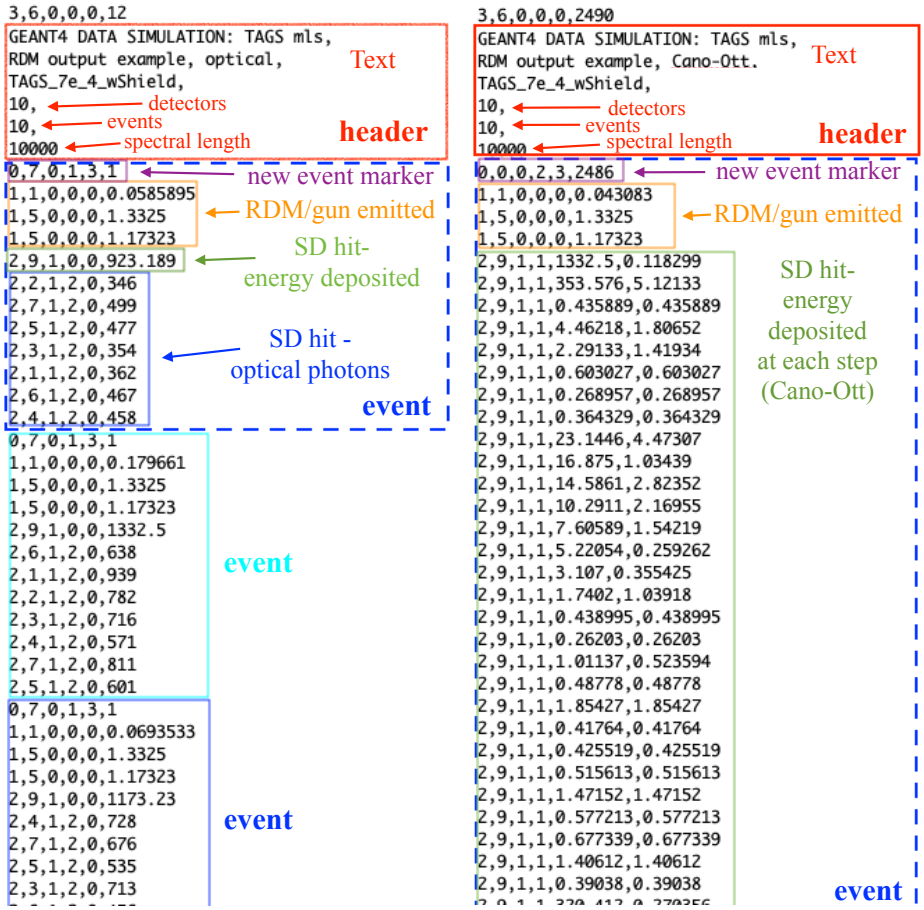

Figure 3.1: Example of text data output showing the format for 2 cases of the ATAGS model with a ^{60}Co source, showing a) an optical example and b) when Cano-Ott correction is implemented. The binary data is decoded as text above, with each line representing the 3x 32-bit words. Detector 9 is the summed energy deposited in ATAGS, while detectors 1 to 7 are the individual tubes. 10 events are generated in these examples.

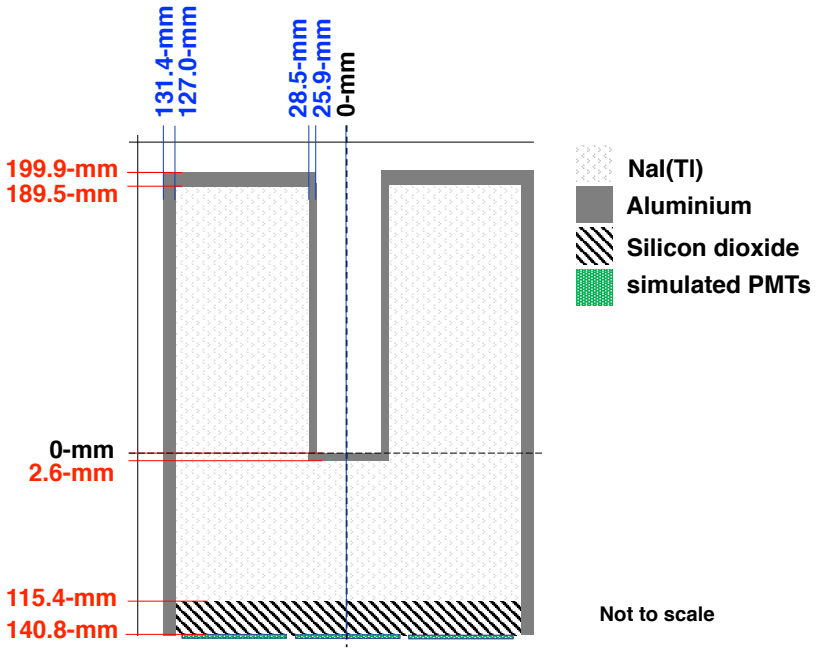

Figure 3.2: Simplified schematic of the ATAGS detector showing the composition and dimensions (not to scale). Internal dimensions based on Greenwood [Gre92b].

The shielding had not been included in most simulations as it had not been designed at the time of the majority of the simulation work. The shielding that was used at CARIBU for the commissioning experiment was built by UMass Lowell[†] (Figure 5.2, and Section 5.1.1) and was added to the ATAGS model at a later stage. Figure 3.4 shows the OpenGL rendering of the lead shielding that was added to the model after the commissioning work to match the experiment.

In the vicinity of CARIBU, the ^{252}Cf source and residual radiation from slits and beam stops contribute to the background radiation. The experimental background is complicated and always changing and there is little value in attempting to simulate this when it can be measured and subtracted experimentally. A very good approximation can be made with no shielding enclosure materials included in the simulations as most effects are removed in the experiment with background subtraction. The exception is when the source to be measured is introduced inside of the shielding enclosure, since then the backscattering and bremsstrahlung from interactions in the shielding material are not accounted for. The discrepancy between the simulations with and without shielding will be in the back scattered γ rays and bremsstrahlung from the extra material surrounding the detectors.

3.3 XSAT model

A Monte Carlo model of the XArray and SATURN detectors (XSAT) was built using GEANT4.10.2.patch03. The XArray consists of four standard clovers, labelled as "A", "B", "C", and "D" and a larger super clover labelled "S" (see Section 2.4.1 and Fig. 2.5).

[†]UMass Lowell The University of Massachusetts, Lowell

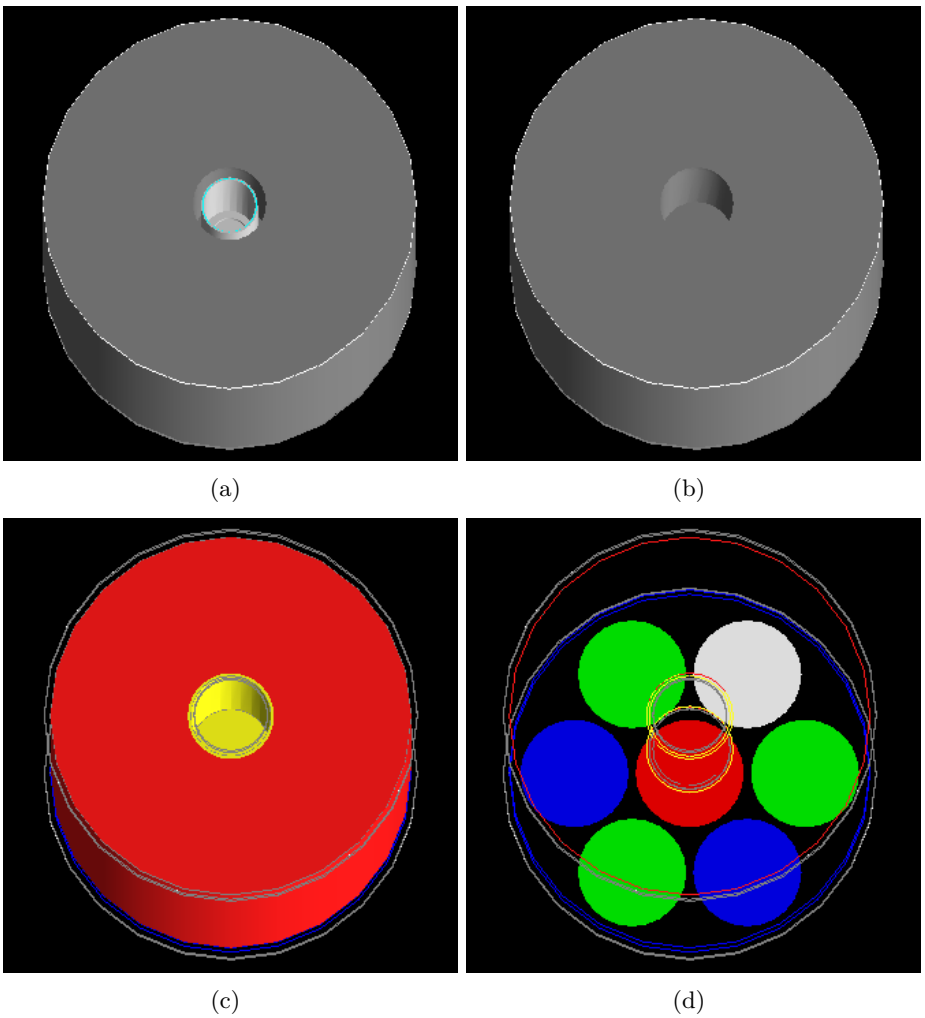

Figure 3.3: OpenGL rendering of the ATAGS simulation showing the sequence of outer components removed; (a) the detector (dark grey) with the vacuum pipe inside of the well [light-grey], (b) the bare detector, (c) the NaI(Tl) volume with the active sensitive detector [red] and the well dead layer [yellow], (d) the 7 light collection PMTs for the optical-photon simulation. Viewed from the front - in an anti-clockwise direction are PMT 1 [white], 2 [green], 3 [blue], 4 [green], 5 [blue], 6 [green] and 7 [center - red].

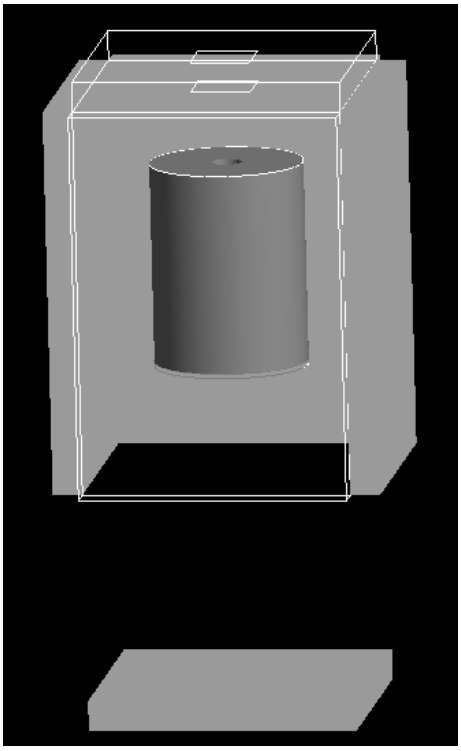

Figure 3.4: OpenGL rendering of the ATAGS simulation showing the location of ATAGS relative to the shielding. The top and one side of the lead has not been rendered so we can see inside (outlined in white). This is the shielding designed by UMass-Lowell and used for the ATAGS commissioning experiment at CARIBU.

The standard clovers 'A' to 'D' were built as copies of each other and the super clover "S" was a later addition to be positioned in line with the beam axis. The super clover has larger crystals (70 mm diameter) compared to the standard clover crystals (60 mm diameter) but they are housed within the same sized vacuum can. The differences between the standard and the super-clover crystal shapes are shown in Figure 3.5. The High Purity Germanium (HPGe) crystals of each of the clovers are coaxial in shape with two sides cut off to fit them closer together. The central contact is used to hold the detectors in place. The specific engineering of the mounting of these detectors is guarded by Canberra as proprietary information. Canberra did provide some details of materials and thicknesses required to simulate the bulk materials without divulging proprietary information. The outer aluminium housing shape was simplified to a cube at the corners as this would not significantly change the amount of material in the simulation.

When XSAT is used, the SATURN detector is installed onto one of the CARIBU beamlines making up part of the vacuum system. The main components are a brass collimator directing beam onto a tape that is surrounded by a plastic scintillator. Figure 3.6 shows a picture of the SATURN detector with the outer aluminium can removed to show the plastic detector, the materials used to mount the plastic and the tape. This is compared with the openGL rendering of the simulation with the various outside components being made progressively transparent.

All of the component dimensions in the simulation were built from the dimensions given in technical drawings where available. A number of key dimensions were not provided; in this case an approximation is used and the results compared to experiment for validation (see Chapter 8). The model is placed in the world volume such that the beam implants onto the tape at the origin (the green lines in Fig. 3.6 indicate the X=Y, axis, Z=0, starting at the origin). The individual clovers can be positioned independently and the model has the ability to simply remove the detectors from the experiment by means of hard-coded flags. Note the orientation of the individual clovers relative to experiment may differ. The active detector of SATURN will be referred to as the "plastic detector" or simply "plastic". Figures 3.7 and 3.8 show the positioning of the SATURN detector within the XArray.

As described earlier (see Section 3.1.2), the model can utilise the Radioactive Decay Module (RDM) to produce complex decay events in addition to single emissions from the GEANT4 particle gun utilised via a macro file or command line. A hard-coded flag switches between these two input options. The RDM modules uses a library of radioactive data to produce a "decay"; the information is sourced from ENSDF files that are harvested for information at the time of the GEANT version update. Macro files for modelling β-decay using the particle-gun option can be generated by a Beta Decay (BD) program written by LLNL [Sci].

Data is output via a custom written binary list format that includes information on the simulated event and the individual responses in each detector (see Section 3.1.5). For further analysis, the individual interaction hits making up these events can also be collected. The data is analysed and converted to ROOT or RADWARE file format via sorting scripts written in C++ that are callable using PYTHON.

The final Figure 3.8, shows the comparison of a picture of XSAT at CARIBU with the entire simulation rendered.

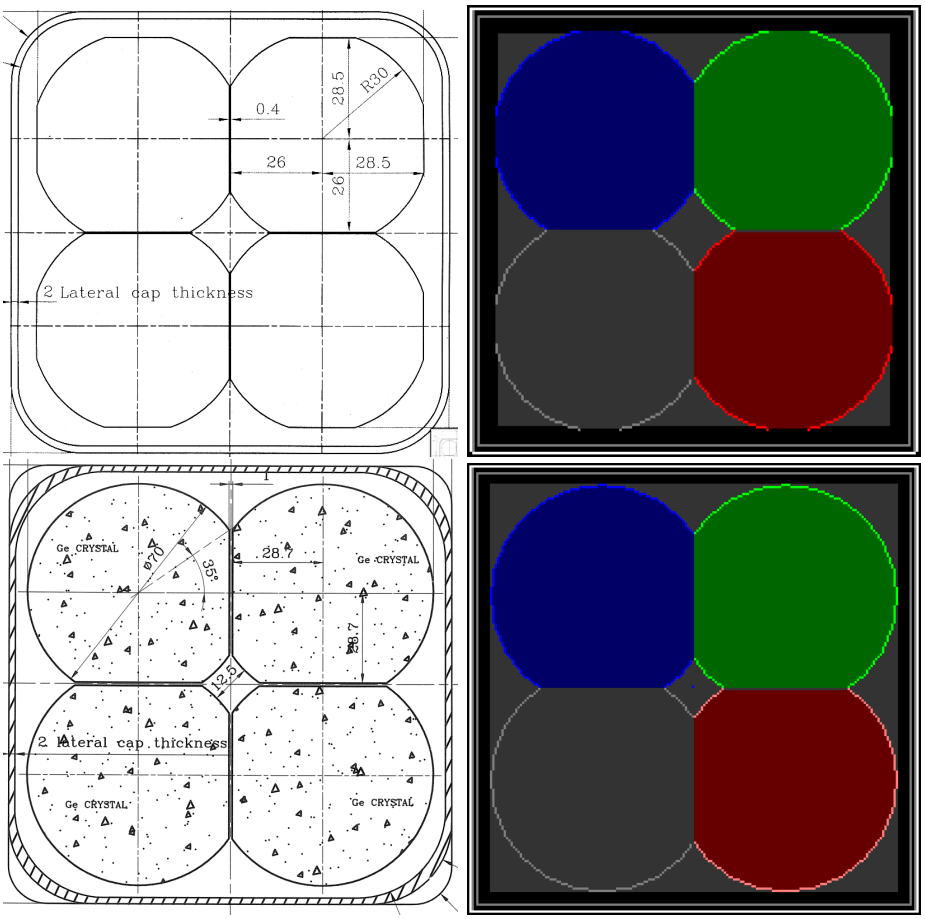

Figure 3.5: Comparison of the XArray Clover detectors specifications (left) with the simulation visualisation (right) for the standard clover (top) and the super clover (bottom). The clover leaves in the simulation are coloured differently to distinguish the orientation (Clover leaf 1-[grey], 2-[red], 3-[green] and 4-[blue]). The super clover (bottom) has larger crystals (70 mm diam.) compared to the standard clover (60 mm diam.). The highlighted lines surrounding the crystals indicate the simulated dead layer and the grey aluminium cooling plate is shown in the background behind the crystals.

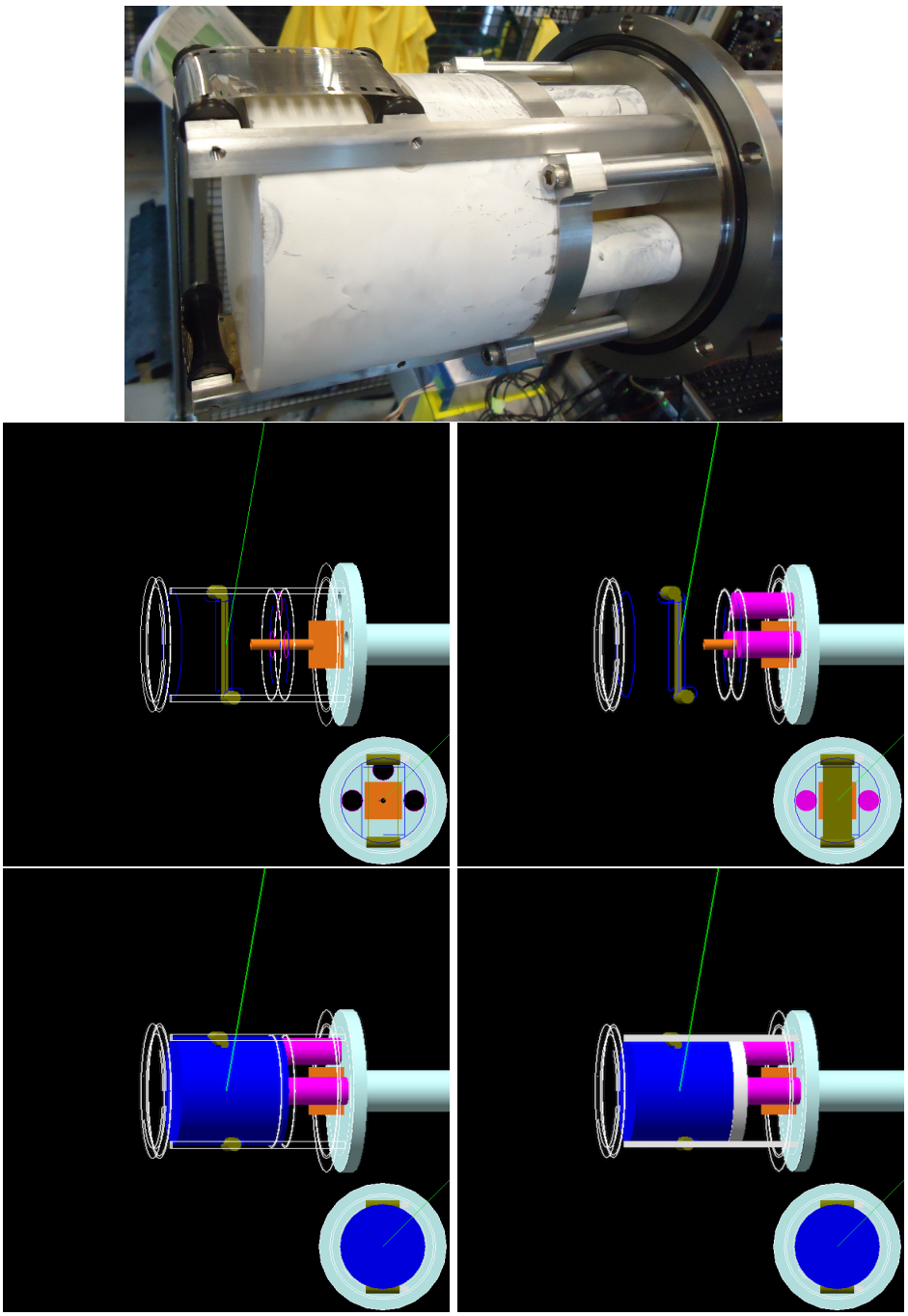

Figure 3.6: OpenGL rendering of SATURN and its components compared with a photograph. The SATURN simulation visualisation has the components made progressively transparent, shown both from the side (beam direction is right to left through the beam pipe) and looking up the beam-line (inset for each panel). The X=Y axis is shown by the green line starting at X=Y=Z=0. [top] Photo of the SATURN detector with the top hat removed (repeat here for convenient comparison), [middle-left] the brass beam collimator [orange], tape and tape pulleys [brown] [middle-right] the light pipes [pink], [bottom-left] the plastic scintillator [blue], [bottom-right] the aluminium detector and pulley support structure [silver]. The PMTs are not displayed and would be seen on the right side of each figure attached to the light-guides.

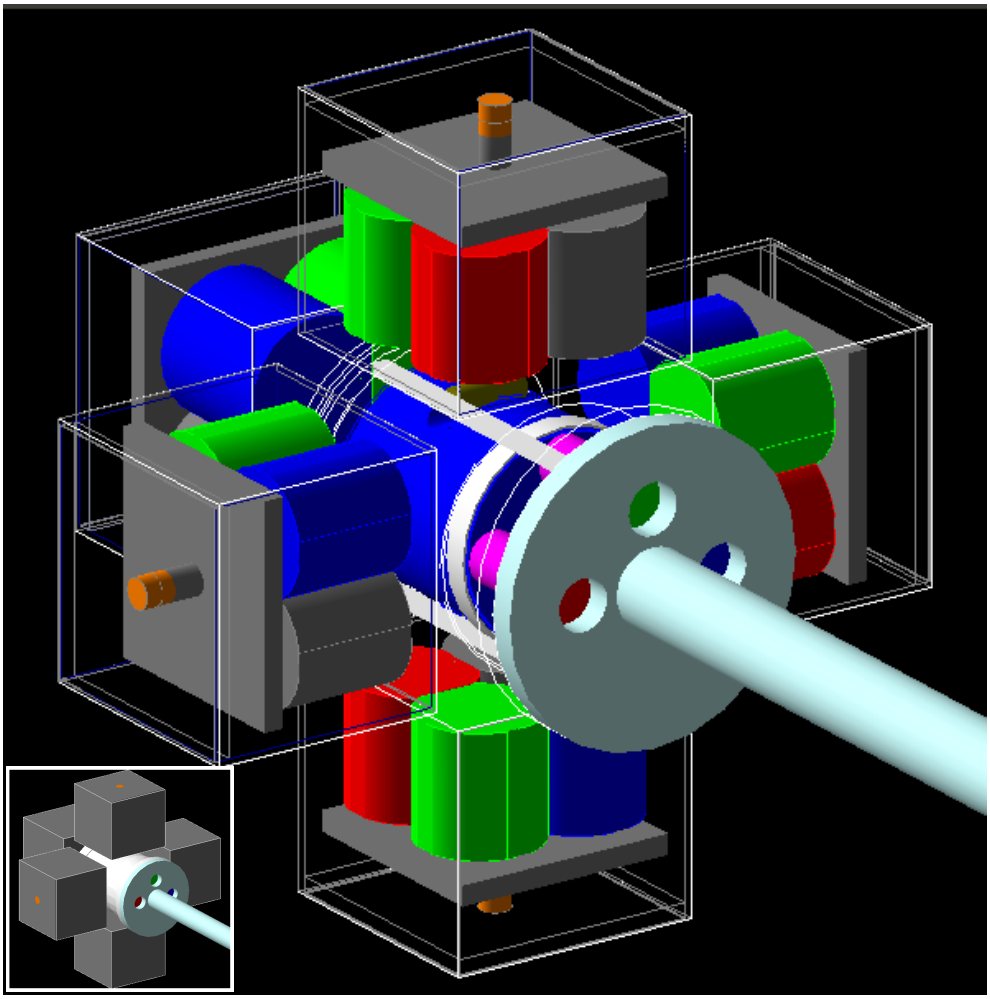

Figure 3.7: OpenGL rendering of XSAT showing the components of SATURN relative to the XArray. The array with outer materials visible is shown in the inset, while the large diagram shows the detector with the outer material transparent. The clover leaves are all made of HPGe but are coloured differently to demarcate the detector volumes and show the clover orientations. The SATURN PMT photocathodes are also coloured differently to distinguish the orientation for data output.

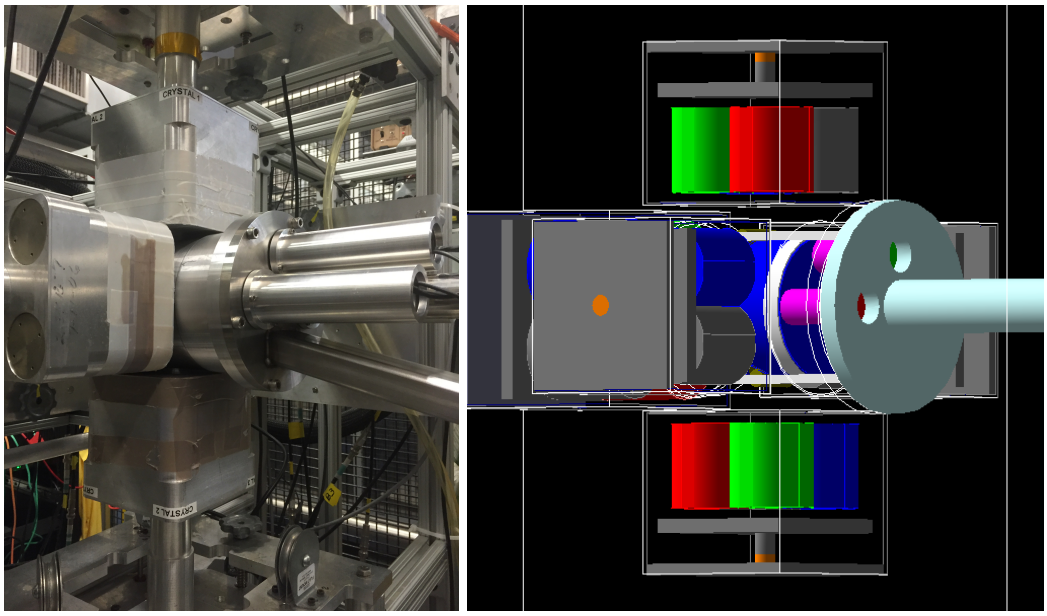

Figure 3.8: XSAT photograph compared to final simulation.

3.4 Model validation and experimental protocols

The Monte Carlo models developed in this chapter need to be validated against experimental data before they can be used in a quantitative way to evaluate and/or correct experimental observations. Chapters 4 and 5 describe the validation of the Geant4 model for ATAGS by comparison of the model outputs against sealed source measurements as well as full measurements with CARIBU radioactive ion beams that are well known and understood. With confidence in the model, some results for β-feeding intensities in new nuclei are presented in Chapter 7.

The validation for the XSAT model is given in Chapter 8, along with a discussion of how this model was applied to a number of experiments for extraction of important measured quantities. The new results, analysis and interpretation are given in less detail, since the author was not leading these experiments, in contrast to the ATAGS measurements.

Chapter 4

ATAGS characterisation and modelling

A large component of this thesis is centred around TAGS measurements using the Argonne Total Absorption Gamma Spectrometer (ATAGS) (see Sections 2.3 and 2.3.1). The ATAGS is a large cylindrical shaped NaI(Tl) detector with dimensions of 254 mm (diameter) by 305 mm (length), with a well of size 57 mm (diameter) by 190 mm in length located along the central axis (shown in Figure 3.2). Originally commissioned by a group at INEL in the early 1990's (see Section 2.3.1), the ATAGS was relocated to Argonne National Laboratory in Chicago around 2007 for the purpose of re-commissioning the detector and undertaking TAGS measurements at CARIBU (Sect. 1.2.2).

This chapter looks at the characteristics of NaI(Tl) scintillator detectors for γ-ray spectroscopy, specifically the ATAGS detector and the considerations required for TAGS measurements. The motivation for understanding and accounting for these characteristics is to gauge the complex processes and interactions that will be measured by ATAGS, to guide the experimental methodology, and determine measurement limitations. The other motivation is to accurately model all aspects of the detector and validate the model against experimental measurements. The Geant4 model described in Chapter 3 accounts for a large amount of physics for interactions and transport on an event by event basis. The characteristics investigated in this chapter are often not accounted for in the base model, requiring additions that then need to be validated. Ultimately, this model will guide the interpretation of the experimental TAGS data and the accuracy will impact on the overall uncertainty of the final results.

Physical access to ATAGS for characterisation measurements was limited due to it being primarily located at ANL in Chicago, with a period of time where it was at at UMass Lowell. Some preliminary characterisation work of ATAGS was undertaken in 2008 and 2010 during extended stays to ANL, consisting of several months. This period of time coincided with the building of CARIBU, which took priority over experimental instrumentation development. The next opportunity to access ATAGS didn't arise until the recommissioning in 2015. Experimental characterisation of NaI(Tl) to compare with modelling was achieved using several scintillator detectors of different sizes and design between gaining access to ATAGS. Information for testing the model was largely obtained from published data of ATAGS from when it was operated at INEL.

4.1 Digitisation of published data

In the absence of raw data from the ATAGS detector at the time of measurement, published data from ATAGS when at INEL was used to benchmark the earlier versions of the Geant4 model. Digitisation of the published graphs was achieved using a program called "Engauge Digitizer" [Dig]. The program works by importing a PNG image of the graph and overlaying the details by pointing and clicking. The axes scales are set at the beginning of the digitisation process and the results are produced in the form of a CSV file, giving (x, y) data positions relative to the set axes. All of the figures in Greenwood's 1992 paper use a log scale for the y-axis. This can produce significant errors when digitising a small image for points near the top of the graph. To reduce errors, PNG files of at least 1800 pixels/inch were used.

As an example of the digitisation method, Greenwood's measurement of ^{60}Co with ATAGS in 1992 is digitised (Figure 4.1) and compared to the original (Figure 3 of Greenwood [Gre92b]) shown in the inset of Figure 4.1. The spectrum shows ^{60}Co experimental data indicated by the dots; it has been collected in 'singles' mode. The solid line shows Greenwood's simulated data fit. The digitisation result is shown plotted in a similar scale to allow a visual comparison of the success of the digitisation process.

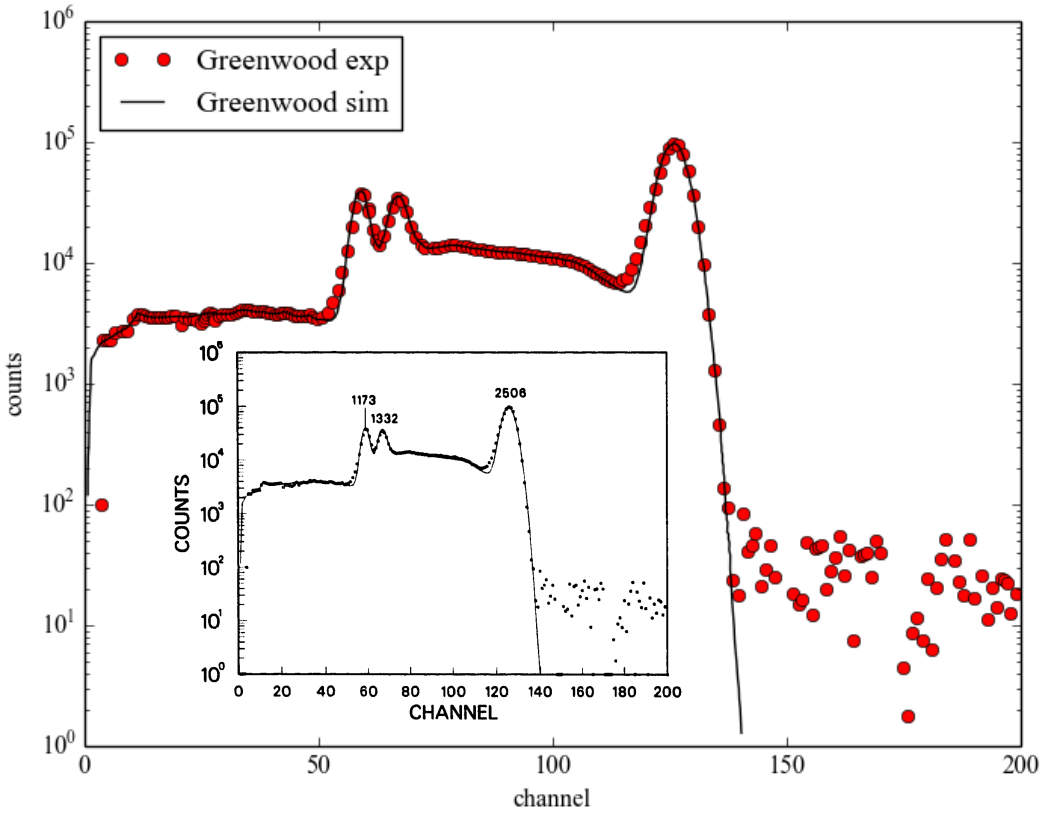

Figure 4.1: Digitisation of ATAGS ^{60}Co spectrum from Figure 3 in Greenwood *et al.* [Gre92b]. The inset shows a reproduction of the figure from the original reference for comparison.

4.2 NaI(Tl) scintillator detector design

Thallium-doped Sodium Iodide (NaI(Tl)) is a commonly used inorganic scintillator material first discovered and used as a radiation detector by Hofstadter in 1948 [Hof48]. It is inexpensive, easy to grow as large crystals, and is often used for large-volume, high-efficiency detectors that can be machined into irregular shapes. Sodium Iodide is an inorganic crystal that is hygroscopic* and as such, requires being sealed inside the detector "can". Thallium is added at a concentration of about 10^{-3} mole fraction to provide activation sites amongst the crystalline structure with the effect of producing scintillation light instead of energy being reabsorbed into the lattice.

The original RCA S83021E PMTs provided with ATAGS are a ten-stage hybrid potassium-cesium-antimonide (bialkali) dynode structure. They were designed by RCA in collaboration with Brookhaven National Laboratory (BNL) to make use of the entire photo-cathode area and increase the efficiency for use with a large NaI(Tl) detector [San84].

The ATAGS detector was built to undertake TAGS measurements, with the main design criterion being a large detection efficiency requiring a significant sensitive detector volume (see Sect. 2.3.1). The large volume can introduce some unique properties that need to be better understood before the TAGS method can be successfully applied. The basic properties of ATAGS were investigated directly at ANL whilst visiting Chicago.

In addition to the measurements with ATAGS, the characteristics of NaI(Tl) detectors were investigated through the use of a number of smaller scintillators, each having a different size, geometry, manufacturer and/or age. These detectors were used in lieu of access to ATAGS to measure the characteristics of NaI(Tl) as a function of geometry and design. The age and condition of each of the detectors varied giving a wide range of characteristics. This variety of detectors will identify and separate characteristics that appear in the spectrum. The detectors were given an abbreviated name according to the owner and their size in inches (diameter x length). They are ANL3x3, ANL4x4, ANU5x5 and ANSTOwell6x5. Further details of some of these detectors are given in Appendix A.

4.3 The ATAGS PMTs and gain matching

The 254 mm diameter surface of ATAGS requires seven 76 mm diameter PMTs to provide adequate light collection. When ionising energy interacts in the crystal, photons are created at the scintillation centres of the NaI(Tl); the number of photons is proportional to the energy of the interaction. The emitted photons transit the scintillator volume in all directions that, if not absorbed, will eventually interact with one of the seven PMTs creating seven individual energy signals that together represent a single interaction. To recover the original total energy for the event, these signals need to be combined. The magnitudes of the electric signals are dependent upon the PMT High Voltage. Although the PMTs are of the same type, the response of each tube is unique and must be taken into account when used to combine components of the total signal. The adjustment of the individual PMT HV's to give a consistent relative energy response will be referred to as Gain Matching.

The final ATAGS event response comes from combining the component analogue signals generated from the seven PMTs. The methods for determining the operating HV,

*Hygroscopic materials absorb water from the atmosphere.

gain matching and combination of these signals are discussed in this section in the context of ATAGS.

4.3.1 Operating high-voltage

The recommended operating HV of a PMT can be determined from the specifications given by the supplier as an upper limit and a range. In the absence of this information, the operating HV (and resultant gain) can be measured by experiment. Operating information of the RCA S83021E PMT was available on the internet [BII90]. The specifications give a recommended voltage of 1100 V, with a maximum of 1700 V between the anode and cathode. To test the functioning of these tubes, the values were determined by direct measurement. Using a fixed source to produce a suitable count rate, the number of counts above a low-level threshold is measured with a scaler, as a function of the HV. Figure 4.2 shows the HV response of the original ATAGS PMTs (type RCA S83021E), measured using a ^{137}Cs source placed at a fixed distance along the ATAGS axis to limit the overall detection rate so as to not introduce unwanted count rate effects into the spectrum. The numbering of the tubes is shown in Figure 2.4.

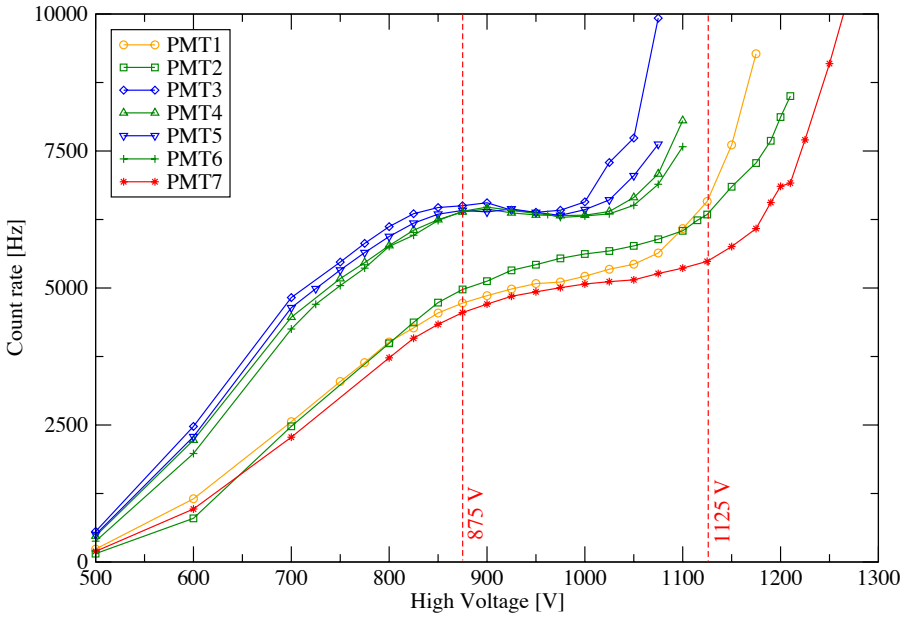

Figure 4.2: HV responses from original (type RCA S83021E) ATAGS PMT tubes showing the operating plateau of each tube. The operating region for PMT7 is shown. The responses were determined as described in Section 4.3.1, measured with a ^{137}Cs source placed at the front of ATAGS in a fixed symmetrical position.

The multiplication of the signal is generated by the interaction of primary electrons produced at the photo-cathode striking the dynodes. The electrons near the surface of the dynode will be free to interact in the potential and create additional secondary electrons at each dynode stage to create a signal representative of the original amount of light [Kno99]. When the photo-cathode is not illuminated by light, the PMT can produce an anode current from the multiplication of residual electrons through this biased dynode chain known as dark-emission or dark-current [bur89, Ham07]. The increase in dark-current

with voltage is not constant but increases with gain. The source of these electrons can be from various sources, including thermionic emission from the photocathode or dynodes, leakage current, scintillation from the glass envelope of the PMT, residual gas ionisation, or production of electrons from cosmic rays [Ham06].

Across the many stages of dynodes, the multiplication factor initially grows as the HV is increased. It hits a plateau once all of the photo-electrons emitted from the photo-cathode have been accelerated to the point where they are all multiplied through the dynode chain. The plateau region often shows a slight decrease in the gain as the potential increases, as a result of the increasing penetration of the electrons into the dynode material, resulting in reducing the number of secondary electrons available at the surface for multiplication. This is often offset by the dark-current gain of the tube across the plateau as seen in PMTs 3 to 6, compared to 1, 2 and 7, in Figure 4.2.

Beyond the plateau region is a sharp increase in the count rate response caused by the break-down of the potential between dynodes resulting in leakage current. Operating in this region can lead to damage via regenerative effects such as the creation of minute residual gases from components, production of scintillation light in the tube wall, stripping of metal from the photo-cathode, and the compositional changes to the materials that result from these processes [RCA, Ham07]. The HV response function can also be measured without a source to investigate the noise response of the PMT when under bias. This background function can then be used to better determine the start of the ideal HV operating range and provide signal to noise information as a function of bias voltage [Ham07].

Figure 4.2 shows the measured count rate response of each tube as a function of HV. The HV plateaux are typically in the range of 875 V to 1125 V and are shown for each of the tubes in Table 4.1.

ATAGS PMT	Measured HV plateau region
1	850 - 1050 V
2	925 - 1075 V
3	825 - 1000 V
4	875 - 1025 V
5	850 - 1000 V
6	900 - 1025 V
7	875 - 1125 V

Table 4.1: High-voltage plateau regions for the original PMT tubes (type RCA S83021E) used in ATAGS. Regions determined from measurement of the count rate response to a ^{137}Cs source as described in Section 4.3.1 (see also Figure 4.2).

The resulting values are in agreement with the nominal 1100 V power supply and 1700 V maximum limit. These tests show no obvious signs of PMT degradation.

4.3.2 Gain matching methodology

The HV bias on a PMT strongly influences the magnitude or gain of the measured signal. Provided that the bias is great enough to adequately produce a response proportional to the collected light (plateau region, see Section 4.3.1), the resolution of the generated signal will be optimised. For the case of a large detector with the light detection occurring via multiple PMTs, the relative gains of the individual signals needs to be also considered. Although the PMTs employed are of the same type and design, small variations in the

manufacturing, long-term use and degradation, result in unique responses. Gain matching is the fine-adjustment of the relative bias of each tube to obtain a comparable signal response which allows the combining of the signal components.

The use of a single large detector with multiple tubes is not very common, so the method of gain-matching is outlined here largely based upon a manufacturers recommended procedure [SG]. It involves the use of a simple γ-ray source with a well known spectrum such as ^{137}Cs or ^{60}Co. With the source placed in a symmetric position, the response of each individual tube is measured at a set HV. The smallest response and the largest responses are compared so that the lower and upper limits of relative HV adjustment range are determined. The remaining tube HVs can be adjusted to match the response while staying on the HV plateau (see Section 4.3.1). The original RCA S83021E PMTs had an additional gain adjust potentiometer built into the tubes to provide an offset to the HV, so that a single consistent HV supply can be applied to all of the tubes and yet they can still be gain matched.

An assumption of this procedure is that the PMTs share a symmetric view of the detector and are directly comparable. This is not the case for ATAGS with the central tube (PMT 7 in Figure 2.3) having a different view of the detector when compared to the outer tubes (PMTs 1 to 6 in Figure 2.3). Applying the above procedure to the outer PMTs, the central tube can be adjusted by the optimisation of a spectral feature such as the resolution of the ^{137}Cs 662 keV peak.

As ATAGS was acquired from another laboratory, the condition of each tube was unknown. The relative responses of the outer tubes can be directly compared if one assumes that the detector is homogenous. The gain adjustment using the above peak optimisation method may hide any damage the central tube may have. A more thorough comparison can be taken by removing tubes and sequentially coupling them to a smaller crystal and directly comparing the responses.

A direct comparison of the central PMT to an outer tube of ATAGS was attempted. By finding the only detachable NaI(Tl) crystal available at ANL, the ANL4x4, the process was first undertaken with another PMT to develop the procedure and minimise the risk of damaging the tube. The major issue was the discrepancy of the size of the three inch tubes to the four-inch crystal and the lack of a waveguide to couple the two together. The comparison is further complicated by variations in the quality of the coupling to the detector and exposure of the scintillator directly to light; these can be mitigated in principle, by using consistent methods.

The PMT tube 4 from ATAGS was removed and coupled directly to the ANL4x4 crystal after careful wrapping. The exposed surfaces were wrapped in black optical tape, covered in many layers of Aluminium foil and left for 24 hours to allow for deexcitation of the scintillator caused by direct light exposure. The energy resolution was found to be broad and the response sensitive to symmetrical source position shifts. It was determined that this particular crystal was not suitable for a direct comparison and rather than risk damage to the central tube for a non optimal test, this process was discontinued.

4.3.3 Passive summing of PMT signals

Passively summing is the coupling of each of the analogue PMT signals to each other by means of connectors (before or after pre-amplification). The signals from each of the PMTs are then summed by virtue of being connected to each other on a single cable. Greenwood, Helmer *et al.* [Gre92b, Hel94c, Gre92a, Hel94b, Gre95, Gre97] operated ATAGS with the

energy response collected via this method in all of their publications.

There are some assumptions required with using this technique to avoid introducing distortions or timing differences between the components. Significant delays between component signals can be avoided by using the same cable types, impedance and lengths. The passive summing of the signals can be done pre or post the first stage amplifier (pre-amplifier). The simplest method in terms of minimising equipment is to sum the raw PMT signals prior to the use of a single pre-amplifier, as implemented by Greenwood and Helmer *et al.*. Care must be taken to avoid transmission line reflections of signals at the point of combination, causing ringing in the resultant amplified signal, potentially dominating low energy pulses with this noise.

An alternative method is to passively sum the signal after the first-stage amplification requiring seven pre-amplifiers with matched shaping times. The advantage would be the combination of the signal at a higher gain reducing the overall noise. There would be a concern for fluctuations in the individual pre-amplifers relative to each with changing environmental conditions. The fundamental disadvantage of the variations of this summing method is the inability to monitor the relative stability or to make any corrections to this data once summed. An alternative data collection methodology is discussed in section 4.8.

4.4 Energy calibration and NaI(Tl) non-proportionality

The response of a scintillator detector is most often proportional to the amount of ionising energy deposited in the active crystal. The relationship between the energy and the response is usually represented in the form of

$$E = E_0 + E_1 C + E_2 C^2, \tag{4.1}$$

where:

E = known energy of the peak;
C = centroid of the peak response;
E_0 = energy coefficient 0 (offset);
E_1 = energy coefficient 1 (linear); and
E_2 = energy coefficient 2 (quadratic).

This function is often simplified to a linear equation with $E_2 = 0$. The calibration of this response (in terms of γ-ray energy), is achieved via the use of commonly used nuclides such as ^{137}Cs and ^{60}Co. Figures 4.3 and 4.4 show the ATAGS spectra for ^{137}Cs and ^{60}Co with the associated decay schemes. Cs-137 decays to stable ^{137}Ba by β^- emission, most often via a single γ-ray emission at an energy of 662 keV. Co-60 decays to ^{60}Ni via a β^- emission, and predominantly via two sequential γ rays of energies 1173 keV and 1332 keV (Fig. 4.4(b)). As the energy resolution of NaI(Tl) is broad compared to HPGe, calibration sources that emit one or two predominant γ ray lines are used for the calibration so that multiple peaks do not overlap in a spectrum.

There are three additional considerations for the energy calibration of NaI(Tl) scintillator detectors: the change of the energy calibration due to count rate effects, the stability of the energy response as a function of temperature, and the deviation from linearity. The shifting of the energy spectrum due to count rate effects will be dealt with in the following section (Section 4.7), the latter two will be discussed here.

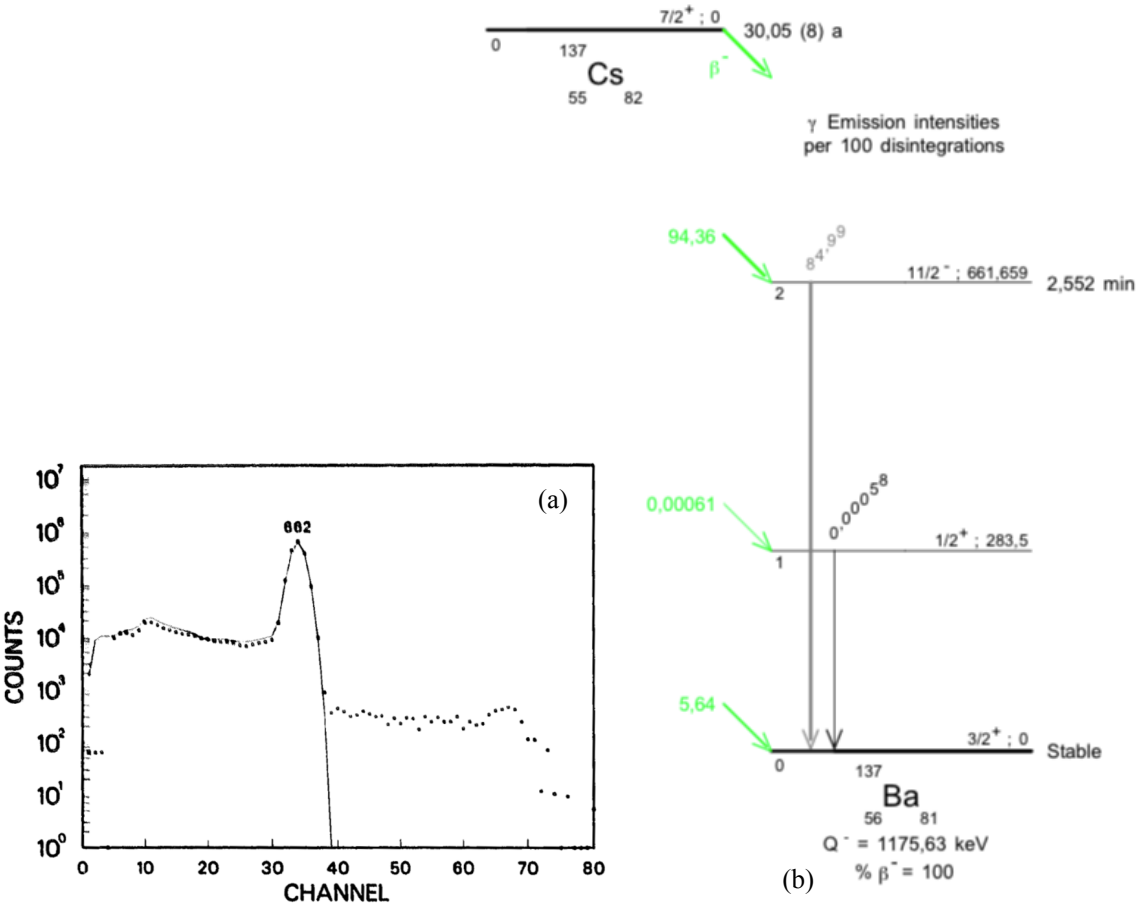

Figure 4.3: ATAGS measured ^{137}Cs spectrum and associated decay scheme. (a) Figure 16 reproduced from Greenwood *et al.* [Gre92b] shows the measured spectrum (points) and calculated fit (solid line) [20 keV/channel]. (b) The decay scheme of ^{137}Cs reproduced from DDEP [LC].

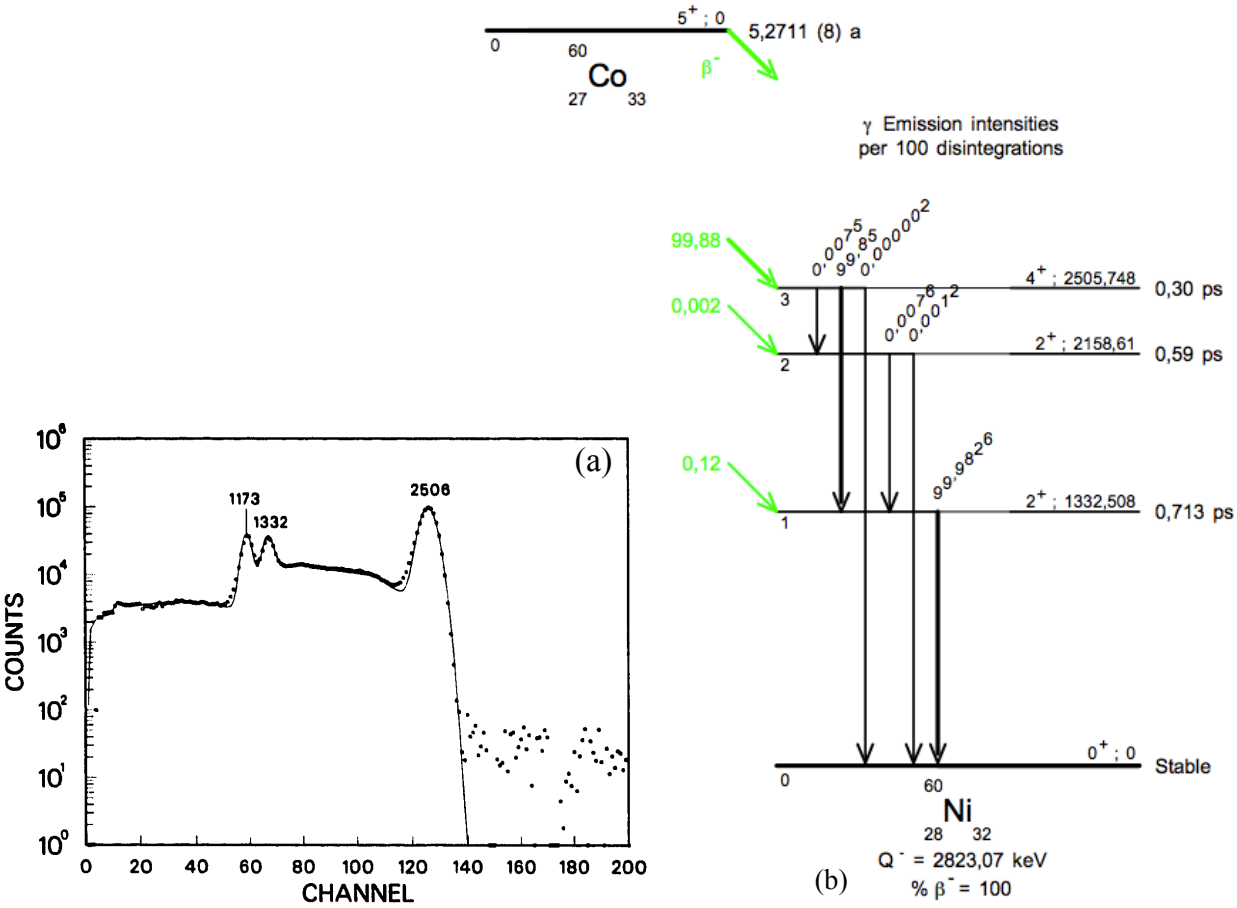

Figure 4.4: ATAGS measured ^{60}Co spectrum and associated decay scheme. (a) Figure 3 reproduced from Greenwood *et al.* [Gre92b] shows the measured spectrum (points) and calculated fit (solid line) [20 keV/channel]. (b) Decay scheme of ^{60}Co taken from DDEP [LC]

4.4.1 Stability of the energy calibration

The are a number of stages involved in producing an electrical response from a scintillator detector. The energy calibration of this response assumes that all the processes involved remain stable. A deviation of the conditions of any one of the processes will result in the variation of the response away from the established calibration. One such influence on these changes is the temperature. It is well established that NaI(Tl) detectors are sensitive to variations in temperature, influencing the amount of scintillation light emitted, the scintillator decay constant, the PMT gain and the electronics systems [Mit16b, Cas12, Ian07, Mel88, Sch83]. Any stability issues need to be addressed, since TAGS measurements require both a reliable energy calibration and also stability of this calibration over long data acquisition periods.

A method often employed to maintain stability of the calibration with temperature is the use of active temperature stabilization such as that used by the Berkeley Total Absorption Spectrometer (TAS) (see Section 2.3.2)[Nit95]. In the case of TAS, monitoring is achieved by using a light pulser coupled directly into the scintillator via fibre-optic cables. The system incorporates an additional 76 mm x 76 mm NaI(Tl) detector manufactured from the same batch material as TAS. The spectral position of a fixed ^{60}Co source is monitored by the additional detector for changes due to temperature. By observing the TAS response to the pulser (in each tube) and comparing this to the smaller detector's reference source peak position (^{60}Co), the response of each tube can be monitored. A computer control system automatically adjusts the high-voltage (HV) of each tube to account for shifts due to temperature instability. In addition to active temperature stabilization, the TAS was operated inside of an air-conditioned enclosure within the experimental area.

Alternative methods of active compensation of scintillators can be found with the use of SiPMT's for Positron Emission Tomography detectors. A thermocouple is used to monitor the temperature of the scintillator and apply gain changes according to the predictable response of silicon [Lic15, Lic13]. This method is not suitable for NaI(Tl) detectors because of the complicated, often opposing, changes in the PMT and scintillator responses with temperature. One method involves the use of a software algorithm to correct for deviations in the spectrum on the data itself, using either a measured temperature or a known background peak (^{40}K) to reference the adjustment [Cas12]. This method requires an accurate measurement of the temperature properties specific to the detector and assumes that the background peak will be identifiable and resolved within the spectrum. It also assumes that the measured temperature dependance is accurate and will not change.

The fitting of TAS-like fibre optic cables to ATAGS PMTs was investigated at an early stage of the project and found to be too costly. This would also require an additional reference detector matched to the scintillator material of the ATAGS, which is not available. Knowledge of planned air-conditioning of the CARIBU experimental hall would mitigate the daily temperature changes during a measurement campaign. This effect also must be weighed against the significance of the change compared to potential energy shifts due to count rate (see Section 4.7). A data collection method discussed in Section 4.8 allows the monitoring of any shifts throughout the collection period and also effect a means of post-collection adjustment if necessary.

4.4.2 Scintillator non-proportionality

Scintillator non-proportionality is associated with a non-linear energy response. This is best observed with measurements of nuclides that include a number of γ-ray transitions

in a cascade, creating a sum peak. Taking ^{60}Co as an example that emits two γ rays in a cascade (refer to Figure 4.4), one might first expect the sum peak to be the height of the component single pulses, in this case (1173 keV + 1332 keV) = 2505 keV. If an energy calibration were performed, based on the centroid positions of single γ-ray peaks only, this summation peak is found at a centroid position approximately 1% higher than expected. The shift in position of the sum peak to higher energy is attributed to the non-proportionality of the scintillator [CO99a].

In simple terms, the non-proportionality can be thought of as a saturation effect of light in the scintillator centres. The density of the interacting energy in the scintillator will be higher for the case of a fictitious mono-energetic 2505 keV γ ray and is more likely to suffer from losses due to saturating light centres. This is then compared to the case of the two γ rays, (1173 keV and 1332 keV), which are of lower overall energy and are more likely to take different physical paths, resulting in a lower density of interacting energy that would be less susceptible to saturation. The multiplicity of a cascade from a level will affect the potential shift of the resulting response [CO99a]. This phenomenon is of considerable interest for TAGS measurements, as the method relies on the detection of summed γ rays from levels that will typically have large multiplicities with different pathways. The non-proportionality will effect the interpretation of the β-feeding levels if the model does not take this phenomenon into account.

A brief history of non-proportionality in NaI(Tl)

There has been a renewed interest into the cause of non-proportionality in the last decade, with the prospect of improving the overall energy resolution of scintillator detectors. The effects of non-proportionality are often overlooked, since the effects are less significant for small volume detectors. Although there has been much research into this phenomenon [Mos08], the origins of non-proportionality are still largely unknown.

The first observation of a non-linear response in NaI(Tl) detectors can be traced back to the 1950s [Pri50]. In 1956, Engelkemeir investigated a number of different NaI(Tl) detectors of various geometries produced by the same manufacturer [Eng56]. Deviations of up to 20% from linearity were found for the low energy regions. The non-observation of this effect prior to this time, was attributed to insufficient sensitivity.

Observation of the non-proportionality was made more apparent by a method introduced by Peelle et al in 1960 [Pee60]. The method observed the shift in position of the sum peaks produced by sources decaying via cascading γ-ray transitions. Using a 3" x 3" NaI(Tl) detector, deviations of 27 keV (^{88}Y sum peak from 898 keV and 1836 keV transitions) and 44 keV (^{207}Bi sum peak from 569.6 keV and 1063.7 keV transitions) were observed from the expected sum peak positions, relative to a calibration of energy using only single-γ-ray energy peaks.

The method of measuring the shifts in sum γ-ray transitions was extended by Kantele [Kan61]. A 4π geometry was created by placing two 3" x 3" NaI(Tl) detectors together, face to face and passively adding the output into a single acquisition system. The larger solid angle increased the probability of detecting a sum event and thereby increased the statistics of non-proportionality measurements. A consistent sum-peak deviation was observed even when one of the detectors was removed from the source without altering any cables, amplification or voltage. Kantele *et al.* conclude that non-proportionality is the same for summing in a single detector compared to the independent events being summed across two detectors.

In 1961, Zerby et al created a Monte Carlo model of a 2.5" x 2" NaI(Tl) scintillator by looking at the specific interaction processes in the crystal and not simply the energy deposition [Zer61]. They modelled the non-proportionality in the γ-ray response $L(E_\gamma)/E_\gamma$, where $L(E_\gamma)$ is the light response from the scintillator due to a γ-ray event of energy E_γ. They concluded that the non-proportionality effects do not originate from γ-ray processes but are instead caused by electron processes. Using this model and a measured γ-ray response, they deduced the non-proportional response for different energy electrons. Since this publication, many groups have focused on the measurement of the relative scintillator light yield of NaI(Tl) as a function of the electron energy, which is generally accepted as the underlying mechanism. Figure 4.5 provides the digitised results of the yield from a collection of representative publications using both measurement and calculations [Zer61, Por66, Roo96, Val98, CO99a, Reu07].

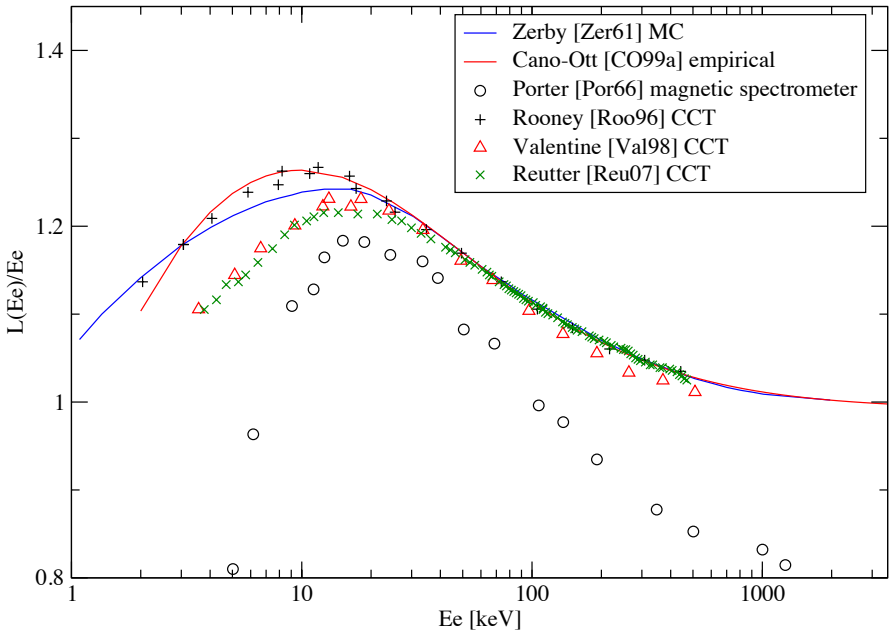

Figure 4.5: Summary of published relative light yield responses of NaI(Tl) - the amount of light produced in the scintillator (L) from the interaction of an electron with energy E (E_e). Data digitised from Refs. [Zer61, Por66, Roo96, Val98, CO99a, Reu07] with all curves (excluding Porter) normalised to 1 at an electron energy of 3 MeV.

The Compton Coincidence Technique (CCT)

A direct measurement of the electron response is difficult due to the attenuation of β-particles by the glass envelope encasing the hygroscopic NaI(Tl) as well as the light-tight aluminium can. An indirect method is made possible by use of the Compton Coincidence Technique (CCT) [Val94, Roo96, Roo97, Men02]. The CCT method uses a collimated beam of mono-energetic γ rays that illuminate the scintillator being measured. Mono-energetic γ rays can undergo Compton scattering in the scintillator, producing an electron and a scattered γ ray. In the event that the scattered γ ray exits the scintillator without any further interactions, the Compton electron is the only event that deposits energy in

the scintillator. By use of an external collimated detector, (usually HPGe for resolution purposes), the scattered γ ray can be detected and used as a trigger for the Compton electron event in the scintillator. By gating the scintillator detector with the HPGe detector trigger, the Compton electron response can be isolated and the energy of the electron can be calculated using the angle of collimation and the detected γ ray energy of the HPGe.

There are numerous publications reporting the non-proportionality of NaI(Tl) measured using the CCT method and using other fundamental techniques. Figure 4.5 shows the digitised publication results compared for Porter [Por66], Rooney [Roo96], Valentine [Val98] and most recently by Reutte [Reu07]. The overall shape is consistent but there are deviations, particularly for the low energies, depending on the chosen nomalisation energy. Besides the differences in technology and statistics of each of these measurements, the other variations to consider are the manufacturer and age of the NaI(Tl) crystals used. It was shown by Hull that there is a deviation of this response for nine NaI(Tl) samples obtained from different manufacturers (Figure 4.6 reproduced from Figure 1 of Hull [Hul09]). Some of the samples from the same manufacturer show a significant disparity in response, leading Hull to conclude that the particular electron light yield response may not be an inherent characteristic property of NaI(Tl) [Hul09].

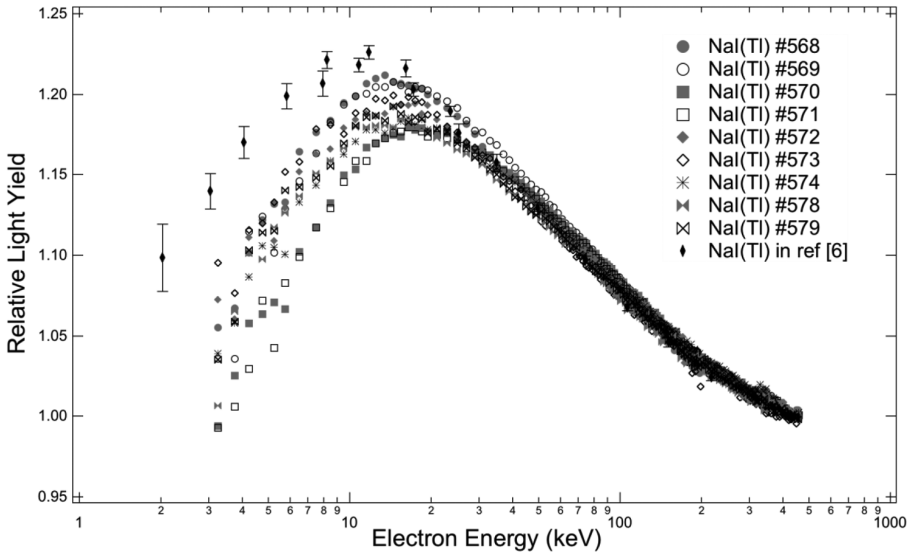

Figure 4.6: Variation of the electron light yield of 9 NaI(Tl) samples from different manufacturers. Reproduced from Figure 1 of Hull [Hul09]. Reference [6] in the figure (narrow diamonds) is a reproduction of Rooney's results [Roo96] for comparison. Normalisation to 1 is performed at an electron energy of 450 keV.

A direct measurement of the electron light yield response of ATAGS would provide the most accurate means for applying non-proportionality corrections to the Geant4 model. As a feasibility study, the CCT method was applied to the ANU5x5 and ANSTOwell6x5 detectors using ^{137}Cs and ^{60}Co sources of approximately 37 kBq in activity; this formed part of an Honours project† for Gabriel Collin [Col11]. A number of angles were attempted to obtain a measured response that covered a usable range of energy. This was limited by

†The author of this thesis was a co-supervisor for Gabriel's project.

statistics, which could be improved by increasing the activity of the illuminating collimated source up to the count rate limit of the detector, or by counting for very long periods of time. Safety and time limitations for the project constrained both options. Apart from the low statistics, it was concluded that there is an offset in the electron energy making it difficult to anchor the response. A direct CCT measurement on ATAGS in Chicago was determined to not be feasible given the source activity and time required. It was decided to use an empirical approach to the non-proportionality correction as explained in the following section. The CCT measurements for ANU5x5 and ANSTOwell6x5 are included in Appendix D.

4.4.3 Application of the Cano-Ott method

Non-proportionality corrections to the model could in principle, be implemented based around the known electron light yield response of ATAGS measured using the CCT technique, as discussed in the previous section. The difficulties encountered in implementing this technique, the safety concerns of the source activity required, and the limited time in accessing ATAGS, meant that another approach was required. This led to the adoption of a parametrisation for the non-proportionality following the method described by Cano-Ott *et al.* on the TAS [CO99a]. This will be referred to here as the Cano-Ott method.

Cano-Ott used a combination of experimental data below 500 keV from Rooney [Roo96] and Monte Carlo (MC) data above 500 keV from Zerby [Zer61], to produce a fitted curve, shown in figure 4.5. The form of the parameterisation is

$$\frac{L}{E_e} = \frac{a_1(1 - e^{a_2 E_e}) + a_3 E_e + a_4 E_e^2}{a_5 + a_6 E_e + a_7 E_e^2}, \tag{4.2}$$

where:

L = NaI(Tl) light yield;
E_e = electron energy in units of MeV;
a_1 = fit coefficient 1= 1.6(2);
a_2 = fit coefficient 2= 0.058(8);
a_3 = fit coefficient 3= 0.580(4);
a_4 = fit coefficient 4= 0.00490(2);
a_5 = fit coefficient 5= 0.25(2);
a_6 = fit coefficient 6= 0.479(4); and
a_7 = fit coefficient 7= 0.00494(2).

The application of this function within the MC simulation occurs at each step of energy deposition in the sensitive NaI(Tl) material, using

$$\Delta L = L(E) - L(E - \Delta E), \tag{4.3}$$

where ΔL is the amount of scintillation light generated for a single interaction step, determined by the difference in the total potential light of the interacting particle before the interaction (E) and the energy ($E - \Delta E$) remaining after the interaction [CO99a].

The total light generated by a complete interaction is simply the sum of the light that is generated at each step, which is dependent upon the total interaction energy available at each step. Alterations to the MC code were required to record the pre- and post-step energy deposited at each interaction point. This allows the Cano-Ott correction to be implemented after the simulation in post-analysis.

Testing of the implementation of the correction was undertaken by generating the photon light yield response curve using by the Geant4 model of ATAGS. Figure 4.7 shows the response from simulating mono-energetic γ rays with step size of 5 keV up to 50 keV and 50 keV steps from 50 keV to 7000 keV. The shape is comparable to the photon light yield measured by Aitken [Ait67] and calculated by Rooney [Roo97], (data for both are digitised from Figure 5 of Rooney [Roo97]). Variations of the γ-ray response between these data are due to the different sizes of the NaI(Tl) detectors being compared.

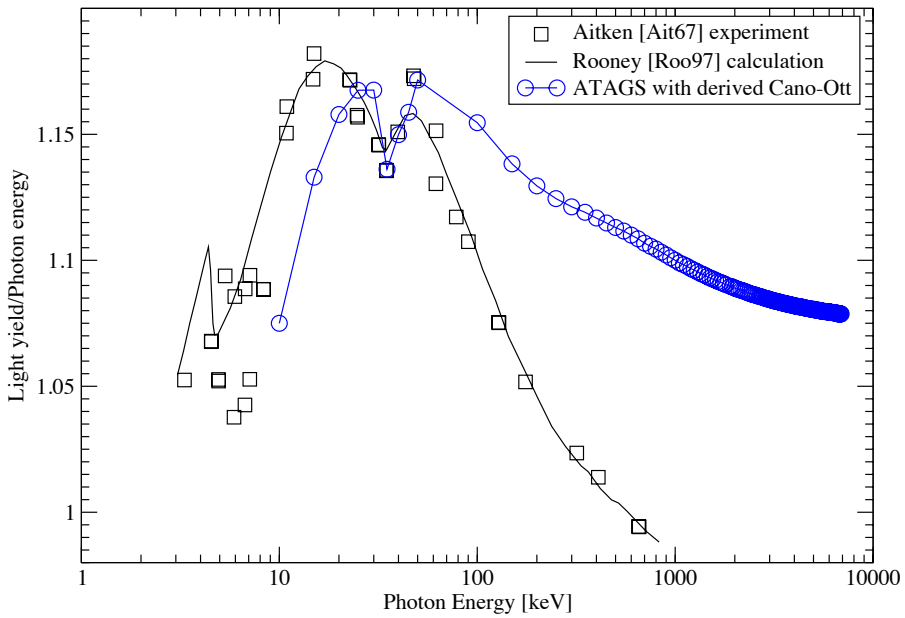

Figure 4.7: Derived photon light yield of ATAGS derived using the Cano-Ott non-proportionality correction to the Geant4 model. This is compared to digitised data of a smaller detector, obtained from Figure 5 in Rooney [Roo97], giving a comparable shape.

4.5 Energy resolution and efficiency

The broad energy resolution of NaI(Tl) detectors compared to HPGe, is a result of higher statistical uncertainty due to the low numbers at each of the following detection processes:

- the conversion of ionisation energy into photons in the scintillator;
- the loss of light in the scintillator due to scattering, reflection and refraction across different boundaries;
- the conversion of light to electrons in the photo-cathode; and
- the multiplication process of electrons in the dynode chain.

Sources of ^{137}Cs and ^{60}Co are commonly used for γ-ray calibrations. Using NaI(Tl), the convenient close spacing of the energies of ^{60}Co quickly indicates the resolution by inspection as to how well the two peaks are resolved, while the relative intensity of these peaks compared to the sum peak (2506 keV) indicates the solid angle subtended, and the quality for total absorption measurements. Figures 4.3 and 4.4 show the ATAGS response to ^{137}Cs and ^{60}Co spectra, measured respectively in the 1990s [Gre92b], together with the decay schemes [LC].

4.5.1 Energy resolution

The resolution of a detector is dependent upon the geometrical size of the scintillator crystal. This is a consequence of the larger volume that needs to be transited by the scintillation light and the ensuing higher probability of optical losses. Figure 4.8 shows a comparison of ^{60}Co measured using three different detectors (ANL3x3, ANU5x5 and the ANSTOwell6x5 see Appendix A). This is a qualitative comparison normalised to the 1173 keV γ-ray peak, with different source positions and activities for each detector. Also included is the digitised spectrum of ^{60}Co measured by Greenwood in 1992 for comparison (Figure 4.4a). The source positions are located inside of the well for both the ANSTOwell6x5 and the ATAGS detectors.

The energy resolutions of the 1173 keV, 1332 keV and 2505 keV γ rays are shown in Table 4.2. The energy resolution is measured as the Full Width at Half Maximum (FWHM) presented as a percentage of the centroid. Qualitatively, the resolution becomes broader for each γ-ray energy, as the detector size increases. There is a slight decrease in the resolution at 1332 keV in going to the larger ATAGS. This is likely due to the ATAGS spectrum having a lower background, and being less influenced by the 1460.882(6) keV γ ray from ^{40}K, as a result of being shielded as compared to the non-shielded ANSTOwell6x5 detector in this comparison.

Detector	1173 keV FWHM	1332 keV FWHM	1332 keV peak -to-valley ratio	2505 keV FWHM	2505 keV Δ
ANL3x3	5.29%	4.66%	10.66	3.42%	+4.6
ANU5x5	6.82%	6.01%	3.62	4.04%	+25.8
ANSTOwell6x5	8.25%	7.27%	1.63	5.46%	+41.7
ATAGS in 1992	7.40%	6.52%	1.75	5.39%	+23.6

Table 4.2: Comparison of energy resolutions for ^{60}Co γ-ray peaks with four different sized NaI(Tl) detectors. ATAGS data is digitised from Figure 3 of Greenwood *et al.* [Gre92b].

The 2505 keV sum peak is seen to dramatically increase in magnitude as the detector size increases. This can be used as an indicator for the solid angle subtended by the source. Also shown in Table 4.2 is the resolution of this sum peak and the approximate non-proportional deviation compared to a simple calibration using only the 1173 keV and 1332 keV peak centroids (see Section 4.4.2 on non-proportionality). This is a simplified comparison as the effects of count rate are not taken into account and we assume the energy coefficient E_0 to be 0 keV, which has a large effect on the measured numbers (see Appendix D). Another indicator of the resolution using this source is the resolvability of the valley between these two γ rays, given here as the ratio of the height of the 1332 keV peak compared to the valley located between the 1173 keV and 1332 keV peaks (Table 4.2).

The resolution as a function of energy was sought from the published data for ATAGS

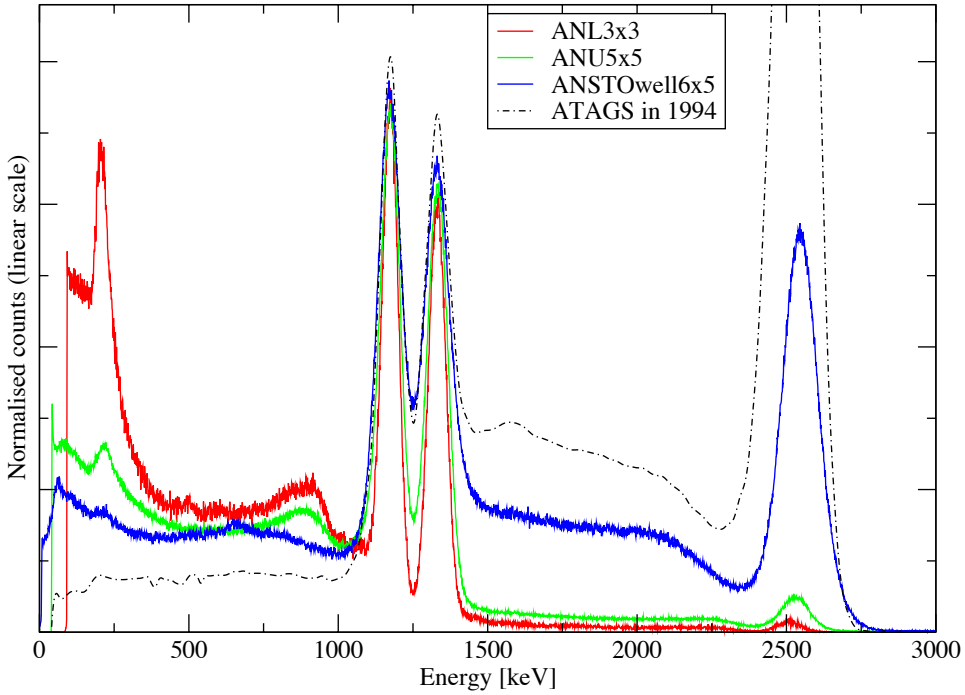

Figure 4.8: Comparison of energy resolution for four, different-sized NaI(Tl) detectors, measured with a ^{60}Co source and normalised to the 1173 keV peak. Spectra are measured with the ANL3x3, ANU5x5, and the ANSTOwell6x5. This is compared to the digitised ATAGS spectrum measured by Greenwood in 1992 (Figure 3 [Gre92b]). Background subtractions have not been performed, except for ATAGS.

with the aim of using these data as input parameters to a resolution broadening function (discussed in Section 4.5.2). However, this resolution data did not show a clear trend, leading to the conclusion that it is highly dependent upon the count rate of the detector (see Section 4.7).

The energy resolution can be parameterised using the following equation:

$$FWHM = F_0 + F_1\sqrt{E}, \tag{4.4}$$

where:

$FWHM$ = Full Width at Half Maximum;
E = energy of the peak;
F_0 = FWHM coefficient 0 (constant term); and
F_1 = FWHM coefficient 1 (square-root term).

In lieu of access to ATAGS to undertake measurements of the resolution, digitisation of the published data [Gre92b, Hel94b] from typical γ-ray spectroscopy sources was used. The energy resolution (FWHM) plotted against $\sqrt{E}$ is shown in Figure 4.9. This assumes the applicability of the relation shown in Equation 4.4. Some uncertainty would be introduced from the digitisation method while there is a varied range of resolutions dependent upon their count rate during collection. Figure 4.9 shows the estimated FWHM coefficients that will encompass a range of the energy resolutions expected during ATAGS commissioning, depending on count rate.

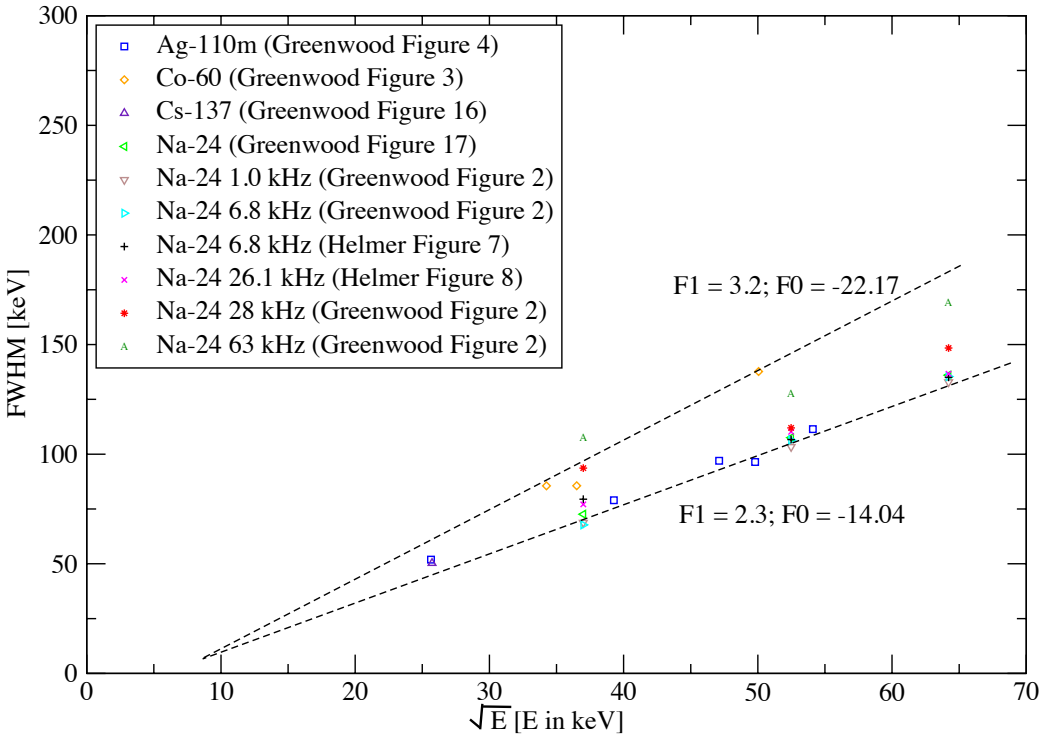

Figure 4.9: ATAGS energy resolutions (FWHM) extracted by digitising published figures in Greenwood *et al.* [Gre92b] and Helmer *et al.* [Hel94b]. The dashed lines represent the minimum and maximum fits to the resolution values.

4.5.2 Resolution broadening for the MC model

The Geant4 model produces discrete data of the energy deposited in the sensitive detector region within the simulation geometry (see Section 3.1.3). To enable a comparison of the simulated data with experiment, a resolution broadening method needs to be imposed on the spectrum to take into account the experimental energy resolution. This is achieved by convolving a gaussian with an energy-dependent width on each channel and redistributing the resulting counts. Figure 4.10 shows both the raw data that is produced by the simulation and the resolution broadened spectrum.

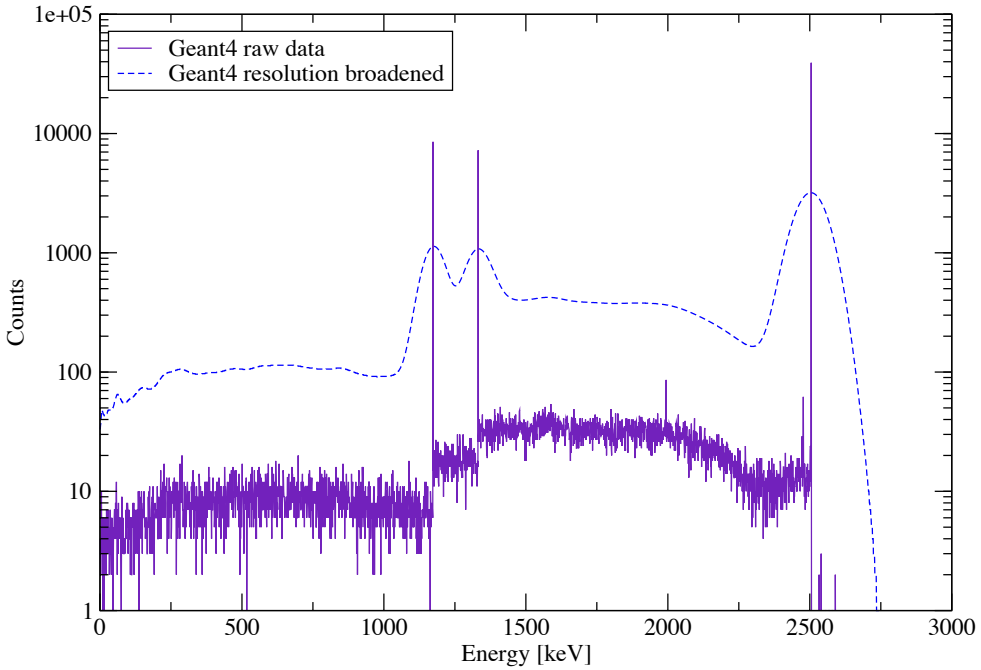

Figure 4.10: Geant4 simulation produced data of a ^{60}Co source in ATAGS. The data is shown before and after convolution with a gaussian function (FWHM coeffs F_0 = -22.3, F_1 = 3.28).

A C++ script was written to produce the resolution broadened spectrum. This script takes the Full Width at Half Maximum (FWHM) coefficients (F_0 and F_1 in Equation 4.4) as inputs. It can be called as a function from within PYTHON, which is the program used for the majority of the analysis. Additionally, the script uses a magnitude scaler and an energy multiplier as variables for its use within a fitting routine, so as to provide flexibility for gain and intensity matching or other analysis tasks.

4.5.3 Dead layers in the ATAGS model

The dimensions required to accurately model the ATAGS were initially provided in publications by Greenwood *et al.* [Gre92b], with later additional details published in 1994 by Helmer *et al.* [Hel94b]. This updated information provided additional components of the detector with more accurate dimensions of their ATAGS model to better fit the experiment. Although there is a good amount of information on the specifications, some parameters that are missing require experimental data to guide parameter selection. Before the model is used in anger, it must be validated against experimental data to give confidence regarding its effectiveness.

An unknown parameter of this model is the dead layer in the well described in Section 3.2. A dead layer is not typically considered for scintillator models; it is usually introduced in solid-state detectors like HPGe to account for inactive contacts (see Section 8.4.2). Helmer *et al.* found that there was a low energy discrepancy of their model compared to experiment, that was believed to result from a thin inactive layer in the ATAGS well caused by deterioration [Hel94b]. To avoid changing their model dimensions, this effect was modelled by Helmer *et al.* by increasing the density of the aluminium oxide reflective layer in the well so as to be more absorptive.

An equivalent dead layer was added to the model in this thesis by making a thin layer of NaI(Tl) material in the well inert, i.e. not a sensitive detector volume (shown in Figure 3.3c). The thickness of this layer can only be determined through the matching of simulations to experiments for low energy X or γ rays. The dead layer will affect low energy γ rays through the additional attenuation it provides above that required to transit the 0.6 mm thick aluminium wall. This becomes less critical to the model as additional attenuation material is added, for example from the vacuum-pipe housing the implanted tape required for the experiments. As the TAGS method is predominantly used for summing γ-ray cascades of nuclides with large Q values, the low-energy threshold matching in the simulation is not crucial to the success of the interpretation.

4.5.4 ATAGS shielding

The external ATAGS shielding had not been included in the simulations of this chapter as it had not been designed at the time the simulations were performed. In the vicinity of CARIBU, the ^{252}Cf source and residual radiation from slits and beam stops contribute to the background radiation. The experimental background is complicated and always changing, there is little value in attempting to simulate this when it can instead be measured and subtracted experimentally. A very good approximation can be made with no shielding in the simulations as most effects are removed in the experiment by background subtraction. The exception is when the background source of interest is introduced inside of the shielding; then backscattering and bremsstrahlung from interactions in the shielding material are not accounted for.

4.5.5 Validating the ATAGS model of energy deposition

A number of regularly used γ-ray sources were simulated using the ATAGS model, with the resultant spectra being energy broadened using the script described in Section 4.5.2. These simulated spectra were then compared with spectra digitised from the INEL publications. The spectra used for comparison were ^{60}Co, ^{137}Cs, ^{110m}Ag and ^{24}Na. The results for a simple case (^{60}Co), and a more complicated case (^{110m}Ag), are described in this section. Additional comparisons using ^{137}Cs and ^{24}Na are provided in Appendix B.

^{60}Co

The starting point for this comparison is the digitised ^{60}Co spectrum measured using ATAGS and published by Greenwood in 1992 [Gre92b]. This was first shown in Figure 4.1, but it is reproduced again in Figure 4.11 to show both linear and log scales compared to the simulated spectra. The published data collected using single-hit events (no veto of β's with a silicon detector), was used in lieu of access to the ATAGS instrument at the time of this work.

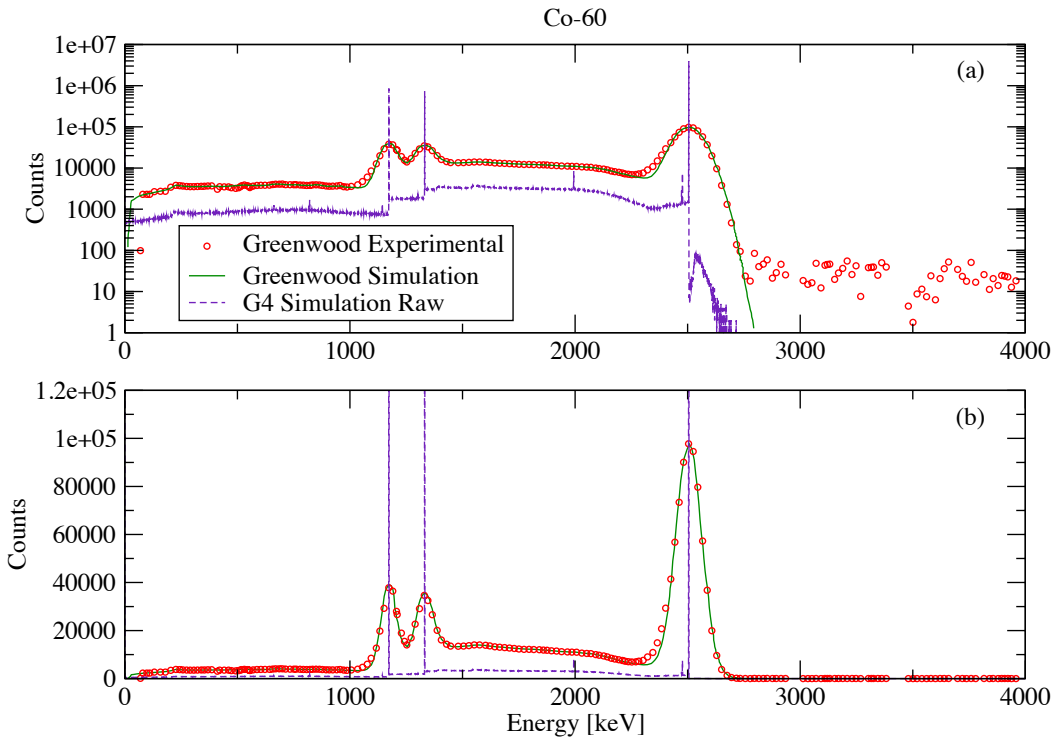

Figure 4.11: Digitisation of ATAGS ^{60}Co spectrum from Greenwood *et al.* [Gre92b], shown in both log and linear scales and compared to the MC simulation. The "Raw" (non-resolution broadened) spectrum is shown for comparison using (a) log-scale and (b) linear scale.

The GEANT4 model of ATAGS was run for 1 x 10^7 events of ^{60}Co decays with a point-geometry ^{60}Co source placed 25 mm above the bottom of the well, replicating the conditions of Greenwood's measurement. The GEANT4 model utilised the GPS module to generate the decay of ^{60}Co and is significantly simplified with neither external shielding nor attenuating materials in the ATAGS well included in the model.

The non-broadened raw spectrum, shown in Figure 4.11 (labelled G4 Simulation Raw), was fitted to the digitised Greenwood measured data and the Greenwood simulation spectrum using Python script to resolution-broaden the GEANT4 raw spectrum and interpolate to the discrete points obtained from the digitisation (see Section 4.5.2). Another parameter was used to vertically scale the magnitude of the GEANT4 spectrum to account for the number of events in the measurement compared to the simulated number. The energy coefficients of the digitised spectra were also varied in this routine to allow for slight variations of the energy conversion, and there is an implicit assumption that the simulated spectrum has the correct energy.

The differences between these spectra are shown in Figure 4.12. The residuals are shown as a percentage of the value of the Greenwood data, i.e. a positive residual indicates the Greenwood data is larger than the GEANT4 simulation. Overall the fit looks good, with the largest discrepancies seen on the low energy side of each peak. The Greenwood measured spectrum is reported to be background subtracted [Gre92b]. The background is shown in Figure 6 of Reference [Gre92b] (reproduced here in Figure 4.13) and has a considerable slope from 0 to 3000 keV. A slight underestimation of the background subtraction factor by Greenwood *et al.* may be the cause of the low-energy tails present in each peak in the experimental residuals, but we cannot be certain using the digitised

data.

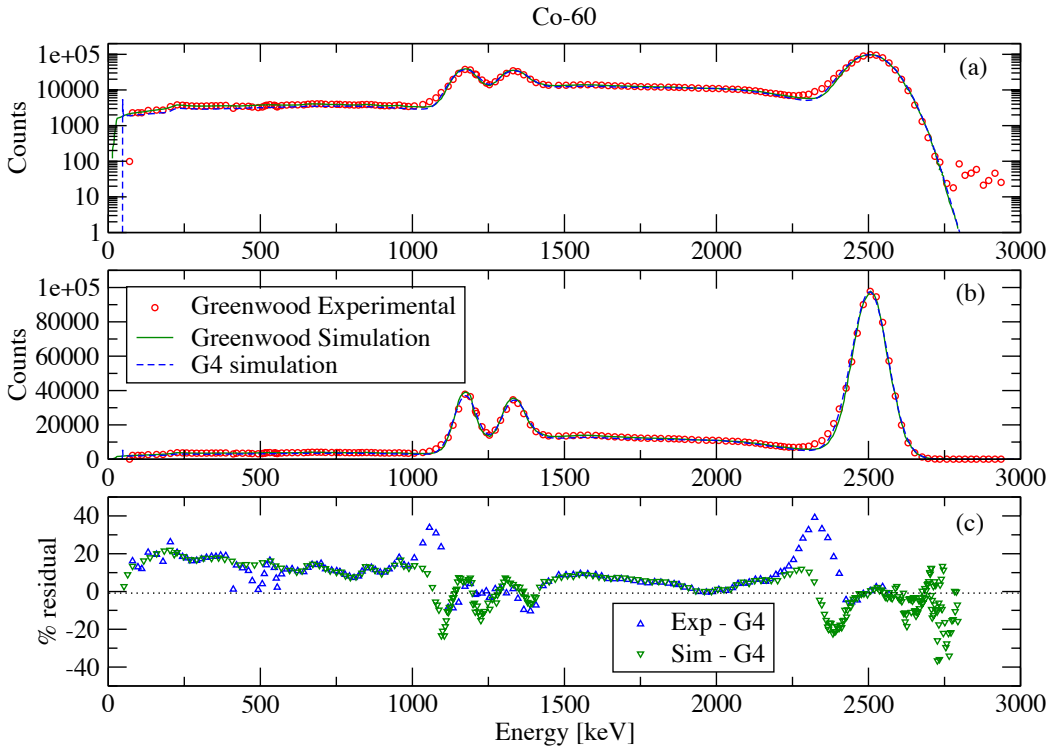

Figure 4.12: Comparison of ATAGS simulation of ^{60}Co with Greenwood's 1992 measurement (Figure 3 of Greenwood [Gre92b]). The GEANT4 simulation is a least squares fit of the raw simulation data to the digitised Greenwood results, varying the energy gain, FWHM and count scaling parameters, shown in (a) log-scale and (b) linear-scale. The percentage residuals for each fit are shown in (c).

^{110m}Ag

In this example we compare a ^{110m}Ag source that decays via β^- with a Q-value of ~3010 keV. This radionuclide is more complicated than our previous two examples; it has 22 levels fed via multiple γ-ray pathways to the ground state. Figure 4 from Greenwood [Gre92b] is corrected for background and has had a slight energy shift to better align the peaks. This may have been done to compensate for the non-linearity (see Section 4.4.2) in this more complicated example.

The residuals below 600 keV show significant deviation, likely due to the experimental background, which would include other components not accounted for in both the GEANT4 and Greenwood simulations. The other deviation in the residuals is at an energy of 2700 keV, which corresponds to the background or dip in front of the final peak at approximately 2920 keV. The larger number of counts in the measured data in this region might be accounted for by the presence of multiple background peaks (see Figure 4.13).

4.5.6 Optimal source position

One of the design requirements for the TAGS method is to have as close to 4π detection geometry as possible (Section 2.3.1). The emission solid angle subtended by the source can be improved by the optimal positioning of the source in the well along the axis of the

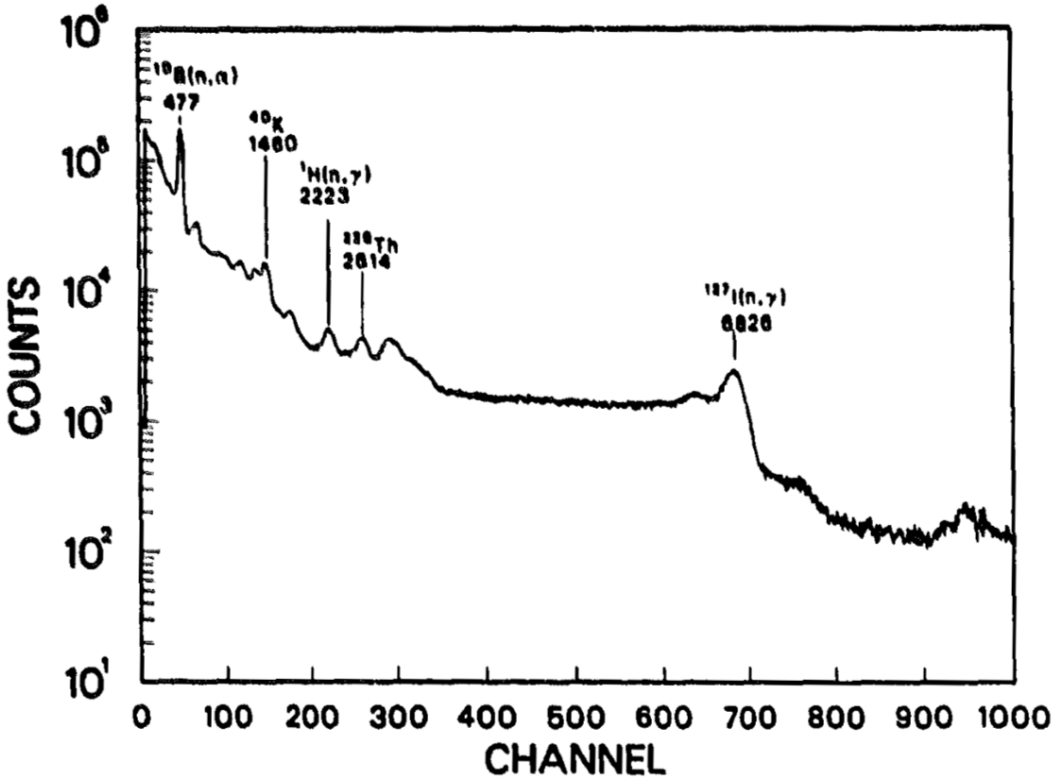

Figure 4.13: Reproduction of the background spectrum from Figure 6 in Greenwood [Gre92b]. The horizontal scale is 10 keV/channel.

detector. The experimental measurement requires a tape with implanted source to be fed into the well of ATAGS and returned under vacuum with the possibility of an auxiliary β detector located inside the well such as that used by Greenwood *et al.* [Gre92b]. At the time of these simulations, the exact design of the beam pipe in the well was not known. Hence the γ-ray efficiency of ATAGS was determined through using the Geant4 model of ATAGS with a bare source placed at various points along the symmetrical axis in the well (z), measured relative to the 'origin' (the bottom of the well). The resultant information was used to guide the design of the materials required for the final experiment at CARIBU.

The total and Full Energy Peak (FEP) efficiencies were determined by undertaking multiple monoenergetic γ-ray simulations across a range of energy, referred to here as a "picket fence" approach. One-hundred thousand γ rays were generated for the energy range from 50 keV to 500 keV with a 50 keV spacing and then 500 keV spacings up to 10 MeV. The FEP efficiency for each energy or "picket" is determined by the number of detected γ rays in the peak of the simulated response as a ratio to the number of γ rays generated. The total efficiency is computed from the integral of all detected counts. Picket fences were simulated with the source position at z positions of 1 mm, 50 mm, 100 mm, 150 mm and 200 mm.

The total (a) and FEP (b) efficiencies are shown in figure 4.15. The contour plot is a result of interpolating the efficiency between the simulated "pickets". The peak efficiencies are at an energy of approximately 200 keV, consistent across each of the z values, giving 87% and 99%, FEP and total efficiency, respectively. The total efficiency of 99% for a 200 keV γ-ray energy is in agreement with that reported for ATAGS [Gre92b]. The ideal position is the very bottom of the well but this shows a very small increase of efficiency

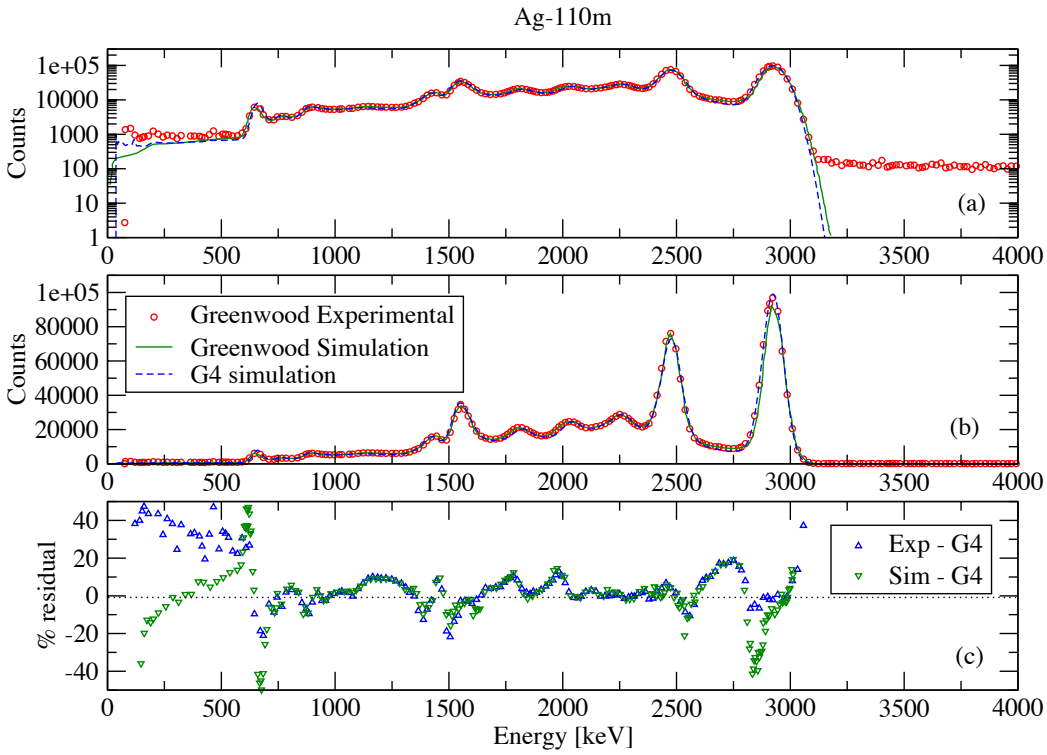

Figure 4.14: Comparison of the ATAGS simulation for ^{110m}Ag with Greenwood's 1992 measurement (taken from Figure 4 of Greenwood [Gre92b]). The GEANT4 simulation is a least squares fit of the raw simulation data to the digitised Greenwood results, varying the energy gain, FWHM and count scaling parameters. Data is shown with the y-axis in (a) log-scale, and (b) linear-scale. The percentage residuals for each fit are shown in (c).

(0.3%) compared to the 50 mm height for low energies.

These plots show that the variation of the efficiency for both the total and FEP efficiency is approximately 3% from the bottom of the well to the source placed at z = 50 mm, and an additional 6% loss in efficiency when moving from 50 mm to 100 mm distance. These simulated results show the overall trend in the efficiency and are a test of the energy deposited component of the simulation. Using this information, the experiment should aim for a source position as close as possible to the bottom of the well, or ideally not exceeding a distance of 50 mm. Additionally the inclusion of materials should be minimised to reduce the impacts on the efficiency, and, be of low atomic number and thickness. The value that was used in the later experiments was a height of 25 mm, which is the same height as used by Greenwood *et al.* [Gre92b]. This will be referred to as the source position.

4.6 Implementing the optical-photon model

The transport of optical photons from scintillation light was added to the Geant4 model of ATAGS. The energy-deposited model is limited to the interaction of energy within the sensitive volume at the point of interaction. The complicated interaction of the scintillation light transport and the inefficiencies of collecting this light is added by including this capability. The model adds another layer of information and helps with the understanding of various physical characteristics that are not provided in this basic energy-deposition model. It involves the inclusion of the optical-photon class in Geant4 that generates photons in a nominated volume, in numbers that are proportional to the energy deposition at each step. The addition of this model provides parallel information that is complimentary to the basic energy deposited data, albeit at a significant additional cost to simulation time.

The model requires the definition of the optical properties of each material and the boundary properties involved in the process. Some of the material characteristics available for definition include: the refractive index, the scintillation yield, the fast and slow emission spectrum, the absorption length, and the reflectivity. For NaI(Tl) in this simulation, a value of 38 optical photons generated per keV of energy deposition is used. The optical photons are counted when they interact with a simulated photo-cathode representing the PMT (see Figure 3.3). As the optical photons are discrete, the simulated PMTs count the number of photons that are 'detected'. This number of photons generated at the interaction location, is proportional to the energy deposited via the optical yield value (i.e. detected photons = optical yield × energy deposited). Additional losses occur as a result of the optical processes involved in the transport of these photons through the different volumes in the simulation, before eventually being detected in the simulated PMT.

Figure 4.16 shows the openGL rendering of a single 20 keV γ ray being emitted into the ATAGS detector from the source position. The deposition of the relatively small 20 keV energy into the scintillator produces up to 760 optical photons that are transported around the geometry interacting with the various boundaries in the model (the photon paths are represented by the green lines in Figure 4.16). The side view of ATAGS shows the collection of the photons across the silicon dioxide layer into the simulated PMTs (RHS of Figure 4.16b). Once the optical photons are counted, they are killed in the simulation to avoid further unnecessary tracking and associated computer simulation time.

The results from the optical simulation provide a measure of the statistical broadening of peaks from the contribution of inefficiencies in the transport and collection of optical

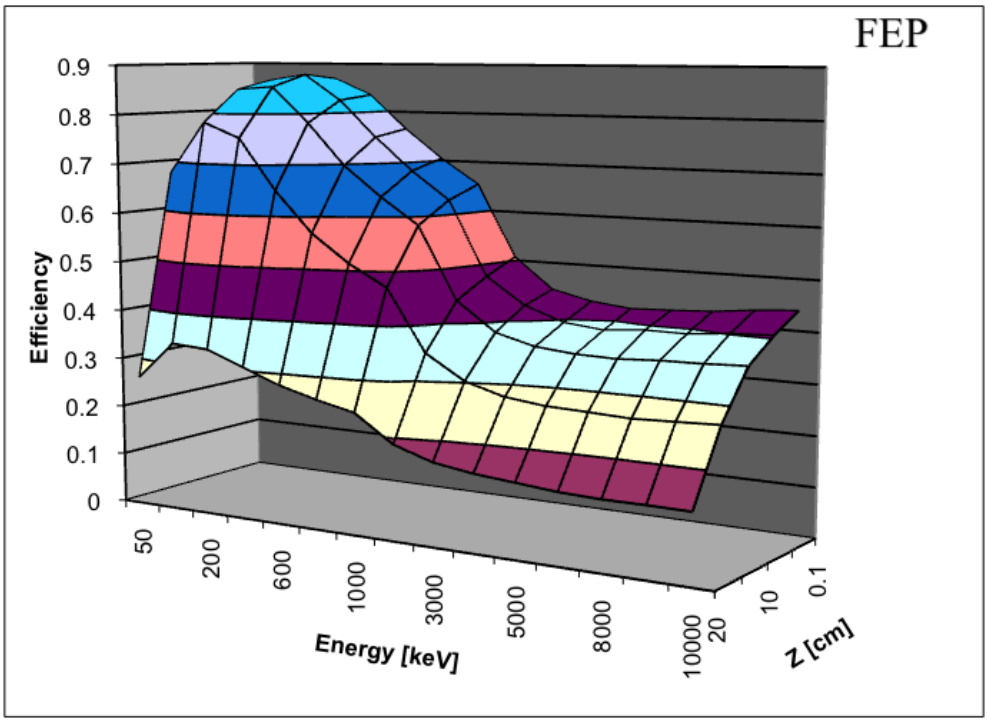

(a)

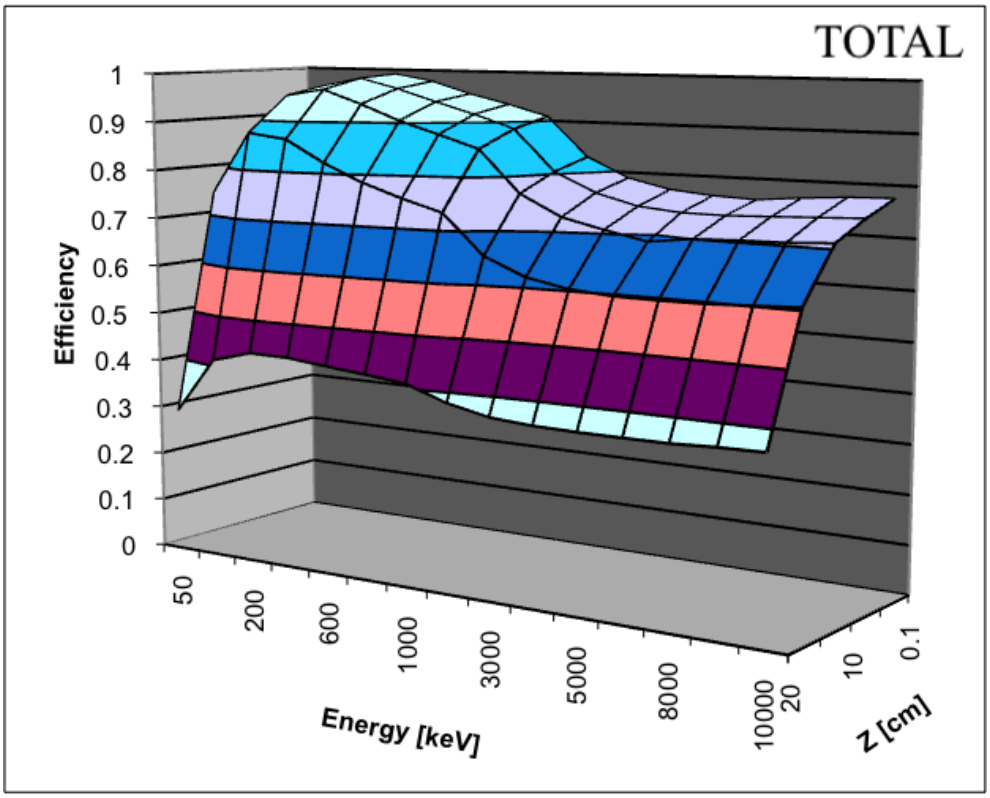

(b)

Figure 4.15: ATAGS γ-ray efficiencies for a simulated γ-ray picket fence as a function of the source position (z) above the well bottom. 100 k events were generated for each energy and the contour plot is interpolated between these simulated points for both (a) the Full Energy Peak (FEP) and (b) the total efficiency (TOTAL).

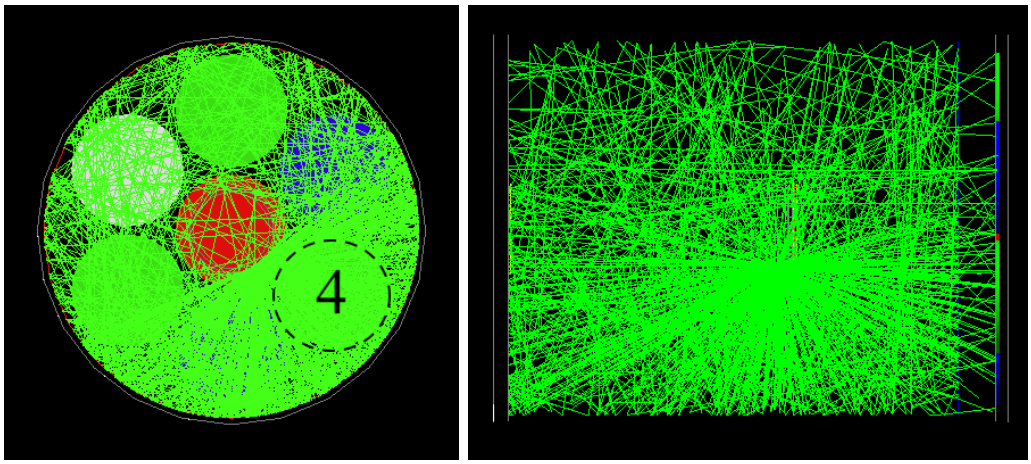

(a) (b)

Figure 4.16: OpenGL rendering of optical-photon transport in ATAGS with green lines showing the photon path. This is the result of a single 20 keV γ ray emitted from the source position toward PMT 4, shown looking (a) down the well, and (b) from the side with the PMTs on the right of the figure.

photons. It allows the identification of the contribution to broadening; in this case the broadening is due to the transport and collection of the light within the detector, with the remaining broadening assumed to originate from the PMT amplification and data acquisition processes that are not modelled. The linear nature of the emission of optical photons means that the inclusion of this model will not add any fundamental non-proportionality (see Section 4.4.2) in its basic form. The alteration of the emission yield does allow another avenue to inject a non-proportional response, but the response would use a similar function to Cano-Ott and hence would produce no advantage over the existing implementation for non-proportionality.

Figure 4.17 shows the overall optical simulation (sum of photons in all 7 tubes) of the ATAGS detector for simulated ^{60}Co decays at the source position. Note that the statistics of photon production and transport give some intrinsic broadening of the peaks (more on this later). The additional spectra are the optical photons collected at the individual simulated PMTs (Figure 4.17a) which add event-wise to produce the ATAGS sum (Figure 4.17b). The outer tubes (PMTs 1 to 6 in Figure 2.4) show essentially the same shape response as each other. This makes sense as the collection of the photons for these PMTs would be equal given that the source is positioned on the axis and they each have a symmetric view of the crystal. The central tube spectrum (PMT 7) is much more resolved and has a shape that resembles the shape of the final summed spectrum, although the integrated counts in each of the individual spectra are similar.

When the source is not placed along the symmetry axis, there is a shift of the shapes and the distribution of the light for the outer tube spectra. This change was found to not be significant when the source is within the well of the detector, resulting in only slight changes in the individual tube spectra and a minor effect on the final summed spectra. However, there is a significant overall change to the individual and combined spectra when the source position is external to the detector well.

The combined spectrum produced by this model agrees with the total counts and general shape of the electron deposited result shown in Figure 4.10 (data labelled as

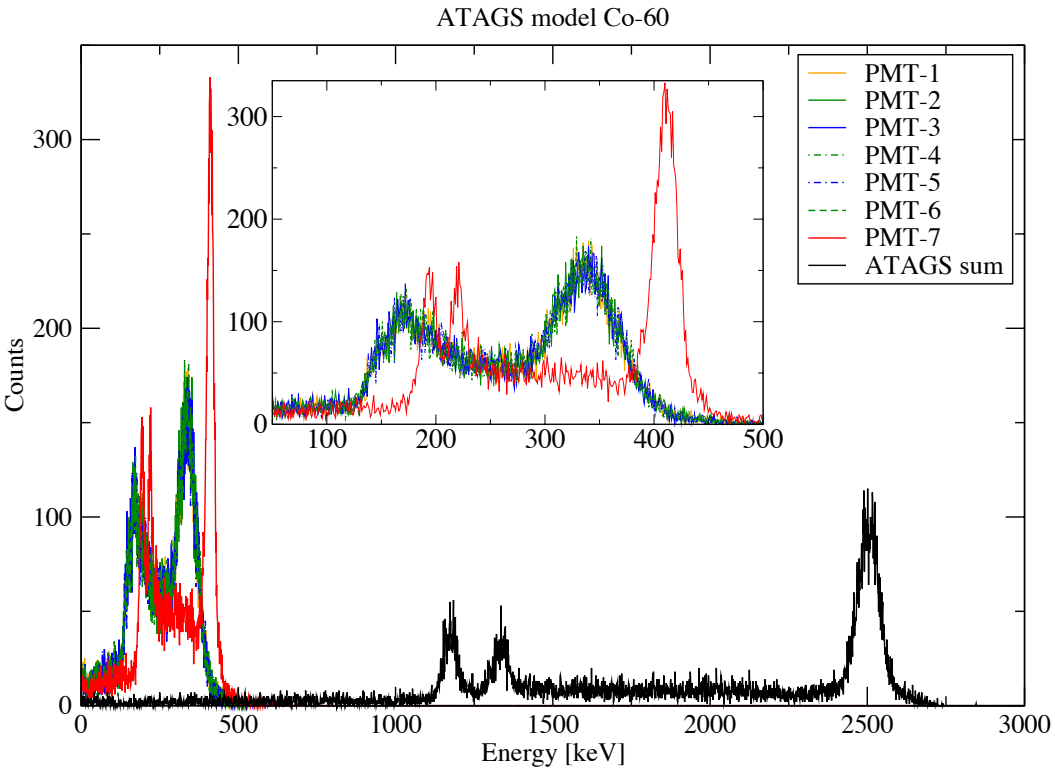

Figure 4.17: Optical-photon simulation of the relative gains of ATAGS responses for ^{60}Co. The inset zooms in on the individual PMT responses at low energy. Note that PMTs 1 to 6 show very similar results that lie essentially on top of each other.

Geant4 raw). There is some inherent energy resolution broadening that results from the model, but it is only a small component of the overall experimental broadening, hence to reproduce the experiment still requires application of the resolution broadening function. Both the energy deposited and the optical-photon data can be accumulated simultanously in the list mode data format for analysis (see Section 3.1.5).

The additional information provided by the individual PMT responses needs to be weighed against the significant additional time required to run the model with this component activated. The optical model is selectable via a switch in the model. Depending on the properties of the optical light and the scintillation yield, up to 100 fold or more increased time is required to run with the optical simulation.

4.7 Count-rate effects

The 4π solid angle, large sensitive volume, and high efficiency requirements for the TAGS technique can be a disadvantage, since even a relatively weak source can result in a large detector count rate and cause pile-up effects. Shifts in the position or shape of the ATAGS spectrum due to a high count rate can significantly impact the ability to perform TAGS measurements. This section looks at the contribution of count rate changes to NaI(Tl) scintillator spectra as a function of detector size. The understanding of these properties will provide guidance on the experimental parameters needed to minimise the influence of count rate for use with ATAGS at CARIBU.

4.7.1 Minimum count rate

The minimum count rate achievable for the detection of a nuclide is constrained by the magnitude of the background radiation in which it is measured. Due to the design requirements, the contribution of background in a TAGS detector can be significant, reducing the minimum detectable amount of activity of a sample. A detector will have an upper limit to the acceptable count rate before other effects start to be introduced (discussed in the next Section 4.7.2). If the detector background is high, this will reduce the overall dynamic range of count rate available for measurement. The nuclides of interest in TAGS measurements are typically short lived, requiring the detector to be in the vicinity of the source generator; this is usually associated with higher background radiation.

The unshielded background count rate of the ATAGS measured in a laboratory free of other sources, is of the order of 900 Hz, with a threshold set just above the noise pedestal for the combined spectrum. For this work, ATAGS will be located inside the CARIBU beam hall in proximity to the ^{252}Cf source shielding cask and hence will be susceptible to stray radiation from the ^{252}Cf source, the isobar separator and associated beam lines. The shielding for this project was designed and built by the UMass Lowell[‡] to incorporate γ and neutron shielding (see section 5.1.1) to minimise this background count rate.

4.7.2 High count rates

At high detector count rates, pile-up becomes significant. Pile-up effects are an inherit problem of the finite processing times of electronic acquisition systems so that signals close in time cannot be separated [Ten84]. To retrieve information from the collected charge,

[‡]The University of Massachusetts Lowell

preamplifiers integrate this charge, then are reset (most commonly by means of resistive feedback). The result is a sharp rising signal followed by a long decaying tail. Amplifiers then integrate and differentiate this signal to produce a Gaussian-like signal whose pulse height is proportional to the collected charge in the tail pulse. If events are occurring at great frequency in the detector, there is an increased probability of another pulse arriving whilst the first event is still being processed. If the event arrival is close enough in time, the signals will ride on top of each other, resulting in a single output signal with a height equal to the sum of the component heights, were the signals measured separately.

The effect of count rate on the original ATAGS detector tubes can be seen by measuring the central and outer PMT response to an 11 kBq ^{60}Co source as a function of source position along the central axis, labelled as $\hat{z}$ with the origin located at the bottom of the ATAGS well (Fig. 4.18). The central PMT was chosen for detailed comparison as the spectral features are more readily recognisable than the outer tubes as was also shown by the optical-photon model (see Section 4.6). The central location of the PMT makes this tube more likely to detect components for events that do not trigger all seven PMTs. These measurements were undertaken with an unshielded ATAGS in a laboratory free of other sources, producing background count rate between 0.93 kHz and 1.07 kHz. The 1173 keV and 1332 keV lines form a single unresolved peak at approximately channel 140 of the central tube spectrum (Figure 4.18a). The peak located at approximately channel 280 is the ^{60}Co sum peak (2506 keV), which increases in relative magnitude as the source is moved into the well, as expected (note that the ATAGS well opening extends to $\hat{z}$=20 cm). These two features are marked with similar lines for the outer tube 4 in Figure 4.18b.

For the higher count rates, there is a notable broadening and shift of the first peak position above a count rate of 6.7 kHz. If a single event triggers all tubes within ATAGS (multiplicity of 7), then we can assume that the total count rate for a single tube is the same as or similar to the total. This is in agreement with the total count rate limitation of 4 kHz suggested by Greenwood *et al.* as an upper limit for TAGS measurements with ATAGS [Gre92b].

High-count rate effects were also investigated using the ANL3x3, ANU5x5 and ANSTOwell6x5 detectors, which are presented in Appendix C. Some of these effects include, energy shifts, peak broadening, count rate summing and PMT gain drain. Table 4.3 summarises the additional measurement count rates and sources used that are presented in Appendix C.

detector	source	Figure	count rate [kHz]
ANL3x3	^{60}Co	C.1	0.1, 0.6, 4.1, 17.8
ANU5x5	^{60}Co	C.2	2.4, 3.1, 4.9, 14.0
ANU5x5	^{137}Cs	C.3	2.6, 32.0
ANU5x5	^{56}Co & ^{60}Co	C.4a	5.2, 5.6, 6.3, 15.1
ANU5x5	^{56}Co	C.4b	4.9, 46.9, 58.7
ANSTOwell6x5	^{137}Cs	C.5	52.0, 76.0
ANSTOwell6x5	^{60}Co	C.6	4.5, 7.2

Table 4.3: High-count rate measurements presented in Appendix C.

4.7.3 Artificially creating pile-up in the model

The motivation for understanding and accounting for the effects introduced by pile-up, is to accurately model all aspects of the detector in order to understand the complex processes

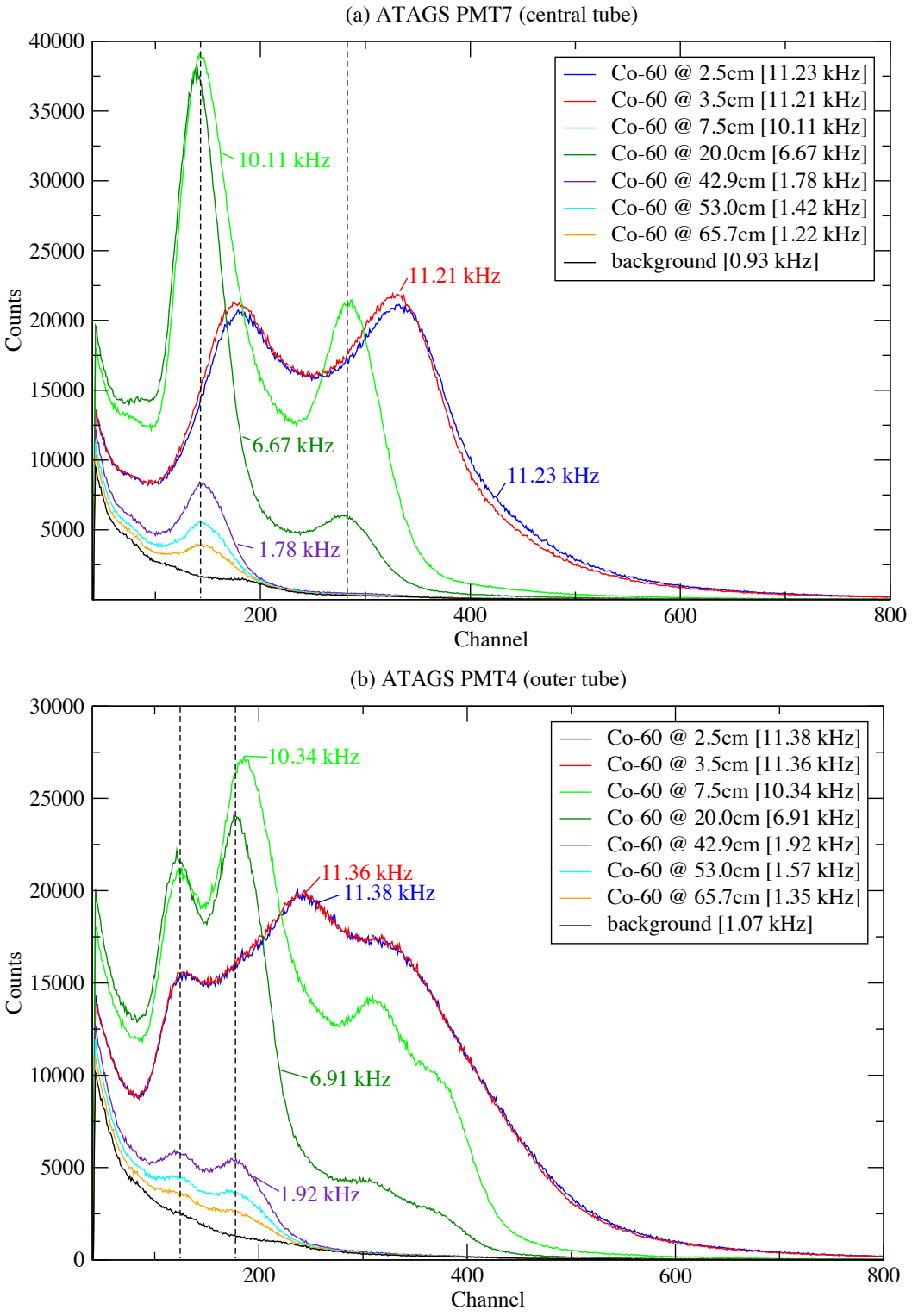

Figure 4.18: Spectra from individual ATAGS PMTs demonstrating count rate dependant effects observed with an 11 kBq ^{60}Co source at varying distances along the detector symmetry axis ($\hat{z}$), where 0 cm is at the bottom and 20 cm is flush with the top of the well. Spectra are for (a) the central tube PMT 7 and (b) a representative outer tube PMT (tube 4) for these original RCA S83021E type PMTs . The background spectrum (no source) is shown at the bottom in black in both spectra.

and interactions that can occur in measurements by ATAGS. If the effects cannot be mitigated by controlling the detector operating conditions, then a method is needed to model these effects in the simulation.

Pile-up was introduced in Section 4.7.2 and is the effect of individual pulses occurring in quick succession so that they sit on top of each other or pile-up, altering the energy signal detected by the acquisition system. The significance of the pile-up event is determined by the arrival time of the second event relative to the first. When the second event arrives on the tail of the first event, a slight increase or decrease in the second event's amplitude can occur. Referred to as tail pile-up, this manifests itself as asymmetry of a peak, typically on the high energy side when the pole-zero of the amplifier has been properly adjusted, otherwise undershoot of the first event can cause a decrease in the second peak height. When the time interval is reduced even more, a significant component of the first event is added to the processed height of the second. When the second event falls within the resolving time of the first event, the acquisition system will treat both pulses as a single event with the combined energy response, known as summing pile-up. This is summing based upon the statistical collision of independent events as seen by the acquisition system. This should not to be confused with the summing of events from a cascade from a single decay process that is utilised in the TAGS method.

Monte Carlo simulations typically work on an event by event basis and produce only discrete data for each separate event. In the present case, GEANT4 does not directly model pile up, so these effects must be taken into account outside of GEANT4. A script has been written to artificially produce the effects of pile up on simulation data, taking the average count rate as input. The distribution of time intervals between adjacent events takes the form of an exponential distribution,

$$I(t) = re^{-rt} \tag{4.5}$$

where:

t = time between adjacent events;
$I(t)$ = time distribution function between adjacent events; and
r = average rate.

Equation 4.5 is derived assuming a Poisson random process looking at the distribution of time between random events of nuclear decay [Kno99]. A random-exponential function in C++ is utilised to produce this time between the events, with the shape and decay determined by the count rate (r) being applied. A tail-pulse shape and decay time are calculated using the simulated pulse height of the energy event and assumed pre-amplifier characteristics.

The time between two adjacent events (t) is found from the exponential random function and compared to the calculated pulse shape or tail length (t_{tail}) of the earlier event and the resolving time ($t_{resolving}$). In this simplified model there are four possibilities:

- $\mathbf{t > t_{tail}}$
  no pile-up; both events are unaffected,
- $\mathbf{(0.7 \times t_{tail}) \leq t < t_{tail}}$
  tail pile-up; the second event height is adjusted by the tail of the leading pulse overshoot, first event not affected;

- $(\mathbf{0.2} \times \mathbf{t_{tail}}) \leq \mathbf{t} < (\mathbf{0.7} \times \mathbf{t_{tail}})$
  component pile-up; second event height is increased by a component of the first, first event not affected,

- $\mathbf{t} < (\mathbf{0.2} \times \mathbf{t_{tail}})$
  summing pile-up; both event amplitudes are summed.

The pulse amplitude in latter three cases is determined from a fitted function based on the observed pre-amplifier pulses of the ANSTOwell6x5 detector with a nominal resolving time ($t_{resolving}$) of 1 μs. Figure 4.19 shows the result of the pile-up script applied to the raw energy deposited simulation of ^{60}Co in ATAGS with simulated count rates of 5 kHz, 15 kHz and 30 kHz. As the count rate is increased in the script, more events are likely to cause pile-up generating events that exceed the 2505 keV sum peak energy.

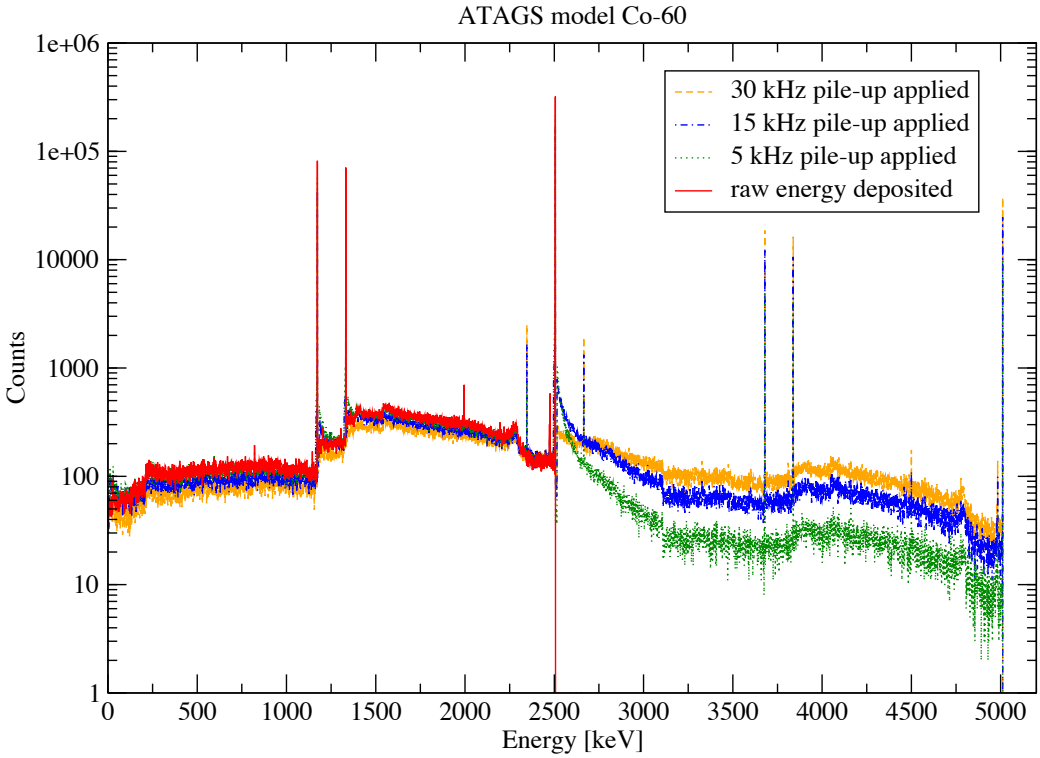

Figure 4.19: GEANT4 simulation of a ^{60}Co source in ATAGS including the effects of pile-up.

The pile-up script is applied to the ^{24}Na simulation and compared to experimental data collected with 63 kHz count rate as shown in Figure B.3 of Appendix B. The simulation data of Figure 4.20 is fitted using the same methodology of FWHM and energy parameters as used in Figure B.3, in this case the pile-up generator is applied to the raw data prior to fitting. The parameters of the fit were not found to deviate from the previous numbers significantly. The pile-up script required an adjustment of the count rate by a factor of $1 + \frac{1}{15}$ in order to produce the magnitude of the shoulder beyond 4 MeV, compared to the magnitude of the features less than 4 MeV. It is not clear why there is a large difference between the theoretical count rate produced by the random generator compared to the experiment, but this factor produces a similar comparison for the other cases of ^{24}Na with count rates of 28 kHz, 6.8 kHz and 1 kHz. The fitted data shows a discrepancy of the peak at 8.2 MeV both in position and in magnitude. The magnitude of this summing

peak feature could be adjusted in the pile-up script by refining the time boundaries for the overlap, which would better reflect the experimental acquisition conditions. The pile-up generator was applied to the non-proportional Cano-Ott result, but this did not result in any significant change in the relative positions of the peaks across the spectrum due to pile-up.

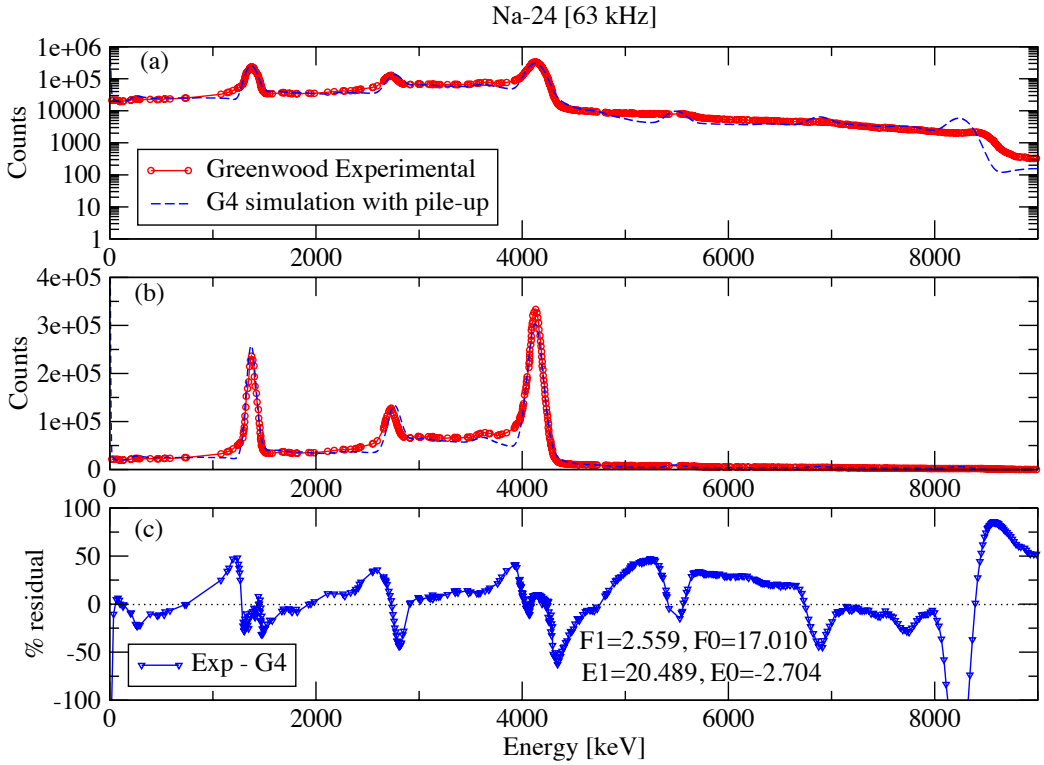

Figure 4.20: Greenwood's experimental data for ^{24}Na at 63 kHz compared to the GEANT4 simulation with pile-up applied [Gre92b]. Data is shown with the y-axis in (a) log-scale, and (b) linear-scale. The percentage residuals for each fit are shown in (c).

4.7.4 Count-rate effects summary

High count rate effects have been shown to be present for NaI(Tl) scintillators, with the larger volume well-type detectors being more susceptible. Experimental measurements with ATAGS will have to be undertaken within a strict count rate window so that the effects are avoided, or when this is not feasible, the effects are quantified and can be corrected. High count rate effects can be mitigated by the limiting of the total count rate below 4 kHz, in agreement with Greenwood's work [Gre92b]. To allow for flexibility of the experiment, count rate regions around this limitation should be measured and characterised using the acquisition system intended for the experiments. With restrictions in access to the ATAGS for testing and refining this number, the 4 kHz value has been adopted. The low limit will be defined by the shielding that surrounds ATAGS and the background radiation and proximity to the CARIBU source. This section highlights the importance of maintaining a low, constant count rate in order to perform TAGS measurements using NaI(Tl).

4.8 ATAGS data collection methodology

The energy spectrum from ATAGS is a result of summing the seven spectra from the individual PMTs on an event-by-event basis. This has been achieved in the previous work of Greenwood, Helmer *et al.* by passively summing the components (see also Section 4.3). An alternative summing method is to collect the individual signals using the data acquisition system and sum the individual tube data together in software post collection. This proposed method will require a means to adjust the relative responses of the individual signals akin to the physical gain matching traditionally achieved via differences between the applied HV on each tube. The additional data will also allow the monitoring of the individual tube responses for drift over the large collection durations. This method of software-gain matching is investigated in this section using GEANT4 simulated data in lieu of access to ATAGS.

The collection of these seven individual signals requires a low-level threshold for each signal. The threshold is required to remove the dark current inherent in PMT signals at low energies. If all the tubes have equal responses, then the magnitude of a single tube would be 1/7th that if the summed signal. The collection of these smaller signals each with their own threshold could potentially result in a loss of real signal, particularly if the threshold is incorrectly set. The impact of the individual low-level thresholds on the summed response is also investigated here.

4.8.1 Result of gain-shifting of individual PMT components

The gain-shifting of individual component PMT responses and its effect on the resolution is investigated here. Using ^{60}Co simulated optical-photon data, an individual tube is shifted by a software multiplier to emulate a HV shift. Figure 4.21 shows the slight shape change in the summed response due to PMT1 and PMT7 being each individually scaled by 0.4. The effect is not obvious with these statistics, but a degradation of the peak shape can be seen via changes in the valley between the 1173 and 1332 keV peaks. This suggests that if individual PMT data is collected in experimental conditions, then a software adjustment of the individual tube responses could be undertaken to adjust for drift and maximise energy resolution.

4.8.2 Low-level threshold effects on individual PMT collection

Two data acquisition methods for ATAGS produced data were proposed; one method involves passively summing the pre-amplifier signals into a common signal, the other is to collect all of the individual data signals directly into the acquisition system and sum them via software. The latter suggestion is the preferred method as it provides a means of correcting the HV gain adjustment post acquisition. A possible concern with this approach is the loss of a low-energy signal that is caused from unequal low-level discrimination on the individual signals and their cumulative effect on the summed response. This is in contrast to the passively summed method where the low-energy signals are summed with the other low-energy signals and therefore are collected above the single digitizer threshold. The optical-photon model is used here to investigate the effect of setting a low-level threshold on the individual PMT responses, which will give more insight into how the individual components add to give the final result and help to evaluate the final collection methodology. The previously developed optical-photon data for ^{60}Co is used in this section.

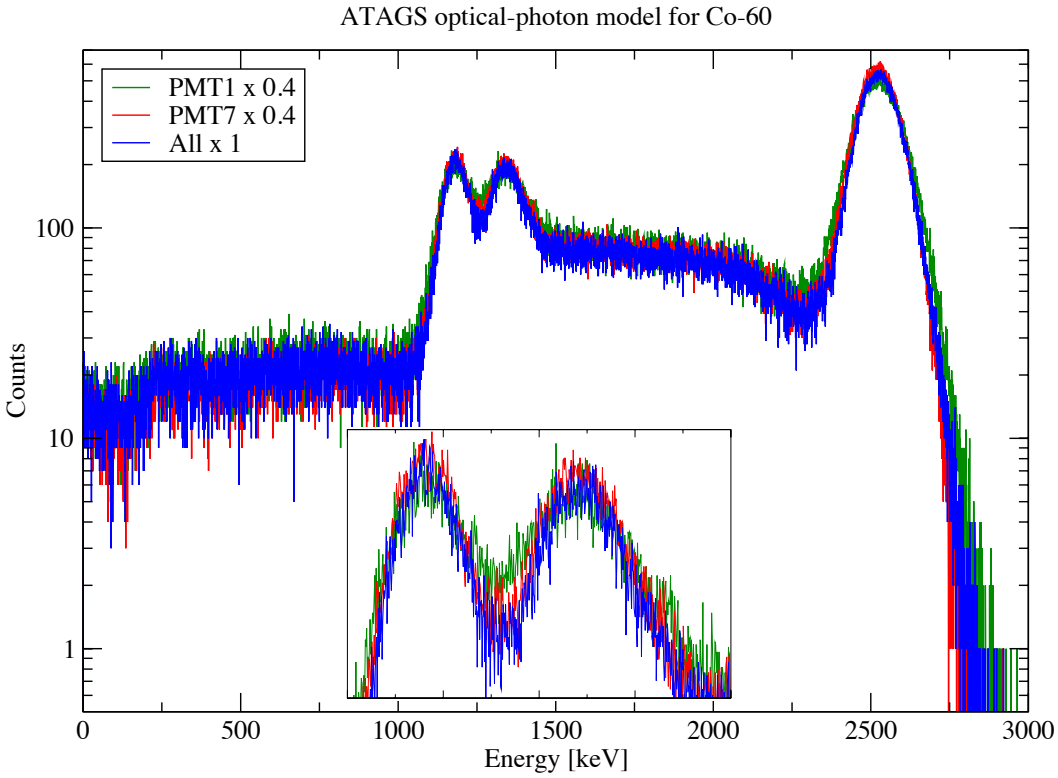

Figure 4.21: Simulated optical-photon model of ATAGS for a ^{60}Co source showing the combined PMT components and the effect of scaling individual PMT components. The inset shows a zoomed section of the valley between the 1173 and 1332 keV peaks.

The threshold was set at 3 different energies, 32 keV, 64 keV and 128 keV and applied equally across the individual PMT component responses. The range of these low-level thresholds is quite significant in terms of the individual components and represents a worst case scenario. Figure 4.22 shows the individual model responses for the outer PMTs and the central PMT with the low-level thresholds indicated.

The combined response of the ATAGS with the low-level thresholds applied is shown in Figure 4.23. The spectrum of counts lost is the difference between the zero threshold spectrum and the imposed threshold spectrum. The majority of the low-level threshold component is from the Compton continuum and does not affect the sum peak. The application of a threshold at 128 keV across all responses does start to affect the intensity of the 1173 keV peak.

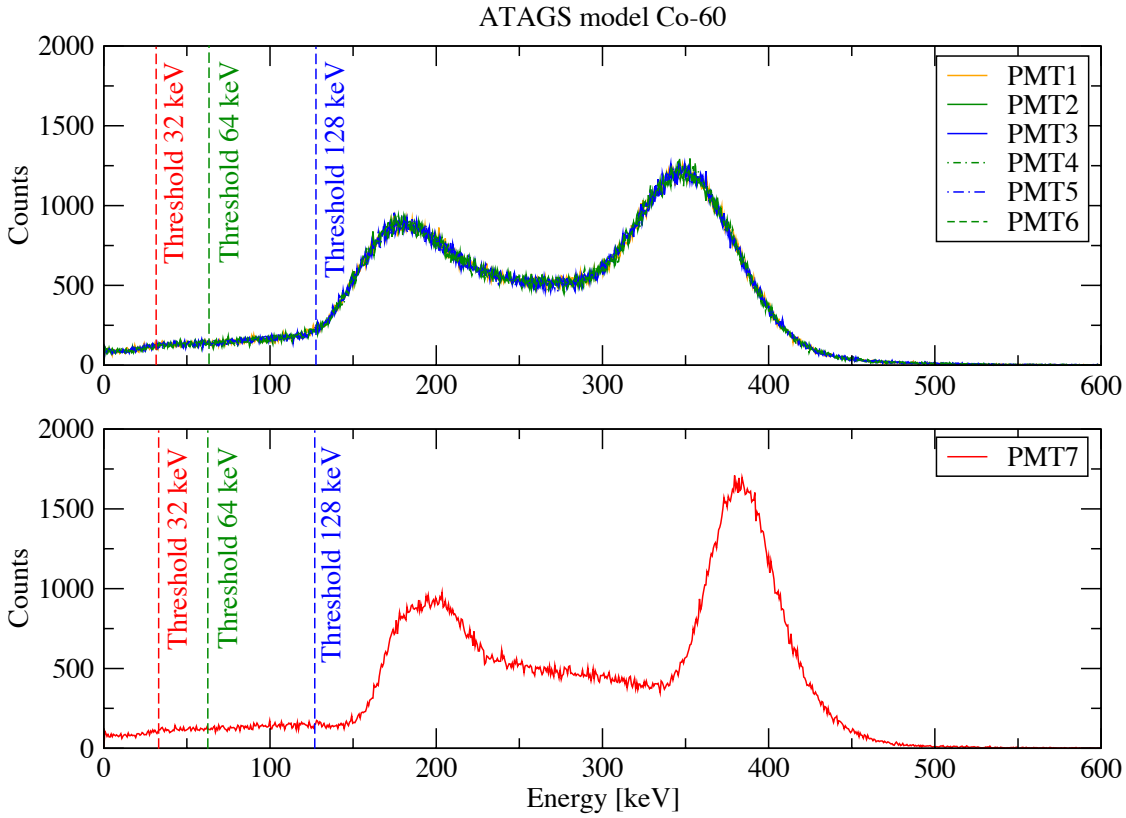

Figure 4.22: Individual ATAGS tube spectra from the optical-photon model applied to a ^{60}Co source. Low-level thresholds that were used to demonstrate a summation comparison are indicated.

Table 4.4 provides a summary of the count losses due to these thresholds. The losses were found to only affect the low energy part of the summed spectrum for the energy range up to 128 keV. The thresholds applied here are significant on the individual components and unlikely to occur at this extreme range for all tubes simultaneously. As such, these results should be used as a guide to the upper limit of losses to the overall counts in the spectrum. Any inadvertent exclusion of real signal will be isolated to low energies. The potential losses from having a threshold incorrectly set are insignificant compared to the advantage of being able to gain match the individual PMT tubes post data collection, so as to account for any shifts due to drifts or count rate changes etc (see also gain matching in Section 5.2.3).

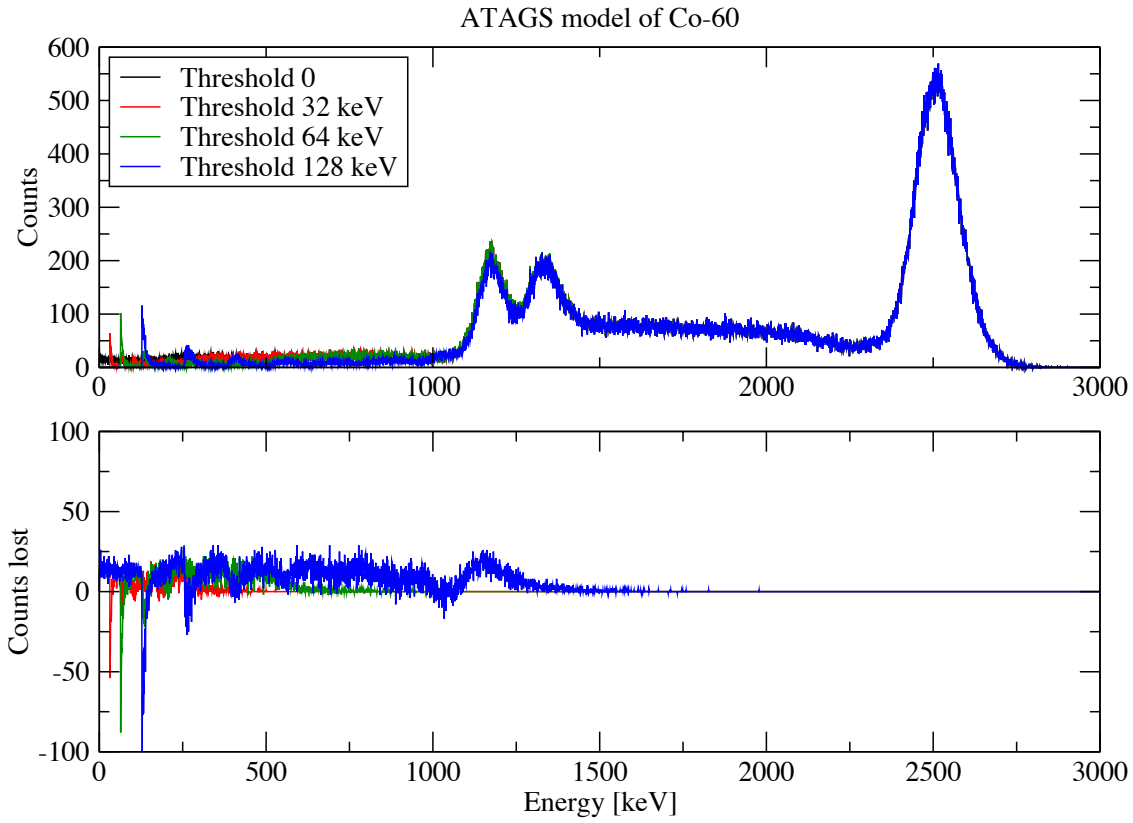

Figure 4.23: Loss of counts in the combined ATAGS optical-photon model due to low level thresholds applied across all of the component tubes. The optical-photon model generated 50 k events of a ^{60}Co source for each PMT tube (components shown in Figure 4.22). These components have low energy thresholds of 32, 64 and 128 keV applied equally to each tube. The effect on the overall combined spectrum (bottom panel) to these low energy thresholds is limited to low energies (see Table 4.4).

Threshold	Sum loss	% loss
32 keV	3,485	1.01
64 keV	8,851	2.57
128 keV	20,771	6.03

Table 4.4: Loss of counts in the combined ATAGS optical-photon model due to low-level thresholds applied across all of the component tubes (see Figure 4.23 and text). The application of these thresholds gives count percentage losses as presented in this table.

4.9 Initial inspection of ATAGS at ANL

The performance of ATAGS at INEL during the 1990's has been well documented by Greenwood, Helmer *et al.* [Gre92b, Hel94c]. Sixteen years after commissioning, it is clear that the important questions are "what is the performance of the ATAGS detector upon receipt at ANL?" and "how does this compare to the previous performance?". More importantly, is the ATAGS suitable for TAGS measurements with CARIBU produced beams?

Calibration sources were measured at ANL as a preliminary evaluation of the detector health. The performance of ATAGS was compared to previously published results, starting with the energy resolution.

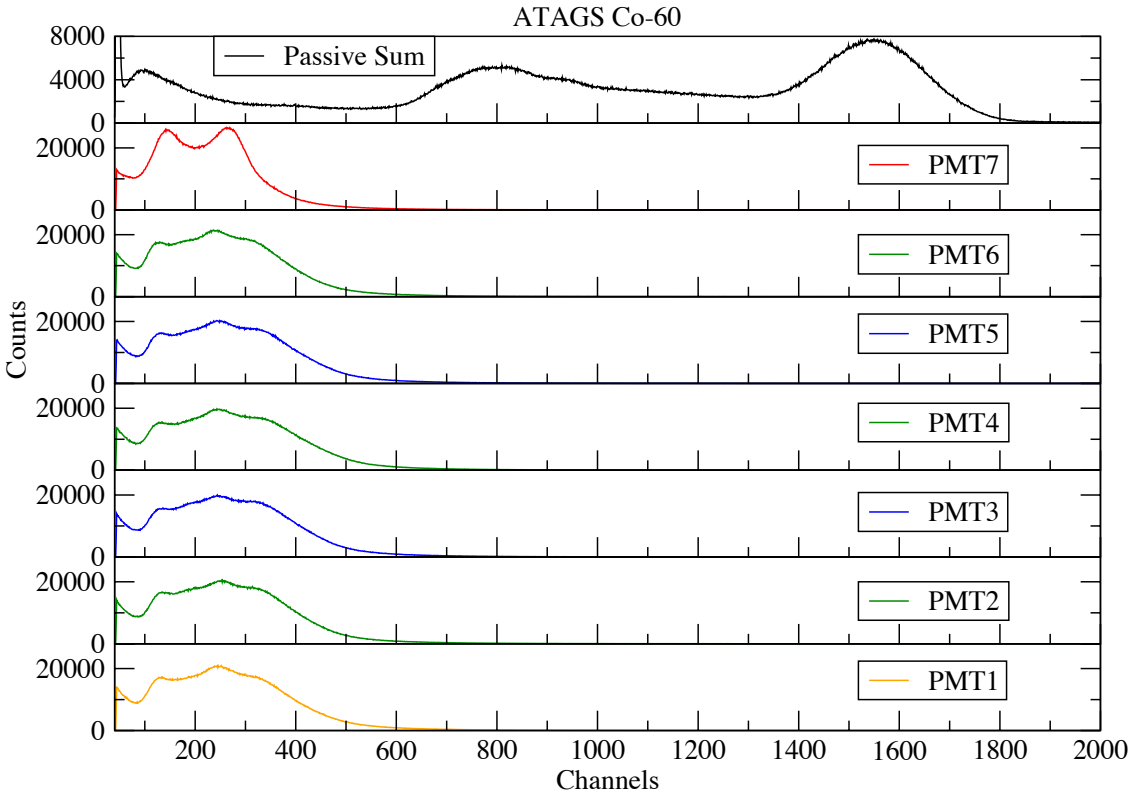

Figure 4.24: Initial measurement with a ^{60}Co point-source located 25 mm in front of ATAGS (outside the well) along the main axis. From top to bottom, the spectra are the passively summed total response from all tubes, then the individual responses of tubes from 7 to 1. Spectra were measured with the original RCA S83021E PMTs at a nominal resolution of 1.67 keV/channel.

The individual PMT spectra and the summed response were measured using point sources at various locations around ATAGS. The electronics consisted of a Lecroy HV4032A high-voltage supply, an ORTEC113 preamplifier, a Tennelec TC244 shaping amplifier, and a Canberra Multiport2 Multi-Channel Analyser (MCA). The PMTs initially used with ATAGS were the original RCA S83021E PMTs. Figure 4.24 shows spectra for the individual PMT responses, and the summed spectrum, for a ^{60}Co source located 25 mm from the well opening along the main axis. The individual PMT responses do not show any immediately recognisable spectral features associated with the expected spec-

trum of the measured source. When the individual PMT signals are added together by means of tee-connectors (passively summed), either before or after the preamplifier stage, all of the tube components for a single event add to give the complete spectrum (event-wise summing). PMTs 1 - 6 have similar responses to each other while PMT 7 has a significantly different shape that was predicted by the optical-photon model of ATAGS (see Figure 4.17). The major difference with the measurement compared to this model is the much worse energy resolution. Amplifier settings were varied in an attempt to improve the overall resolution. The shaping time was altered between 0.5 μs and 6.0 μs, and the Pileup Rejection function was utilised but resulted in no significant change to the resulting shape of the spectra.

The gains were adjusted so that the responses matched each other while using a consistent set of equipment. This is a very rough way of gain matching the spectra and was not necessarily expected to be optimised or ideal. The consistent equipment eliminated any issues with voltage dividers, preamplifiers or high-voltage (HV) supplies. Six of the seven PMTs are located around the ATAGS, viewing the scintillator symmetrically. The responses of these PMTs (1 to 6) to a source located on the symmetrical axis, show similar shape and features. The central tube's response (PMT 7) is different to the outer tubes due to the differing geometrical position and view of the scintillator crystal as shown by the optical-photon model (Section 4.6). This relative response of the central tube compared to the outer tubes was not known at the time, so the HV was adjusted such that it aligned as shown in Figure 4.24. The gain matching of the PMTs is not fully optimised in this data, the gain-matching method is discussed in Section 4.3.2.

Owing to the large sensitivity of the ATAGS, Greenwood *et al.* implemented an upper total count rate-limit of 4 kHz to minimise pile-up and random summing effects (see Sections 2.3.1 and 4.7) [Gre92b]. A ^{60}Co source fitting this criterion was not available during these measurements, the lowest available activity for ^{60}Co was 11 kBq. With this source located 20 mm from the bottom of the well of ATAGS, a total background-subtracted count rate of 10.1 kHz was measured, showing significant signs of pileup. The expected doublet of γ rays from ^{60}Co could not be resolved.

In the absence of a calibration source with a more suitable activity, the 11 kBq source was positioned external to the well of ATAGS in order to get a resolved spectrum. Figure 4.25 shows the various positions of the ^{60}Co calibration source that were used with the measured total count rates, and the resulting passively-summed spectra. The spectrum with the largest count rate (Top middle), is due to this position having the largest solid angle subtended of active NaI(Tl). It is this spectrum that would be expected to have the greatest energy shift of all of the spectra due to pileup effects. This is not the case with the top rear position having the most change. There is a shift in the energy response with the change in the source position, the effect of which is not due to pile-up alone.

The performance of ATAGS at INEL in 1992, is shown by points in Fig. 4.4(a), which is the passively summed ^{60}Co spectrum reproduced from Greenwood *et al.* [Gre92b]. The resolution for the 1173 keV and 1332 keV γ rays of ^{60}Co were approximately 7.40% and 6.52% respectively, as deduced from this digitised spectrum (see Table 4.2 in Section 4.5). The 'on axis' spectrum is the only result that has a total count rate within Greenwood's 4 kHz limit, with the resolutions measured to be 8.8% and 10.2% for the 1173 keV and 1332 keV peaks, respectively. Another indicator of performance is the peak (1332 keV) to valley (minimum between the 1173 keV and 1332 keV) ratio. The most recent value measured is 1.09, which is quite poor compared to the value of 1.75 measured in 1992 (Table 4.2).

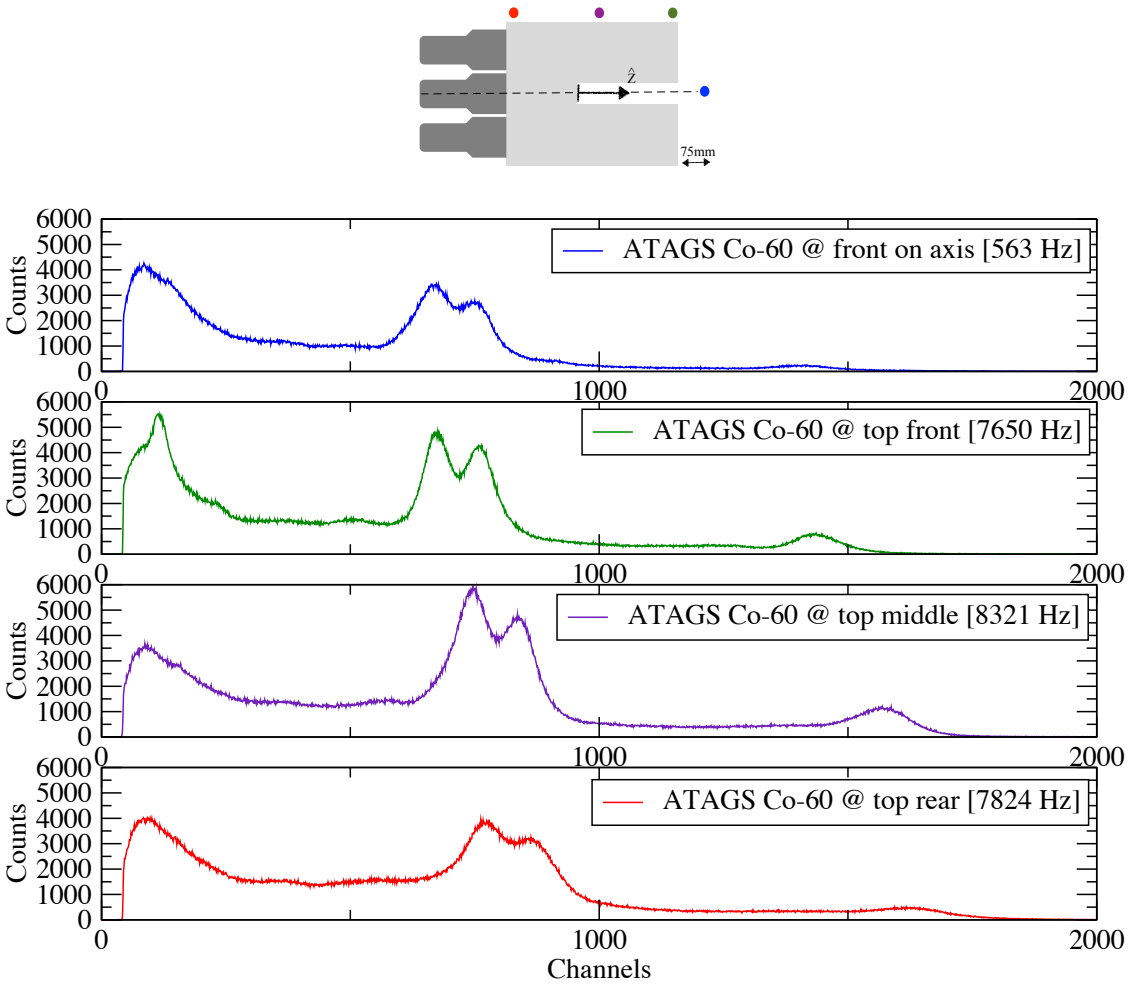

Figure 4.25: ATAGS measured spectra of a ^{60}Co source placed at differing positions with a schematic diagram of ATAGS indicating the source positions measured. These were collected using the original RCA S83021E PMTs and passively summing the PMT signals.

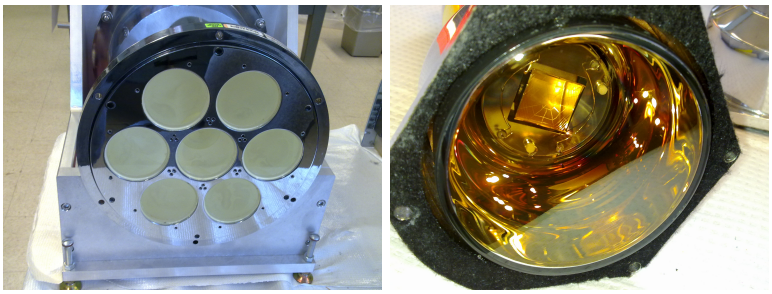

(a) (b)

Figure 4.26: Photographs of the rear of ATAGS with PMTs removed showing (a) no major problems visually with the crystal and (b) the photocathode of one of the removed RCA S83021E PMTs.

This initial assessment indicated a degraded energy resolution when compared to 1992. The most likely causes of worsening resolution of this type of detector are a degradation of scintillator material or of the PMTs. The PMTs of ATAGS were removed to visually inspect both the scintillator and tubes. The scintillator was found to be transparent with only a very slight yellow colour (Fig. 4.26a). This indicates the integrity of the glass envelope and aluminium-can around the hygroscopic NaI(Tl) crystal, which, if compromised, would turn a dark yellow in colour. No fractures or damage in the crystal material could be seen, but there is a small gas bubble feature nearest to PMT positions 3 and 4 that looks to have originated during manufacture. The PMT photocathodes showed no obvious signs of stripping or damage based upon a visual inspection of their uniformity (see Fig. 4.26b).

The optical coupling had dried, requiring application of optical grease to all of the tubes. The optical coupling was replaced and the detector re-assembled with the original RCA S83021E PMTs. There was no significant improvement in the resolution of ATAGS with the reassembled tubes. Owing to the age of the PMTs and the unknown history of the detector between Greenwood's work and its arrival at ANL, it was thought that the PMTs might not be optimal, and might be affecting the resolution.

The only improvement opportunity attainable for ATAGS was through the replacement of the PMTs. Replacement 12-stage PMTs with specifications as close as possible to the RCA S83021E PMTs were found from Hamamatsu (type H6559). The timing of the arrival of the replacement tubes at ANL resulted in the assembly, modifications and additional testing being done by collaborators from the University of Massachusetts Lowell (UML), immediately prior to experiments with CARIBU.

Chapter 5

ATAGS re-commissioning at ANL

An experimental campaign was undertaken in July of 2015 to re-commission the ATAGS detector at the CARIBU facility of Argonne National Laboratory (ANL). The objectives were to install ATAGS, evaluate its condition and also to benchmark the simulations presented in this thesis, with an emphasis on developing an understanding of the analysis methods and the resultant limitations on measuring β-feeding intensities using the TAGS technique. Over a three-week period, a collaboration from the ANU, UMass-Lowell, and ANL worked to dismantle the XArray and SATURN instrument from the previous experiment, install ATAGS with shielding, electronics, beam-lines, and a tape station, in preparation for a week of allocated CARIBU beam time.

5.1 The experimental setup at CARIBU

5.1.1 Installation of ATAGS and shielding at CARIBU

Prior to the allocated beam-time, the group of UMass-Lowell built a shielding assembly and pneumatic lifting device for ATAGS, which was oriented vertically with the well opening positioned in the upward direction, as can be seen in Figure 5.1(a). This allowed a vertical beam pipe to be set into the detector. This work formed a Master of Science project for a UMass-Lowell student, in which the student was responsible for building the ATAGS shielding and experimental setup for ATAGS measurements at CARIBU. Vacuum beam-pipes, junctions and pulleys were manufactured at UMass-Lowell for this project, with the final adjustments to the beam-line made at ANL by the physics workshop during the installation.

The shielding structure consisted of aluminium framing (T-slot 80/20) built to support both the detector and the shielding (Fig. 5.1). The framing provided a housing for lead bricks (each 50.8 mm thick x 101.6 mm height x 203.2 mm width), that were machined flat. This enabled them to stack on top of each other, creating a wall that sat between the inner and outer walls of the frame. Once assembled, each lead wall measured 50.8 mm thick, 458 mm wide and 661 mm high, around ATAGS. Lead bricks of the same thickness were assembled on top of the ATAGS detector, supported by a stainless steel cover plate with a hole to allow access to the ATAGS well. Additional lead bricks were placed under the frame assembly on the concrete floor to shield the detector from both scattered room radiation and intrinsic radiation from the concrete.

This amounted to approximately 1.4 tonnes of lead shielding that was supported by the ATAGS shielding frame. Figure 5.1(c) shows the support frame together with aluminium-plate covers around the lead walls. A piece of borated polyethylene was placed over the top layer of lead bricks. Four 20 mm thick lead blankets with dimensions 305 x 914 mm,

(a) (b)

(c) (d)

Figure 5.1: ATAGS shielding assembly at the CARIBU facility with the beam-line coming in from the right of each picture. (a) Top of ATAGS also showing the end-cap of the beam-line containing the tape pulley for the well position; this end-cap eventually sits inside at the bottom of the well. (b) ATAGS orientated vertically, supported by pneumatic lifter, with the vertical beam-line pipe containing the tape, looking from the top of the assembly. ATAGS is in the lowered position to show the beam-pipe (the photo was taken during setup prior to alignment of the pipe); (c) ATAGS shielding assembly (centre) during installation showing the aluminium plates covering the lead-brick walls; (d) Completed shielding assembly showing: borated polyethylene top cover [pink], lead blankets covering the corners [grey] and the borated polyethylene sheets [black]. The tape station is shown in the foreground of panels (c) and (d).

were tied around the assembly at the corners to cover the gaps caused by the aluminium support frame. Sheets of borated polyethylene were added around the blankets from the ground to the top of the frame. The final shielding assembly is shown in Figure 5.1(d) with the top piece of borated polyethylene (pink), the lead blankets (grey) and the sheets of borated polyethylene (dark brown).

Figure 5.2 shows a photograph and a simplified schematic of the setup used at CARIBU. The ion beam enters this beam-line on the right of the picture indicated by a red arrow and implants ions onto the tape inside of the first T-shaped vacuum box (T-box). Inside the custom-made T-box are passive pulleys that provide guiding and tension of the tape at the implantation position. A standard clover detector (clover A, see Section 2.4.1) was removed from the XArray support frame and was used to collect high-resolution spectra of γ rays from the implanted ions for diagnostic purposes. The clover was located at 90° to the beam-line with a view of the implantation T-box. The back of the clover's green liquid nitrogen dewer can be seen in Figure 5.2(a) and is indicated by the transparent grey block over the T-box in Figure 5.2(b). The tape is moved in a clockwise direction, driven by a stepping motor in the programmable tape station on the far left; the latter also houses the vacuum system for the beam-line (see Section 2.4.2).

5.1.2 The Digital GammaSphere Data AcQuisition system (DGS-DAQ)

The Digital GammaSphere Data AcQuisition system (DGS-DAQ) is a pulse processing data acquisition system that uses signal digitisers and Field-Programmable Gate-Arrays (FPGA), built to replace the analogue acquisition system of Gammasphere [ANLe] at ANL [And12]. The DGS-DAQ was originally developed by ANL and Lawrence Berkeley National Laboratory (LBNL) for use with the GRETINA (Gamma-Ray Energy Tracking In-beam Nuclear Array) detector [GREb] but has since developed into a versatile acquisition system, enabling its use with all detector systems at ATLAS.

DGS-DAQ consists of a number of digitiser modules linked to trigger modules via a VME* bus. Experimental Physics and Industrial Control System (EPICS) is commonly used free software that is used to run the DGS-DAQ hardware. Multiple digitiser boards can be utilised in the system, each having 10 analogue channels with 14 bit ADCs operating at 100 MHz digitisation rate, sampling the waveform at 10 ns intervals. The ADCs are connected to an FPGA on each board that processes the digital signal. The system is networked so that the collected data can be written to remotely mounted disks [And09, Cro08, And12].

DGS-DAQ can collect data in either normal mode or trace modes. In trace mode, the digitised waveform is recorded for each event. Figure 5.3 shows an example of traces of a single event as a function of time produced in viewing a ^{60}Co source. The trace length in this case is limited to a maximum of 4000 ns or 400 samples to minimise the overall FPGA and board rate, starting at an offset from the initial trigger [Cro08]. This particular example is missing an event in PMT5, while PMT4 has a trigger offset half the value of the other tubes. The normal mode consists of the FPGA processing each trace to obtain an energy for each trace, which is based upon the post-rise and pre-rise information. Both collection modes were used at various times during the present work.

Data produced from the DGS-DAQ are in a binary format which can be sorted using general purpose codes written in C++/CINT referred to as GEBSort and GEB-

*VME stands for 'Versa Module Europa' or 'Versa Module Eurocard' and is a communications bus able to link standard modules conforming to ANSI/IEEE standard 1014-1987.

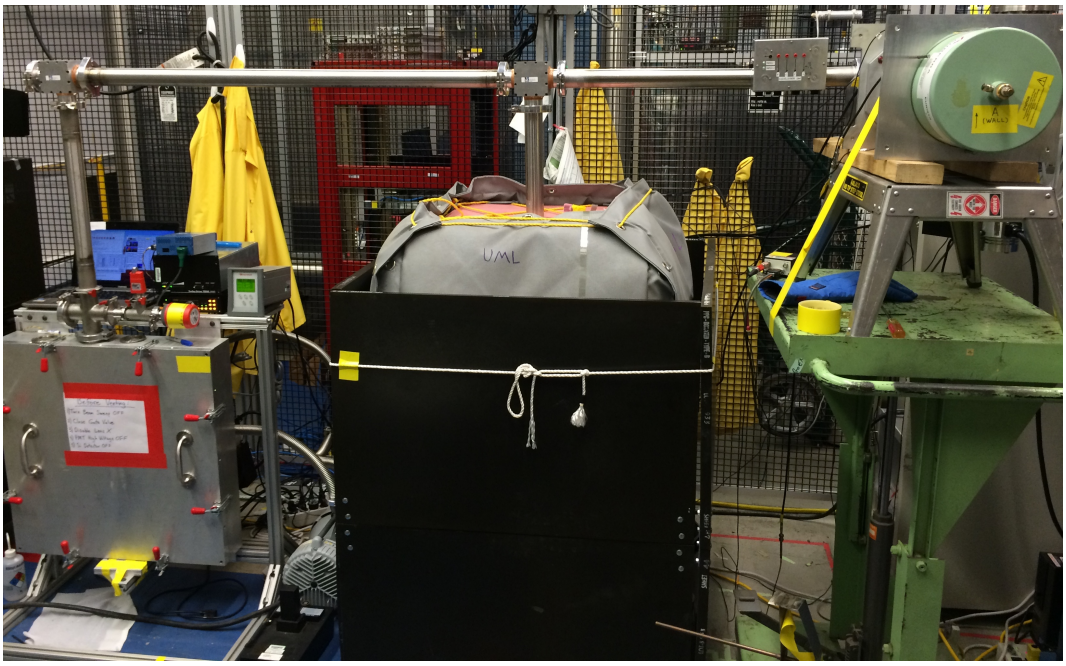

(a)

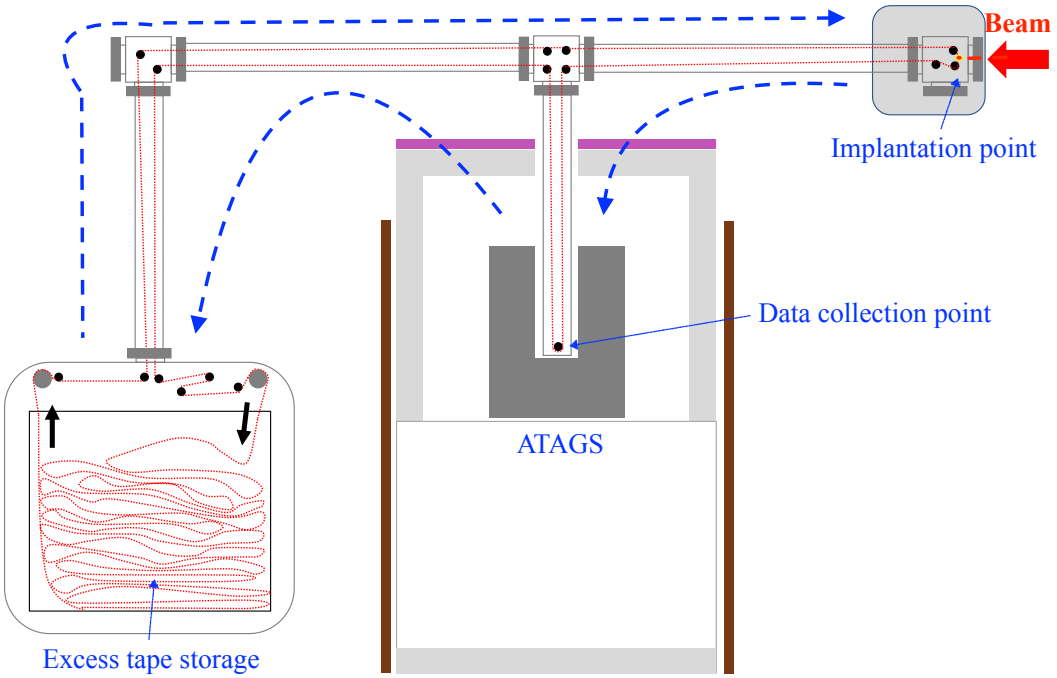

(b)

Figure 5.2: Setup of ATAGS at the CARIBU beam-line: (a) photograph, and (b) schematic in the same orientation. From left to right, the tape station feeding tape to the experiment in a clock-wise direction, ATAGS in lead shielding (grey), surrounded by borated polyethylene [pink and dark-brown] and a standard HPGe Clover detector at the implantation T-box (far right of (a) and transparent grey box in (b)). The red arrow indicates the CARIBU beam direction at the point of implantation on to the tape. The CARIBU HV cage can be seen in the background of the picture, with the back of the CARIBU source cask beyond this (top left of the photo). The location relative to CARIBU is the dotted line in Figure 1.1.

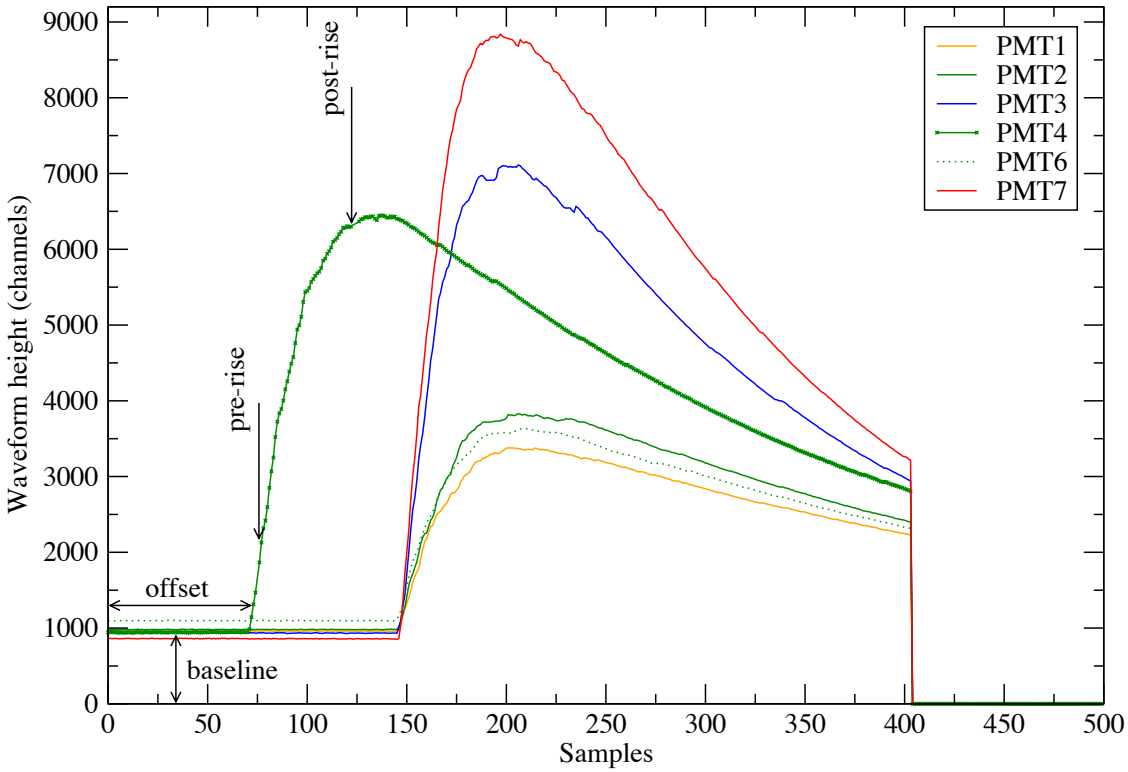

Figure 5.3: Detector signal traces for each ATAGS PMT produced by the DGS-DAQ for a single event measuring a ^{60}Co source. The pre- and post-rise time positions are shown for the PMT4 trace. The difference in heights of these positions can be used to establish the energy result for the event. PMT4 trace has a smaller offset value in this example compared to the other traces.

Merge [ANLc]. These functions were written by ANL to organise and manipulate the collected data into histograms using CERN ROOT [CERb]. In addition to some modifications to the ANL software, multiple scripts were created to analyse the produced data using C++, Python and ROOT.

The DGS-DAQ was also set up to collect energy signals from the pre-amplifiers of the four HPGe crystals of the clover implant monitor detector. The ATAGS energy signals for each tube were collected individually to allow gain-matching before they are summed. Each of the seven ATAGS energy signals were produced by coupling the PMTs to their own preamplifier (Canberra model 2005). A trigger signal produced by the tape controller was also recorded that can be used to synchronise the start time of the tape cycle with the associated detectors (see Sect. 5.1.3).

5.1.3 The tape station duty cycle

For the measurements with ATAGS, the general-purpose tape station was utilised to move the CARIBU ions into ATAGS located some distance from the beam-line implantation position (as shown in Fig. 5.2). The system has the advantage of transporting radioactive ions over a distance to ATAGS, therefore providing enough space to allow for the significant shielding required. The disadvantage is the time required to transport the ions that will limit the capacity to measure shorter-lived nuclides. Figure 5.2b shows that clockwise movement of the tape provides the shortest point-to-point distance along the tape path from implantation position to ATAGS. Standard, 35 mm width, perforated aluminised mylar tape was used in the XArray experiments. A thinner mylar tape was utilised for ATAGS, with no metallised version available at the time of the experiments.

The tape movement system is programmable so as to set a duty cycle specific to the nuclide of interest. The overall cycle generally consisted of a beam-on, tape movement and collect sequence - although it is completely customisable. Figure 5.4 shows an example of the tape cycle including the tape motion, implantation and subsequent decay of ions from the perspective of (a) the tape at the implantation site, (b) the HPGe clover, and (c) ATAGS. The duration of each sequence is tailored to maximise the yield of the ions of interest implanted on the tape and moved into ATAGS before they decay, while also allowing for the compromise between maximising the counting statistics for the target across four half-lives, whilst removing unwanted progeny.

Figure 5.5 shows the logic of the tape station controller. A Programmable Logic Controller (PLC) is used to control and coordinate the tape stepper motor, the low-energy beam-line kicker and the DGS-DAQ (Sect. 5.1.2) start trigger, that all together create the tape and measurement cycle. A 10 Hz continuous clock signal is used to synchronise the tape controller with the CARIBU control system. A TTL[†] trigger signals the beginning of the cycle to the DGS-DAQ, recorded in the data as a time-stamp from the acquisition system clock. A separate TTL signal controls the low-energy beam-line kicker, effectively switching the CARIBU beam on and off as needed. During the setup, a section of tape was threaded through the system under tension while various points were carefully marked. The length of tape between the implantation point and the measurement position in ATAGS was measured to be 1.672 m. This information was then used as input into software on the Windows computer to set the required physical length to move the tape

[†]Transistor-Transistor Logic: a voltage between 2 and 5 V represents a high state, while between 0 and 0.8 V represents a low state.

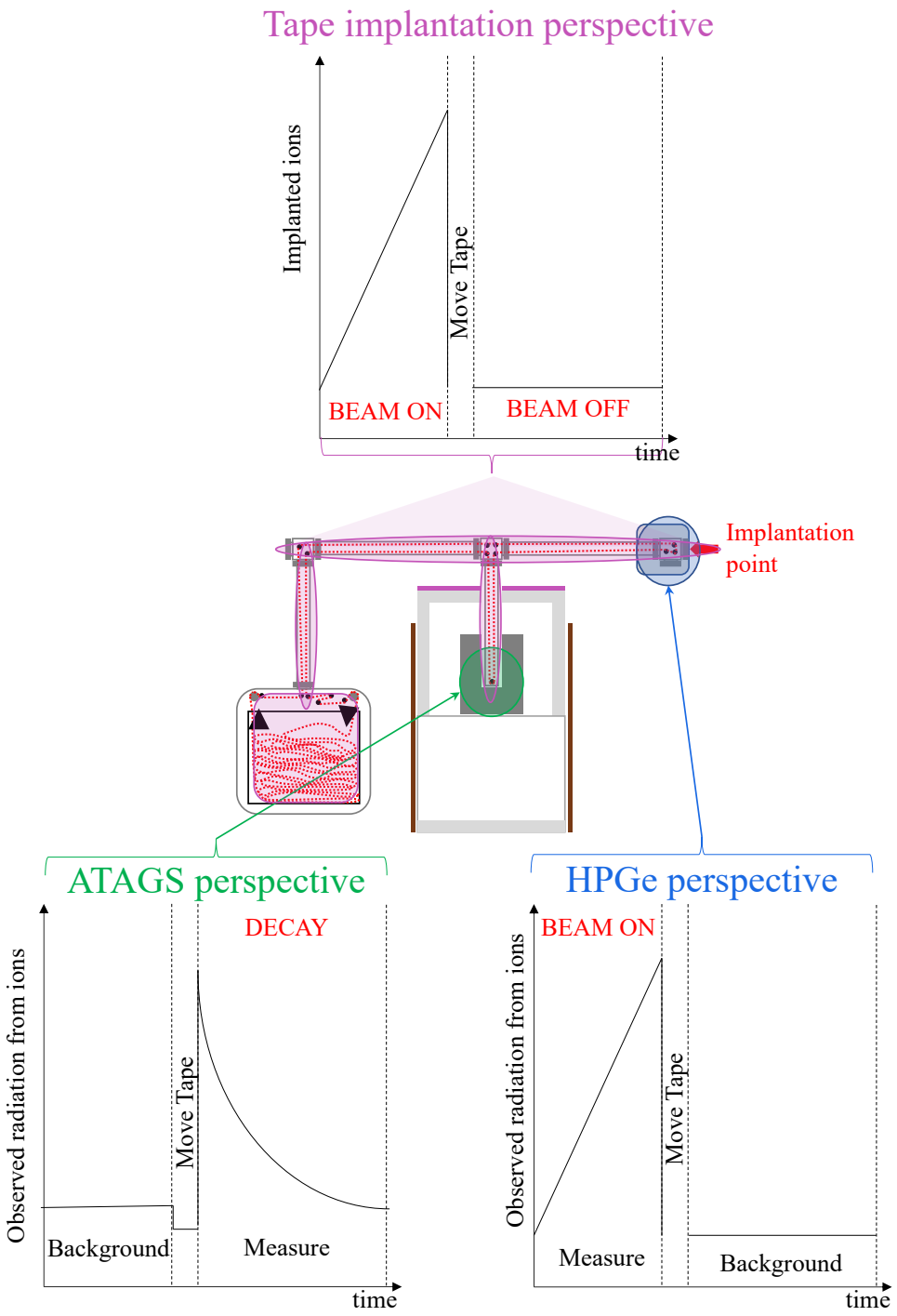

Figure 5.4: Schematic illustration of the beam implantation and tape movement cycle from the perspective of (a) the moving tape position where the beam is implanted, (b) clover HPGe detector at the ion implantation position, and (c) ATAGS.

in each cycle.

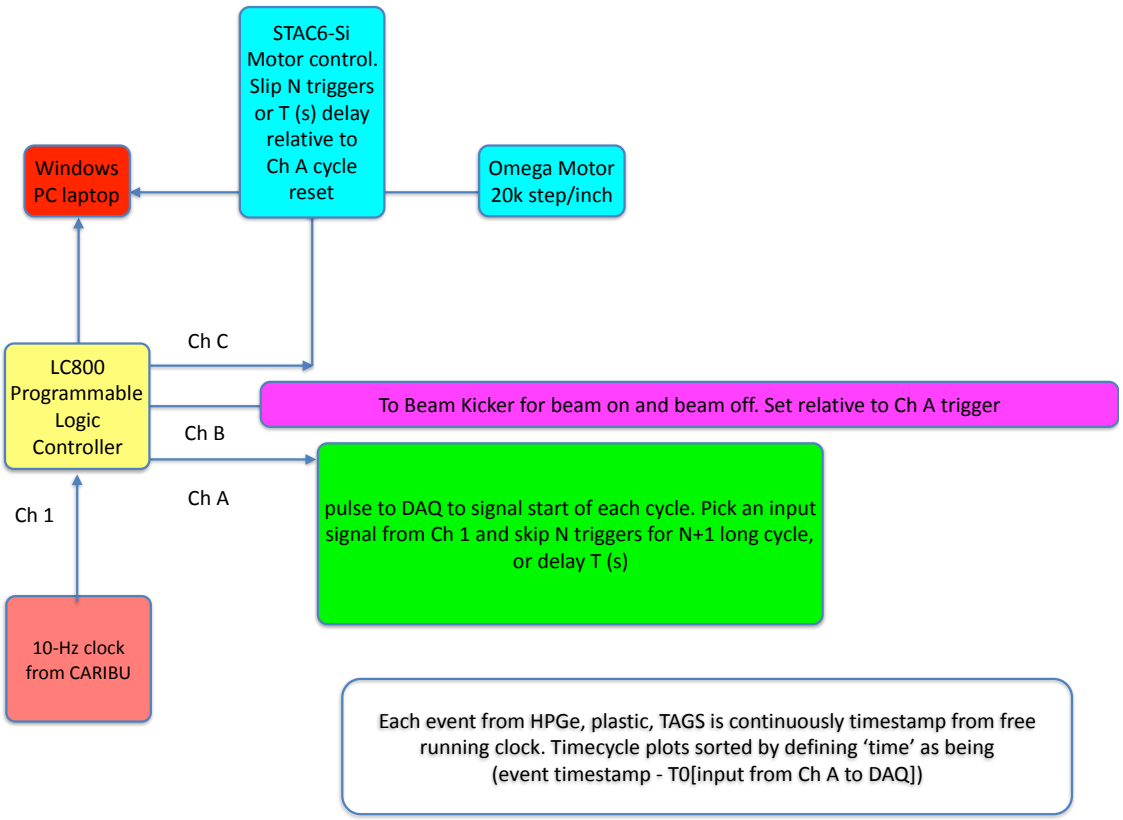

Figure 5.5: Tape station controller logic used to control and coordinate the CARIBU low-energy beam-line kicker, the tape station motor and the data acquisition system.

An alternative instrument setup was initially tested, involving the addition of the β-particle detector from SATURN to the tape path. The tape length from the implantation point to ATAGS was significantly longer at 3.2 m, requiring a faster tape speed to achieve the timing of the simplified setup described above. Testing found that increased friction caused by the additional pulleys and longer tape caused frequent jamming. The decision to simplify the tape arrangement to that shown in Figure 5.4 occurred in the early stages of the experiment and the alternative setup will not be mentioned further here. Nevertheless, the simplified setup also encountered periodical tape jams during the experiment, causing some delays in data collection. Adjustment of the tension in the tape is important; too much tension and there is a large burden on the drive motor and increased build-up of static directly on the tape due to movement through the pulleys, while not enough tension causes slack in the tape at the implantation position and uncertainty in its position. It was visually estimated that the uncertainty in the tape positioning due to tape slack was no larger than 5 mm.

5.2 Data optimisation methodology

High-resolution spectroscopy with HPGe detectors results in discrete photo peaks that can generally be easily resolved from the broad continuous background and from each

other. This allows identification of the many γ rays from a mixed radioactive source, while applying time-gates on the individual peaks and fitting the decay-time curve can help associate specific γ rays with different nuclides. In contrast, in a TAGS spectrum that utilises NaI(Tl) with a poor energy resolution and sums all of the contributions together, all of the γ-ray signatures are convolved into a continuum with broad features. To separate and identify the components for a TAGS spectrum, a different approach is required.

The isobar separator magnet is tuned to select the mass over charge ratio (m/q) of the nuclide of interest. But, due to the spread in the velocities, some contaminants are present in the beam depending on the mass difference between the isobars and their relative intensities (see Fig. 5.6). Given this contamination and that the nuclides decay into each other, each measurement can use a different tape duty cycle in order to separate nuclides within the mass chain, utilising the differences in the half-lives. A series of measurements were undertaken to optimise the tape duty cycle for each of the intended CARIBU beams. Once optimised, the settings for CARIBU remained constant while the data were collected.

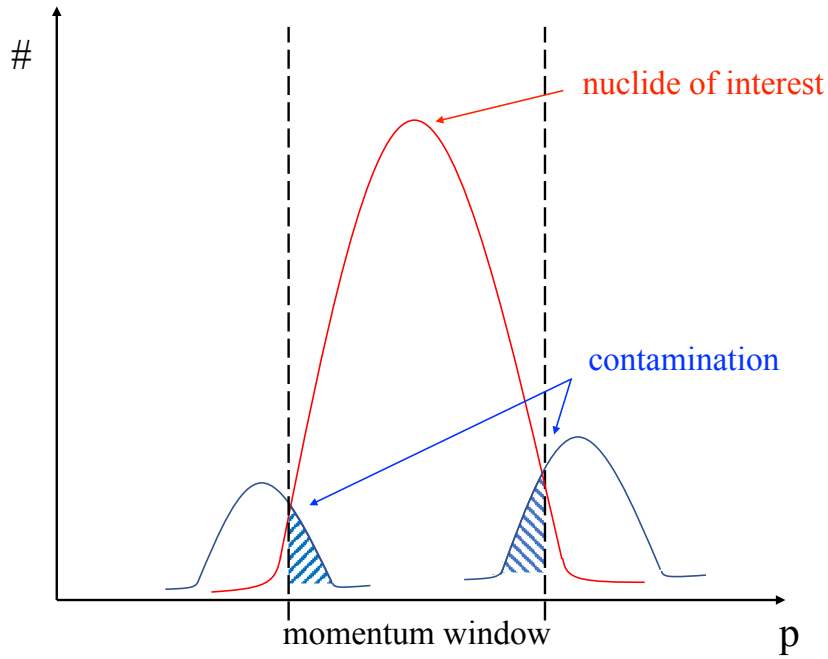

Figure 5.6: Diagram of CARIBU isobar separator showing how the momentum window of the selected nuclide can encompass the tails of the isobars and cause contamination in the beam.

The initial task with the ATAGS data is to merge and sort the binary data into usable format, followed by finding the optimal sorting parameters affecting energy resolution. There are two areas for data optimisation: they are the baseline or pole-zero (PZ) correction that is used in the algorithm to evaluate the energy from a particular signal waveform, and the gain-matching, particularly of the seven separate PMT signals. Both are achieved when sorting the data in software. A number of data sets were collected using sealed γ-ray calibration sources of ^{60}Co, ^{137}Cs and ^{22}Na. The ^{60}Co source in particular, was placed in various positions in the ATAGS well for comparison with Geant4 simulations. The methods used in determining the optimal sorting parameters are outlined and presented in this chapter.

5.2.1 Merge and sort of DGS-DAQ data

A data set for a specific nuclide was typically broken into multiple runs acquired over a time period of approximately 1 hour each. These individual runs are concatenated and sorted using ANL codes written with ROOT libraries [CERb] (see Section 5.1.2). This method has the advantage of checking each smaller sub-run for errors in timing or deviations that can then potentially be excluded from the final data. Energy and timing information measured by the ATAGS and HPGe (clover "A") detectors were recorded in the data stream.

5.2.2 Pole-zero correction

The DGS-DAQ sorting code incorporates the ability to produce a base-line correction to a data set, analogous to a Pole-Zero (PZ) correction in analogue electronics. Typical peak-height vs. time traces are shown in Figure 5.3. The form of the PZ correction used in GEBSort is shown in Equation 5.1:

$$Energy = \frac{(E_{post} - E_{pre} * C_{PZ})}{M * G} - G * B * (1 - C_{PZ}) + G_{offset}, \tag{5.1}$$

where:

$Energy$ = pole-zero (PZ) corrected energy response;
C_{PZ} = PZ correction factor;
M = multiplier;
G = gain;
G_{offset} = gain offset constant;
E_{pre} = pre-rise signal;
E_{post} = post-rise signal; and
B = asymptotic baseline sample.

The difference in magnitude between the post-rise and pre-rise signals is effectively the energy associated with the waveform. In Equation 5.1, the post- and pre-rise signal levels are compared to a base line which has a slope that is adjusted by the pole-zero correction. A C_{PZ} value of 0 would suggest that the baseline has no slope. Optimal PZ values are determined from a 2D histogram of the asymptotic baseline (y-axis) as a function of the energy (x-axis). This baseline parameter is a running average of the baseline evaluated at the time of the waveform trigger.

The PZ adjustment is a trivial task when looking at high-resolution spectrometer output from instruments such as the X-Array or Gammasphere. Discrete photo peaks in the histogram form distinct straight lines that are fitted as a function of the baseline variable. The C_{PZ} value is adjusted until these spectral lines are at the same channel (perpendicular to the baseline variable value).

Finding the optimal pole-zero correction for ATAGS is more difficult owing to the broad resolution and the seven components coming from the individual PMTs, each requiring a separate PZ adjustment. Large adjustments of the C_{PZ} value of a featureless baseline histogram can seem to make little change. To overcome this, several baseline gates of various widths were applied across the baseline histogram and projected to make the effect of the C_{PZ} adjustment more apparent, as shown in the schematic of Figure 5.7. The

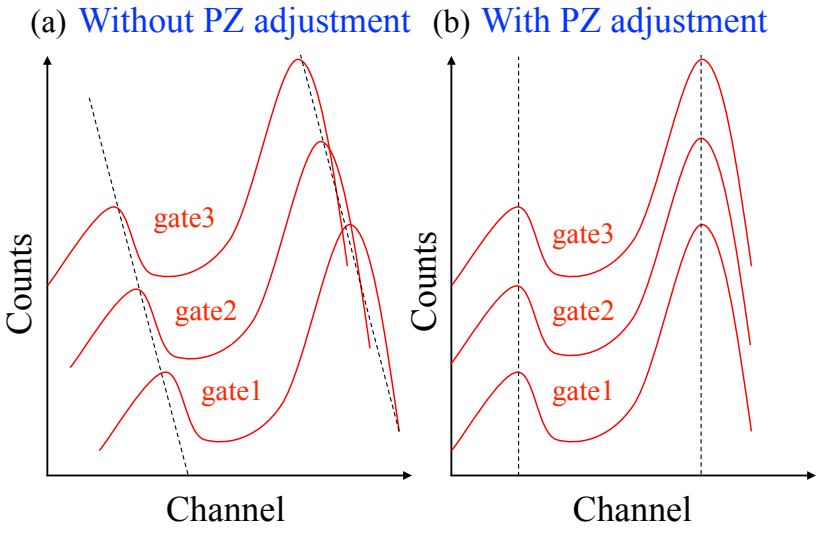

Figure 5.7: Schematic of the PZ adjustment method. Gates of variable width are taken across the baseline histogram and the resultant spectra are compared to determine the pole-zero correction C_{PZ}. An incorrect value will produce a miss-alignment of the spectra as in (a). When adjusted correctly, the gate spectra align vertically as in (b).

features from these projections are then aligned in a fashion similar to the high-resolution case, that is, making adjustments to the C_{PZ} value until the spectra in the gates are aligned (as shown in Figure 5.7b).

5.2.3 Gain-matching parameters

The seven PMT energy signals are collected by the DGS-DAQ as individual channels, each with a separate low-level threshold. The technique of adding individual energy signals and the effect of varying the low-energy thresholds was investigated in Sections 4.8.1 and 4.8.2.

It was found that the loss of low-energy components of the individual signals contributes to a minor loss of the low-energy portion of the summed spectrum. It was decided that the risk of these losses was justified compared to the benefits of being able to improve the overall resolution by post-collection, software gain-matching of the individual PMT signals. This section outlines the software gain-matching methodology used, with the goal of minimising the energy resolution of the ATAGS summed energy spectrum.

Since the replacement PMTs (Hamamatsu H6559) do not have 'adjust gain' potentiometers like the original ATAGS tubes, the relative shift of the high voltage of each tube must be adjusted by the supply. Each PMT requires its own HV supply which can be individually adjusted; a multi-channel programmable HV unit capable of providing the seven potentials was used.

The physical HV values were set at the beginning of the experiment using a 22 kBq ^{22}Na source located near the top of the ATAGS well. The initial HV value for each of the tubes was set to -1800 V. The output signals were observed using a digital scope to identify the 511 keV and 1275 keV signals from the pre-amplifier output and to ensure that these pulse heights were well above the tube low-energy threshold and had a similar magnitude. The final value used for each of the tubes was -2000 V, which falls within the manufacturer's specifications for the tubes and allows a finer adjustment via software post collection. A low-level threshold was used to suppress the low-energy, dark-current

noise from each tube; the chosen thresholds were based upon observing the same features in each signal and matching the count rates.

5.2.4 Selection of time parameters

The tape station duty cycle is optimised for each CARIBU measurement by adjusting the duration of each movement sequence and the speed of the tape (see Section 5.1.3). The criteria for the selection of the tape duty cycle are:

- to measure the activity in ATAGS for long enough to be able to separate the nuclides of interest from contaminants;
- to limit the losses of short-lived components by minimising the time between implantation and transport to ATAGS; and
- to implant a suitable number of radioactive ions onto the tape.

The CARIBU low-energy beam-line delivers radioactive nuclides from the chosen mass chain at an approximately fixed rate. Separation of components within a beam is achieved by leveraging the different half-lives and varying the tape duty cycle to correspond with these differences. Short-lived nuclides arriving from CARIBU are allowed to decay within the implantation and tape movement steps, allowing the build-up of the longer-lived activity of interest on the tape. A fraction of the short-lived nuclides will survive the implantation and movement steps, but typically at much reduced intensity. The method used to remove them from the ATAGS spectrum is to have a measurement time period of at least ten times the half-life of the shorter components, allowing them to have effectively decayed and leaving only the longer-lived isotope of interest at long times. For the mass chains under investigation in these experiments, there are usually two main components (one short and the other long) that require separation. Although a time that covers up to ten half-live periods for both would be ideal, this gives lower effective yield, whereas, an accurate measurement of the half-life requires a minimum of approximately three half-lives. Hence the measurement time was typically a little more than three times the longer half-life. A long implantation time can result in the saturation of the number of implanted nuclides due to decay competing with the build-up of additional implanted nuclides. The implantation time is therefore consistent with the short-lived half-life contaminant.

Sufficient statistics for the nucleus of interest can be obtained by multiple repetitions of this short cycle.

The time required to transport the nuclides from the point of implantation into the measurement position of ATAGS can be minimised by reducing the distance of separation of these two points physically and by increasing the speed of the tape. The distance between the two positions is fixed by the requirement for substantial shielding and the associated floor space required (see Sects. 5.1.1 & 5.1.3). The tape speed can be increased to minimise this time, but there is an upper limit due to the maximum speed of the drive motor. More practically, the tape velocity is limited by tape jams that have an increased frequency with greater tape speed. A similar range of tape speeds were used in all of the current measurements (1.3 to 1.7 $\mathrm{m}s^{-1}$).

The energy information from the HPGe clover and the ATAGS detectors can be incremented in 2D histograms versus the time relative to the start of the tape cycle. Energy projections with various time gates provide a way to interrogate the data. In the case of a measurement of a nuclide mass chain with little or no information about the half-lives,

the information contained within these histograms can be used to guide the selection of the tape duty-cycle parameters.

5.2.5 Validation of the beam species using the HPGe detector

The composition of the low-energy CARIBU beam can be determined by observing γ rays from nuclides at the implantation point. A HPGe γ-ray spectrum is acquired during the implantation of the CARIBU beam onto the tape. The HPGe clover detector was located at 90° to the beam-line viewing the tape implantation T-box with only minimal lead shielding around the detector head (see Fig. 5.2).

The summed signal from the four leaves of the HPGe clover detector provides greater levels of statistics due to the larger solid angle, which is important when considering the short collection times involved. A drawback of the summed clover energy can be false coincidences from different γ-ray hits in separate clover 'leaves' at high count rates, which was not found to be an issue for these measurements. The combined clover efficiency is approximately 4 times higher than an individual HPGe detector and further improvements can be achieved using add-back techniques. The individual leaves were energy calibrated using a ^{152}Eu source.

To separate γ rays produced in the beam from the continuum background, a time-gate of the HPGe energy-time histogram is taken across the implantation sequence (beam on) and compared to a time-gate after the radioactivity has been transported into ATAGS (beam off and radioactivity moved). Typically, the tape sequence has a short beam implantation period when the HPGe can observe implantations, compared to the long ATAGS measurement period, when the HPGe observes background. The longer background time-gate can be scaled to match the collection duration so that a normalised subtraction removes the majority of the CARIBU beam-hall continuum from the data. The γ-ray photopeaks are identified using the energy-calibrated HPGe centroids, with standard peak fitting routines and known data from ENSDF [ens].

When the selected nuclide or contaminant has limited or questionable data, verification of the identity for some γ rays could in principle, be achieved by measuring the decay half-lives for each measured γ-ray in the HPGe data. However, this would require an additional diagnostic decay time with the beam-off after the activity has been deposited onto the tape and before it is moved into ATAGS. This additional delay time would be at the expense of short-lived decays reaching ATAGS. Alternatively, additional HPGe measurement campaigns could be performed using, for example, XSAT. Sufficient energy information is known for the nuclides measured in these experiments so that neither of these additional steps were necessary.

5.3 PAC-approved beam time at CARIBU

A week of beam-time was allocated for the testing and commissioning of ATAGS with the neutron-rich fission nuclides ^{141}Cs, ^{141}Xe, ^{140}Cs, ^{140}Xe and ^{104}Nb/^{104}Nb^{m}, produced at the CARIBU facility.

For clarification of the nomenclature used in this chapter, ^{A}X will be used to identify the β^- decaying parent and the intention was to measure the β-decay intensities I_β. These intensities are derived from the total absorption γ-ray signature produced by the γ-ray transitions observed in the daughter, ^{A}Y. When a nuclide is described in this chapter

without explicit reference to the decay or quantity being measured, it should be assumed that it is referring to the parent nuclide ^{A}X that undergoes β decay.

The first priority of this campaign was to evaluate the health of ATAGS through comparison with measurements previously undertaken by the Idaho group when the detector was at INEL. Beams of ^{141}Cs and ^{140}Cs were chosen for this purpose due to the accessibility of these beams with CARIBU and the prominence of these two nuclei in the previous work [Gre92b, Hel94c].

Measurements were then extended to more difficult cases. The selection of candidates followed recommendations made in an International Nuclear Data Committee (INDC) report [Dim15] of the International Atomic Energy Agency (IAEA), that identified nuclei with little or no available data and which were likely to suffer from the pandemonium effect. The committee prioritised TAGS measurements for these nuclides based upon their need for decay-heat calculations with uranium/plutonium or thorium/uranium fuel and also for other nuclear reactor applications, for example the so-called anti-neutrino problem (see Section 1.1.1). The list of potential nuclides for this experiment was further limited to nuclides that had not been measured by other groups (at the time of the proposal), and to the availability of these nuclides at CARIBU. The cases of ^{140}Xe and ^{104}Nb/^{104}Nb^{m} were chosen, based upon their half-lives and the calculated ^{252}Cf spontaneous-fission yields expected from CARIBU (see Section 1.2.2). The data collection process and results are presented in this chapter, while the more detailed analysis and interpretation is presented in the following chapter.

5.3.1 A=141 nuclides

^{141}Cs is a neutron-rich fission product that has previously been investigated through various 'classical' measurement techniques [Ada73, Mor75, Ote76, Bor79, Yam82]. This nucleus was chosen to evaluate the performance of ATAGS compared to previous results measured by Greenwood, Helmer *et al.* [Gre92b, Hel94c, Hel94b, Gre97]. In addition, this nuclide was identified as 'priority 2' by the IAEA for understanding the antineutrino problem [Dim15].

The evaluated data for ^{141}Cs [Nic14] includes a significant contribution of the β-decay intensities measured using ATAGS at INEL. Figure 5.8 shows the A=141 isotopes with CARIBU yields shown when the isobar separator is optimised for that nuclide [Sav05, ANLb]. These values are determined from both measurements and calculations (the latter indicated with an asterisk).

The CARIBU beam yield of 1.0 x 10^5 ions/second on target combined with a distinct half-life of 24.84(17) s allows the temporal separation of ^{141}Cs from the isobars of ^{141}Ba (18.27(7) min) and ^{141}Xe (1.73(1) s) using the tape station and with an appropriate tape cycle (see Section 5.1.3). The parent nucleus ^{141}Xe was not a part of the original experimental proposal but can be extracted since it was a short-lived contaminant in the beam. Xenon-141 is identified by the IAEA report [Dim15] as 'priority 2' for nuclear reactor applications (antineutrino problem).

5.3.2 A=140 nuclides

The experiment proposal included the measurement of ^{140}Cs. Like ^{141}Cs, it has been investigated by classical spectroscopy techniques [Alv68, Ada73, Sch73, Sch74, Mor75, Alq76, Dec81, Rob86, Mac89, Aud03] and has also been extensively measured by Greenwood, Helmer *et al.* [Gre92b, Gre92a, Hel94a, Hel94b, Gre96, Gre97], which makes it useful

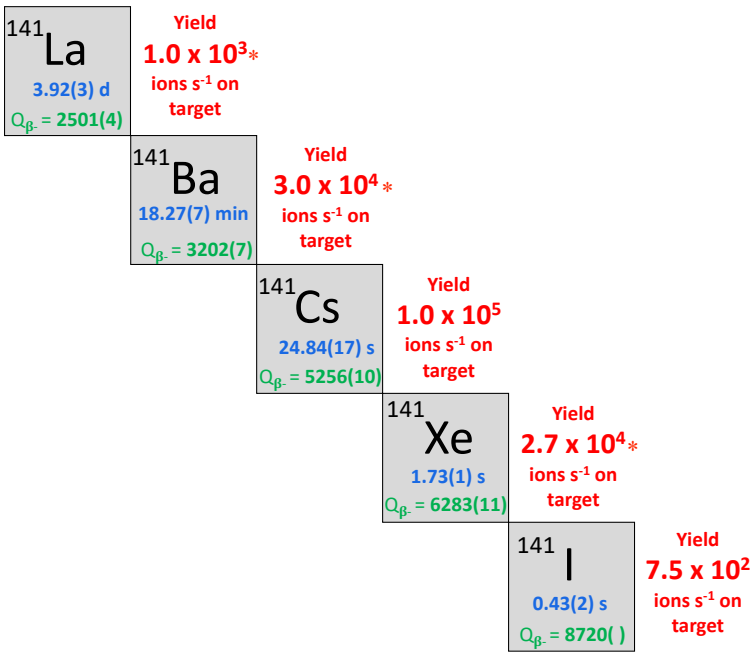

Figure 5.8: Schematic of the decay sequence of the A=141 chain (data from [Nic14]). The measured or calculated(*) intensities from CARIBU's isobar separator are shown for each nuclide [Sav05, ANLb].

for detector performance evaluation. The A=140 nuclides obtainable from CARIBU are shown in Figure 5.9. The high expected CARIBU intensity and the relatively long half-life of ^{140}Cs make this ideal for separation from the other components and transportation into ATAGS via the tape station. Cs-141 is identified by the IAEA as 'priority 1' for nuclear reactor applications (antineutrino problem).

In the data analysis it is also possible to isolate ^{140}Xe as a contaminant; this nucleus is a priority for decay-heat calculations of uranium/plutonium (priority 1) and thorium/uranium fuels (priority 2) [Dim15]. It is estimated that ^{140}Xe contributes 1.58% of the decay heat in the first 10 s after reactor shutdown [Dim15]. At the time of this experiment there had not been any TAGS measurements of this nuclide, although classical spectroscopy measurements had been performed [Sch71, Ada73, Ada74, Mor75, Ote81, Aud03].

The parent of ^{140}Xe is ^{140}I, which has a short half-life of 0.86(4) s and a CARIBU yield of 3.1 x 10^3 ions s^{-1}, compared to 13.60(10) s and a yield of 6.9 x 10^4 ions s^{-1} for ^{140}Xe. The different half-lives mean it will be possible to build up the ^{140}Xe population without contamination from ^{140}I, although there will be considerable contamination from ^{140}Cs that is also produced with high intensity from CARIBU. The half-lives are different enough (13.6 s vs. 64 s) that temporal separation should be possible, while the subsequent ^{140}Ba decay with a half-life of 12.8 days can be removed by tape cycling.

5.3.3 ^{104}Nb/^{104}Nb^m

Nb-140m is identified by the INDC report as 'priority 2' for understanding the antineutrino spectrum. We consider these nuclei to be excellent test cases with which to compare discrete line spectroscopy with TAGS spectroscopy and develop our understanding of the

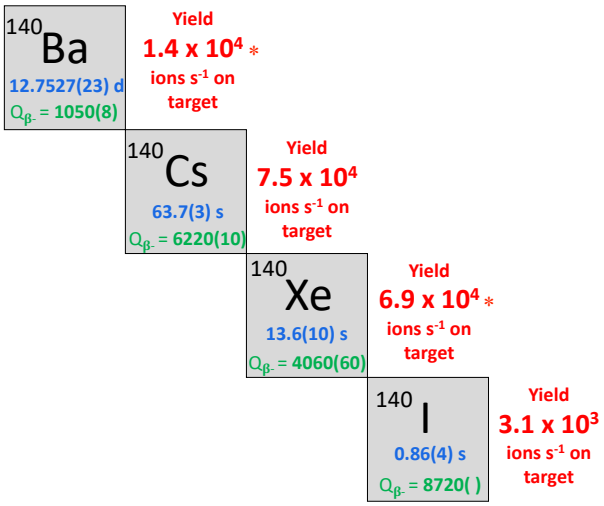

Figure 5.9: Schematic of the decay sequence of the A=140 chain [Dim15]. The measured or calculated(*) intensities from CARIBU's isobar separator are shown for each nuclide [Sav05, ANLb].

analysis methods and limitations.

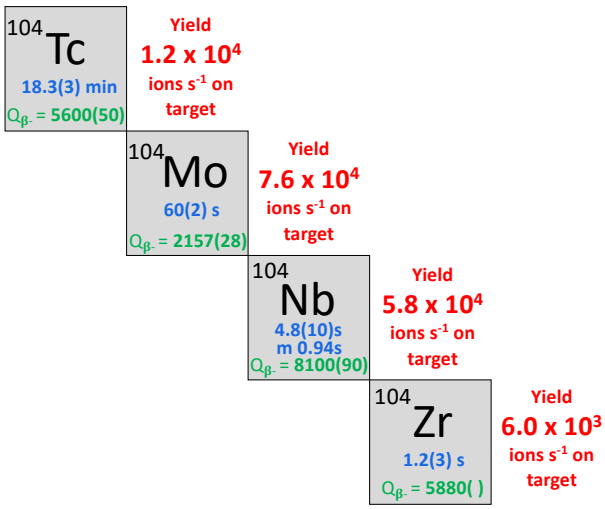

Figure 5.10: Schematic of the decay sequence of the A=104 chain [Dim15]. The measured intensities from CARIBU's isobar separator are shown for each nuclide [Sav05, ANLb].

The high Q(β^-) value of 8746(15) keV for ^{104}Nb^m [Dim15] is predicted to result in a large pandemonium effect and a high-statistics measurement of the discrete γ-ray spectroscopy for both these decays measured with the XArray is also available. Ion beams of ^{104}Nb are expected to be high yield and essentially contamination free, while the decay half-lives as shown in Fig. 5.10, are sufficiently different to enable separation of the two Nb decays (0.94 s and 4.9 s) from the ^{104}Mo daughter (60 s).

5.4 ATAGS re-commissioning results

5.4.1 Sorting parameters and final energy resolution

Optimisation of the detector energy resolution was performed via a pole-zero correction and software gain-matching as described earlier in Section 5.2.2 and 5.2.3. The final parameters are shown in Table 5.1.

ATAGS PMT	C_{PZ}	gain
1	0.950	1.000
2	0.950	1.000
3	0.950	0.675
4	0.950	0.693
5	0.950	1.184
6	0.950	1.283
7	0.900	0.938

Table 5.1: Final pole-zero and gain corrections applied to optimise energy resolution of the ATAGS data.

Merge and Sort of the DGS-DAQ data

The collected data from each run is merged and sorted using ANL supplied scripts written using ROOT [CERb]. The resulting data includes diagnostic information that can be used to judge the quality of the individual runs. A problem was identified in the DGS-DAQ data in the form of missing tape cycle reset triggers. Figure 5.11 shows the measurement of ^{141}Cs using ATAGS. The number of ATAGS event counts is shown as a function of the time across an individual data collection lasting 2950 s (49 minutes). The measured times of the tape reset triggers are overlaid and correspond with the expected rise in counts and subsequent decay of the measured nuclide.

Across all experimental runs, the initial part of the data (0 - 200 s in this example), is consistently missing the initial trigger, while there are other missed triggers throughout the data with no discernible pattern. It is believed that the cause of the missed initial triggers is from the way the logic controller was programmed at the time. Not allowing for this will cause out-of-phase data to be added to the concatenated data. The missed triggers will also result in extension of the time cycle beyond what is expected. After the identification of this issue the data was resorted to exclude the initial out-of-phase data while any data beyond the expected tape cycle time was suppressed. Higher statistics would result from interpolating the missing triggers, but the increase would be marginal.

Large spikes are seen occasionally in the data, such as the example at 4918 seconds in Figure 5.11. Figure 5.12 shows the finer detail of this spike, which was identified as low energy noise by projecting the energies associated with the spike and comparing it to neighbouring projections.

5.4.2 Pole-zero correction results

Parameters for the pole-zero correction were evaluated using the baseline gate method described in Sect. 5.2.2. Figure 5.13 shows the baseline histogram for pole-zero correction of the ATAGS central PMT when measuring ^{60}Co in the bottom of the well. This data set

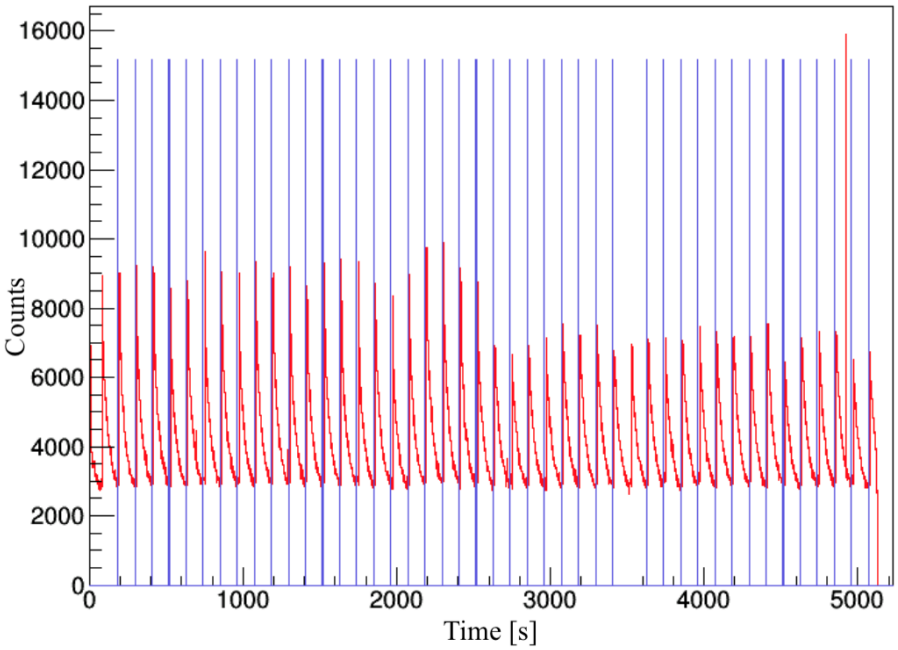

Figure 5.11: Spectrum for of an individual ^{141}Cs data acquisition of 5130 s ATAGS event counts vs. time (red) with tape cycle reset triggers overlaid (blue). Example of missed tape cycle resets can be seen at approximately 100 s and 3400 s.

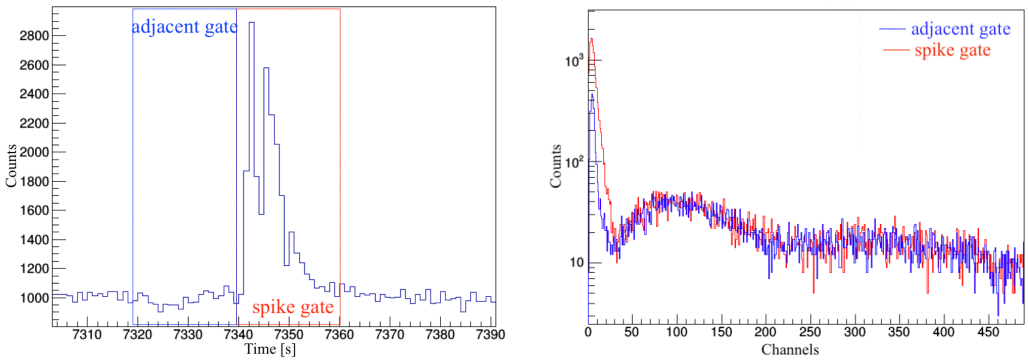

(a) (b)

Figure 5.12: ATAGS event counts vs. time showing (a) a transient spike in the data (see Figure 5.11 at 4918 s), and (b) the energy projections of the spike (red) and an adjacent gate (blue). This transient spike in the data is identified as low energy noise.

was chosen to derive the C_{PZ} values as it has easily identifiable spectrum features within the individual tube responses.

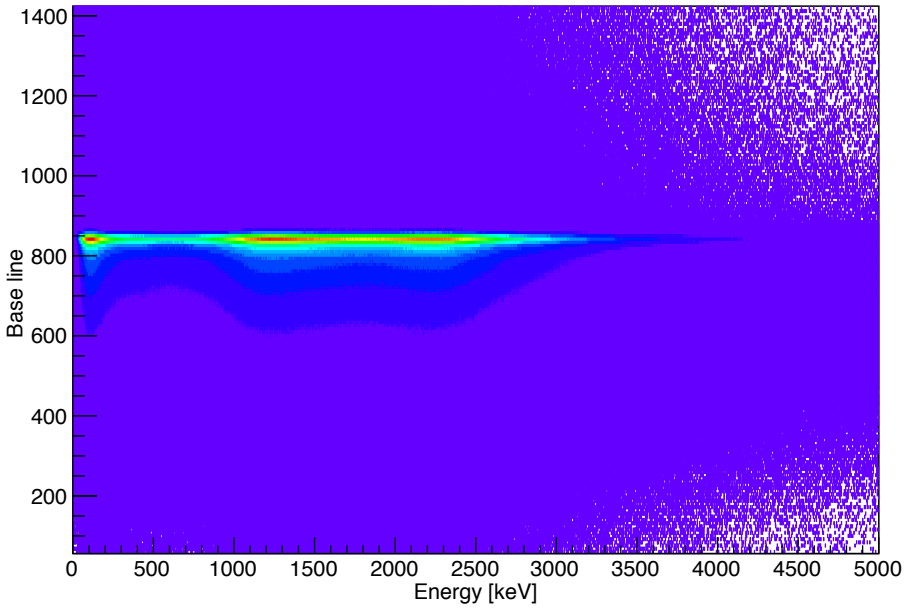

Figure 5.13: 2D baseline histogram for the ATAGS central PMT measured with a ^{60}Co source located at the bottom of the well. The histogram is pole-zero corrected and shows the DGS-DAQ baseline parameter [y axis] vs the ATAGS energy [x-axis]. (See Sect. 5.2.2 for more details.)

Figure 5.14 shows the projections with various baseline range gates applied. A comparison of the gated projections with 5.13 shows the distribution of events for this central tube, with most events occurring between baseline values of 500 and 870. The correctness of the C_{PZ} value is seen by the fact that all the projections show features aligned in energy. The final C_{PZ} values for all ATAGS PMTs were recorded in an input file for the GEBSort code and were fixed for all subsequent data sorting.

This baseline gate technique was applied to a more complicated source as a final check of the C_{PZ} values determined using the ^{60}Co source. Figure 5.15 shows the ATAGS central tube (PMT 7) projections for combined ^{141}Cs and ^{141}Xe data. This combined source has a relatively featureless spectrum. However, the alignment of the spectral features can be seen, confirming the appropriate PZ corrections have been applied.

The final C_{PZ} values obtained with the ^{60}Co source and shown in Table 5.1 were found to be the same for each of the outer PMTs, with a slight difference for the central tube. Similar checks were performed for other sources and each data set to ensure these C_{PZ} values were appropriate in all cases.

5.4.3 Gain-matching results

The software gain-matching methodology (see Sect. 5.2.3) was difficult to apply to ATAGS across the seven individual PMTs since the sum spectrum only changes marginally when performing individual PMT gain adjustments.

A brute-force method was first applied to a data set collected with a ^{60}Co source in ATAGS. The method consisted of iterating over the software gain multipliers, with a fixed

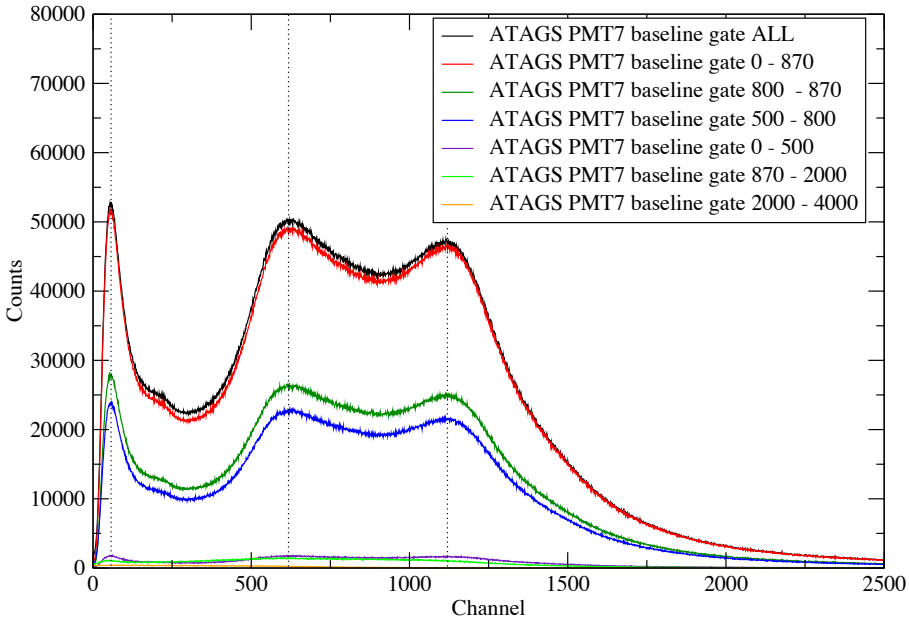

Figure 5.14: Gated projections from the baseline vs energy 2D histogram used for pole-zero corrections (Figure 5.13) for the ATAGS response to a ^{60}Co source placed at the bottom of the well. These spectra with different baseline gates applied are aligned after the PZ correction has been applied; the dashed lines demonstrate the alignment.

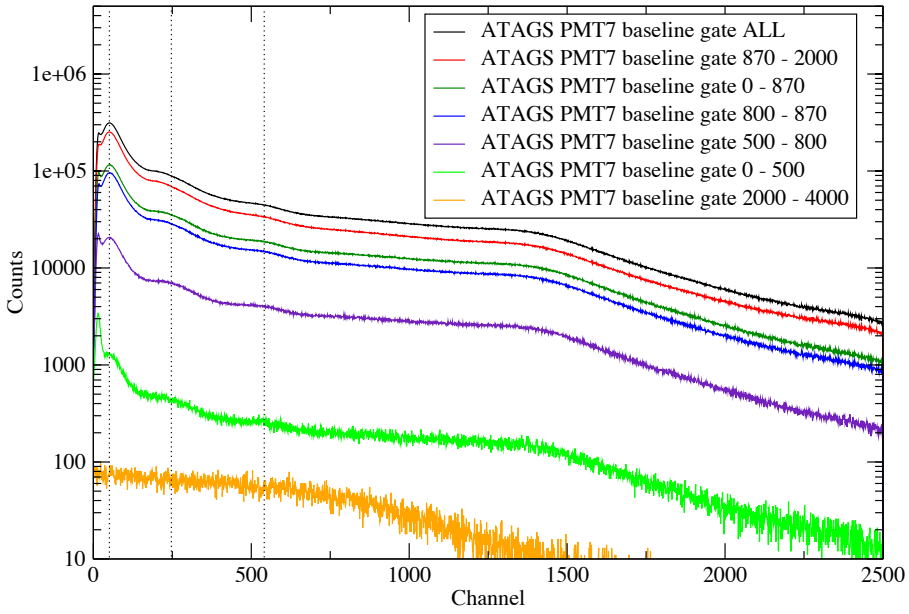

Figure 5.15: Gated projections from the 2D histogram for the ATAGS response to a ^{141}Cs source placed at the bottom of the well. These spectra with different baseline gates applied are aligned after the PZ correction has been applied; the dashed lines demonstrate the alignment.

step size, within upper and lower boundaries. One of the tubes was held at a fixed software gain while the remaining six tubes were varied systematically. The expected shape and separation of the 1173 keV and 1332 keV γ rays was evaluated for the resulting summed spectrum for each combination of gains. A large number of multiplier combinations yielded a spectrum like that expected. These were then tested against a ^{137}Cs data set, but this approach did not provide a clear direction.

The final gain multipliers instead take guidance from the relative positions of optical simulation results in Section 4.6, specifically Figure 4.17, which has been reproduced here as Figure 5.16b for convenience. Figure 5.16a shows the result of the ATAGS PMTs after software gain-matching for a ^{60}Co source measured with DGS-DAQ. The source was placed off-centre in the ATAGS well, adjacent to the beam-pipe. The source activity was 7.6 kBq at the time of measurement, which agrees with the total count rate collected, assuming 100% efficiency. However, this exceeds the suggested 4 kHz total count rate limit used by Greenwood *et al.* to minimise the effects of pile-up [Gre92b], which is not ideal for adjusting the gain. Nevertheless, this was the only source available at the time of measurement and this data was used for gain adjustment.

Assuming ATAGS is symmetric, the individual tube responses for a source placed equidistant to each of the outer tubes (on the main axis), should result in comparable spectra. The optical simulations of ATAGS show a symmetrical response (Fig. 4.17 and 5.16). Therefore the software gains adopted for the outer tubes are determined by aligning the experimental responses to mimick the simulations. Hence, the spectral shapes of the outer tubes (1 to 6) are gain matched to look very similar in Figure 5.16. Note that the shapes of the spectra are different between experiment and simulation; the main goal is to make each tube identical.

It was more difficult to gain match the central tube (red in Fig. 5.16), as it has a different view of the scintillator compared to the outer tubes and hence it is predicted to have (and does show) a significantly different response. The optical simulations and characterisation show that the central tube has a response similar in shape to the final summed response, in this case ^{60}Co, although the simulation does not include resolution broadening inherent in the quantum efficiency and subsequent electron multiplication process of the PMTs. The comparison of the simulation suggests the experimental central tube response has poor resolution, as shown by a lack of separation of the 1173 keV and 1332 keV γ-ray peaks.

The software gain for the central tube was approximated by using the relative positions of the central to outer tube responses of the optical simulation as guidance.

Since there are no distinct comparable features in either the simulated or experimental responses for the central PMT, the correct software gain value is difficult to determine. A range of software gains for the middle tube were investigated. Using a set of fixed software gains that match the outer tubes, the middle tube multiplier was varied between 0 and 20. Figure 5.17 shows these results. The contribution of the central tube response starts to dominate as the multiplier is increased above 7.0, i.e the combined response looks like the central tube response. As long as there is a measured response from all tubes and all multipliers are chosen in the range between 0.1 and 1.5, the resolution is relatively insensitive to changes.

Hence the gain of PMT7 was chosen so that the relative position of its response compared to the other 6 gain-matched PMTs response, and was similar to the simulation positions in Figure 5.16b. The final gain-matching values used for sorting all of the ATAGS experimental data are shown in Table 5.1.

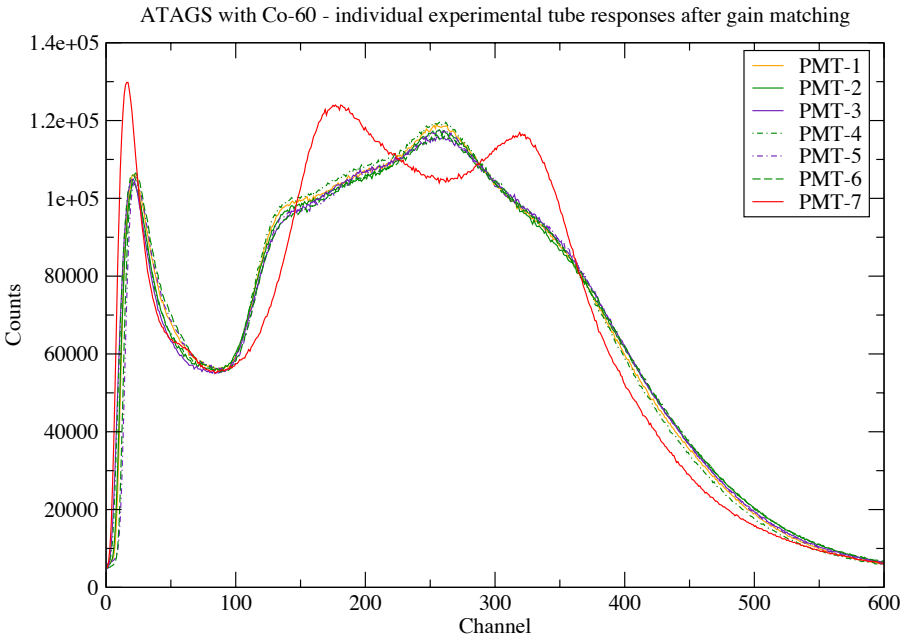

(a)

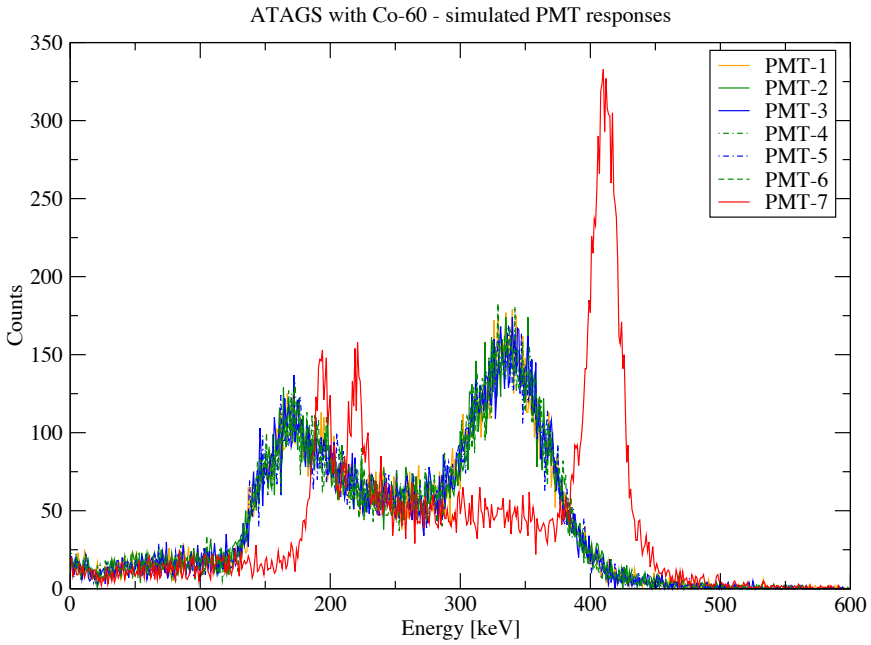

(b)

Figure 5.16: ATAGS individual PMT responses to a ^{60}Co source after software gain-matching is applied and compared to an optical-photon model. (a) Experimental ATAGS tube components with the source located off centre in the ATAGS well, adjacent to the tape vacuum pipe. The outer tubes (1 to 6) have similar shape and have been gain matched to each other via software. (b) Optical-photon model results of the relative gains; this figure is reproduced from Figure 4.17 for convenient comparison with (a).

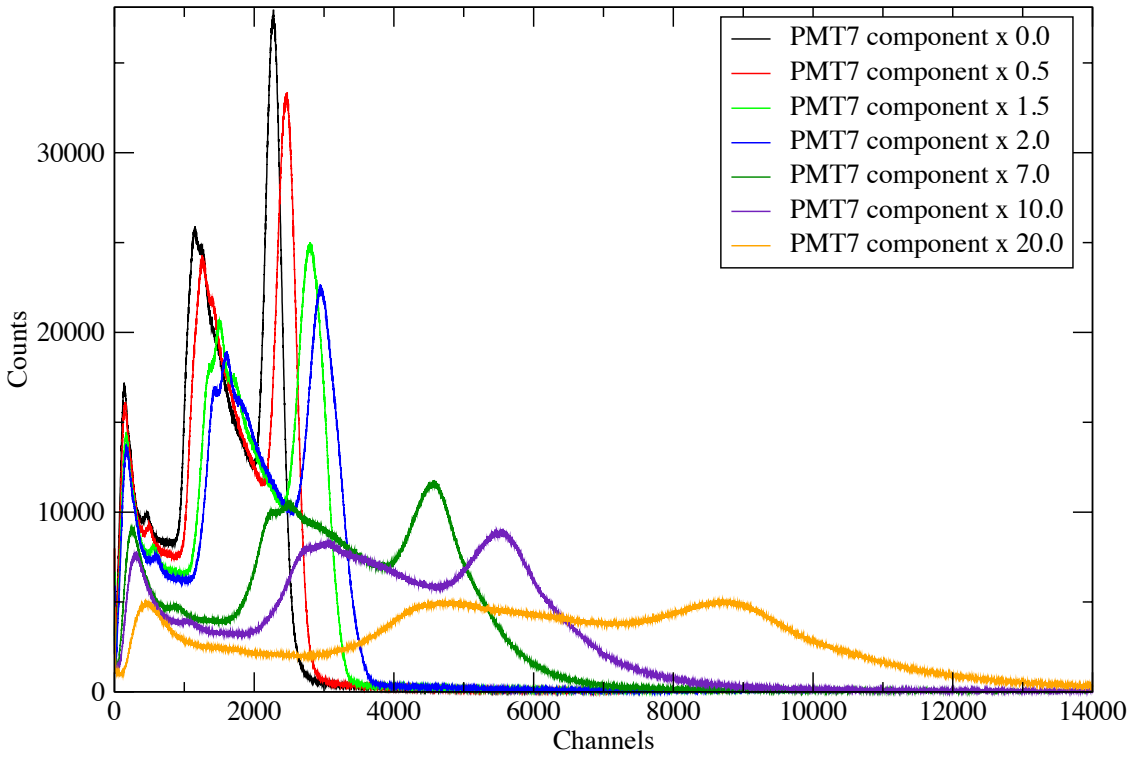

Figure 5.17: ATAGS summed response to a ^{60}Co source, with PMTs 1 to 6 software gain-matched and varying the software gain for the central tube between 0 and 20.

5.4.4 Optimised energy performance of the detector

Figure 5.18 shows the ATAGS resolution measured with a ^{60}Co source, comparing a measurement from 1992 (Figure 3 of Greenwood *et al.* [Gre92b]) with the present results. The background is acquired separately with no sources present in ATAGS.

Figure 5.18b and c show the ATAGS response with passively summed PMTs for the same ^{60}Co source located at different positions in-front of ATAGS to achieve a lower count rate. Despite the work put into optimising the resolution via gain-matching and replacing the PMTs (Fig. 5.18d), the more recent results show an inferior resolution when compared to the 1992 performance. Although the source used for the present measurements is not ideal, it seems clear that the resolution of ATAGS has diminished, which may be due to the age of the scintillator material.

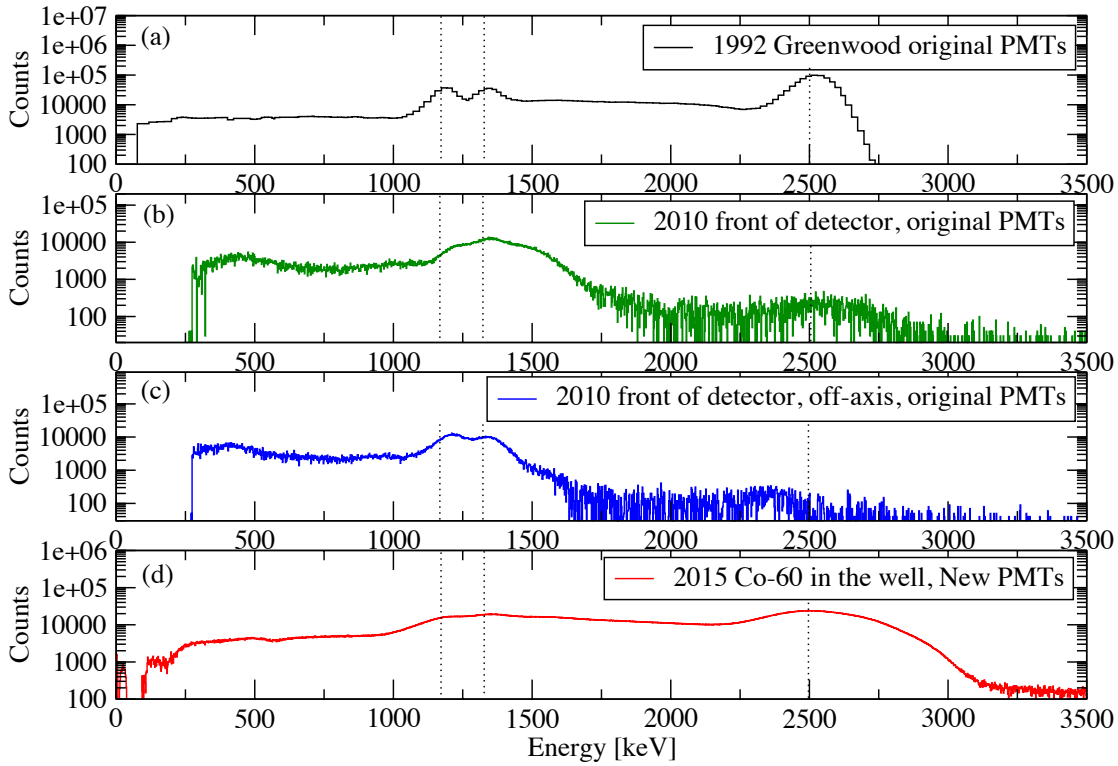

Figure 5.18: Comparison of the ATAGS resolution for a ^{60}Co source using different PMTs, including (a) ATAGS-produced spectrum digitised from Figure 3 of Greenwood *et al.* [Gre92b], (b) measurement of a ^{60}Co source at the front of the detector, (c) measurement of a ^{60}Co source off-axis, and (d) measurement of ^{60}Co in the well. Spectra (a), (b) and (c) are measured with the original PMTs (RCA S83021E) and are compared to (d) measured using the new PMTs (Hamamatsu H6559). The new measurements with the original tubes were using a source too high in activity, requiring distance between the source and detector to reduce the rate. The source was positioned at 229 mm from the front of the detector face, aligned with the main symmetry axis for measurement (b), and then moved perpendicular to this axis for measurement (c). The measurement with the new PMTs is done with the source in the well, using the DGS-DAQ (d).

A least squares fit of the simulated ^{60}Co spectrum was performed to the experimental data from Figure 5.18d with the FWHM coefficients as varying parameters of the fit, as

done previously in Section 4.5.2. The fit coefficients were found to be $F_0 = 202$ and $F_1 = 12.9$. This is well outside of the expected performance of the ATAGS energy resolution that was seen in the 1990's ($F_1 = 2.3$ to 3.2 as shown in Figure 4.9).

Results obtained using ATAGS with degraded energy resolution for this work at CARIBU limit the accuracy of matching features in the data with the simulations, which will restrict the effectiveness when unfolding β-feeding intensities for different levels from the data. However, the ATAGS data should still be able to yield a measurable Q_β value and give some idea of whether there is significant new β-feeding intensity, albeit with the level energies poorly defined.

5.5 CARIBU beams

CARIBU was tuned to deliver ions with an energy of approximately 4 keV and 100 ms wide pulses for the experiment without the use of the MR-TOF separator (see Section 1.2.2 for a description of CARIBU).

5.5.1 ^{141}Cs and ^{141}Xe

The first data set collected was for the A=141 decay chain, since this had the highest expected CARIBU beam intensities out of the proposed measurements. The isobar separator of CARIBU was tuned to A=141 and the tape cycle was 10 s beam on, 1 s tape move, 100 s collect. Figure 5.19 presents the 2D histograms of time vs energy showing the tape cycles for the (a) HPGe and (b) ATAGS, detectors. This is a data set from a combination of multiple 1 hour runs, with a total accumulation time of approximately 10.2 hours equating to 330 measured cycles.

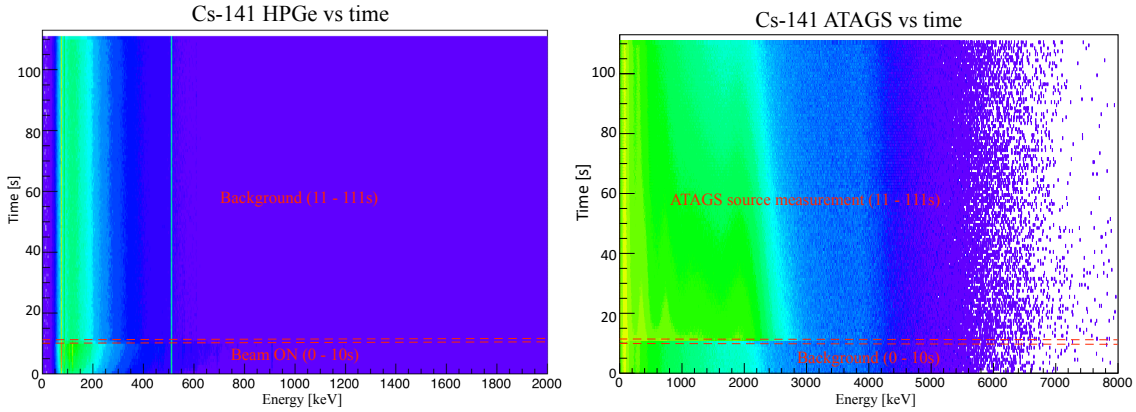

(a) (b)

Figure 5.19: Time-energy histograms for the A=141 measurement where time is the elapsed time after the tape cycle reset. Panel (a) is for the HPGe clover viewing the tape implantation position and (b) is for ATAGS. 330 cycles of data were collected with a tape cycle of 10 s beam on, 1 s tape move and 100 s data collection.

Total time projections are shown in Figure 5.20, normalised by the number of completed cycles to give the average count rate in each cycle. The sequence of tape moves can be seen from the perspective of each detector via their respective count rates. The first

10 seconds of the HPGe time histogram shows the implantation of the beam measured by the sum of the four clover crystals. The rate increases in Figure 5.19a and is flat in Figure 5.19b. The tape moves and then the radioactive tape is received by ATAGS at t=11 seconds. The HPGe detector in Figure 5.20b observes a subsequent flat background rate while the ATAGS detector in Figure 5.19 sees the initial population of radioactive nuclei and their subsequent decay.

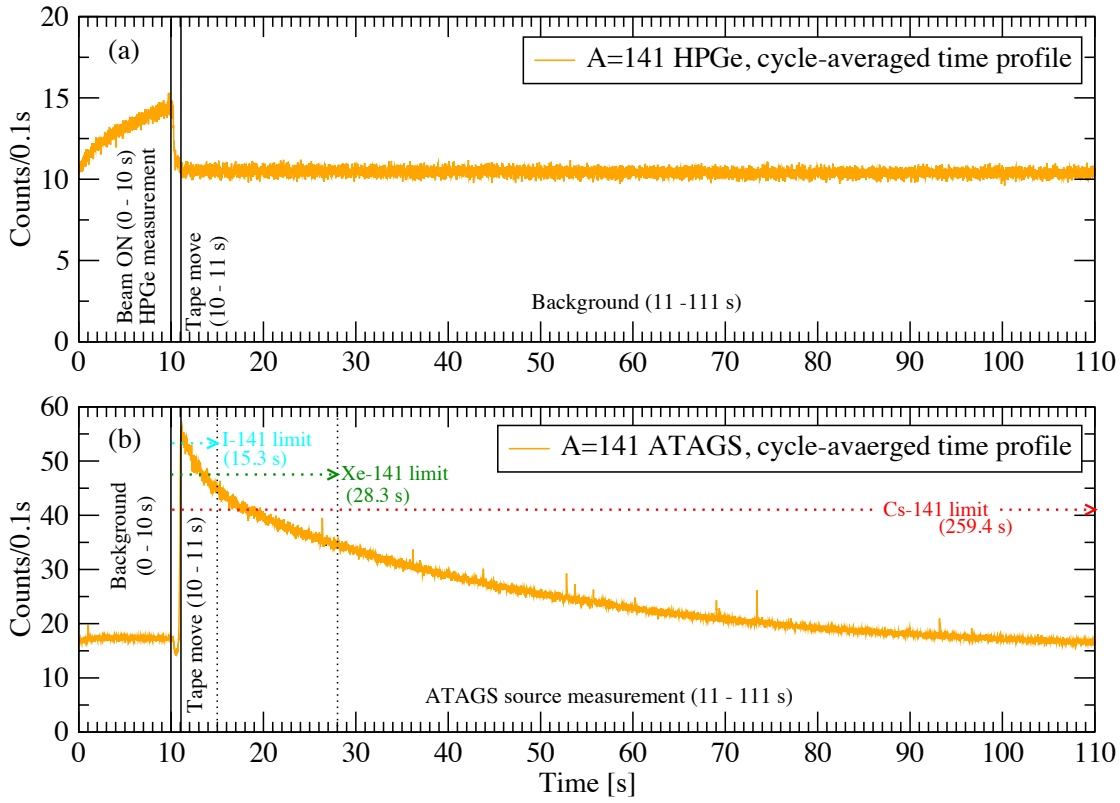

Figure 5.20: Average count rate profiles for a tape cycle measurement for A=141 of (a) the clover detector and (b) ATAGS. Data are projected from the 2D histogram shown in figure 5.19 and normalised by the number of completed tape cycles. The tape transitions for this measurement are apparent. The data are shown as the respective detector count rate across a complete cycle with a time resolution of 0.1 s. The expected presence of the various decay components are indicated by the dashed lines, as predicted from the known half-lives (see text).

The tape backgrounds compared

Figure 5.21 shows the comparison of the average backgrounds from each set of measurements collected. The time factor used to calculate the rate is determined from the sum of the collection time for each measurement, adjusted to account for the proportion of tape cycle time.

The amount of residual activity implanted on the tape will affect the subsequent measurements. The sequence of the measurements during the campaign followed the same order in which they are presented in this work (A= 141, 140 and 104). Figure 5.21 shows agreement in the spectra for energies less than 500 keV and above 5000 keV. Between these

energies, the A=141 and A=140 spectra show the continuum features consistent with the dominant isotope during these measurements. For example, the clean ^{141}Cs spectra of Figure 5.25c shows a broad peak centred around an energy of 3000 keV, which is the same feature seen in the ^{141}Cs background.

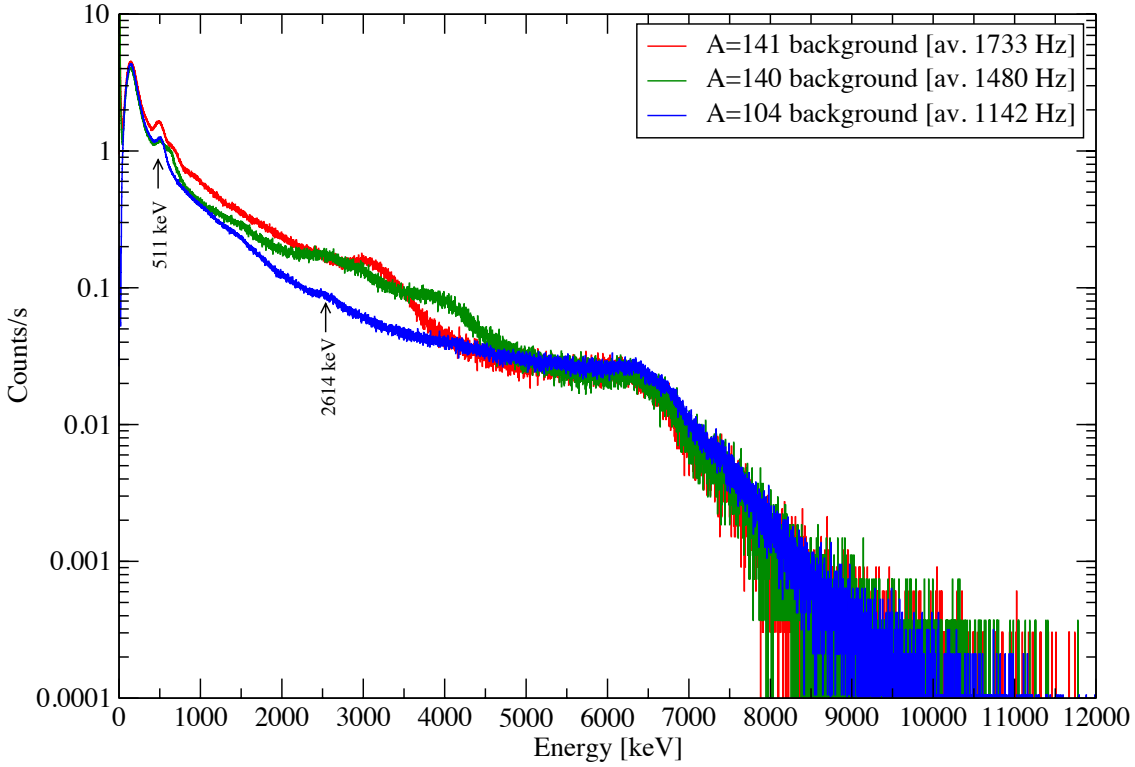

Figure 5.21: ATAGS average backgrounds for each measurement. The rate has been determined from the total collection time and the relevant tape cycle times.

The A=104 measurement had the least amount of implanted activity on the tape and hence may be the best representation of the ATAGS background. The final measurement in the three days of collection was ^{104}Nb. The lack of any remnants suggests that the influence of residual tape activity from previous measurements is minimal. Although difficult to see in Figure 5.21, a spike is seen in the low energy region of both the A=141 and A=140 backgrounds, originating from the transient noise spikes identified during the sorting of the data (see Section 5.4.1). It is interesting to note that the A=104 measurement does not have this feature present, suggesting it is a count rate artefact.

Validation of the beam composition using HPGe data

Confirmation of the CARIBU beam tuning was achieved through identification of characteristic γ rays using the HPGe data. A projection of this time-energy histogram in Fig. 5.19a, was taken for a time-gate covering the 0 to 10 s period. A background spectrum was obtained from the time-gate between 11 to 111 seconds, which corresponds to the time when the implanted tape is being measured in ATAGS. Figure 5.22 shows the comparison of the projected time-gate with the significant continuum of the CARIBU beam-hall background, normalised so that both show count rate.

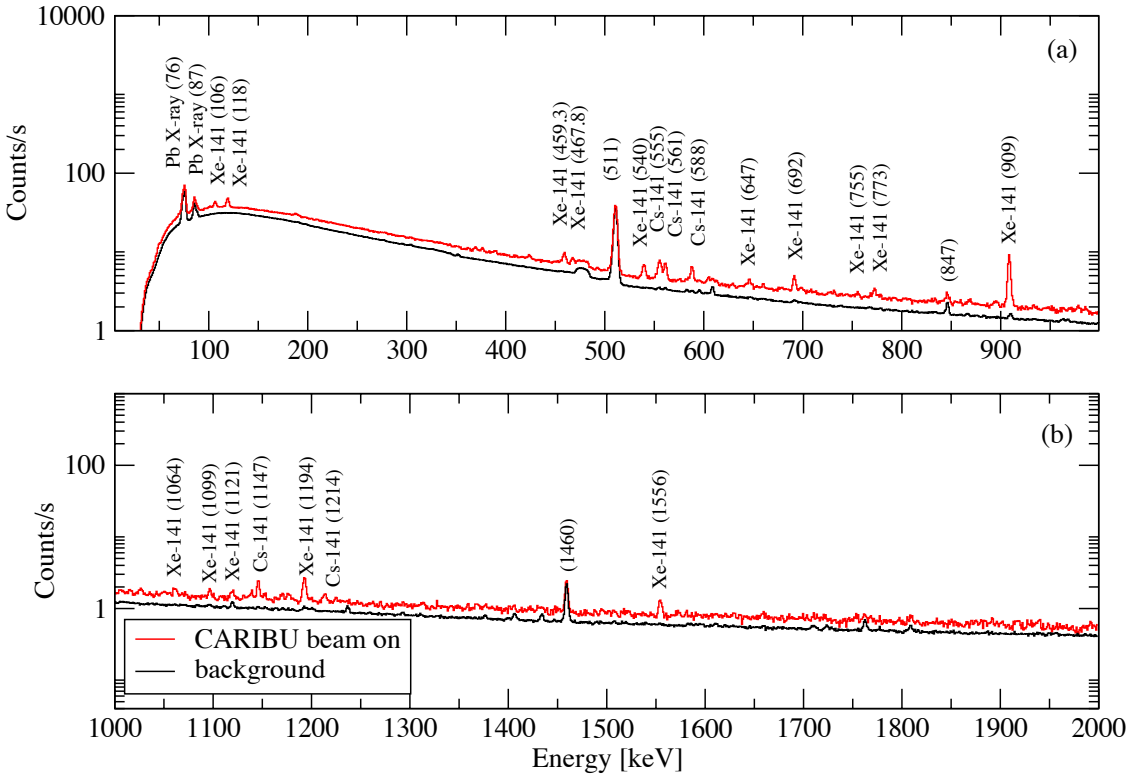

Figure 5.22: HPGe measurement of the A=141 beam for (a) 0 keV - 1000 keV and (b) 1000 keV - 2000 keV. The CARIBU hall background is shown in black for comparison (both spectra are normalised and plotted as a count rate). These spectra correspond to tape implantation times of 0 - 10 s for the CARIBU beam-on and 11 - 111 s for the background. The HPGe detector is located adjacent to the implantation point (see Fig. 5.2b). The γ rays from ^{141}Cs and ^{141}Xe decay were identified from the NDS compilation [Nic14]. All γ ray energy labels are in units of keV.

The resulting γ-ray spectrum from the subtraction is shown in Figure 5.23 with identified γ rays from evaluated data [Nic14]. The measurement confirms that both ^{141}Cs and ^{141}Xe were present at the implantation position.

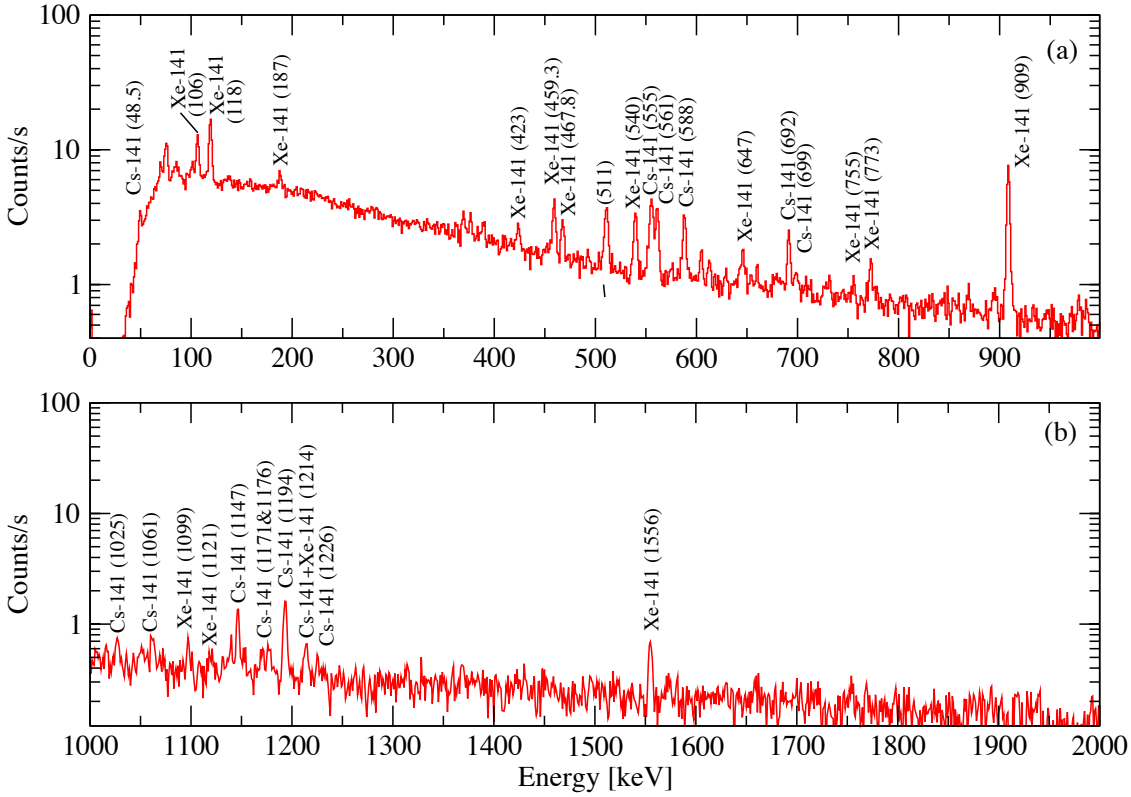

Figure 5.23: HPGe measurement at the implantation position with the background subtracted for the A=141 beam across the energy range (a) 0 keV - 1000 keV and (b) 1000 keV - 2000 keV. The normalised spectrum is from the tape implantation period 0 - 10 s with the corresponding background (11 - 111 s) removed. The γ rays from ^{141}Cs and ^{141}Xe decay are identified from the evaluated data [Nic14]. Labels for γ-rays are given in units of keV.

There is very little information available about the β^- decay of ^{141}I, with the current ENSDF data suggesting four candidate γ ray transitions of energies 338 keV, 414 keV, 475 keV and 574 keV, but no other information. Of these, only a small peak was seen at 574 keV. The tape cycle implemented for these measurements limited the HPGe detector measurement to the period during implantation, i.e. there is no measurement of subsequent decay data that could give time information to probe half-lives and characterise the 574 keV γ-ray. The presence of ^{141}I in the beam cannot be excluded, but it is expected that the contribution of this contaminant in a beam with the isobar separator optimised for ^{141}Cs will be small (see Sect. 1.2.2).

Separation of ATAGS measured components

The decay of implanted ions is present in the 11 - 111 s time region of the ATAGS histogram, while the ATAGS background is present in the 0 - 10 s region, as shown in Figure 5.19b. Figure 5.24 shows the time-gate projection of the ATAGS energy-time

histogram for the combined data set compared to the background (scaled to the time period for the data). The result of the normalised subtraction in Figure 5.24b is to over-subtract the signal at low energies, likely due to the shorter collection time of the background (10 s), as compared to the beam-on time (100 s). There is low energy noise in the data, which is more prevalent for higher count rates (see Section 5.4.1). The average background count rate of the shielded ATAGS in the CARIBU beam-hall was approximately 1.9 kHz, whilst the average source count rate for the A=141 measurement was less than 2.5 kHz.

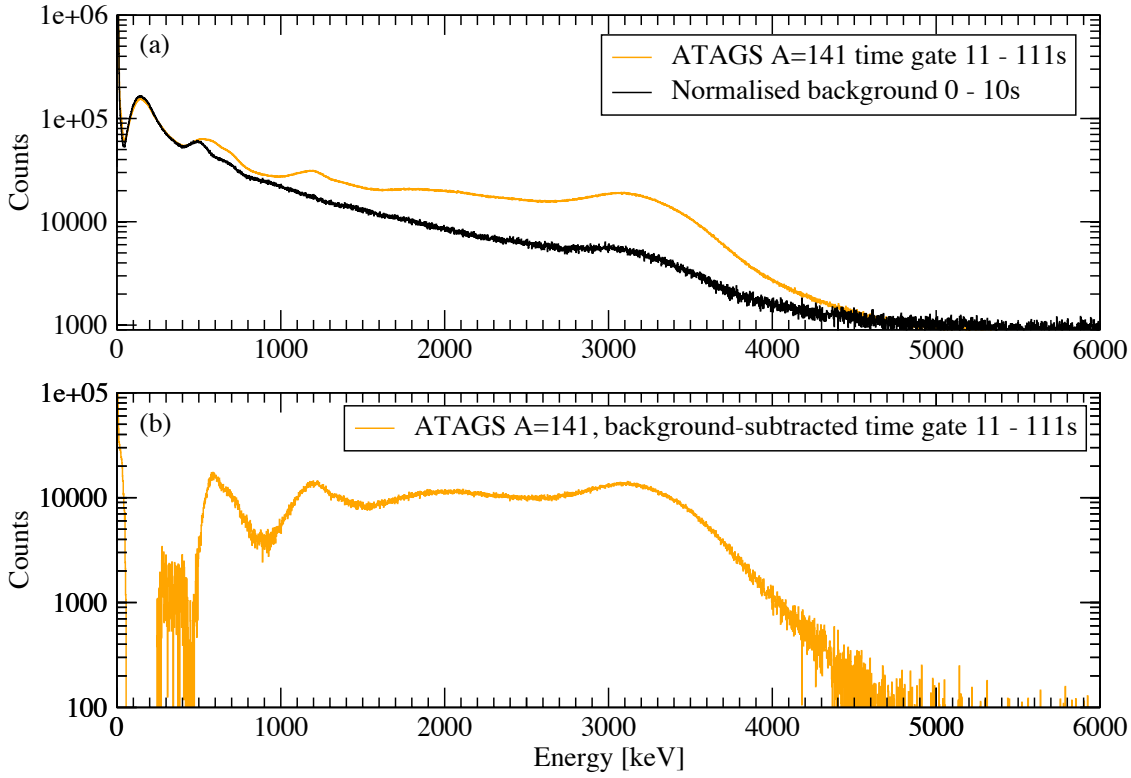

Figure 5.24: ATAGS spectra of A=141 data with a t= 11 - 111 s gate; (a) compared to a scaled background (t= 0 - 10 s gate), and (b) shown with this background removed.

The implantation time of ten seconds plus the additional one second required for moving the tape, sets the lower limit of what nuclides will survive the implantation and be measured by ATAGS. Figure 5.20b indicates the approximate maximum time a component can exist based upon a limit of ten half-lives (vertical dotted lines). For example, ^{141}I with a half-life of 0.43(2) s is not expected in the measurement beyond a time of 15.3 s (11 s implantation/move plus 10 x 0.43 s). Even at early times, the contribution of ^{141}I is expected to be small due to the low CARIBU intensity of 2.7 x 10^4 ions s^{-1} in contrast to 1.0 x 10^5 ions s^{-1} for ^{141}Cs. Limiting the collection time to 111 s results in the longer-lived decays of ^{141}Ba (18.27(7) mins) and ^{141}La (3.92(3) hours) not being measured.

These limits imply the expected intense components in the ATAGS measurement up to 110 s are ^{141}Cs, ^{141}Xe, and ^{141}I. The collection period was chosen to exceed the decay of the Xe ($T_{1/2}$=1.73(1) s), which will only be present up to a time of 27.3 s. After that point, only ^{141}Cs ($T_{1/2}$=24.84(17) s) should be present. Figure 5.25 shows three time-gate regions (Figure 5.20b); (a) the mixed ^{141}Xe /^{141}I/^{141}Cs time-gate (11 - 15 s), (b) the mixed

^{141}Xe/^{141}Cs time-gate (15 - 28 s), and (c) the pure ^{141}Cs region (28 - 111 s), all with the normalised background subtracted. The pure gate region is sensitive to the low-energy noise spike in the background spectrum, resulting in over-subtraction.

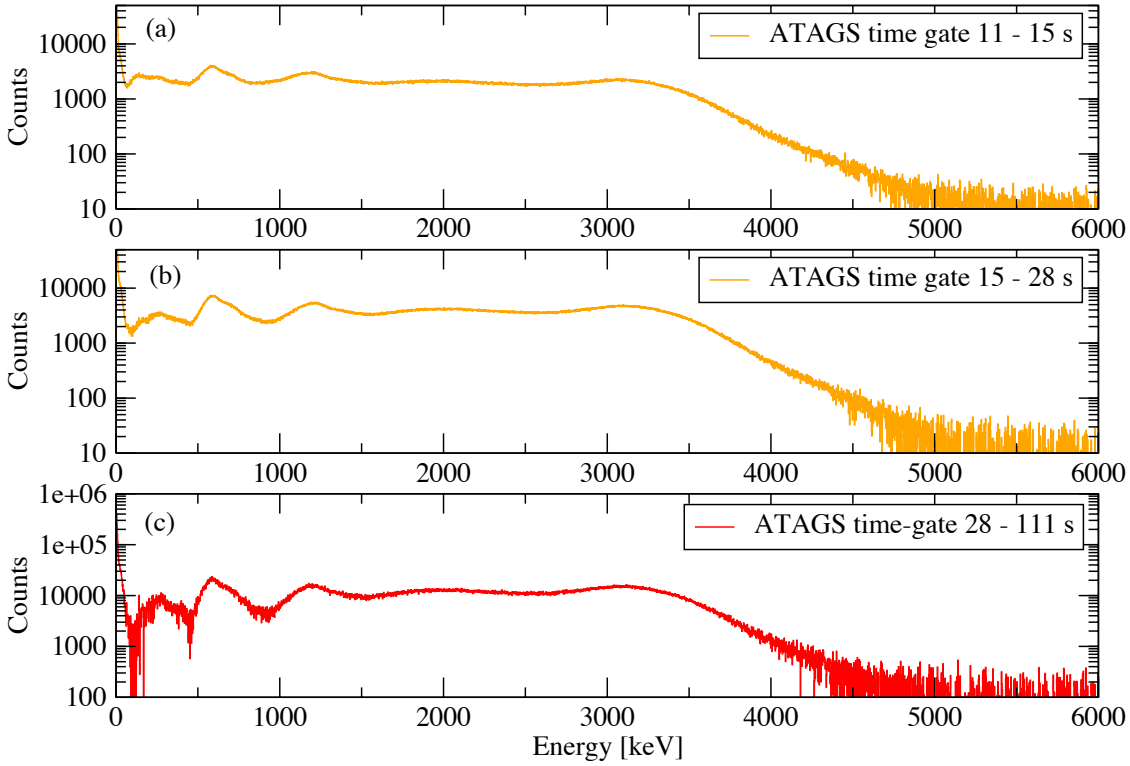

Figure 5.25: Background-subtracted ATAGS spectra for A=141 data with; (a) mixed time gate of 11 to 15 s expecting to see ^{141}I/^{141}Xe/^{141}Cs; (b) a mixed time gate of 15 to 28 s expecting to see ^{141}Xe/^{141}Cs,; and (c) a pure ^{141}Cs region (gate of 28 to 111 s).

Figure 5.26 compares the pure ^{141}Cs time-gate projection (28 - 111 s) (Fig. 5.25c) and the mixed time-gate projection (15 - 28 s) (Fig. 5.25b), with the published ATAGS measurement from Helmer and Greenwood *et al.* [Hel94c]. There is good agreement of the spectral features in both the mixed and pure time-gates, although the measurement from this work has a poor energy resolution compared to 1994.

There is a perceived improvement in the energy resolution of the present measurements with ATAGS compared to the ^{60}Co result shown in Figure 5.18. This is explained by the more acceptable total count rate for the ATAGS with these measurements (average count rate of 2.5 kHz). Nevertheless the aforementioned degradation of the scintillator performance of ATAGS compared to its operation in 1994 is obviously present, which will be a significant limitation when trying to obtain new results.

5.5.2 ^{140}Cs and ^{140}Xe

The CARIBU beam was next tuned to the A=140 chain focusing on ^{140}Cs where seven runs of approximately one hour each were collected. Two different collection modes were adopted for this data, one set recorded traces from the DGS-DAQ (2 hours) and the other was collected using the normal mode (7.15 hours). The latter, larger data set consisted of

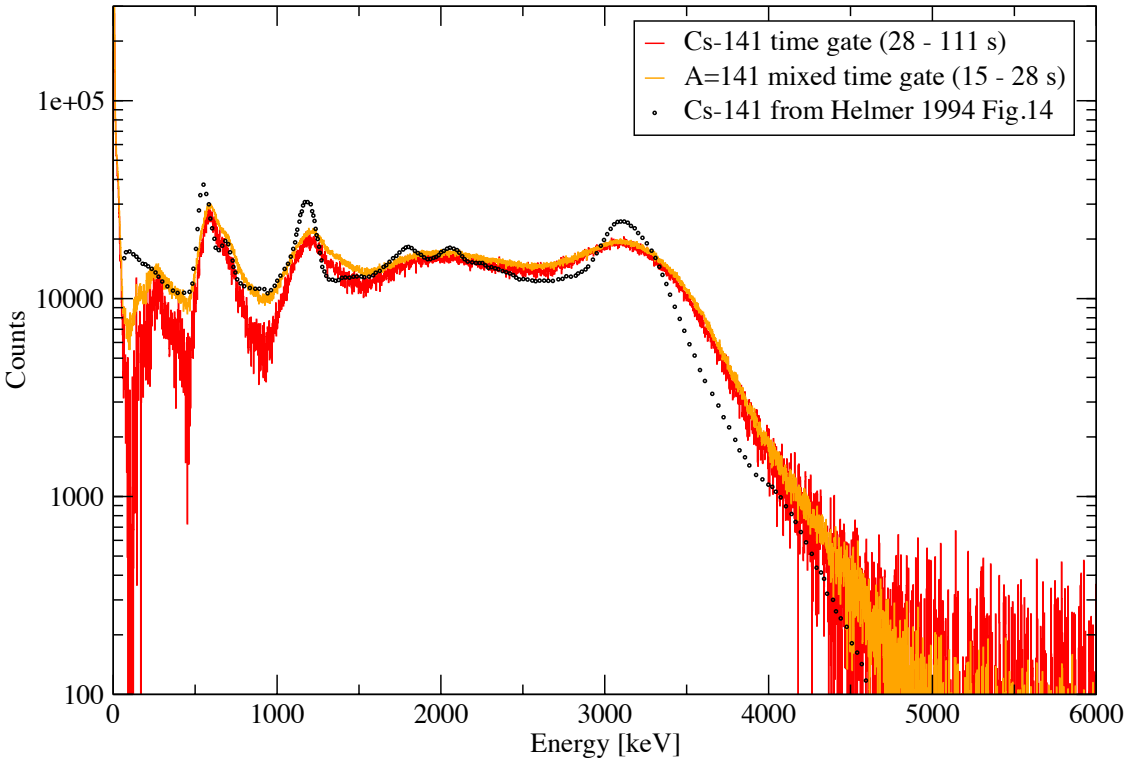

Figure 5.26: Comparison of current ATAGS performance for ^{141}Cs compared to Helmer's 1994 singles measurement at INEL (Figure 10 [Hel94c]). Data are scaled for the comparison and have the background removed.

90 cycles of total data and will be the main focus of this section. A third measurement with CARIBU's isobar separator focused on ^{140}Xe (0.5 hours) will also be presented.

Selection of time cycle

The tape cycle was adjusted to separate the ^{140}Cs from the ^{140}Xe, based on the known information on the half-lives (Fig. 5.9). The tape cycle selected for this measurement consisted of 30 s beam-on, 1.25 s tape move and 254.45 s collect. The longer collection time of 285.7 seconds was chosen to accomodate the 63.7 s half-life of ^{140}Cs.

The projections of the energy histograms produce the time profiles given in Figure 5.27. A similar overall shape is seen compared to the A=141 data, but the implantation and collection times are longer. Although the implantation time is longer, there is less than half the count rate in the HPGe data and approximately 30% of the ATAGS count rate when compared to the previous case. The ATAGS time profile (Fig. 5.27b) indicates the maximum expected components to be present as dotted lines, determined from ten times the known half-lives.

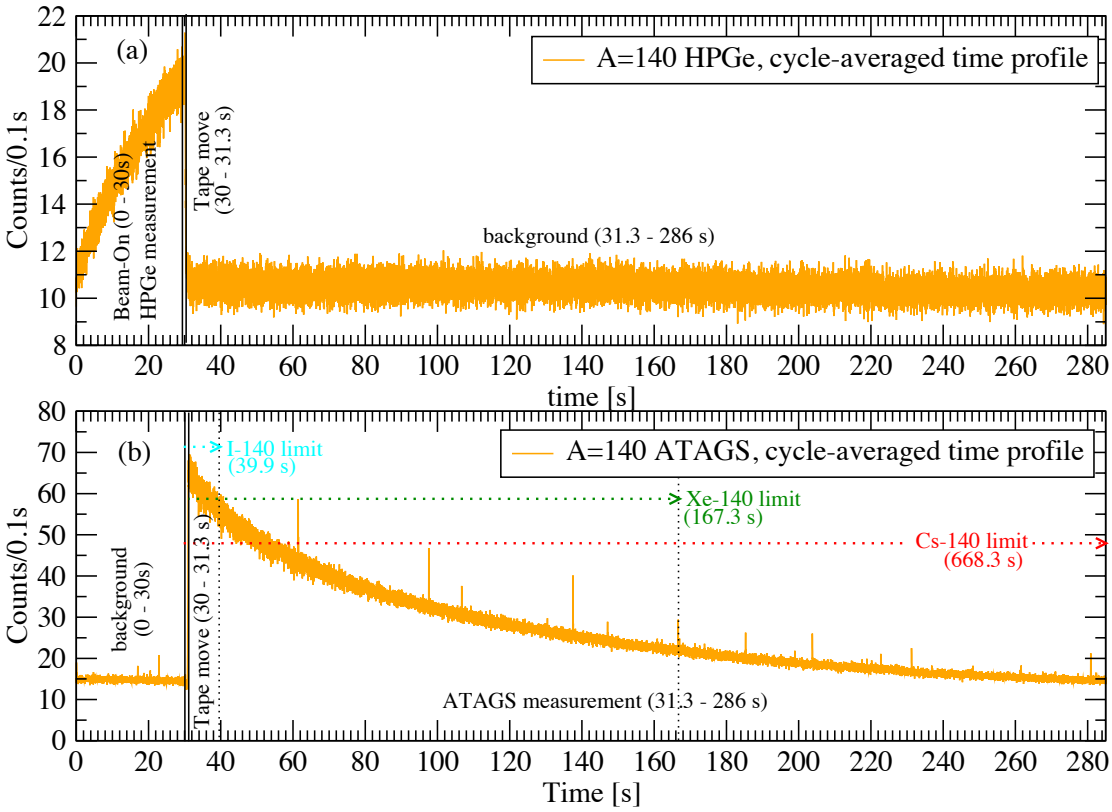

Figure 5.27: Average count rate profiles for A=140 data for (a) the clover detector and (b) ATAGS. Data are projection of the 2D histogram of time vs energy which is then divided by the total collection time (7.15 hours) and shows the tape transitions for this measurement. The data are shown as the respective detector count rate across a complete cycle with a time resolution of 0.1 s. The maximum expected presence of the various components are indicated by the dotted lines as determined from the known half-lives (see text).

Validation of the beam species using HPGe

The energy projection of a 2D HPGe energy-time histogram was produced for a time-gate of 0 s to 30 s (the beam implantation time). A background time-gate projection (31.3 s to 285.7 s) was removed from the spectrum and both were divided by 90 cycles to obtain the average count rate. Figure 5.28 shows the resulting spectrum with γ rays identified from ^{140}Cs, ^{140}Xe and ^{140}I decays. It should be noted that the ENSDF information about ^{140}I is incomplete and as such, all of the significant peaks in the spectrum have been labelled with an energy even if they are yet to be identified [Lin99, ens].

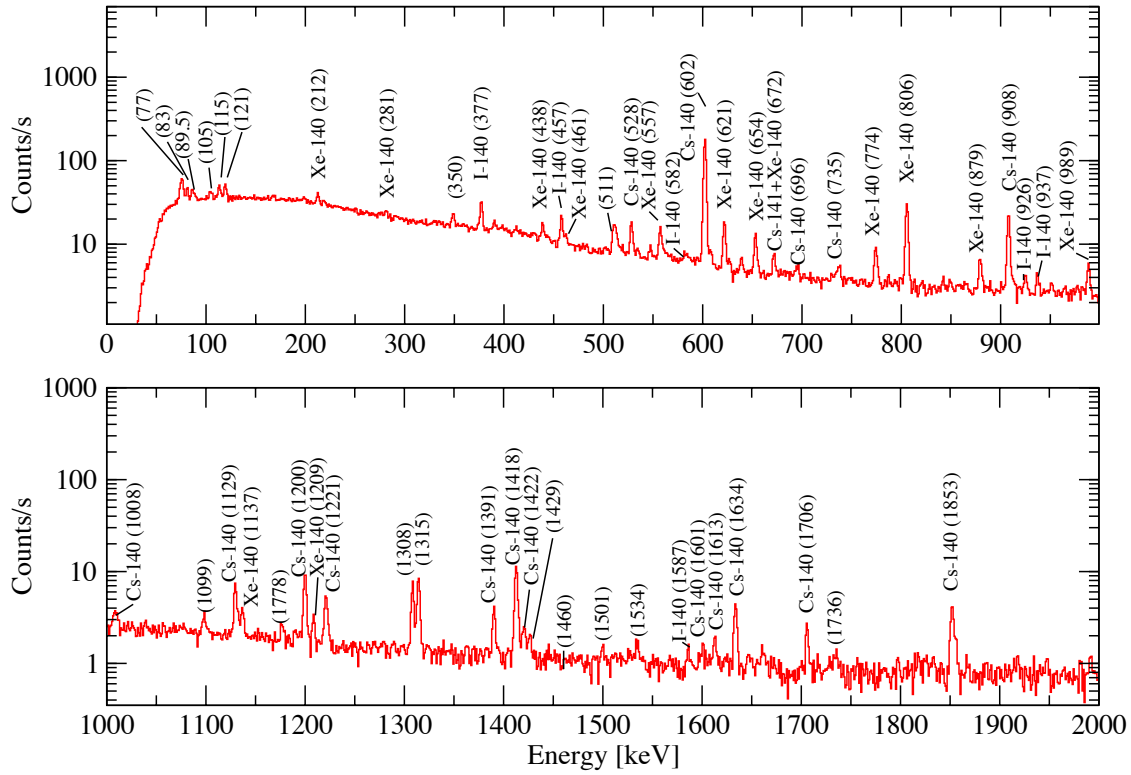

Figure 5.28: HPGe measurement of A=140 beam with background subtracted. The spectrum is a time-gate projection during tape implantation (0 - 30 s) with the normalised background from (31.3 - 285.7 s) removed. The HPGe detector is located adjacent to the implantation point (see Fig. 5.2 b). Gamma rays were identified as being from ^{140}Cs and ^{140}Xe using evaluated data [Nic14], with labels given in units of keV.

Separation of ATAGS measured components

The ATAGS spectrum is compared to the background and shown with the background subtracted in Figure 5.29. The expected maximum times for the shorter lived components are 39.9 seconds for ^{140}I and 167.3 seconds for ^{140}Xe, as indicated on the ATAGS time profile (Fig. 5.27). Figure 5.30 compares spectra with gates on the three time regions (a) 31.3 to 39.9 s (all 3 isotopes might be expected), (b) 39.9 to 167.3 s (^{140}Xe and ^{140}Cs expected), and (c) 167.3 to 285.7 s which should be a pure ^{140}Cs region. There is reasonable agreement with the currently accepted $Q(\beta^-)$ value of 6220(10) keV for ^{140}Cs.

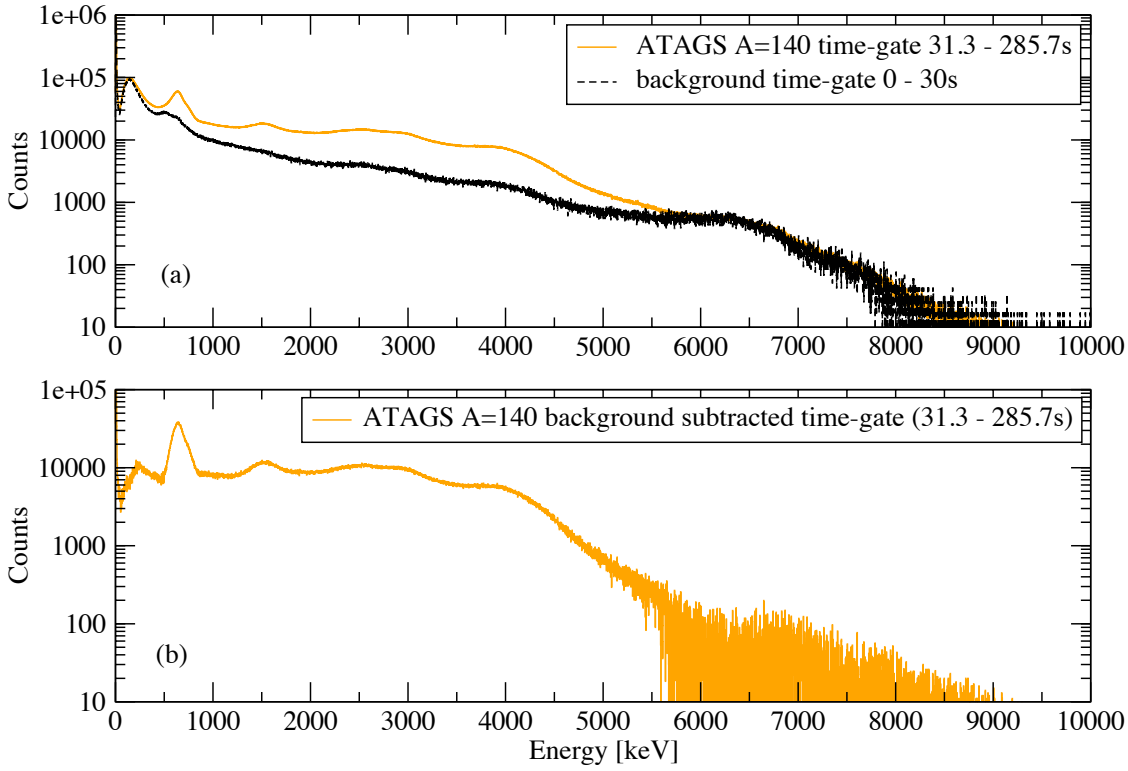

Figure 5.29: Background-subtracted ATAGS spectrum for A=140 data. (a) The time-gate projection for the 31.3 to 285.7 s region is compared to a scaled background and then shown in (b) with this background removed.

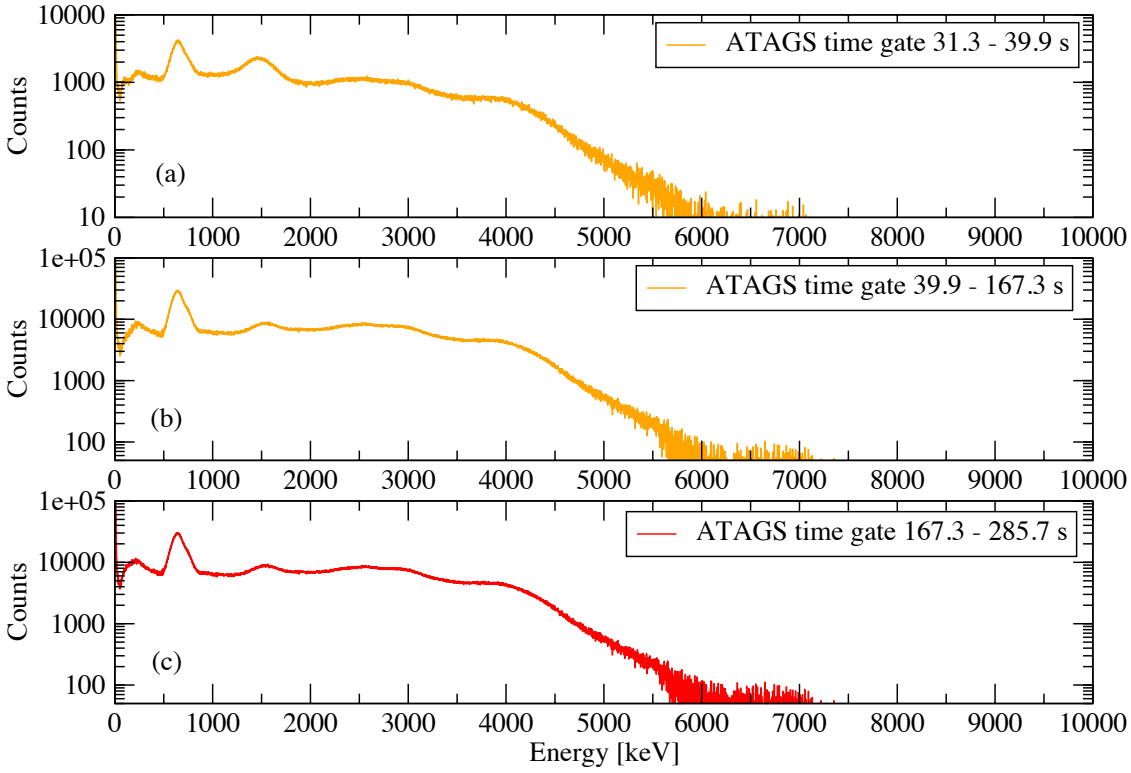

Figure 5.30: Background-subtracted ATAGS spectra of A=140 data: (a) mixed-component time-gate of 31.3 to 39.9 s; (b) a mixed-component time-gate of 39.9 to 1 s, and (c) a pure ^{141}Cs region (gate of 167.3 to 285.7 s).

Figure 5.31 compares the pure gate (Fig. 5.30c) and mixed gate (Fig. 5.30b) with that of Helmer *et al.* [Hel94a]. There is agreement between the overall shape of the clean ^{140}Cs spectrum with the measured result from INEL. The 'mixed' early spectrum shows additional structure that is likely associated with ^{140}Xe and /or ^{140}I.

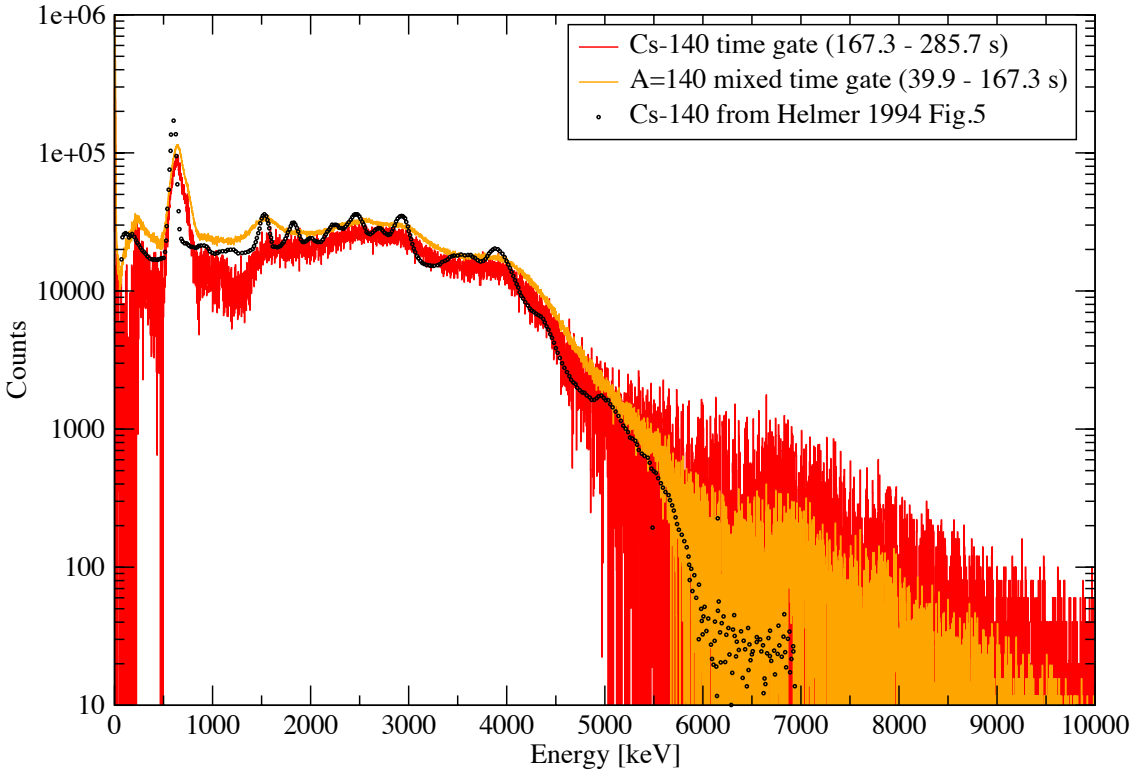

Figure 5.31: Comparison of ATAGS performance for ^{140}Cs with the singles ATAGS spectrum of ^{140}Cs measured at INEL in 1994, reproduced from Figure 5 in Helmer *et al.* [Hel94a]. Data are scaled for the comparison and have the background removed.

5.5.3 ^{140}Xe-focused measurement

In another set of measurements, the CARIBU isobar was tuned in an attempt to undertake a direct measurement of ^{140}Xe. This experiment was abandoned at the time due to pulsing of the implanted beam intensity and consequent difficulty in tuning. The HPGe count rate was fluctuating between the normal background rate and increased rate bursts during implantation. This is an indication of insufficient implantation into the tape, most likely from increased static charge created with the use of a faster tape cycle. The electrostatic charge on the tape repels and deflects the low-energy beam of ions from CARIBU in an unpredictable fashion until the static charge dissipates. Earthing of the tape is usually achieved in design by using tape with a thin metal coating, but unfortunately this was not available for these measurements. Despite these difficulties, 29 minutes of data were collected (28 cycles) using 6 s beam-on, 1.25 s tape move and 54.45 s of ATAGS collection, as seen in Figure 5.32.

Figure 5.33 is a comparison of HPGe measurements of the A=140 nuclides being produced by CARIBU; the Xe-focused data (green) are compared to the Cs-focused data

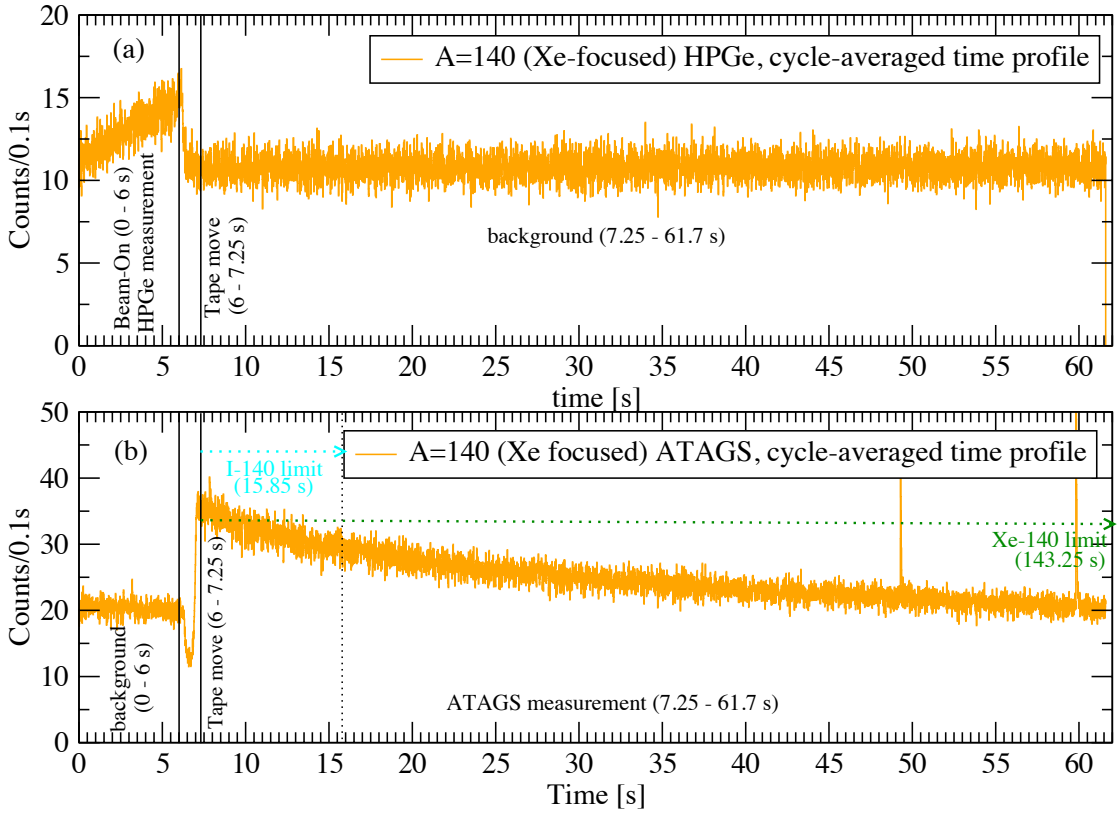

Figure 5.32: Average count rate profiles for the A=140 measurement under Xe-focused conditions. Data are from a projection of the 2D time vs energy histograms, divided by the total collection time (29 minutes or 28 cycles) and show the tape transitions for this measurement. The data are shown as the respective detector count rate averaged across a complete cycle with a time resolution of 0.1 s. The maximum expected presence of the beam components is indicated by the dotted lines as determined from the known half-lives (see text).

of Figure 5.28 (red). Although the data set is limited in statistics, there are several of the more intense γ rays also present in the Xe-focused spectrum that correspond to the presence of ^{140}Cs, ^{140}Xe, and ^{140}I at the implantation position. It is not clear whether the isobar separator settings have increased the relative amount of ^{140}Xe.

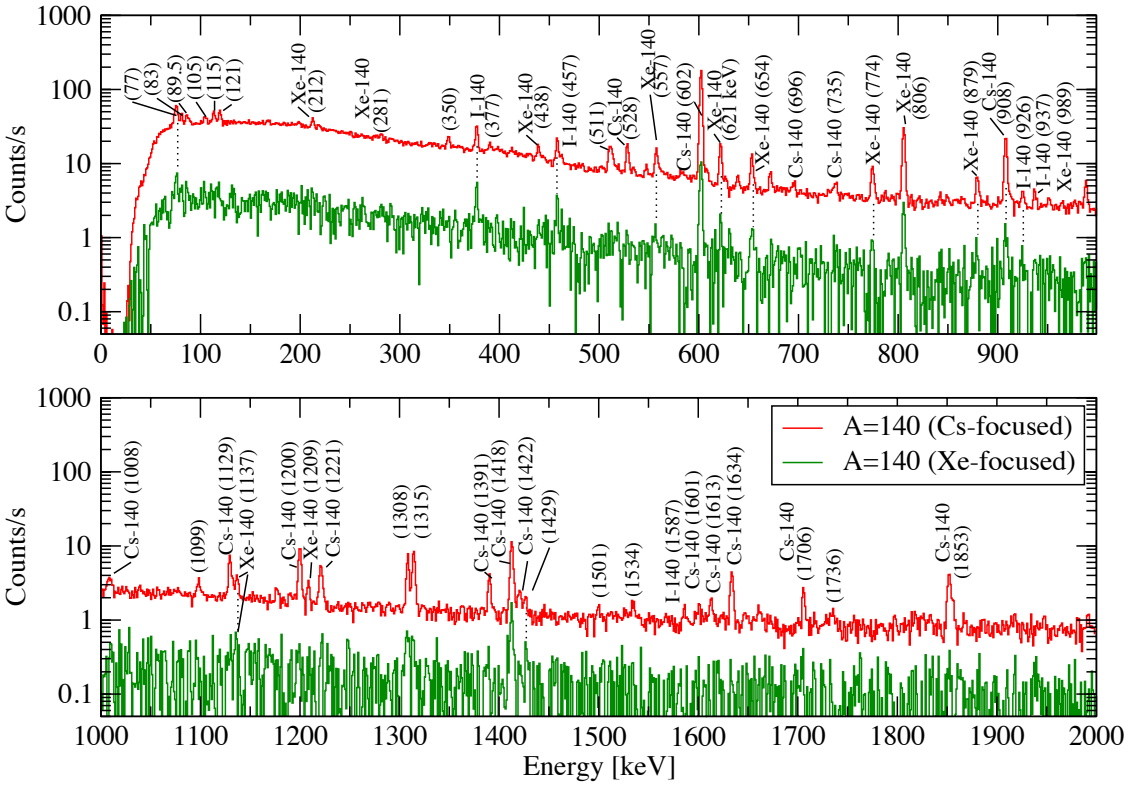

Figure 5.33: Comparison of A=140 HPGe measurements at the implantation site, with background subtracted for the Xe-focused measurement (green) and the previous Cs-focused data from Fig. 5.28 (red).

Figure 5.34 compares background-subtracted ATAGS spectra for the Xe-focused A=140 data with time-gates of (a) 7.25 to 61.7 s, (b) 7.25 to 15.85 s, and (c) 15.85 to 61.7 s. Unlike the Cs-focused A=140 tape cycle, there is no isotopically selective time-gate for these data. If present, we expect to see I/Xe/Cs in the 7.25 to 15.85 s gate and Xe/Cs in the 15.85 to 61.7 s gate. The Xe-focused spectra exhibit a shape difference compared to the Cs-focused spectra in Figure 5.30, specifically the peak at approximately 1440 keV and the spectrum extending to 8 MeV. There are presently no published ^{140}Xe TAGS spectra against which to compare this result. More detailed analysis is presented in the next chapter.

5.5.4 ^{104}Nb and ^{104}Nb^{m}

Selection of time cycle

A data set was acquired for an accumulated time of 13.8 hours with the CARIBU isobar separator tuned to ^{104}Nb. The tape cycle consisted of 5 s beam-on, 1.25 s tape move, and 20.05 s data collection over 1895 measured cycles. Figure 5.35 shows the time vs energy

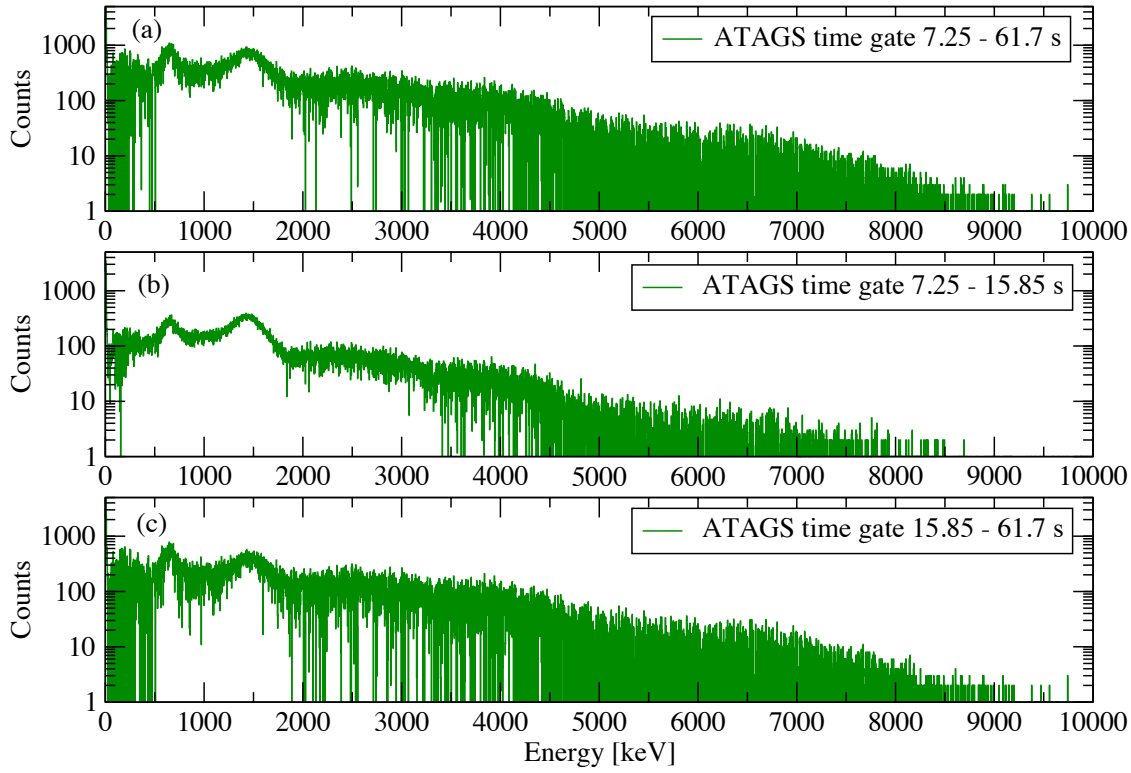

Figure 5.34: Background-subtracted ATAGS spectra of A=140 (Xe-focused) data with time gates on (a) 7.25 to 61.7 s (entire ATAGS data set), (b) a mixed region of 7.25 to 15.85 s (expecting ^{140}I, ^{140}Xe, and ^{140}Cs), and (c) a mixed time gate of 15.85 to 61.7 s (expecting ^{140}Xe and ^{140}Cs).

histograms for (a) the HPGe, and (b) ATAGS, for this data set. The CARIBU beam intensity was much lower than for the previous beams.

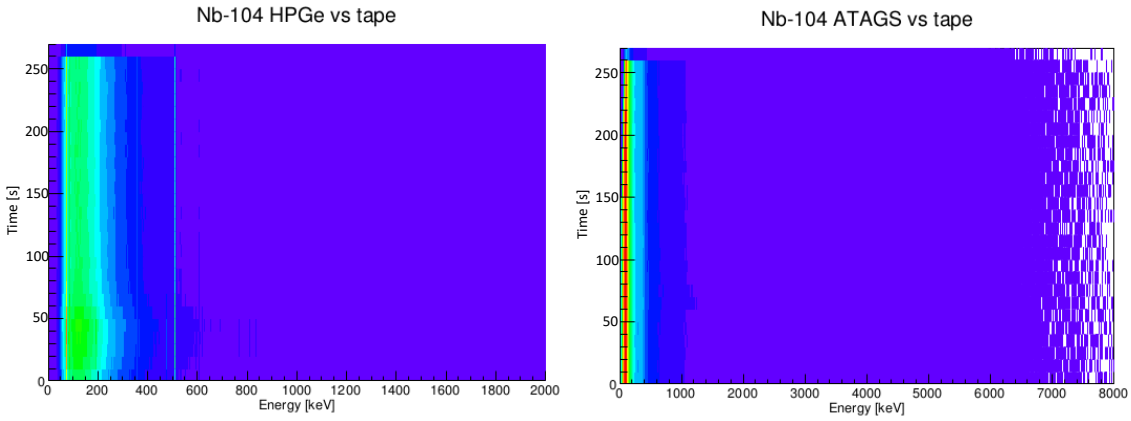

(a) (b)

Figure 5.35: The time-energy histograms from the A=104 measurement for (a) the HPGe clover viewing the tape implantation position, and (b) ATAGS. Approximately 13.8 hours of data were collected with a tape cycle of 5 s beam on, 1.25 s tape move, and 20.05 s collect.

The HPGe time profile is comparable to previous data sets (Figure 5.36a), but there is very little measured count rate above background in the ATAGS time profile (Figure 5.36b).

Validation of the beam species using HPGe

Figure 5.37 shows the high-resolution γ-ray spectrum measured by the clover detector adjacent the tape implantation position. The time-gate projection of Figure 5.35a for the beam on (0 s - 5 s) is shown with normalised background (6.3 s - 26.3 s) subtracted. The γ rays have been identified using the evaluated data from [Bla07], verifying the correct CARIBU beam is being delivered at the implantation location.

Separation of ATAGS measured components

The ATAGS spectrum of the entire ^{104}Nb data set is compared to the background in Figure 5.38. There are very few counts remaining after background subtraction. The data were re-sorted and the first and last hour-long measurements were compared to reveal the same result. It was noted during the experiment that the data acquisition rate would rapidly fluctuate. It seems likely that the ions were not implanting properly into the tape and hence were not being transported to the ATAGS detector, which would explain the lack of ATAGS data.

The mylar tape utilised for all of these measurements did not have a conductive coating. The movement of the tape in combination with the potential difference of the CARIBU platform suggests that the implantation did not occur due to Coulomb repulsion. It is reasonable to argue that the spectrum of Figure 5.38b is a mix of both ^{104}Nb^{m} decay and ^{104}Nb, albeit with a very low number of counts, since the target ions were shown to be present at the point of implantation from the clover-detector measurement. It is noteworthy that the HPGe time profile behaviour (Fig. 5.36a) shows a decay curve after

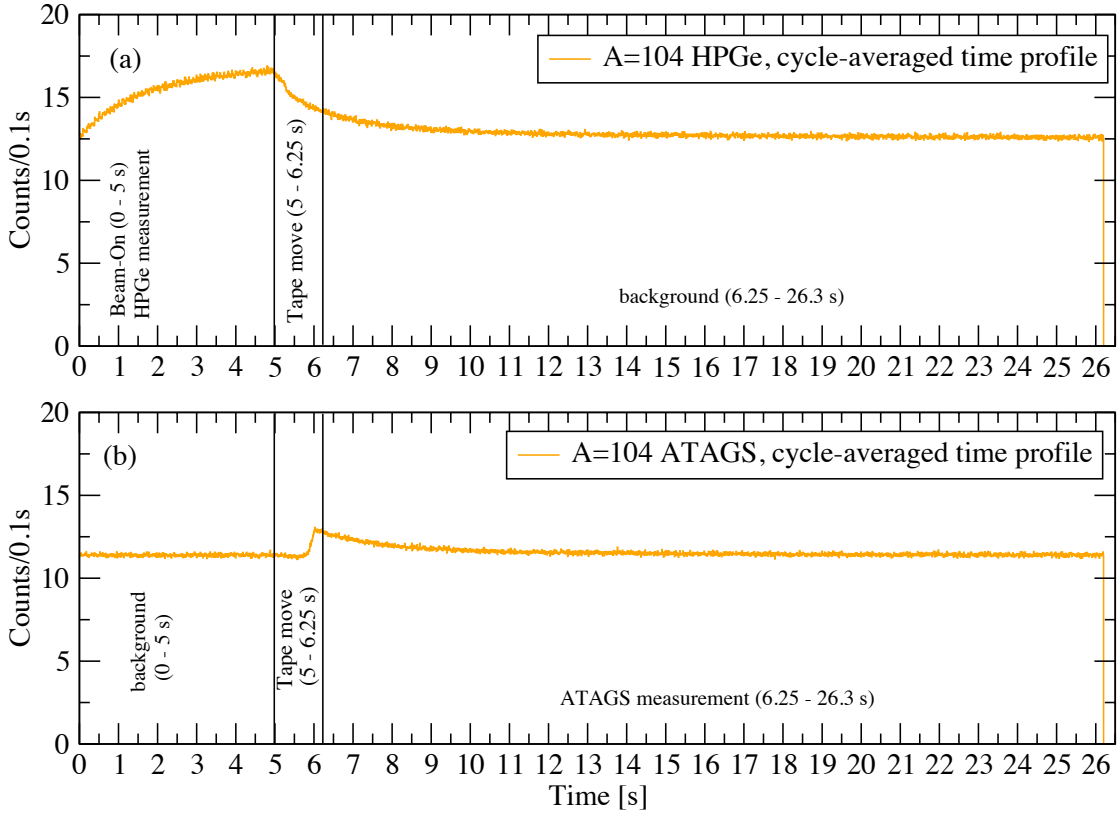

Figure 5.36: Average count rate profiles for A=104 data. Data are projections of the histograms in Figure 5.35 divided by the total collection time (13.7 hours) and show the tape transitions for this measurement.

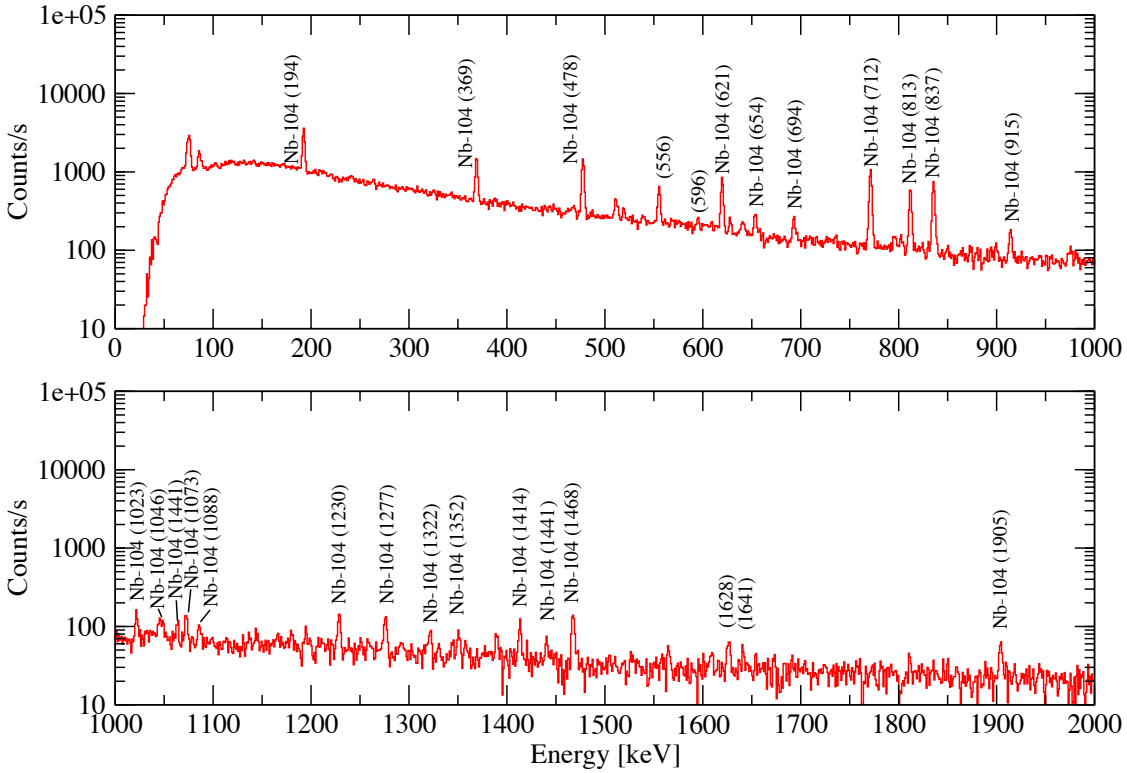

Figure 5.37: HPGe measurement at the implantation position for the A=104 beam with background subtracted. The normalised spectrum is from the tape implantation period (0 - 5.0 s) with the background from (6.2 - 26.3 s) removed. The γ rays from ^{104}Nb decay were identified using evaluated data [Nic14], labels given in units of keV.

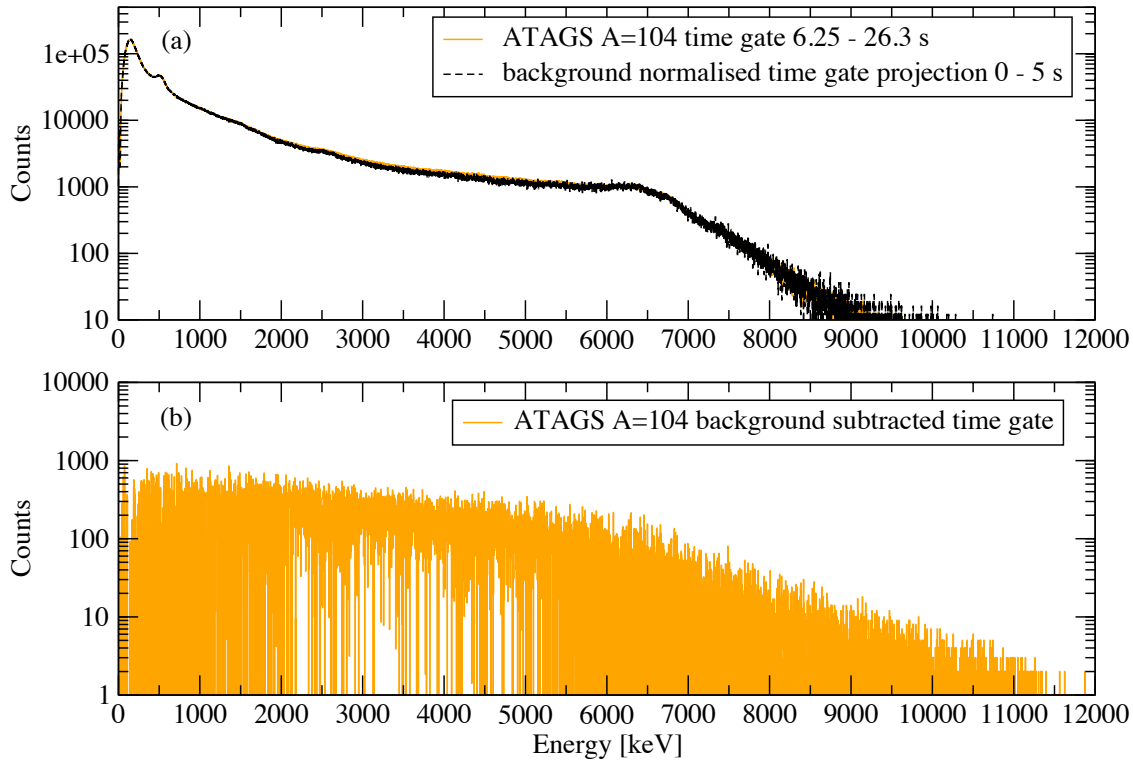

Figure 5.38: ATAGS time-gate projection of A=104 data for the entire data set. The spectrum collected from 7 to 26 s is compared to the scaled background in (a), while (b) shows the 7 to 26 s gate with the background removed. It appears that very little activity was implanted into the tape (see text).

the tape move, indicating nuclei have remained at the implantation site. Such an effect was not seen in the other measurements (Figs. 5.20a, 5.27a and 5.32a). In the absence of better statistics, and given the differences to other measurements for A=140 and A=141, it is difficult to make a firm conclusion as to whether the ATAGS spectrum in Figure 5.38b is a real representation of ^{104}Nb decay.

5.6 Discussion

The greatest problem with this experiment was the use of mylar tape with no conductive coating. The time line for gaining access to CARIBU did not align with the supply of a more suitable alternative while the author did not have control of the experimental preparation prior to arrival at ANL. When a tape system is utilised with the diagnostic station on the CARIBU stub-line or with SATURN, the tape has a thin metal coating to keep the tape at ground potential. The grounding is achieved in the tape-station via grounding brushes. The charging of the tape was further compounded by using thicker and wider tape in this experiment than normal. This extra width was a likely cause of the increased friction seen in the alternative tape setup threaded through SATURN, that was abandoned due to the frequency of tape jams. It is likely that a combination of the tape movement through the pulleys and the buildup of charge due to ions hitting the tape, induced static charge in the tape and reduced the implantation effectiveness due to Coulomb repulsion. The effects are prominent for the measurements focused on ^{140}Xe and ^{104}Nb that had short tape cycles. It is believed that these issues are possibly present in all of the measurements, but were not as significant for ^{141}Cs, ^{140}Cs and ^{140}Xe. It seems likely that using conductive tape would improve the collection statistics.

Another improvement for the experimental setup would be the addition of a removable alignment detector that would assist with the tuning of CARIBU. This detector would be switched into place in a position in front of the intended implantation position during the tuning and provide feedback for minor beam-adjustment, which becomes more critical in the case of the low-intensity beams of greatest interest.

It appears that ATAGS has a degraded resolution compared to its performance when at INEL. This may not be surprising considering the age of the scintillator. This could have been better evaluated had lower activity calibration sources been available during preparation prior to and during the experiment. Despite the degraded energy resolution of ATAGS, TAGS spectra were produced that are broadly comparable to published INEL work. The poorer resolution will be a limitation for deduction of β-feeding intensities in the following chapter.

The combination of the high-resolution γ-ray spectroscopy with the TAGS measurement was very useful for identification of the beam; there would be doubt for identification if ATAGS was operated in isolation. The time tag available with the DGS-DAQ is an essential element of the data and its analysis and is fundamental for isotope separation and identification. An improvement would be to use the full X-Array coupled with a TAGS detector in the arrangement described in the original experimental proposal. This would be possible in principle, but difficult in practice, due to the limited floor space available and the shielding requirements of a TAGS type detector at CARIBU. Another improvement would be greater distance between the low-energy CARIBU beam line experimental area and the CARIBU source cask. This latter improvement is currently being pursued.

Chapter 6

Isobaric separation of ATAGS spectra

Prior to deconvolution of the β-feeding intensities, the ATAGS data requires separation of the spectral components corresponding to each of the isobars. High-resolution spectroscopy can separate and identify nuclides on a peak-by-peak basis. A low-resolution spectrum from a TAGS measurement does not give this fine detail as the transitions are all convoluted into one broad response. In addition, there are occasions where TAGS measurements may be performed on nuclides where the half-lives of the isotope of interest or its neighbours are unknown.

Where the isotopes that are present and their halflives are both known, it may be possible to manipulate gated spectra to extract clean TAGS spectra (see Section 6.2). In the absence of this information, a different methodology is required. A time-difference method is introduced in Section 6.1 and applied to the ATAGS results of Chapter 5.

6.1 Time-difference method

The time-difference method is introduced in this section. It is not intended to replace the more rigorous method of manipulating time-gated spectra with well-motivated time cuts when lifetimes are known; it is an alternative when there is little known about the decay chain. It can be used as an alternative to specifically chosen time-gates, particularly when the presence of the components involved, or their half-lives, are in doubt. The present method is best applied to cases where there are two nuclides involved with significantly different half-lives. The goal here is not to separate the energy spectra, but instead, to integrate the energy spectrum over time and extract time curves that reflect possible 'FAST' and 'SLOW' components in the data to identify if multiple isotopes might be present.

Figure 6.1 shows the schematic representation of the time-difference method applied to a two-component decay involving significantly different half-lives (represented in red and green), imposed on a constant background component. The method involves dividing the data into equal time-slices, based on the minimum time-resolution of the data. These minimum time resolution slices act as the building blocks for resizing the division of the data set into larger time-slices by means of adding sequential slices together. For example, if a data set has a minimum time-resolution of 1 s and the desired time-resolution of the slicing is 5 s, each slice would be made up of five minimum slices added together.

Adjacent data slices, of equal time resolution, are sequentially subtracted from each other. The 'FAST' component is the change in counts between the slices, whilst the

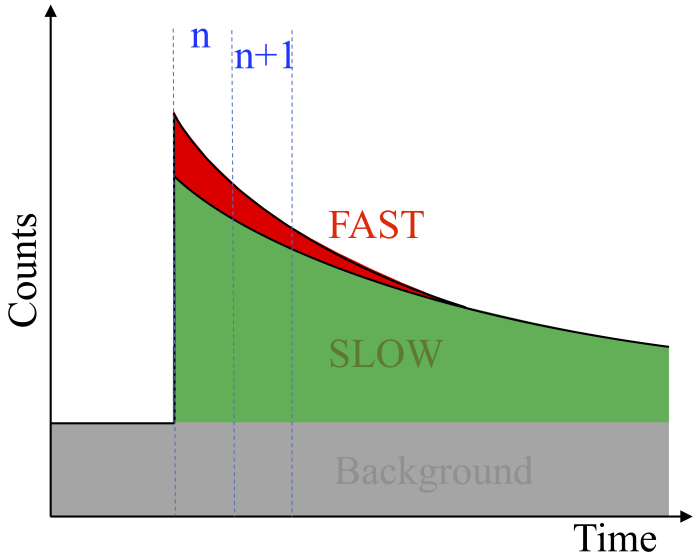

Figure 6.1: Schematic of the time-difference method applied to a two-component decay with significantly different decay half-lives: a 'FAST' decay component (red), a 'SLOW' decay component (green), and a constant background (grey). The data is divided into equal time slices, with the 'FAST' and 'SLOW' components separated by looking at the difference between sequential slices (see text for details).

'SLOW' component is the non-changing part. The time-profiles of each component are determined by iteratively evaluating the components at each time step. The time-difference method can be represented as:

$$T_{FAST}(n) = [T(n) - T(n+1) - norm.BG], \tag{6.1}$$

and

$$T_{SLOW}(n) = [T(n+1) - norm.BG] \tag{6.2}$$

where:

n	= slice index;
$T(n)$	= number of events in slice n;
$norm.BG$	= number of counts in the background spectrum normalised to the width of the time slice;
T_{FAST}	= time profile of the 'FAST' changing component; and
T_{SLOW}	= time profile of the 'SLOW' changing component.

The event counts $T(n)$ and $norm.BG$ are manipulated to extract a time spectrum of the 'FAST' and 'SLOW' components (see, for example, Figure 6.2) The subtractions of the number of counts in the adjacent gates will not completely separate out the components from each other, rather they will remove the majority of the slowly varying component

and amplify spectral changes or trends in the data in the 'FAST' component. In the case of a third decay component that has a much smaller half-life, the associated data will be as part of the 'FAST' component. The limitation of the time-resolution for this work is based upon the minimum bin size of the time-energy histogram used, which is 0.1 s in the case of the ATAGS data.

The method is benchmarked against the better known data (A=141) in Section 6.1.1, then extended to the lesser-known data in Sections 6.1.2 and 6.1.3. It is then compared to the more accurate fitted time-gate methods (see Section 6.2). This latter method can provide a more rigorous separation of data, in particular, it enables the clean separation of the energy components.

6.1.1 ^{141}Cs and ^{141}Xe

The time-difference method described in Section 6.1 is applied to the mixed time region (11 s to 28.3 s) of the A=141 'Cs-focused' measurement (Figure 5.20b of Section 5.5.1). Figure 6.2 shows the time-difference result applied to the entire set using the selected time resolution of 0.5 s. The average background is normalised and subtracted from every 0.1 s time-slice in the data. The 'FAST' component decay curve (green), makes a small contribution to the overall number of counts; that it decays quickly is in agreement with the ^{141}I and ^{141}Xe limit (based on 10 half-lives) as marked by the dashed lines.

The half-life of the total decay profile (orange) is fitted (with the spikes in the data removed), for a time region that should only contain ^{141}Cs (48 s to 98 s). The fitted half-life of 24.83(36) s confirms the sole presence of ^{141}Cs, since the fitted value is comparable to the currently accepted value of 24.84(17) s [Yam82, ens]. A fit in the region from 15 s to 98 s for this total decay profile yields a result of 24.5(1) s, that disagrees with the expected value, likely due to the mixing of a shorter-lived component with this result.

If, however, the separated ^{141}Cs time profile ('SLOW' component - red) is fitted between 15 and 98 seconds, the resulting half-life of 24.97(26) s, is in good agreement with the evaluated value of 24.84(17) s, demonstrating that some of the 'FAST' contamination has been removed. A fit performed on the 'FAST' component across the range 12 s to 30 s results in a half-life of 1.96(23) s, in good agreement with the known half-life of 1.73(1) s for ^{141}Xe. Note that the uncertainties of these fits only account for the statistical errors of the fit itself, and do not include systematic errors associated with the separation method.

As a test of the unknown presence of components and half-lives, the time-difference method shows at least two components and provides the correct half-lives showing promise that this method may be able to identify components. This information can be used to extract a clean 'SLOW' energy spectrum by selecting a time-gate beyond the presence of the 'FAST' component. The unfolding of a 'FAST' energy spectrum can be achieved by integrating the time components to calculate the proportion of 'FAST' to 'SLOW' contribution in a mixed gate region, and subtracting the appropriate amount of the 'SLOW' (clean gate) from it. As the half-lives in this case are well-known, the more accurate time-fitting method (as described in Section 6.1.2), can provide a more accurate unfolding result.

6.1.2 ^{140}Cs and ^{140}Xe

The time-difference method is tested with the 'Cs-focused' A=140 data (Figure 5.27b of Section 5.5.2), using a time-resolution of 1.5 s. The background-subtracted time plot of the 'Cs-focused' A=140 ATAGS data is shown in Figure 6.3. The background is subtracted

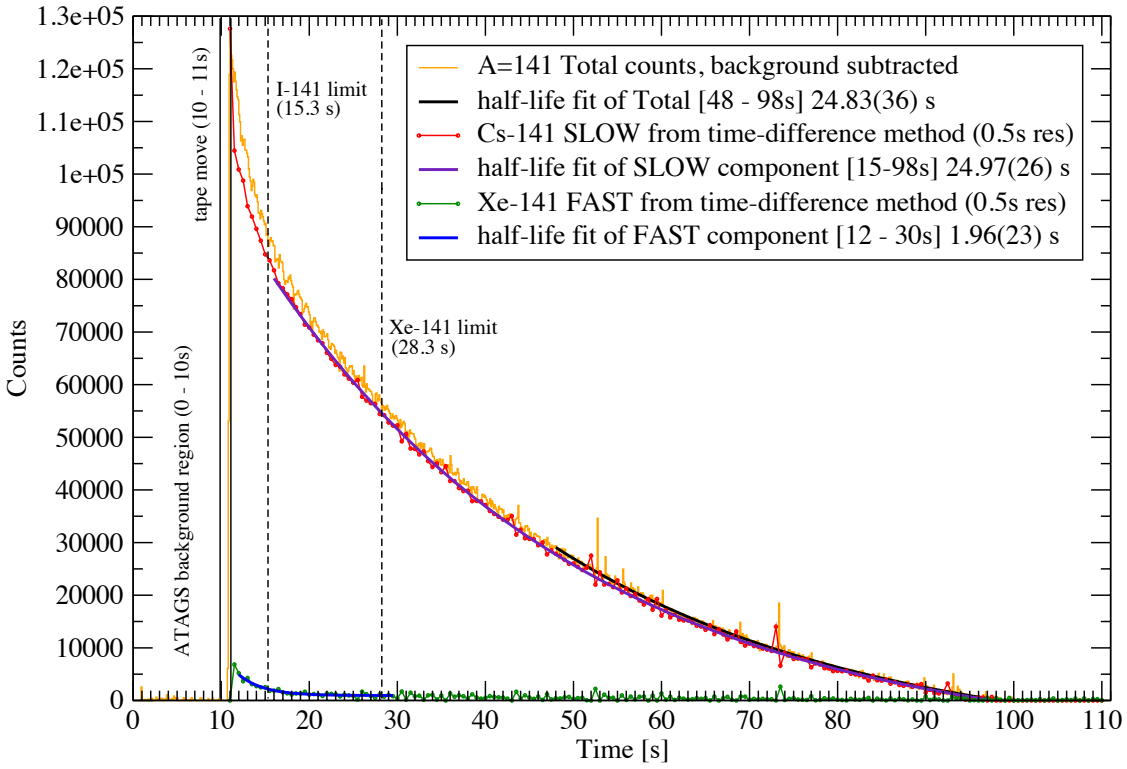

Figure 6.2: Time projection of A=141 ATAGS data with normalised background subtracted at each 0.1s time slice, as well as 'SLOW' and 'FAST' separated components using the methods described in the text. Half-life fits are also shown for various curves and ranges. See text for full details.

from each 0.1 s component in the data. There is a slight over-subtraction resulting in negative values beyond 280 s, caused by statistical fluctuations in the normalised background sample.

The total spectrum in the time region between 168 s and 275 s, where only ^{140}Cs should be present, was fitted with a decay curve, resulting in a half-life value of 63.7(13) s, in agreement with the current evaluated value of 63.7(3) s. This validates the presence of ^{140}Cs in the data. There was some difficulty in obtaining this decay fit, owing to the presence of many spikes in the data, however, removal of the spikes did not change the fit result. A time fit of the total decay data for the region 39.9 s to 167.3 s resulted in a half-life of approximately 45 s, which indicates a mixing of ^{140}Cs, with something shorter lived, most likely ^{140}Xe, whose known half-life is 13.6(10) s. A time fit to the time-region 31.3 s to 39.9 s yielded a value of approximately 4.5 s, likely due to a contribution of ^{140}I (known half-life of 0.86(4) s) in the region that should be dominated by ^{140}Xe.

The separated 'FAST' component was fitted in the earliest time region (31.3 s to 40.3 s), resulting in a half-life of 1.2(3) s. This suggests the dominant presence of ^{140}I (0.86(4) s) in this time region. A similar fit was applied to the separated 'SLOW' data for a later time (40.3 s to 110 s), the half-life value of 13.7(54) s is in agreement with ^{140}Xe (13.6(10) s). The time fit of the 'SLOW' component in the region 40.3 s to 167.3 s yields a value of 47(1) s, suggesting that the time-difference method was not successful in removing all of the ^{140}Xe from this region.

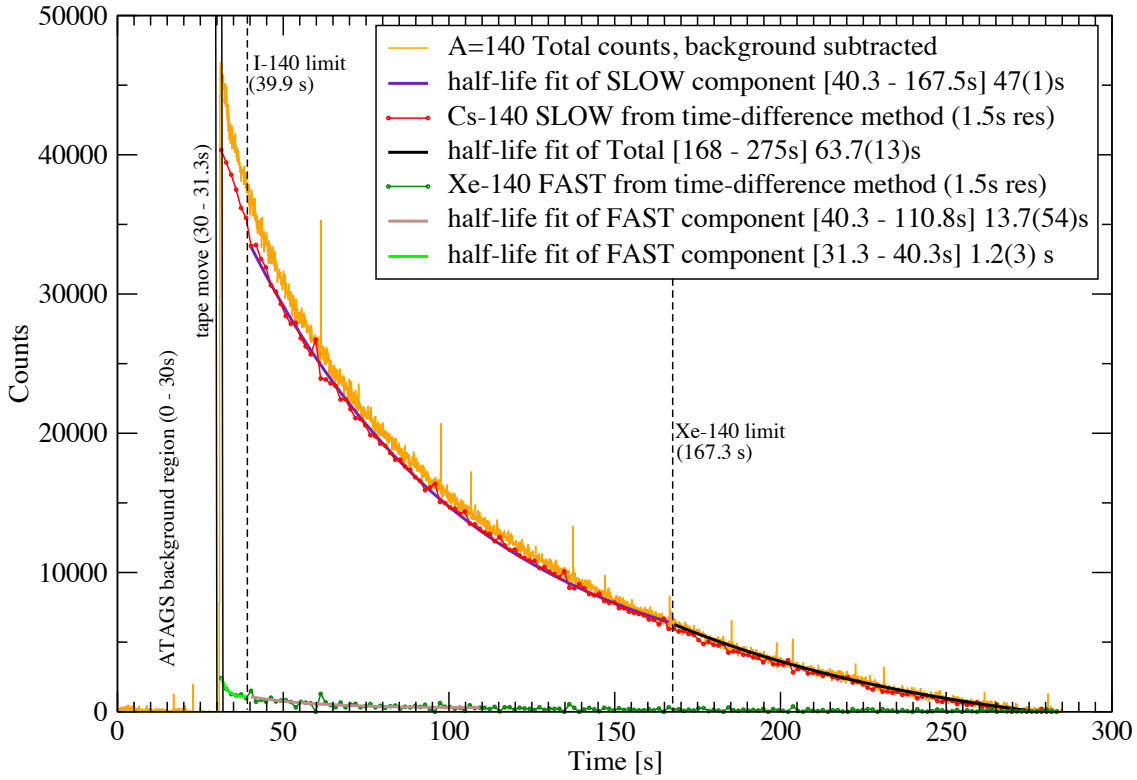

Figure 6.3: Time projection of A=140 ATAGS data with the normalised background subtracted from each 0.1s time slice, as well as 'SLOW' and 'FAST' separated components using the methods described in the text. Half-life fits are also shown for various curves and ranges. See text for full details.

6.1.3 A=140 'Xe-focused' measurement

Figure 6.4 shows the background subtracted time profile of the A=140 'Xe-focused' measurement (Figure 5.32b from Section 5.5.3). The time profile was fitted across the collection time with the spikes removed from the data, yielding a half-life value of 13.9(3) s. This is consistent with the presence of ^{140}Xe (currently accepted value 13.6(10) s). The time-difference method was applied to examine the data for constituent components, namely ^{140}I. A range of time-difference resolutions were applied and found to produce very small differences within the expected ^{140}I period (7.25 - 15.85 s). With only 29 minutes of data collected, statistics were not sufficient to confidently fit the time-profile.

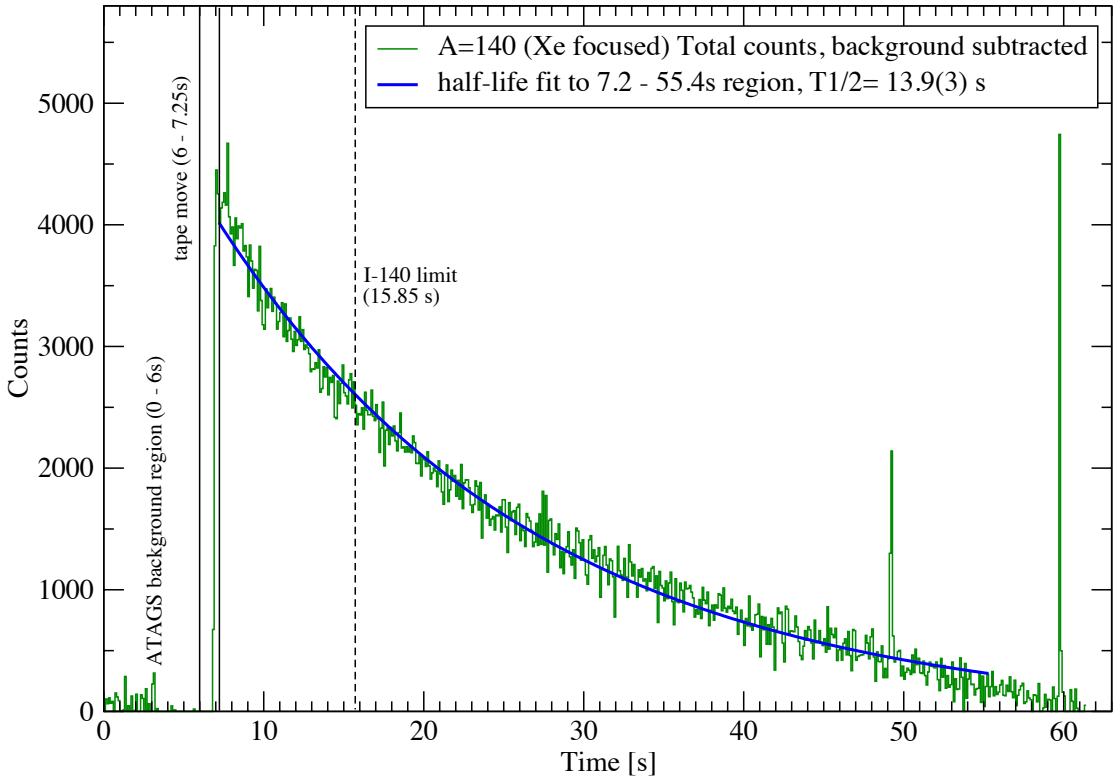

Figure 6.4: Time projection of ATAGS data for the A=140 'Xe-focused' measurement with the background removed. A fit of the time-profile, with the spikes removed, results in a value of 13.9(3) s, which is comparable to the known ^{140}Xe half-life of 13.6(6) s. The data is believed to be mostly from ^{140}Xe, as the time-difference method did not yield any significant contribution that could be associated with ^{140}I (see text for more detail).

Figure 6.5 compares two time-gate projections either side of the expected ^{140}I limit, the first is immediately after the tape move up to ten times the expected half-life of ^{140}I ((half-life period 8.6 s + tape move 7.25 s = 15.85 s), and the other is a significantly longer time period where we do not expect any ^{140}I . There is no significant difference in the general shape between these two regions suggesting there is no significant contribution from ^{140}I.

The spectral shape is dominated by a broad energy feature that extends up to 8 MeV. This is believed to be poor background-subtraction having an influence due to the limited

statistics of this data set (see also Figure 5.21). The aforementioned prominent peaks at approximately 600 keV and 1440 keV are clearly present in both time regions and are likely associated with ^{140}Xe.

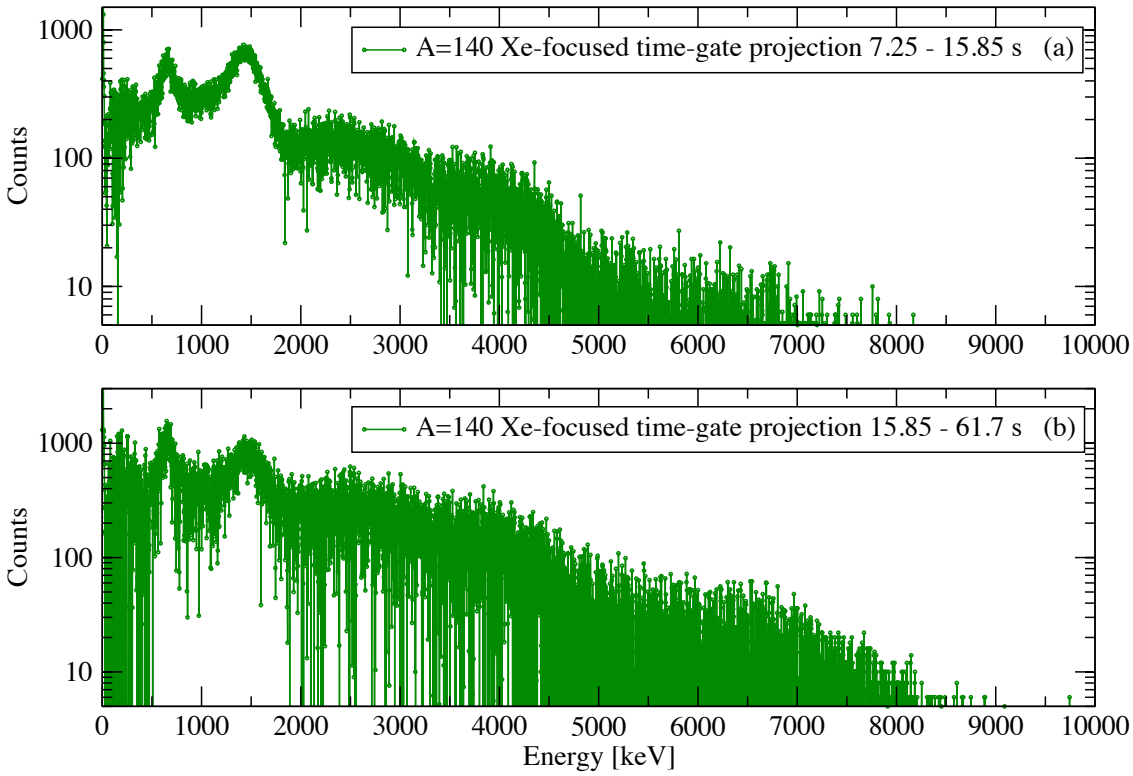

Figure 6.5: Early vs late time-gate projections of ^{140}Xe from the A=140 'Xe-focused' data. The spectra appear to be influenced by the background subtraction due to the small statistics of the sample (29 minutes).

The time-difference method was demonstrated using the better known A=141 measurement and has given some confirmation of the constituents and their half-lives for both of the lesser-known A=140 nuclei. A more rigorous separation of the A=140 'Cs-focused' data will be performed in the following section.

6.2 Time-fitting applied to the A=140 'Cs-focused' data

Separation of components from a data set is possible using the more-rigorous time-fitting method. This method starts with the assumptions that the constituents of a set of data are known, as are their half-lives. For the case of the A=140 'Cs-focused' data, we assume the data has three components: background, ^{140}Cs, and ^{140}Xe. Time-dependent functions for each of these components can be determined using the Bateman equations.
First, the background is considered to be constant in time:

$$C_{Bg}(t) = \frac{\mathrm{d}N_{Bg}(t)}{\mathrm{d}t} = constant, \tag{6.3}$$

The ^{140}Cs intensity consists of an initial component as well as growth from ^{140}Xe decay:

$$C_{Cs}(t) = \frac{\mathrm{d}N_{Cs}(t)}{\mathrm{d}t} = \lambda_{Cs} N_{Cs}(0) e^{-\lambda_{Cs} t} + \lambda_{(Cs)} \left(\frac{\lambda_{Xe}}{\lambda_{Cs} - \lambda_{Xe}} \right) N_{Xe}(0) \left(e^{-\lambda_{Xe} t} - e^{-\lambda_{Cs} t} \right), \tag{6.4}$$

Lastly, there is only an initial amount of ^{140}Xe that decays:

$$C_{Xe}(t) = \frac{\mathrm{d}N_{Xe}(t)}{\mathrm{d}t} = \lambda_{Xe} N_{Xe}(0) e^{-\lambda_{Xe} t} \tag{6.5}$$

In these equations, t is the time, λ_X is the decay constant for the nuclide X, and $N_X(t)$ is the number of atoms of nuclide X at time t. The total time profile can be fitted using the sum of Equations 6.3 through 6.5 and hence one can find values of $N_{Bg}(0)$, $N_{Xe}(0)$ and $N_{Cs}(0)$. Integrating Equations 6.3, 6.4, and 6.5 can give the expected yields as a function of time. The number of events in an experimental time gate between t_1 and t_2 can be calculated as a sum of the expected yields of the components (integrated over the same time range t_1 and t_2). We choose time gates such that: gate1 from t_1 to t_2 has only one component, gate2 from t_3 to t_4 has two components, one of which is the component in the first gate, and gate3 from t_5 to t_6 includes all three components. This enables a set of three linear equations to be formed.

$$\begin{pmatrix} \int_{t_1}^{t_2} gate1 \\ \int_{t_3}^{t_4} gate2 \\ \int_{t_5}^{t_6} gate3 \end{pmatrix} = \begin{pmatrix} c_1 & 0 & 0 \\ c_2 & c_3 & 0 \\ c_4 & c_5 & c_6 \end{pmatrix} \begin{pmatrix} \int_{t_1}^{t_2} C_{Bg}(t) \\ \int_{t_3}^{t_4} C_{Cs}(t) \\ \int_{t_5}^{t_6} C_{Xe}(t) \end{pmatrix} \tag{6.6}$$

where c_1 to c_6 are the fractions of the components within each gate evaluated by the integrals. For this case, gate1 consisted exclusively of background (t_1=0 s, t_2=30 s), gate2 was a region of ^{140}Cs with background (t_3=167.3 s, t_4=284 s), and gate3 included background, ^{140}Cs and ^{140}Xe (t_5=39.9 s, t_6=167.3 s). The decay functions (Equations 6.3, 6.4, and 6.5), are integrated across these respective time regions to determine the corresponding yields, with the half-lives of the functions fixed to the evaluated values of 63.7 s (^{140}Cs) and 13.6 s (^{140}Xe).

Figure 6.6 shows the sum of the components labelled as 'Fitted total decay curve' total fit (green), and the ^{140}Cs component. This was fitted in a region that excludes 10 half-lives of ^{140}I, but then extrapolated back across the whole time region.

The components are integrated within the appropriate time gates to get the values c_1,...,c_6 in Equation 6.6. The component matrix is then inverted to obtain the pure contributions of ^{140}Cs and ^{140}Xe as linear combinations of the experimental gates. Figure 6.7 shows the resulting separated components on linear and log scales. The ^{140}Cs spectrum has features that are consistent with the clean gate time-projection of Figure 5.30c. The ^{140}Xe result is comparable to the overall shape of the 'Xe-focused' experiment data (Fig. 6.5).

6.3 Comparison of separation methods

The time-difference method looked to provide a way of separating the ATAGS components when there is little information about the components or their half-lives. The method

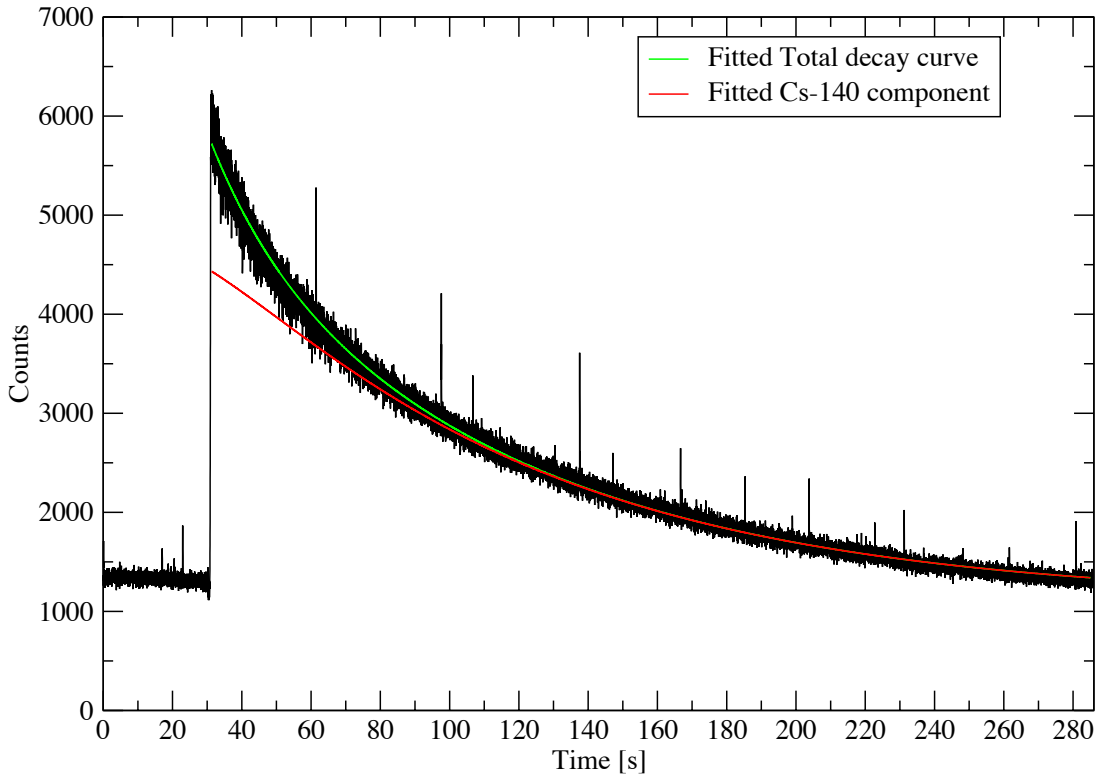

Figure 6.6: Total time-decay curve of the 'Cs-focused' A=140 data with a fit comprising background, ^{140}Xe and ^{140}Cs components, using literature half-lives.

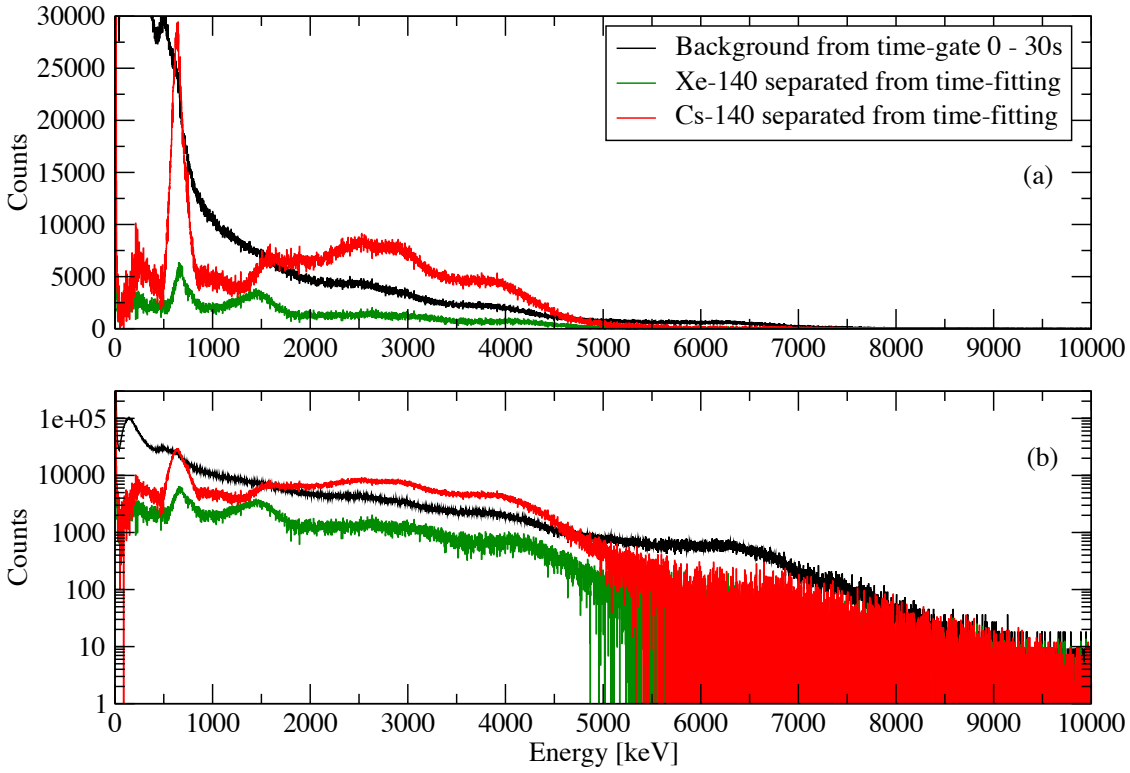

Figure 6.7: Separated components of the A=140 'Cs-focused' data using fitted time gates that should ideally give pure spectra (see text for details). Panels a) and b) are identical spectra but on linear and log scales, respectively.

involves the production of the 'FAST' and 'SLOW' decay curves to show the presence of components, which can be used to determine time gates. The method is limited by the minimum time resolution of the collected data and the success of the separation depends on the half-life differences of the components being separated. The spectra obtained using a separation based on literature half-lives and quantitative unfolding should give the truest representation of the TAGS spectra for the purposes of β-feeding analysis.

The quality of the separated spectra in Figure 6.7 are limited in terms of energy resolution, but they do provide an indication of the $Q(\beta^-)$ values and the broad features. The poor energy resolution puts a greater emphasis on the ATAGS Monte Carlo model to provide some understanding of the results and to evaluate the quality of the data. The following chapter looks at the analysis of these results using a deconvolution procedure to extract the β-feeding intensities.

Chapter 7

Deconvolution of ATAGS results

The indirect measurement of β-decay intensities of nuclides with large decay energies using conventional γ-ray spectroscopy can result in significant errors (see Section 2.2 on pandemonium). This is overcome by using TAGS measurements, however, the complicated detector responses do not provide immediate results and require significant analysis to extract the desired intensities. This chapter outlines the methods used to deconvolute the β-decay intensities.

7.1 Deconvolution Tools

The motivation of this section is to develop the tools required to deconvolve a complex ATAGS-produced spectrum to allow the extraction of the β-feeding intensities. There are two methods developed in this work to model the ATAGS decay-level response: level response building via a) a 'picket fence', and b) the GEANT4 RDM-level response.

The first method uses Monte Carlo to produce an array of mono-energetic model responses for the γ rays, referred to here as the 'picket fence'. The second method involves utilising the GEANT4 Radioactive Decay Module (RDM) to produce the complicated level response for a specific case.

The 'picket fence' provides the building blocks for generating decay-level responses via scripts external to Monte Carlo and on-demand. Once obtained, the advantage of the level building via a 'picket fence' is the iterative process can occur external to the simulation, making this method more favourable for use with fitting algorithms. The RDM-level response method in this work describes the building of decay schemes in the GEANT4 model using the Radioactive Decay Module (RDM) introduced in Section 3.1.2 to manipulate and modify the β-feeding intensities.

These modelled decay-responses are used to interpret the experimental data via unfolding, as discussed in this section. These tools were developed prior to collecting the ATAGS data at ANL and some were not fully utilised in the final deconvolution.

7.1.1 Level response building via a 'picket fence'

The building of the β-decay level response in a piece-wise-fashion, is based upon the work undertaken by the Valencia group [Tai07]. The ideal starting point for obtaining response functions would be to measure these experimentally; this is not possible with the limited availability of nuclides that produce mono-energetic responses across the desired energy range. Instead, we rely on the Monte Carlo model to produce mono-energetic responses for a range of γ-ray energies. The computing time and disk-storage requirements for generating a continuum of γ-ray responses is not feasible. In its place, we generate these

mono-energetic responses at set intervals, when placed in an array, the peaks resemble a 'picket fence'. Figure 7.1 shows an example of a 'picket fence' function for the ATAGS detector using the energy-deposited model, with a spacing of 20 keV. 'Picket fence' responses were generated for both the energy-deposited response in the NaI(Tl) and using the optical-transport modelling for an energy range of 0 to 10 MeV.

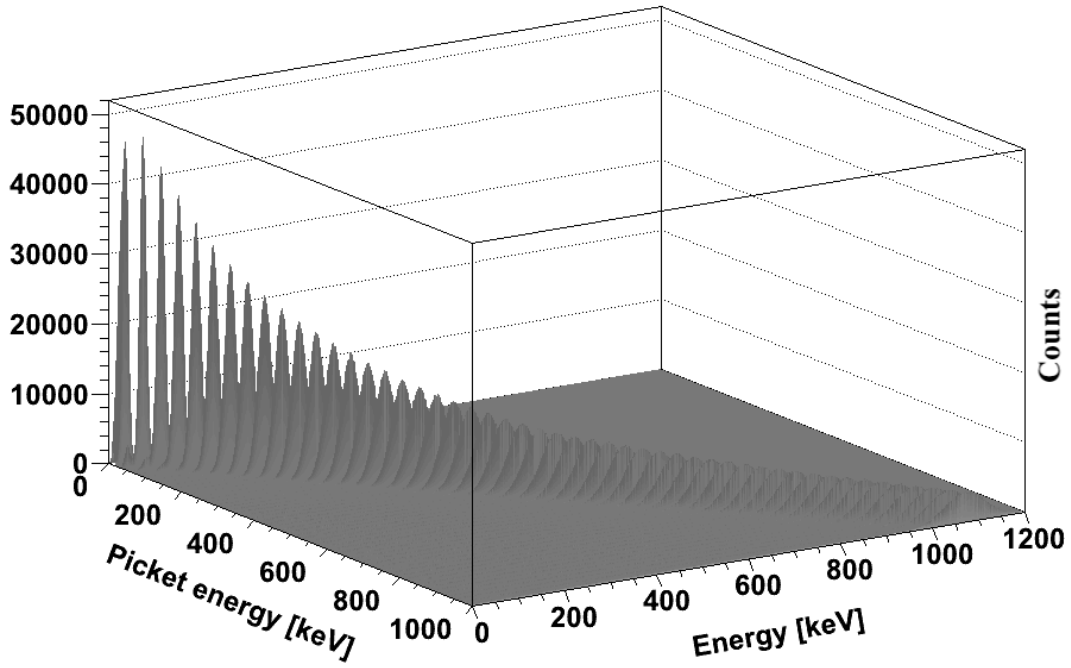

Figure 7.1: ATAGS-modelled response to mono-energetic γ rays for the energy-deposited model. The mono-energetic γ-ray source energies or 'pickets' are generated at 20 keV intervals up to 1 MeV.

The determination of intermediate energies between the 'pickets', relies upon interpolation methods. A script was written to perform the interpolation by compression or expansion of the nearest 'picket' response above or below the desired value, respectively. This approximation works for the shape and position of the FEP* peak, but there are small shifts introduced into the remaining spectral features, such as the Compton-edge or escape peaks, which are more pronounced for large 'picket' energies. To reduce the introduction of these shifts, it was found that a method to interpolate between the compression and expansion is necessary, in combination with limiting the 'picket' size to 20 keV.

The next step in building a γ-ray response is to combine the interpolated 'picket' energies using a convolution algorithm. This algorithm takes the transition intensities as inputs and uses them to combine the spectra into a single total spectrum representative of the cascade. Figure 7.2 shows an example of the cascade builder combining simulated mono-energetic γ rays for ^{60}Co: 1173 keV- intensity 0.9985, and 1332 keV - intensity 0.99826. This is compared to the γ rays from a ^{60}Co spectrum produced using the RDM in Figure 7.2b, with the residual difference shown in Figure 7.2c (Note that Figure 7.2 only includes the energy deposition in the detector from γ rays alone). The mono-energetic γ

*(FEP) Full Energy Photon

rays have light non-proportionality included (see Sect. 4.4.2). This is made apparent by comparing the peak energy of the 2506 keV mono-energetic γ-ray response to the cascade algorithm sum peak energy (Figure 7.2a).

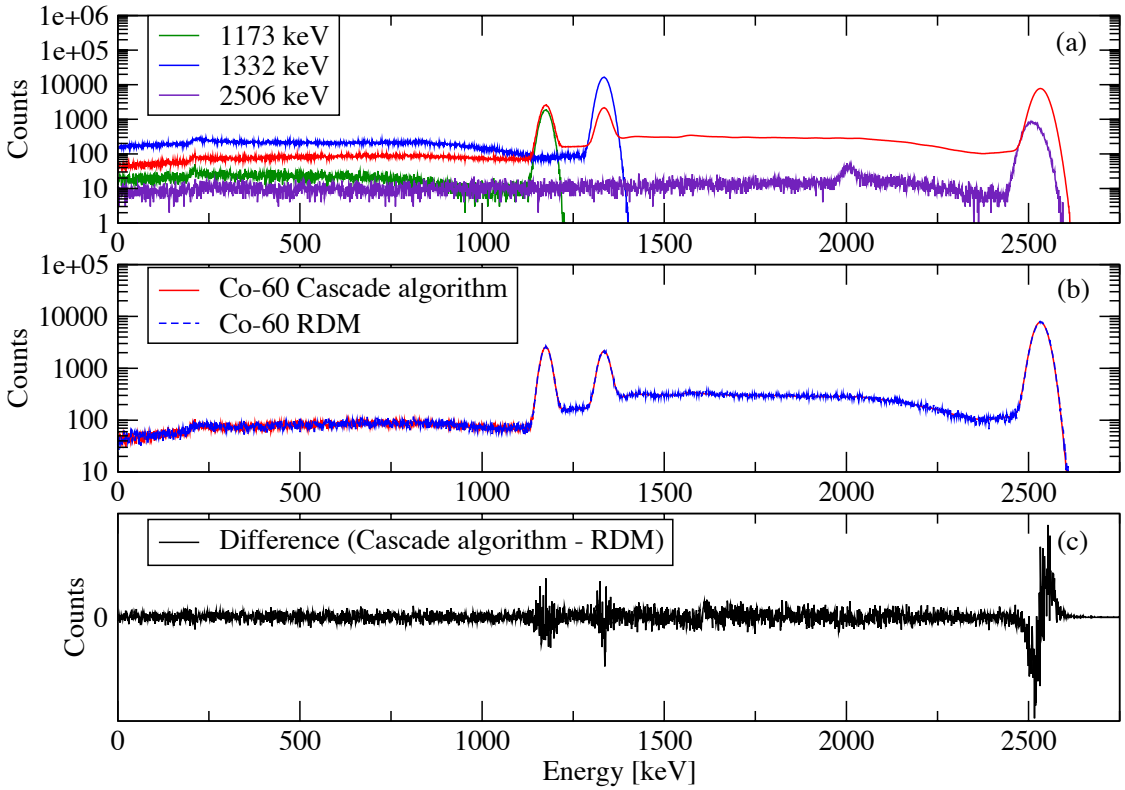

Figure 7.2: Example of the cascade algorithm using Co-60. (a) ATAGS model showing the mono-energetic γ ray component inputs compared to the cascade algorithm result, with light non-proportionality included; (b) Comparison of the cascade result with the RDM generated response; and (c) the difference between the cascade response and the RDM response.

Each of the mono-energetic γ-ray responses was generated using 1x10^6 events, the inherited efficiency of each individual response is based upon this being consistent for all of the combined components. The cascade algorithm was written as a callable function that can be used in an iterative way to produce the level response from the individual components, including the β contributions. When combined with the interpolation method and the 'picket fence' data set, these algorithms make it possible to produce an ATAGS response to a particular energy level - upon demand.

7.1.2 GEANT4 RDM-level response

The Radioactive Decay Module (RDM) introduced in Section 3.1.2, can be used to model the ATAGS response to individual β-decay levels of a nuclide as an alternative to the level response building via a 'picket fence'. The RDM module utilises data files containing decay data that are extracted from the ENSDF[†] database at the time of creating the GEANT4 version. The RDM module generates the relevant energies and intensities of particles associated with the simulated source at a location in the geometry when running

[†]Evaluated Nuclear Structure Data File [ens]

the model. This automatically generates the complex cascade responses within the results. The method can be used in two ways: a) the responses can be generated for the combined decay scheme involving all desired β-feeding intensities; or b) the individual feeding intensity responses can be extracted and used to fit the experiment in terms of β-feeding intensities - external to GEANT4.

In method (a), the RDM data files can be modified to create the combined response for direct comparison with the experiment, but this requires the model to be re-run for every modification. This approach has the disadvantage of extensive computation time required for each small iterative change, but it can be useful for when comparing experiment to known β-feeding intensities.

As an alternative, the RDM data files can be modified allowing the individual decay-level responses to be generated one-by-one. This method (b) allows one to recombine the levels and hence observe the contributions to the overall summed response through varying the relative contributions. The starting point for this method requires a fairly good knowledge of the β levels and the γ-ray transitions from these levels. Figure 7.3 shows an example of the RDM-produced levels for the non-energy broadened data of ^{60}Co, each level with 1x10^6 events. The disadvantage of the method is the requirement to run the simulations for each level before analysis, and assumes prior knowledge of said levels. If, for example, the analysis identifies a missing feeding level, this would require additional simulations to be undertaken prior to analysis. On the other hand, this method has advantages if all of the levels are known and the user only wants to fit or modify existing level intensities.

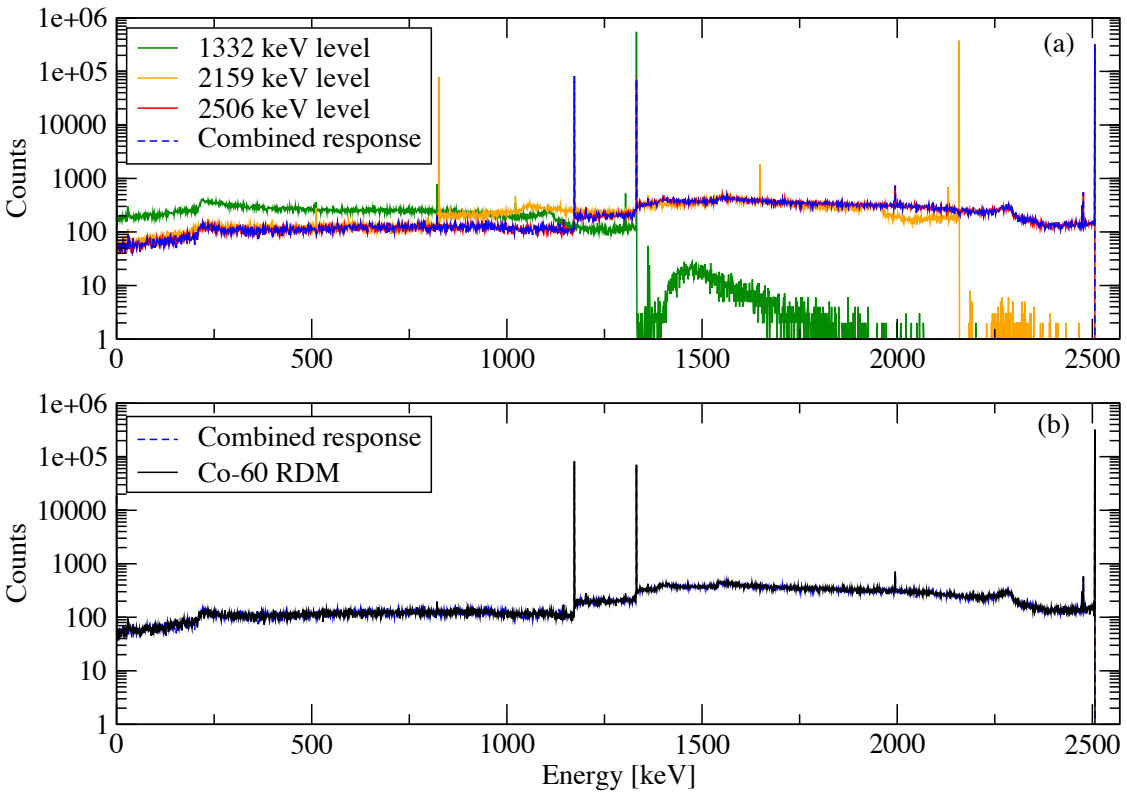

Figure 7.3: (a) RDM generated decay levels (non-energy broadened) for Co-60 individual decay-level responses and the combined result. In (b), the combined result is compared to the RDM produced response.

7.2 Unfolding results

The broad energy resolution of ATAGS produced data will limit the ability to apply the unfolding algorithm methods, particularly the automated level response building via a 'picket fence' (Section 7.1.1). Instead, GEANT4 RDM-level response method (Section 7.1.2) will be used in a limited capacity to unfold the separated ^{141}Cs, ^{140}Cs and ^{140}Xe results of Section 7.1.

7.2.1 ^{141}Cs

The individual RDM produced levels of ^{141}Cs are combined using the evaluated β-feeding intensities from ENSDF. Figure 7.4a shows the model results of the combined levels before and after the resolution broadening has been applied, using resolution coefficients of F_1=6.0 and F_0=1.0. The currently accepted β-feeding intensities from ENSDF for ^{141}Cs are used.

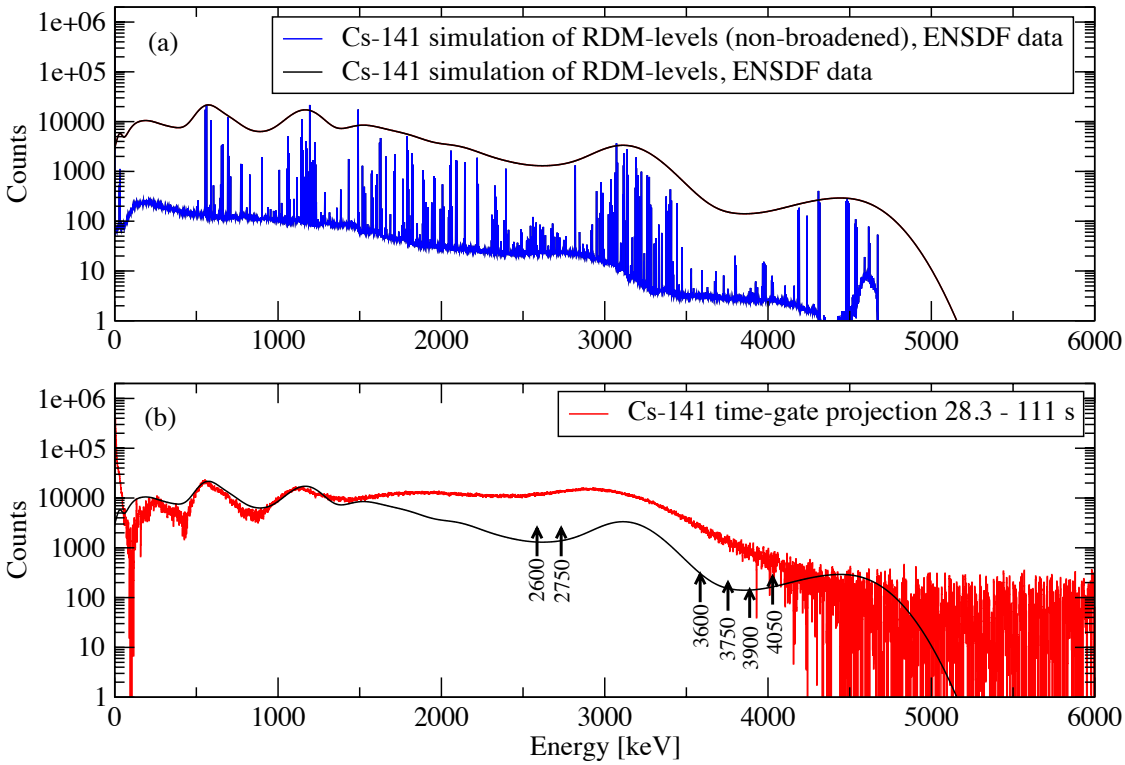

Figure 7.4: RDM-levels produced β-feeding intensity fit of ^{141}Cs. Panel (a) shows the combined response before and after resolution broadening, while (b) compares the Monte Carlo modelled response with experiment (Figure 5.25c). Greenwood *et al.* [Gre97] suggested the addition of pseudo levels to resolve the discrepancy. Arrows show the suggested levels added in keV.

This modelled response is normalised to the data and compared to the ^{141}Cs clean gate measurement in Figure 7.4b. There are discrepancies in the data in the form of missing levels. This was addressed by Greenwood and Helmer *et al.* in their work by the addition of pseudo levels at energies 2600 keV, 2750 keV, 3600 keV, 3750 keV, 3900 keV and 4050 keV, as indicated by the arrows in Figure 7.4b [Gre97]. Figure 7.5 is the ^{141}Cs data measured by Greenwood *et al.* in 1997, reproduced here to show the comparison of

energy resolution. The data collected in this work (Figure 7.4b) agrees with the overall trends in their measured spectrum (Figure 7.5).

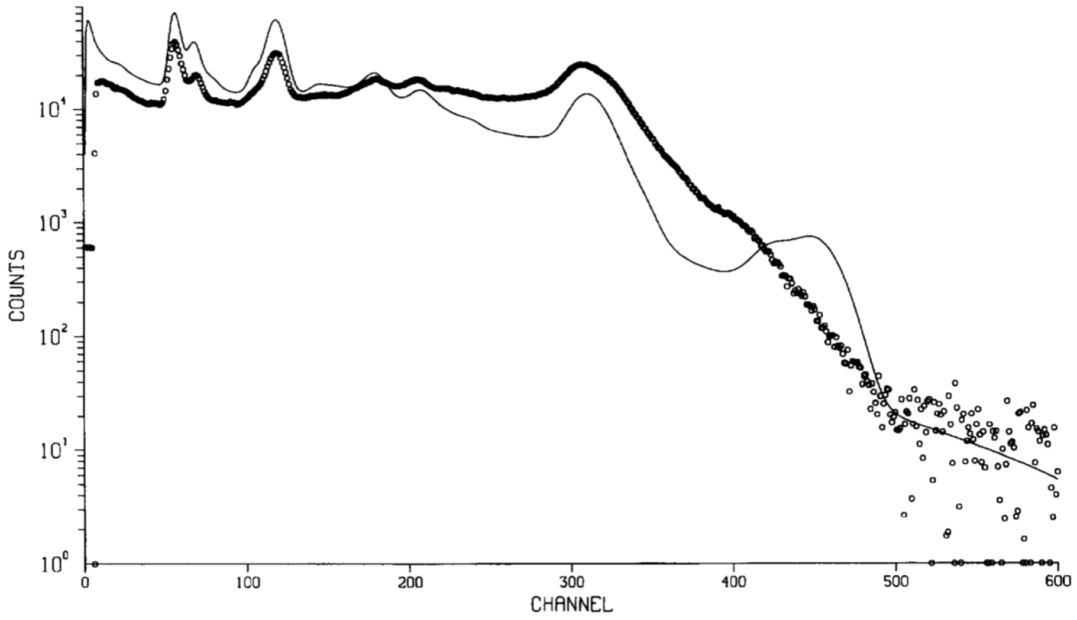

Figure 7.5: Reproduction of Figure 16 of Greenwood [Gre97] measuring ^{141}Cs using ATAGS in 1997 - experiment (points) compared to their simulated fit (line). This data, measured using ATAGS at INEL, has superior energy resolution to measurements using ATAGS in this thesis (see Figure 5.26)

No further analysis was undertaken on ^{141}Cs as we would follow a methodology similar to Greenwood and Helmer *et al.* The data collected in this work have worse energy resolution, limiting our ability to achieve anything beyond what has already been achieved or known. The data sets that have potential for new experimental information are therefore ^{140}Cs and ^{140}Xe. These will be fitted in the following sections.

7.2.2 ^{140}Cs

The currently accepted β-decay intensities for ^{140}Cs were modelled using the RDM-level response with the appropriate intensities applied. The resultant spectrum is normalised and compared to the time-separated ^{140}Cs data of Figure 6.7, as shown in Figure 7.6. The overall fit is essentially good, reproducing many of the low energy features in the spectrum. The experimental data in this thesis has been shown to be in agreement with the experimental results from the INEL group in Section 5.5.2 (see Figure 5.31). The fit using ENSDF data however, shows a discrepancy above 5 MeV with a shoulder that is not observed in the experimental data (Figure 7.6).

Figure 7.7 shows a ^{140}Cs measurement from the INEL group in 1997 reproduced from Figure 15 of Greenwood [Gre97]. The figure shows a discrepancy between the experimental data (points) and a simulated fit (line) that uses the evaluated data from 1994, as indicated by the blue box. Figure 7.6 shows this same trend. The previous and current evaluated data [Nic07, Nic18] references two publications for the source of these feeding intensities above 5 MeV, namely Robinson *et al.* [Rob86] and Greenwood *et al.* [Gre97]. Robinson *et al.* perform an analysis based upon high-spin γ-ray spectroscopy but only

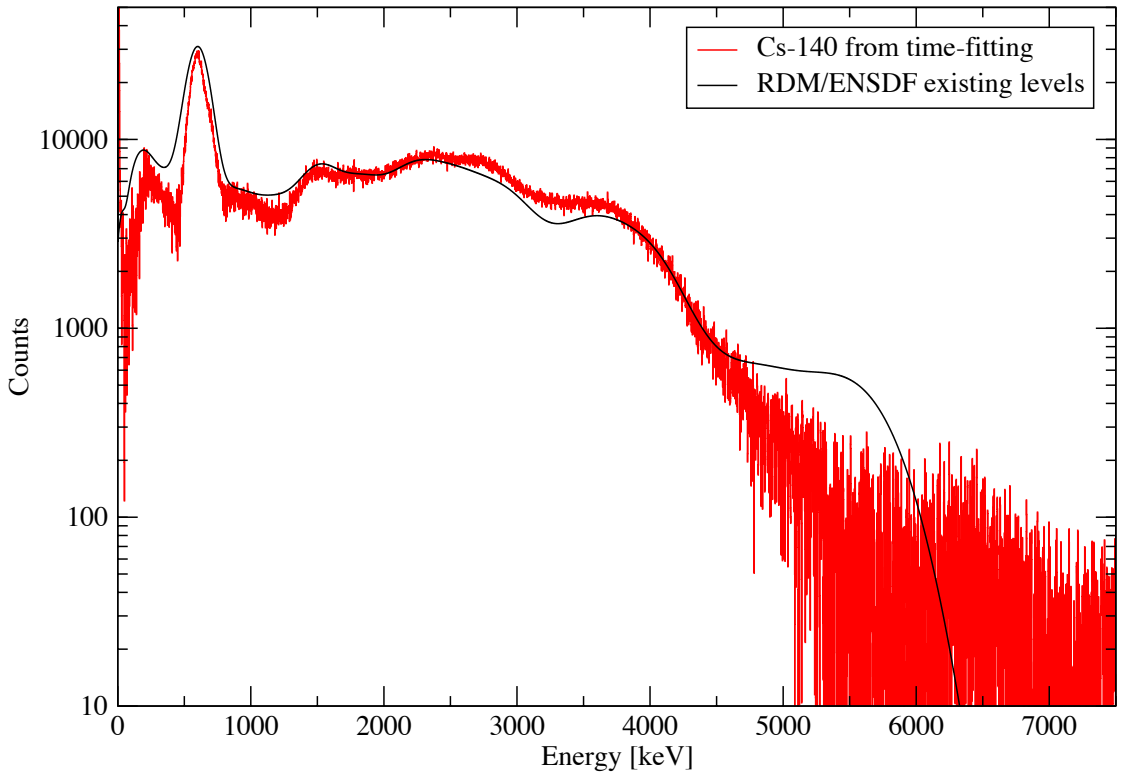

Figure 7.6: Separated ^{140}Cs from the A=140 'Cs-focused' data (Fig.6.7) compared to an RDM-produced fit using the evaluated β-feeding data.

tentatively assign levels above 4.5 MeV. The pseudo levels suggested by Greenwood have been adopted in this region, with energies up to and including 5.388 MeV. Robinson tentatively suggested energies beyond this value, up to the highest energy of 5.765 MeV. The current evaluation [Nic18] includes these higher energy levels in the decay scheme, noting that they are questionable; our data agrees with Greenwood and suggests that these levels are not fed in the beta-decay.

As an approximate fit of the present experimental data, the questionable levels above 5 MeV were removed from the simulation at energies below a cut-off value and re-fitted (Figure 7.8b). These adjusted fits are in better agreement with this data. In the absence of a better energy resolution, we cannot provide any certainty on the levels that should be included or excluded around this nominal 5 MeV. Nevertheless, what is certain, is that the evaluated β-feeding intensities extend too high beyond this 5 MeV value.

7.2.3 ^{140}Xe

The separated ^{140}Xe results were fitting in the same way as the previous sections. Figure 7.9 shows the comparison of the RDM fit with two experimental ^{140}Xe data sets, the 'Xe-focused' measurement (Fig. 7.9a) and the separated ^{140}Xe from the time-fitting of the 'Cs-focused' data (Fig. 7.9b). The highest energy level in the ENSDF data is currently 2324.31 keV although the Q(β^-) value is 4064(9) keV. No clear conclusion can be drawn about potentially missed feeding intensities as the experimental data does not demonstrate consistency with regard to the end-points. Using the 1427 keV peak as a guide for the normalisation factor results in the peak at 653 keV being underestimated by the fit in all

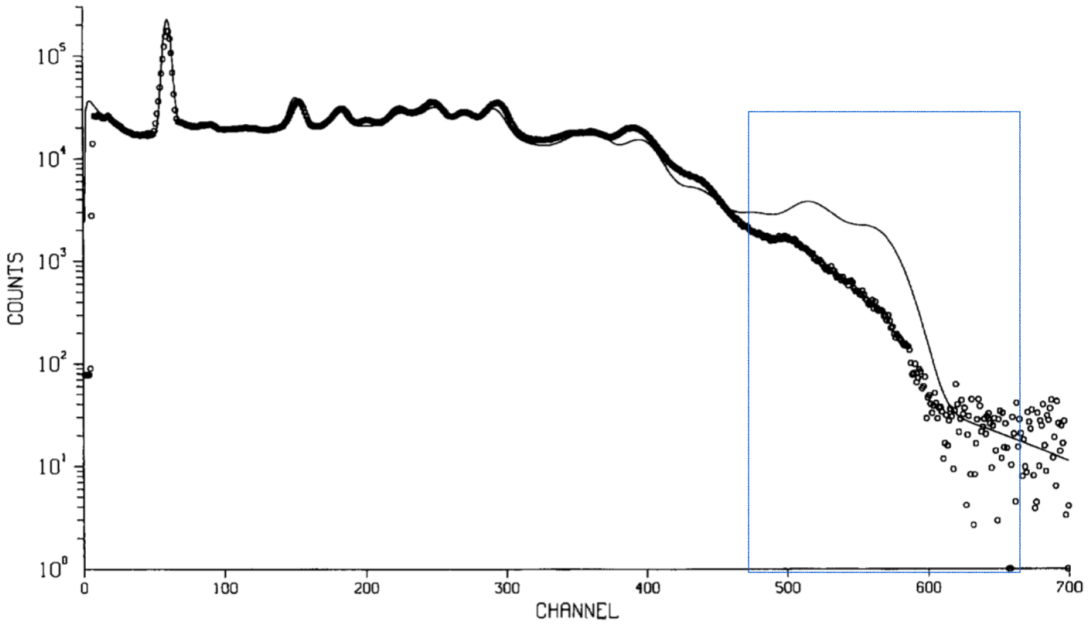

Figure 7.7: Measurements of ^{140}Cs, reproduced from Figure 15 of Greenwood using ATAGS in 1997 [Gre97] showing experiment (points) and a fit using the evaluated data of 1994. The blue box indicates a discrepant region between the experiment and a fit above 5 MeV.

cases. With the limited energy resolution it is difficult to tell if the peak in this region has any contribution from the 602 keV peak of ^{140}Cs, or if there is a background slope causing this trend.

Despite this discrepancy, it is clear there is substantial β-feeding to levels above those in the currently accepted evaluation. With the poor energy resolution, no attempt to infer these feeding intensities is made in the present work, however, it is clear that future work is needed to resolve this issue.

7.3 Discussion

ATAGS was used to measure CARIBU beams of ^{141}Cs, ^{140}Cs and ^{140}Xe. Two methods were developed for the deconvolution of TAGS data leading up to the measurements, although the application of these methods was limited. The results of ^{141}Cs and ^{140}Cs published from the INEL work of Greenwood and Helmer show a superior energy resolution. Although the present results are limited by the energy resolution, there are discrepancies between all of these measurements and the evaluated data at this time.

The measurement of ^{141}Cs shows agreement with the published data and cannot add anything beyond what has already been achieved by INEL. The currently evaluated data for ^{141}Cs (ENSDF) make a mention of the Greenwood β^- feeding intensities, but these have not been accepted. In addition, the evaluator notes the absences of the pseudo levels, specifically 2525 (Iβ=0.48%), 2600 (Iβ=0.71%), 2750 (Iβ=1.90%), 3600 (Iβ=2.32%), 3750 (Iβ=1.19%), 3900 (Iβ=0.54%), 4050 (Iβ=0.71%), 4800 (Iβ=0.013%), and 4950 (Iβ=0.002%).

In the case of ^{140}Cs, this work agrees with the measured spectral shape of the INEL group. The current evaluated levels above 5 MeV for ^{140}Cs, when fitted, do not show

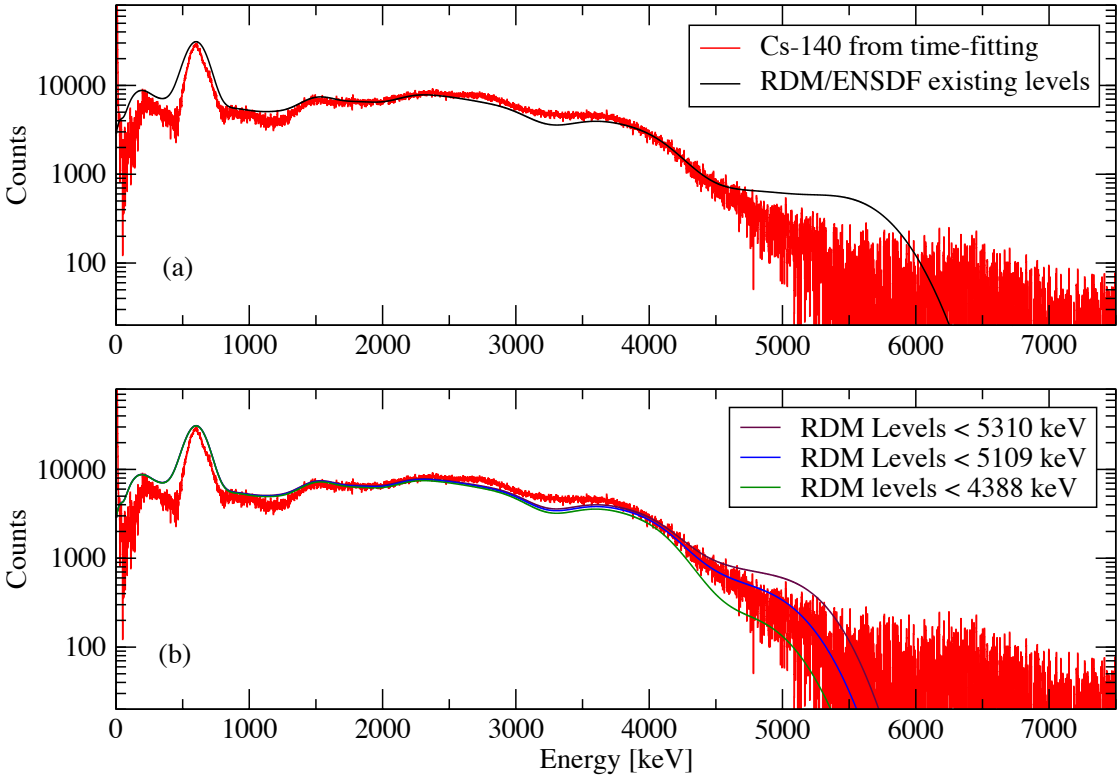

Figure 7.8: The ^{140}Cs experimental spectrum separated using the time-fitting method is compared to RDM level fits of (a) the evaluated ENSDF data, and (b) the evaluated ENSDF data with levels removed above 4388 keV, 5109 keV and 5310 keV. The RDM fit that is shown in (a) produces a shoulder above 5 MeV that is not seen in the measurement. When levels are removed from the RDM fit in (b) there is better agreement.

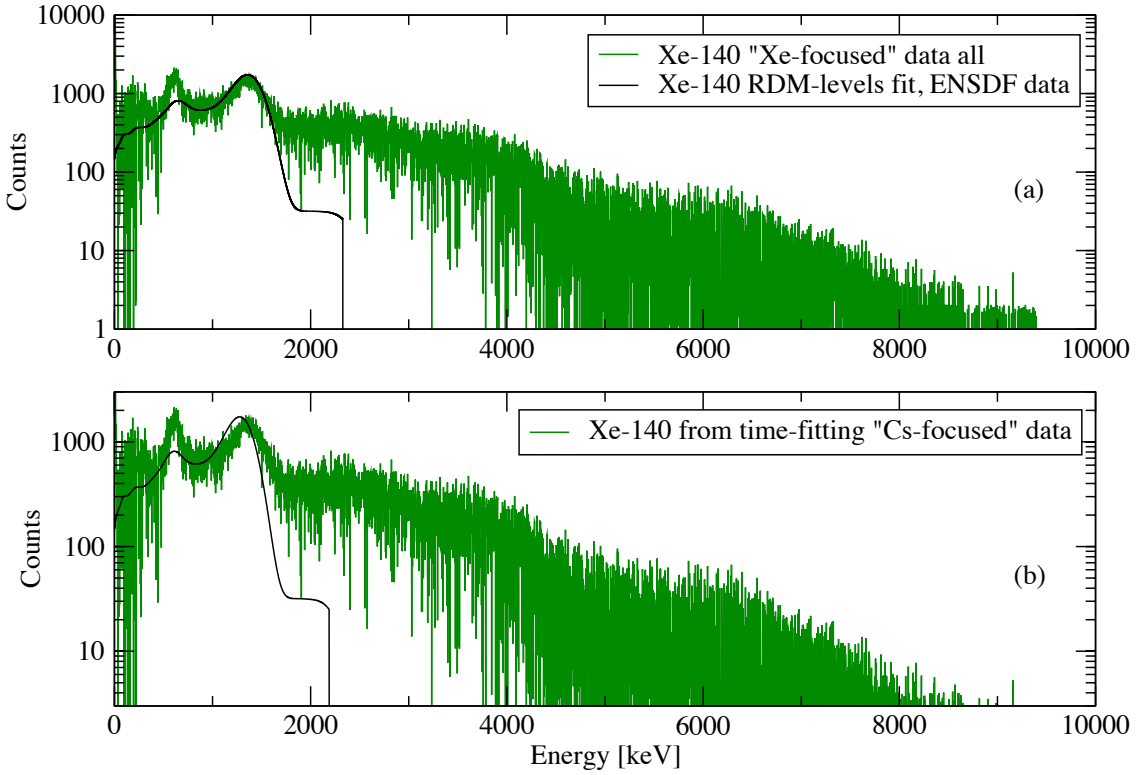

Figure 7.9: Separated ^{140}Xe compared to the RDM-levels fit using β-feeding intensity data from ENSDF. The results are from (a) The 'Xe-focused' data (Fig. 5.34a), and (b) ^{140}Xe from the time-fitting method of the 'Cs-focused' data (Fig. 6.7). Both experimental data sets are fitted with the same RDM fit with only the normalisation value varying.

agreement with the data. The present results are the first recorded ^{140}Xe TAGS spectrum and shows disagreement with the currently evaluated data. The discrepancies show a need to re-measure the β^- feeding intensities of ^{141}Cs, ^{140}Cs and ^{140}Xe via a TAGS method, to rectify these inconsistencies.

Chapter 8

Measurements with XSAT at CARIBU

This chapter presents the validation of the Geant4 XArray and SATURN (XSAT) models that were introduced in Section 3.3, both of which were developed as part of this thesis. Both models are then applied to various aspects of three XSAT experiments undertaken at CARIBU, with the aim of contributing to the understanding and interpretation of the measured data. The objectives for this work are to (1) build the SATURN and XArray models, (2) to compare these models against calibration measurements, and (3) make any adjustments necessary to reproduce the experimental calibration results. The model is then used to provide information about the specific experiments that cannot be measured or obtained experimentally.

Three experiments were undertaken by collaborators in 2015 using the XArray in combination with SATURN coupled to the low-energy beam-line of CARIBU. The first experiment was the measurement of ^{134m}Sb and ^{134}Sb, with the aim to directly measure the half-lives and fission yield ratio of these nuclei. The second measurement was a detailed study of the β decay of ^{92}Rb, to determine deficiencies of the decay scheme. The final experiment was directed toward the measurement of the nuclear structure of ^{104,106}Mo.

8.1 Experimental motivations

8.1.1 ^{134}Sb and ^{134m}Sb

The high- to low-spin yield ratio for an isotope provides information about the spin of the initial fission fragment that was generated in the fission process. These yield ratios are difficult to access because of the radio-chemistry required to produce these isomers and the limited time to measure them in any significant quantity. The isomeric yield ratio of ^{134}Sb and ^{134m}Sb measured in this work would also be useful for decay heat and antineutrino calculations. The ratio for this particular isotope has not been measured directly. Previously the yield of these short-lived nuclides was deduced by measuring their progeny, ^{134}Te and ^{134}I, and working backwards. Significant assumptions on the half-lives and specific details of the experiment were relied upon with this method [Fog90].

The low-energy beam-line of CARIBU provides an opportunity to access the mass-separated Sb nuclide with a higher intensity than previously possible. Figure 8.1 shows a schematic of the decay sequence for the A=134 chain around ^{134}Sb, including the measured or calculated intensities from CARIBU's isobar separator when optimised to select the mass-over-charge ratio for that particular isomer/isotope [Sav05, ANLb]. Unlike the

previous measurements with CARIBU, the MR-TOF* was used in these measurements, providing additional mass resolution and improved isobaric beam purity.

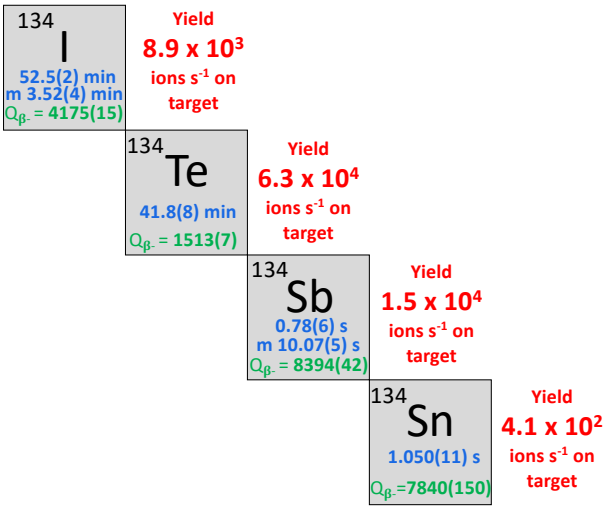

Figure 8.1: Schematic of the decay sequence of the A=134 chain. The nominal intensities from CARIBU's isobar separator are shown for each nuclide [Sav05, ANLb]. Note that both ^{134}I and ^{134}Sb have β-decaying metastable states. The listed Q_β values are for the ground states.

Measurement of the β-particle and γ-ray transitions using the XArray combined with SATURN provides a more complete picture of the level transitions and half-lives, for both the ground state and the isomer of ^{134}Sb. The tape station can provide clean removal of the progeny ^{134}Te and ^{134}I, that have half lives of 41.8(8) minutes, and 52.5(2) minutes, respectively (see Figure 8.1).

Measurement of the isomeric yield ratio requires knowledge of the half-lives of ^{134m}Sb and ^{134}Sb, the timing characteristics of CARIBU to deduce the transit time from source to detector, and the relative efficiency response of the β detector being used. The use of the XSAT Monte Carlo model to calculate the SATURN efficiency for the detection of β-particle decays of ^{134m}Sb and ^{134}Sb, is the subject of this work and represents the authors contribution to the larger project.

For the case of ^{134m}Sb, the half-life was obtained from a measurement utilising both SATURN and the XArray to observe the corresponding β and γ-ray transitions from each component for a period of time after implantation. The half-life of ^{134}Sb was determined from the time-dependence of the β-decay measured in SATURN alone. The efficiency of the SATURN detector is difficult to obtain directly as it would require β sources with similar Q values as the nuclides of interest. Another factor to consider is the sensitivity of the plastic detector to γ rays. The model of SATURN is utilised here to determine these relative efficiencies that are then used as a correction to the experimental results.

The Sb measurements included β-delayed γ-ray transitions that were detected using the XArray. The MC model of the XArray was utilised in coincidence with the SATURN model, replicating the experimental setup. This provides a convenient way to compare the relative β-particle to γ-ray response over a wide-range of energies.

*MR-TOF- Multi-Reflection Time of Flight isobar separator (see Section 1.2.2)

8.1.2 ^{92}Rb

The measurement of ^{92}Rb is relevant due to its contribution to decay heat and as a significant contributor to the 'reactor antineutrino anomaly' [Hay15]. Fission reactors produce a significant flux of antineutrinos that accompany β^- decay from fission products. Large reactor neutrino experiments, such as Daya Bay [An16], Double Chooze [Abe12] and RENO [Ahn12], have been implemented to detect the antineutrino spectrum produced from fission. The expected antineutrino spectrum can be calculated using nuclear data. The anomaly arises when antineutrino models are compared with results from these reactor experiments, producing a discrepancy for energies of 5 - 7 MeV, in the form of a shoulder or 'bump' [Hay15]. It is known that ^{92}Rb contributes up to 16% of the antineutrino energy spectrum in Pressurised Water Reactors (PWRs) in this bump region [Fal17]. Improved knowledge of the nuclear data from ^{92}Rb will contribute to both decay heat calculations and to understanding the reactor antineutrino anomaly.

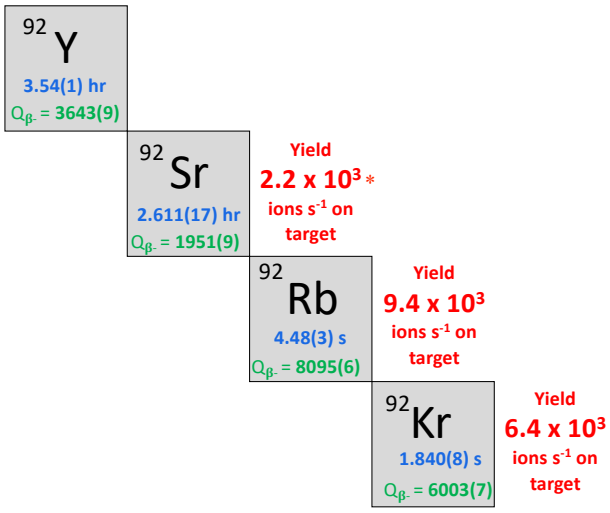

Figure 8.2: Schematic of the decay sequence of the A=92 chain. The measured or calculated(*) intensities from CARIBU's isobar separator are shown for each nuclide [Sav05, ANLb].

Figure 8.2 shows a schematic of the decay sequence for the A=92 chain including the CARIBU measured or calculated yields when the isobar separator is optimised for that nuclide (data taken from Savard [Sav05, ANLb]). ^{92}Rb has a large Q value of 8095 keV and is known to suffer from pandemonium (see Section 2.2). TAGS measurements were performed on ^{92}Rb using DTAS in 2014 at the University of Jyväskylä [Fal17]. This complicated case does not contain many γ-ray transitions and relies more heavily on the model of β^- efficiency of SATURN to interpret the experimental data.

8.1.3 ^{104,106}Mo

Another application of the XSAT model is the investigation of the β-decay properties of the neutron-rich niobium isotopes, ^{104}Nb and ^{106}Nb [Mit]. In these measurements, mass-separated beams of the nuclides were delivered to the X-Array/SATURN decay spectroscopy station for study. Obtaining accurate relative γ-decay branching ratios relies on a combination of β-γ and γ-γ coincidence measurements. However, in the existing analysis,

assumptions are made concerning the performance and efficiency of the plastic scintillator detector. The MC model will allow the performance to be tested and better understood. One particular concern surrounds the interaction of γ rays and the plastic, potentially producing false β-γ coincidence events. The ^{104}Nb case is particularly complex, since there is a long-lived β-decaying isomer, as well as the ground-state β decay to consider. Unravelling the γ decays from the isomer and the ground state is complex, and the MC model developed in this thesis work will aid this process.

These results will also serve to inform an additional experiment involving the Coulomb excitation of ^{104,106}Mo that was performed at ANL with re-accelerated CARIBU beams delivered to the GRETINA gamma-ray tracking array. The aim of this data is to accurately measure the lifetimes of excited states in ^{104,106}Mo, determine B(E2) values and learn about the nuclear shape phase transition that occurs between N=58 and N=60 around A=100. Some branching ratios were measured by implanting radioactive Nb nuclei, but these measurements suffered from the same deconvolution of ground-state and isomer issues described above.

8.2 Experimental setup

The SATURN detector and tape station was used in combination with the XArray as shown in Figure 8.3. SATURN has two versions of the plastic scintillator design, one consisting of segmented plastic paddles to provide some spatial information, and the other is a solid cylinder with a small hole bored at one end (see Section 2.4.2). The latter was utilised for the present experiments.

Figure 8.3a shows the experimental arrangement for the β detector attached to the low-energy beam-line of CARIBU. The tape-station storage box and drives are located below the beamline in close proximity to the implantation position in a compact setup. Figure 8.3b is a simplified schematic showing the tape feed direction with the inset giving more detail of the SATURN detector (top hat). The radioactive ions from CARIBU enter the back of the detector via a circular horizontal bore housing a brass collimator and are implanted on a movable tape (inset of Figure 8.3b). The tape system of SATURN allows the timed removal of longer-lived radioactive ions from the detector, giving some temporal separation ability. The aluminium vacuum chamber of the β detector is affixed to the low energy beamline and makes up part of the overall vacuum system.

The XArray detectors are attached to a support frame that is on castors allowing the movement of the entire array as a trolley (see Fig 2.5). The individual clovers A to D lie in the vertical plane with pairs A-B (Left-Right) and C-D (top-Bottom) facing inward toward each other forming a box-like geometry around the implantation point (as shown in Figure 2.5b). Each detector can be independently adjusted in position toward or away from the centre. The Super clover is upstream and perpendicular to the other detectors and can also be adjusted along its axis toward the center of the array. The detector positions were arranged facing each other so that they enclose the source position and plastic detector, but can be retracted for easy access. For this experiment, the XArray was first rolled in and positioned so that the source implantation position of SATURN was aligned with the centre of the clover A to D plane. The position of the trolley with reference to the A to D plane along the beam line will be referred to as the trolley position. The clovers are then individually adjusted along their axis to enclose the SATURN top-hat and minimise the gap between the SATURN and the XArray as shown in Figure 2.6a.

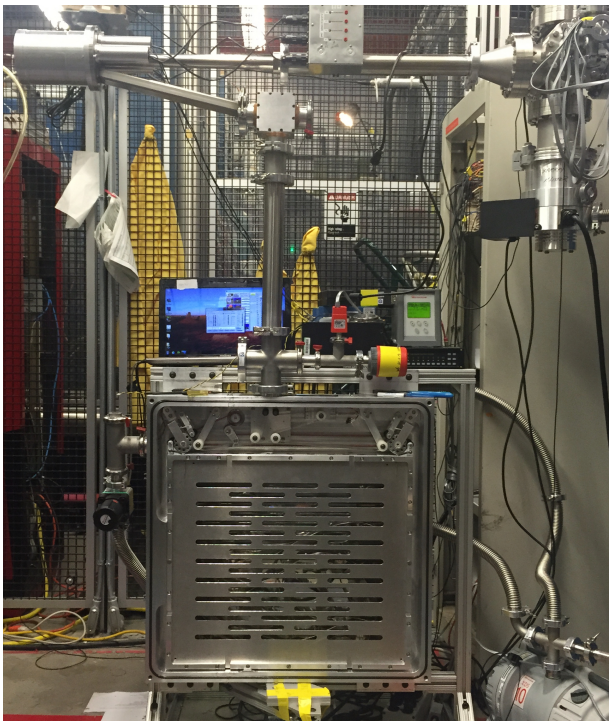

(a)

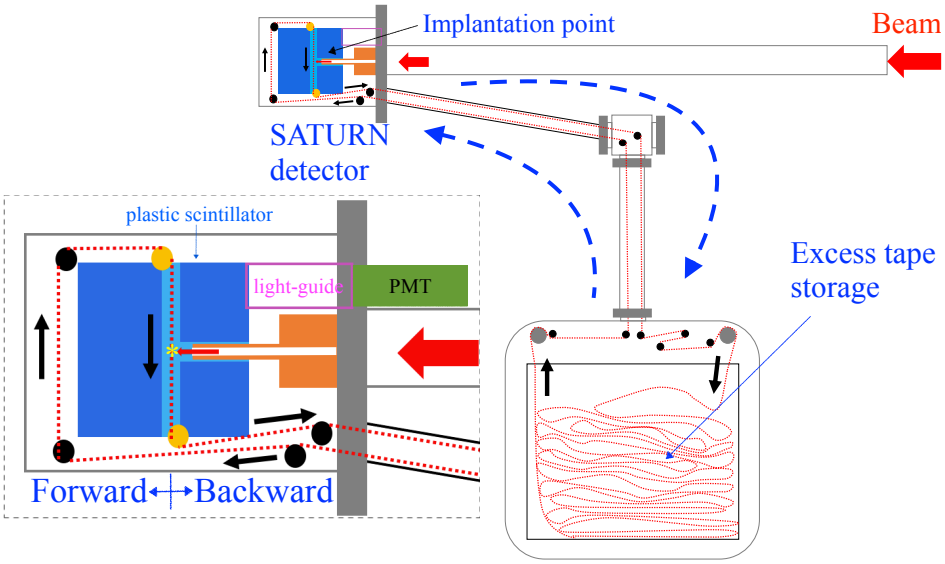

(b)

Figure 8.3: SATURN at the CARIBU beam-line setup: (a) photograph and (b) schematic including a zoomed-in focus on the top hat. The low-energy CARIBU beam enters from the right as indicated by the red arrows. Only one of the three SATURN PMTs are shown in the schematic. The XArray (not in this photo) is positioned around SATURN on the left-hand side. The location relative to CARIBU is the dotted line in Figure 1.1.

8.3 Validation of the SATURN model

The SATURN detector was designed to tag β^- particle events for use with the XArray. Since then, experiments with SATURN have gone beyond this design, with the plastic scintillator being further utilised as an energy spectrometer. The plastic scintillator has a complicated geometry due to the bores and cavities required for the tape implantation to occur in the middle of the detector. The PMTs are located at the beam end of the detector as this is the only available place given the geometry requirements of SATURN. The response in terms of detection of the generated photons is complicated by the geometry. A simple energy-deposited model approach will not portray the complex response of the photon transport inefficiencies. The optical-photon model was utilised to more accurately model the propagation and detection of the scintillator photons by the PMTs.

In order to have confidence in the models of SATURN and the XArray, they need to be validated against experiment. This is done using β^- particle and γ-ray calibration source measurements described in the following section.

8.3.1 Calibration sources

The scintillation light created within the scintillator is detected by three PMTs located on the upstream side of the detector or 'backward' direction as seen in the inset of Figure 8.3. The vertical cavity in the plastic scintillator for the tape has the unwanted effect of creating two halves of the detector with very different responses, as seen in the experiments. Scintillation light within the back-half of the plastic, 'backward' direction with regards to the beam direction, has a greater response than light directed towards the "forward" half. It was surmised that the collection of the light is split into two parts by the rectangular-shaped vertical tape well, compounded by the positioning of the PMTs only on the 'backward' side. Scintillation photons generated in the "forward" portion of the detector are more likely to be scattered and absorbed while transiting the longer and more complicated path to the PMTs.

β^- calibration sources were used to collect spectra using the plastic detector. The calibration sources available at the time of the experiment were ^{99}Tc, ^{36}Cl, and ^{90}Sr/^{90}Y. These β-particle sources were each placed on a section of mylar tape that enabled them to hang down inside the cavity at the source position inside the SATURN well for measurements. The β-particle sources differ with their design depending on the manufacturer, but, in general, they have similar components. The deposited source material is supported by a thick substrate and covered by a very thin polymer to contain the activity while minimally attenuating the emitted radiation. If the substrate is thick enough, this would limit the emission of the β-particles to an angular range of 2π. While some manufacturers intentionally produce sources on thin substrate materials to allow emission in all angles, the specific details of the substrates for each source were unknown.

^{99}Tc β-particle calibration source

Tc-99 decays via β^- emission, predominantly (99.9984(4)%) to the ground state of stable ^{99}Ru, with the remainder decaying via an excited level of ^{99}Ru [Bro17]. The half-life of ^{99}Tc is 2.111(12)x10^5 years with Q(β^-)=297.5(10) keV. The activity of the source was recorded as 0.0714 μCi on the 29^{th} of July 1970, which is equivalent to 2641 Bq at the time of measurement (22^{nd} November 2015).

^{36}Cl β-particle calibration source

Cl-36 decays to ^{36}Ar via β^- emission with Q(β^-) = 709.547(46) keV and a probability of 98.10(10)%, and to ^{36}S via electron capture with Q(ϵ) = 1142.14(14) keV and a probability of 1.90(10)%, of which 0.014(1)% decays via β^+ emission [Nic12]. The half-life of ^{36}Cl is 3.01(2)x10^5 years. The activity of the source was recorded as 0.108 μCi at 10^{th} of October 1968, which is equivalent to 3995 Bq at the time of these measurements.

^{90}Sr/^{90}Y β-particle calibration source

Sr-90 has a half-life of 28.79(6) years and decays via β^- emission to the ground state of ^{90}Y with Q(β^-) = 546.0(14) keV [Bro97]. Y-90 has a much shorter half-life of 2.6684(13) days and decays mostly to the ground state of ^{90}Zr via β^- emission (99.983(7)%), with a small branch to the 1760 keV level. The source is assumed to be in secular equilibrium, so that the Q(β^-) value of 2278.7(16) keV for ^{90}Y is the signature end-point in the β spectrum. The activity of the source was recorded as 0.1 μCi at August 2007. This was taken to be the middle of the month and extrapolates to be 3032 Bq at the time of these measurements.

8.3.2 Energy calibration

The β-particle sources were sequentially placed in the tape cavity of SATURN detector adjacent in the beam implantation position. Taking potential advantage of the assumed limited-emission geometry, data were collected with the sources facing in the 'forward' and 'backward' directions. The sources were hung from mylar tape to best replicate the conditions for the in-beam measurements. The PMT signals were recorded with and without a threshold imposed to remove the low-energy PMT dark-current noise. The threshold and non-threshold values were recorded by the DGS-DAQ. This threshold value was estimated to be set at an energy of 500 ± 200 keV [Sie18].

Figure 8.4 shows the measurement of the ^{36}Cl source placed inside the SATURN cavity in the backward-facing direction (a) without, and (b) with the energy threshold imposed. The measured background in the measurement is also shown.

Measurements for the forward- and backward-facing sources with the background subtracted, are shown in Figure 8.5. The unequal responses to the directions is more apparent in the case of ^{99}Tc, which has the lowest Q(β^-) value of 297.5(10) keV. It is apparent from the data that the forward-facing sources result in a smaller response than the backward-facing sources. This is consistent for all of the sources measured, although the magnitude of the difference varies.

The end-point value of the spectrum for the backward-facing ^{99}Tc source is at approximately channel 400 (Fig. 8.5a), which is not significantly different from the end point of the backward ^{36}Cl with Q(β^-) = 709.547(46) keV (Fig. 8.5b). This discrepancy in end-points may be due to different attenuating materials in the ^{36}Cl and ^{99}Tc sources. The true information regarding source backings is not available, but these uncertainties will have to be taken into consideration when the data is being used for the energy calibration.

The ^{90}Sr/^{90}Y source (Figure 8.5c) shows a more complicated structure with an apparent shoulder feature at approximately channel 400 and 900. The end-points for the backward- and forward-facing cases converge to the same value. The general features of these detector responses need to be understood before we can effectively apply and use an energy calibration.

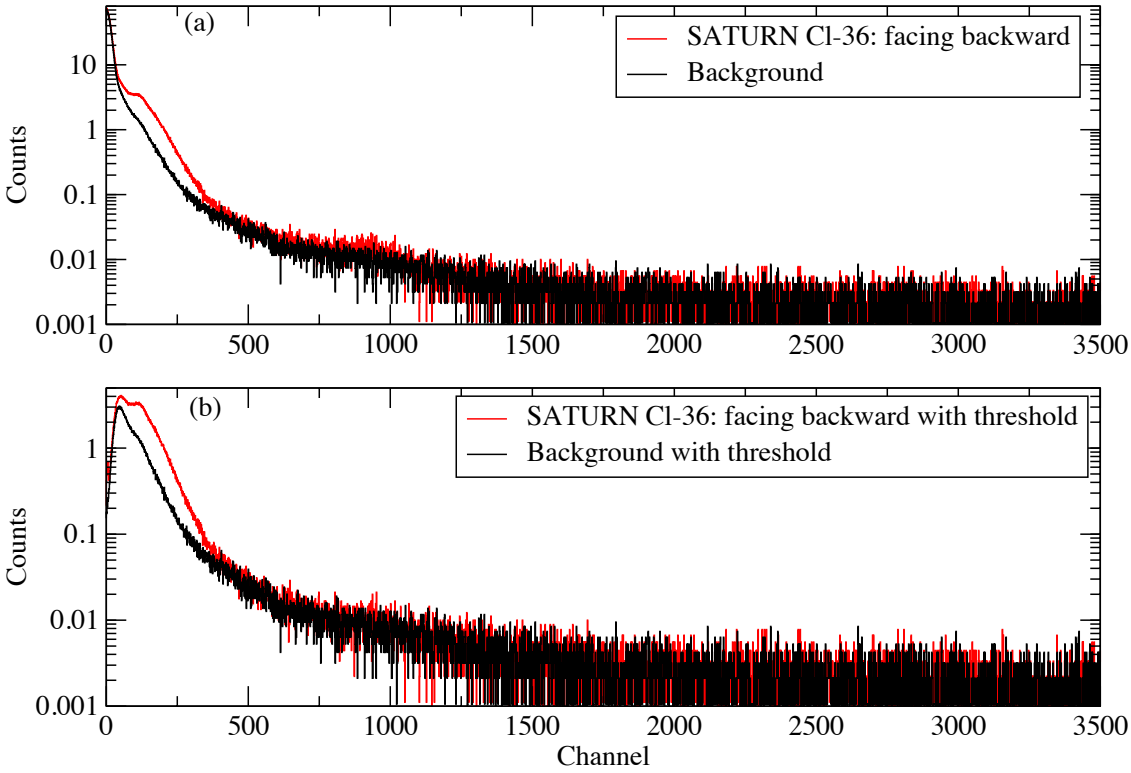

Figure 8.4: Cl-36 calibration source measured using SATURN and compared to the measured background. These spectra are shown for (a) no threshold applied, and (b) with an energy threshold applied.

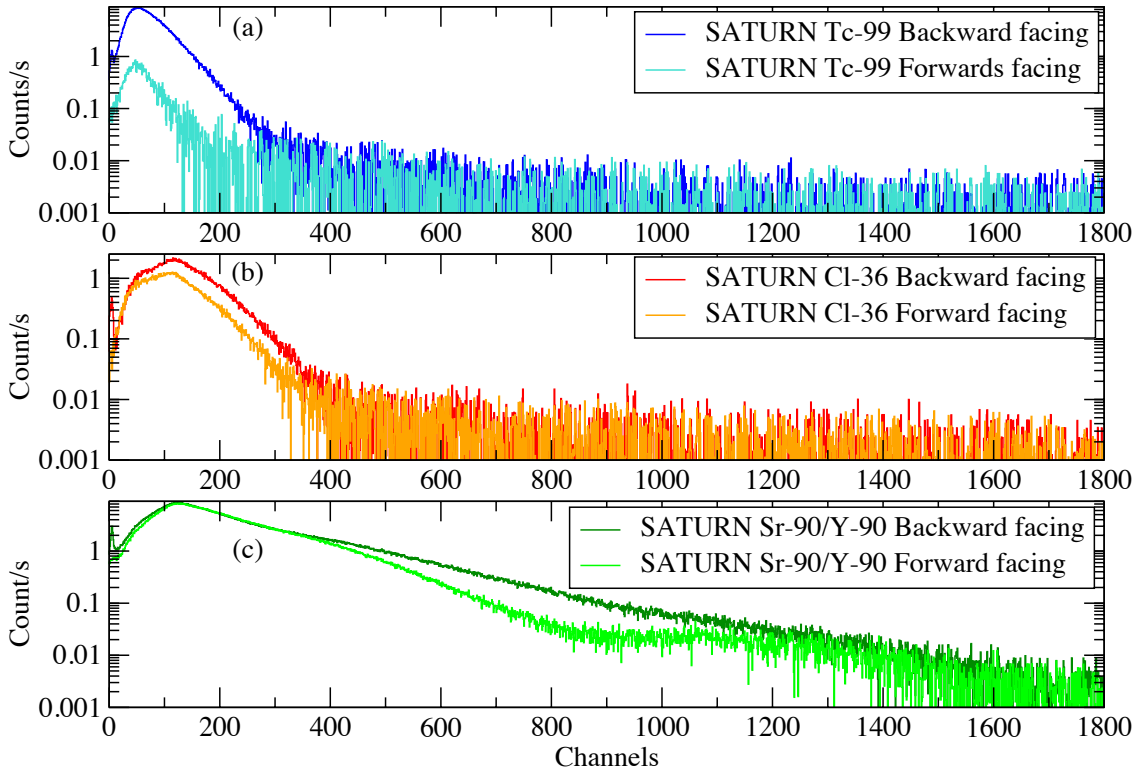

Figure 8.5: SATURN-measured β^- particle calibration sources comparing backward- to forward-facing directions for (a) ^{99}Tc, (b) ^{36}Cl and (c) ^{90}Sr/^{90}Y.

Optical photons are required to model the complicated response of the detector caused by the obstruction of the tape well in the plastic scintillator. The effect of the well can be seen using the SATURN model with optical photons. Figure 8.6a shows the schematic of SATURN's plastic scintillator, approximately divided into two halves by the tape cavity (light-blue). Optical photons are rendered in green to show the paths taken whilst undergoing reflections within the scintillator; this is viewed from above the scintillator looking through the tape cavity (Figure 8.6b to d). Figure 8.6b is the simulation of a single ^{36}Cl beta decay, located at the source position in the tape cavity (yellow asterisk in Fig. 8.6a). The optical photons from this single particle can be seen to transit the entire scintillator volume including the three PMT light guides. The effect of the cavity as a barrier between the respective halves is shown by placing a single photon in each half of the detector (Figs. 8.6c and d).

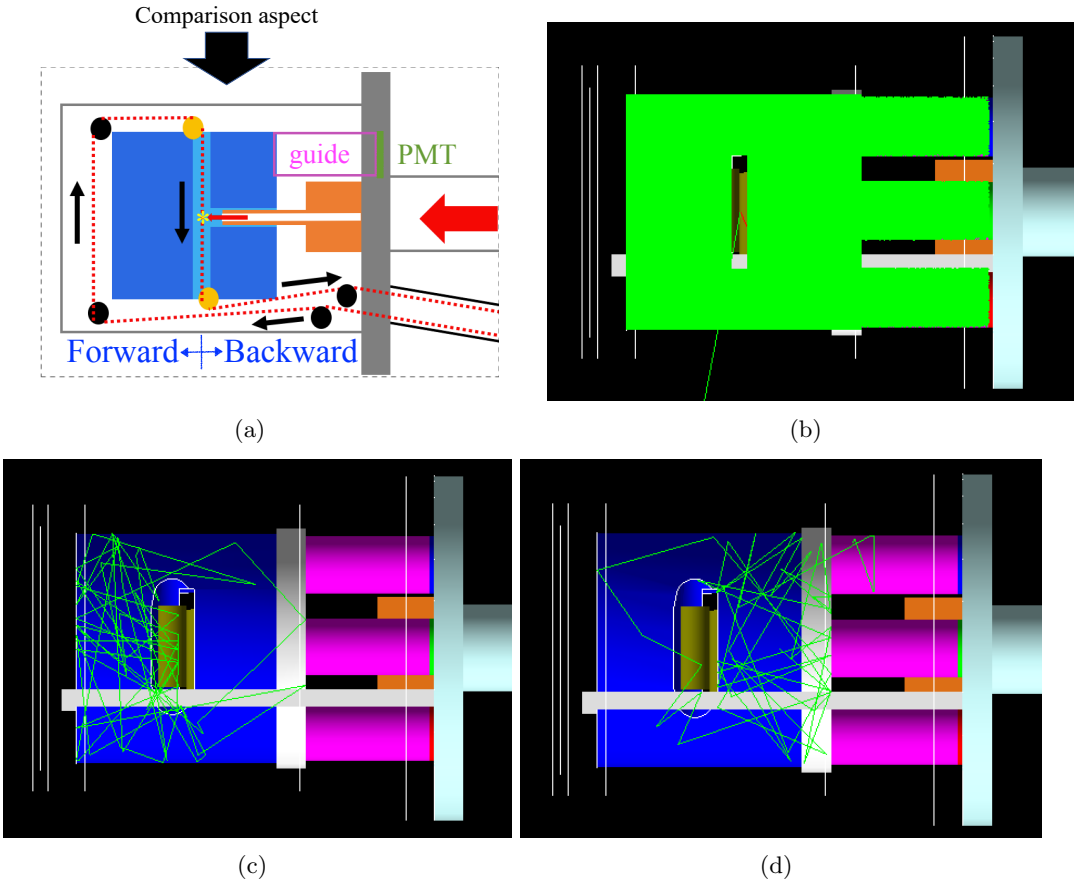

Figure 8.6: OpenGL model of SATURN showing the forward and backward responses to optical photons. (a) Schematic of SATURN detector showing the tape well (light blue), that divides the scintillator detector (blue), into forward and backward halves with respect the direction of the beam (red arrow). The optical light path obstruction is seen in the openGL rendered models viewed from above the detector (direction shown by the large black arrow). Optical photons are shown as green lines for: (b) a single ^{36}Cl decay response at the detector centre (filling the optical components with light), (c) a single optical photon originating in the forward half of SATURN, and (d) a single optical photon originating in the backward half of SATURN. The difference in light collection between c) and d) is readily apparent.

The response of the forward half of SATURN is a fraction of the backward response, due to the lesser amount of light reaching the PMTs. With the highest energy calibration source, the probability of a substrate (of unknown thickness), impeding the particles would be less, resulting in similar responses from particles emitted in both forward and backward directions. This seems to be the case for the ^{90}Sr/^{90}Y source, because the β-particle emitted from the decay of ^{90}Y has energies up to 2.2 MeV (see Figure 8.5c with the spectra having similar end points). This is not true for low-energy sources such as ^{99}Tc in Figure 8.5a. Based upon this understanding of the features in the forward- and backward-facing sources, the energy calibration will be determined from the β-spectrum end points for the backward-facing data only.

A ^{60}Co γ-ray calibration source was used to provide an additional energy point for the calibration, given the inconsistency of the ^{36}Cl end point value. For ^{60}Co it is likely the 317.32(21) keV β-particle will incur some attenuation as the source enclosure is thick (since it is usually used as a γ source). The expected energy is approximated as 1411 keV, derived as an estimated 50% of the β^- particle energy summed with one of the γ rays (1173 or 1332 keV); taken as an average. The energy calibration fit, assumed to be linear, is shown in Figure 8.8 with the intercept set to 0.

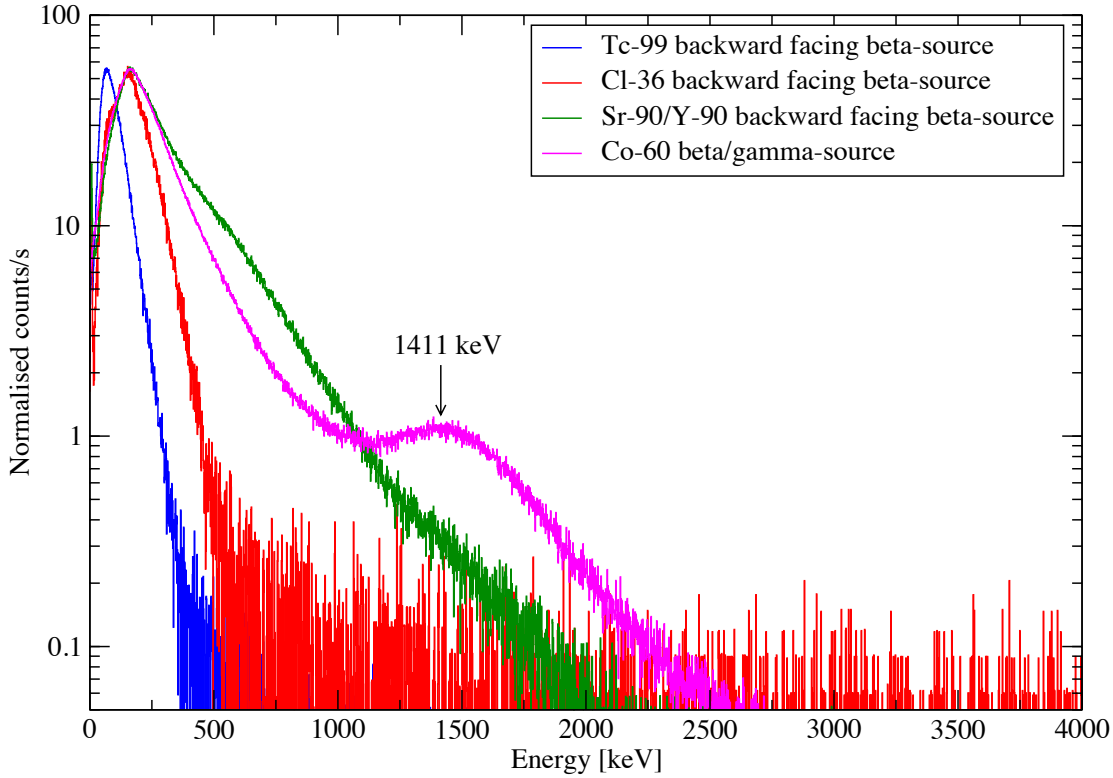

Figure 8.7: Source spectra after energy calibration. The backward-facing β-particle calibration sources are ^{99}Tc, ^{36}Cl and ^{90}Sr/^{90}Y, while ^{60}Co β/γ spectroscopy sources have also been used. All spectra count rates are normalised.

The experimental applied energy threshold can now be determined in terms of this energy calibration. By overlaying the energy calibrated spectra with and without the threshold applied in Figure 8.9, a range of 110+/-40 keV is determined. This is in contrast

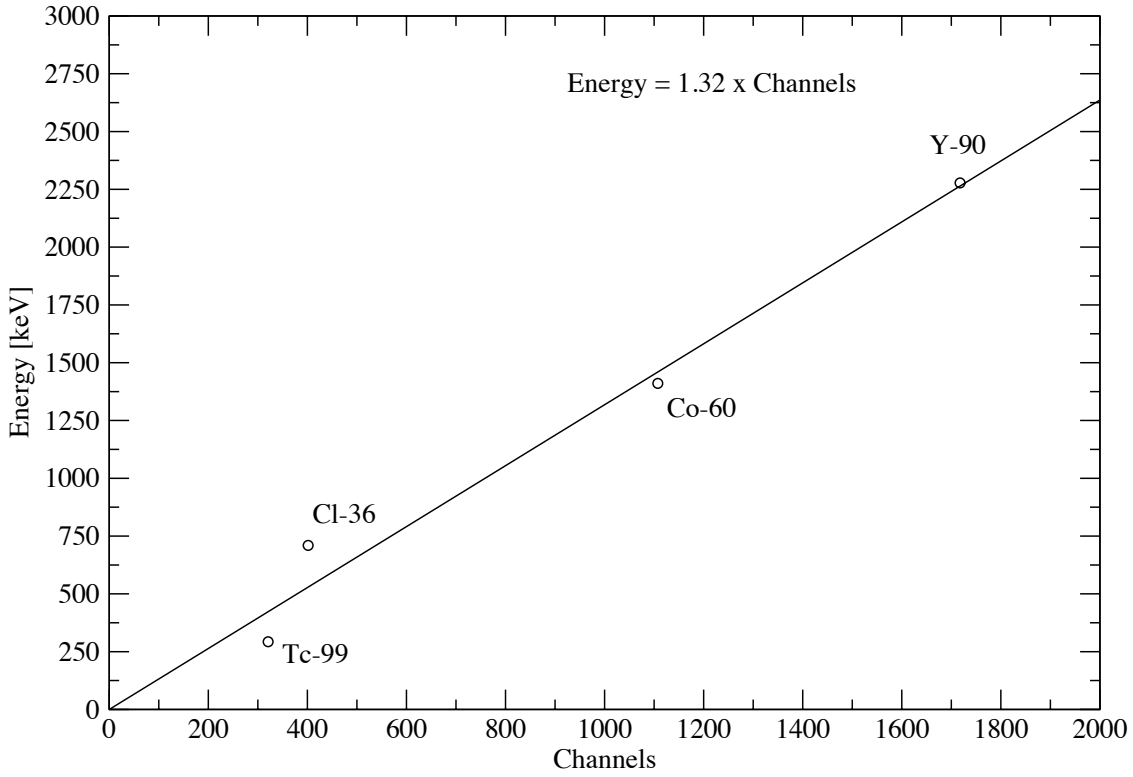

Figure 8.8: Experimental energy calibration for SATURN using data points as described in the text.

to the published value of 500+/-200 keV reported by Siegl [Sie18], which if true, would not allow any events from ^{99}Tc to be detected for either direction.

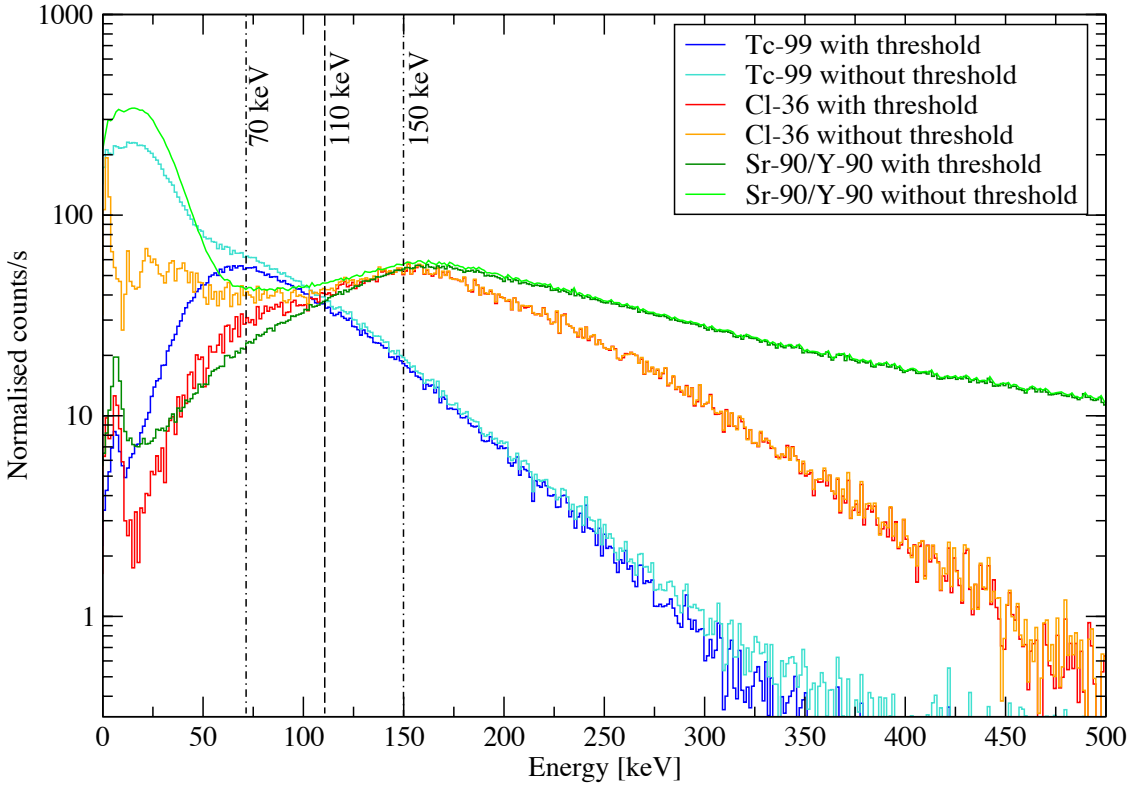

Figure 8.9: Backward-facing β-particle calibration source spectra for ^{99}Tc, ^{36}Cl and ^{90}Sr/^{90}Y. All spectra are given as normalised count rate.

8.3.3 Optical-photon model of SATURN

The asymmetric response of the forward and backward halves of the SATURN detector requires optical photons to be used in the model. The model allows for the collection of both optical photon and direct energy-deposited information. An example of the collected information types is shown for a ^{99}Tc source for both forward and backward-facing directions (Figure 8.10). A 2 mm thick source substrate was added to the model to approximate the nominal conditions of the β-particle calibration measurements.

The decay information for ^{99}Tc was generated from the LLNL-BD program[†]. This Monte Carlo based decay program, was originally developed by colleagues at LLNL as described in Ref. [Sci04]. The β-particle energy spectra for decays of the ^{99}Tc, ^{36}Cl, ^{90}Sr and ^{90}Y β-particle sources were generated using this decay code. The Fermi functions in this code were generated from a cubic spline of the tabulated values in Ref. [Beh69]. The LLNL-BD program produced GEANT4 macro files that were used in conjunction with the RDM module of the SATURN model to generate the decays.

The total energy deposited information (black in Fig. 8.10), is collected for the total

[†]LLNL BD - Lawrence Livermore National Laboratory's Beta Decay program

plastic volume and is shown to have a similar shape as the energy deposited in each respective half. The volume of the front half of the detector is only approximately 1% smaller in volume compared to the back half. The difference in the efficiency of the two halves is coming from the influence of a metalised mylar tape in the model, shadowing the forward half. The majority of the direct energy events occur in the direction of the source, as shown by the forward and backward energy deposited hits (green and red respectively in Fig. 8.10).

The direct energy-deposited model does not fully account for the disparity of the responses seen in the experiment as was shown in Figure 8.5a. In contrast, if the optical photons are collected for each PMT (labelled as PMT1-3), and the sum of these is used to create the final response spectrum labelled as 'Optical Sum' (blue in Fig. 8.10), then the backward and forward responses are clearly different, similar to experimental observation.

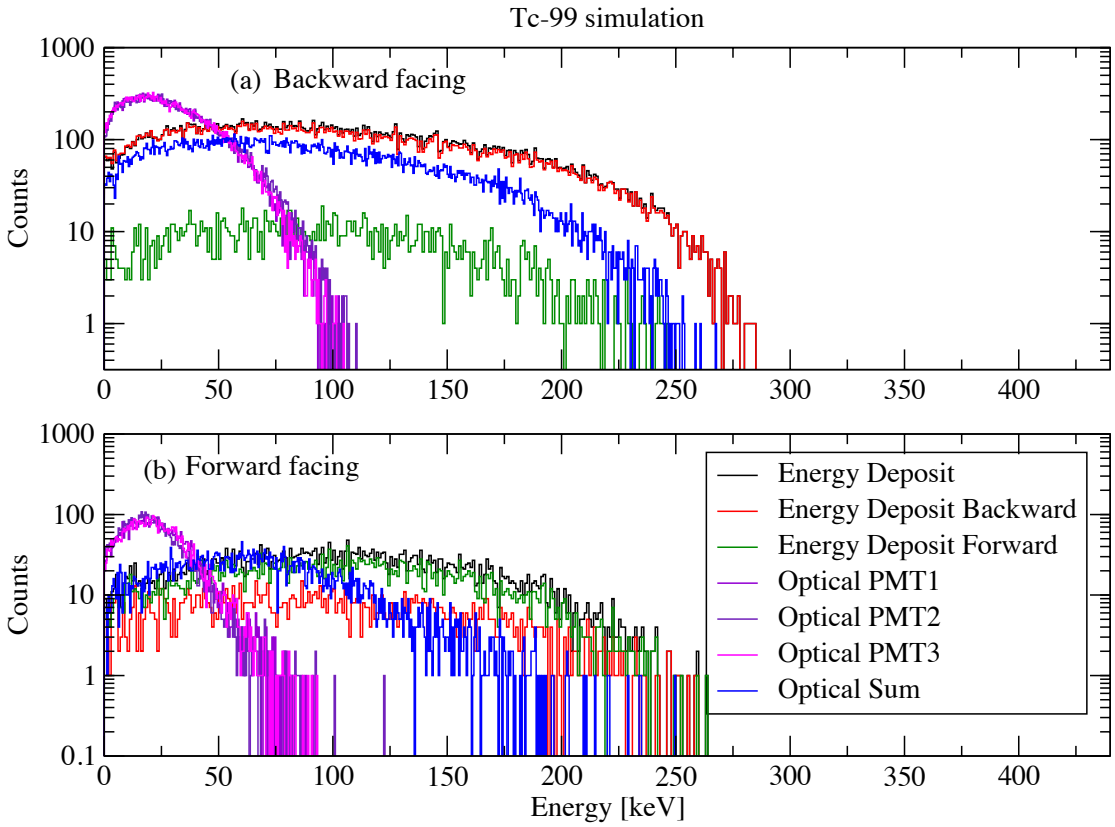

Figure 8.10: Simulation of SATURN for a ^{99}Tc source showing the model components for the backward- and forward-facing directions.

As SATURN was built by collaborators at ANL and UMass Lowell, all of the dimensions and materials are well known. A 150 μm thick dead layer was added to the external surface of the plastic scintillator to model the addition of Eljen-510 titanium dioxide reflective paint. The distribution of the paint in the well of SATURN is uncertain, so we assume it was present and uniform. The main adjustment required in the model was the tuning of the optical reflectivity at the plastic scintillator boundary. The boundary surface properties in the model were varied from 80 - 100% reflectivity. A reflectivity value of 96% was chosen, as giving the best agreement for the ratio of the magnitude of the

backward to forward response, compared to the experimental observations (Figure 8.11 compared to Figure 8.5). This value is in agreement with the specifications of the optical paint (Eljen-510 titanium dioxide paint).

Assumptions were made with the tape thickness and coating of aluminium on the mylar in the ratio of (28% to 72%), implemented in the simulation as a homogenous mix of the two materials across a 50 or 100 μm thick tape.

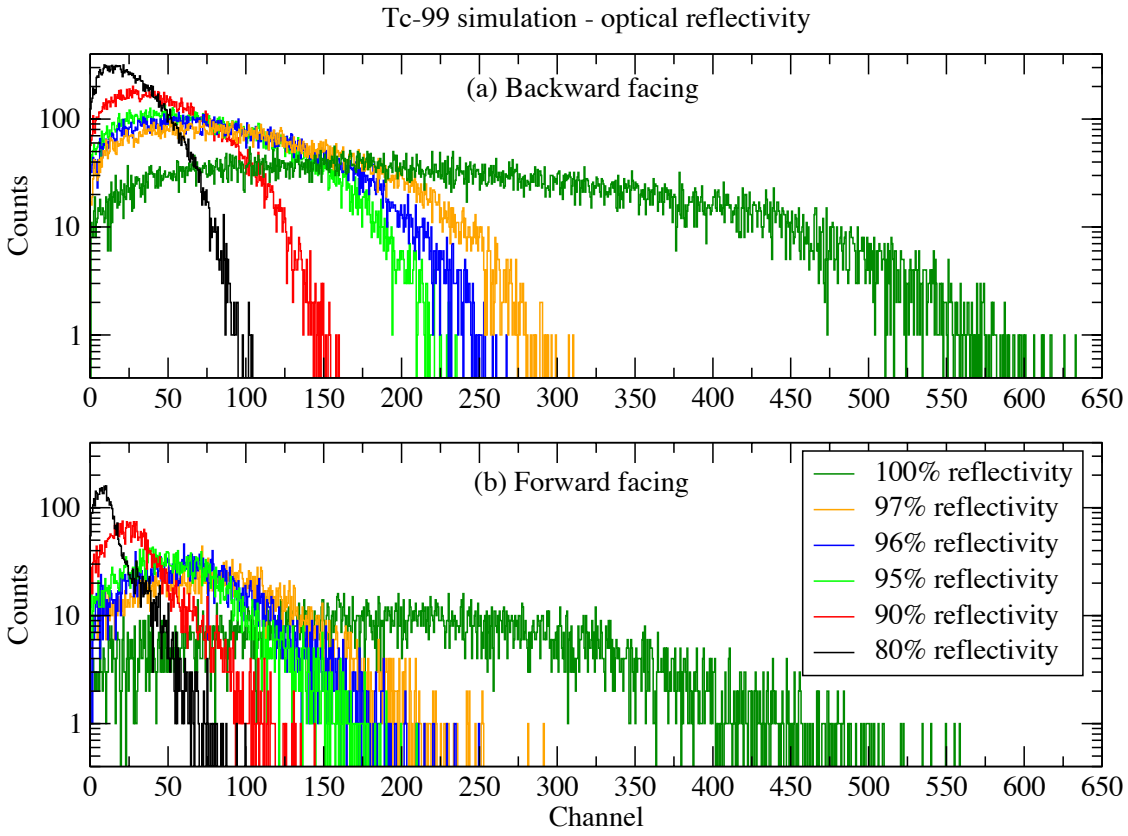

Figure 8.11: Simulation of SATURN for a ^{99}Tc source showing the optical response for the backward- and forward-facing directions as a function of photon reflectivity at the plastic/paint interface.

The model was run for the forward and backward cases for the three calibration sources using the updated reflectivity parameter, using 1x10^5 simulated events. Figures 8.12 and 8.13 show these model results as compared to the experiment. The simulation spectra were all compressed by the same factor to match the 1.32 keV/channel of the experimental data and are scaled by the source activity to obtain the expected number of emissions, allowing direct comparison with the experimental results. Resolution broadened FWHM coefficients were determined by performing a least squares regression fit for the simplest case (^{99}Tc), comparing the model to experiment with these coefficients as free parameters. The resulting coefficients of F_0= 0 and F_1=13 were found to be in agreement for both the forward and backward cases (see Equation 4.4). These values were used for all sources and can be seen to give a reasonable reproduction of experiment for ^{36}Cl, but the overall shape difference between modelling and experiment for ^{90}Sr+^{90}Y make it clear why only the simplest source of ^{90}Tc was used to try and estimate the resolution broadening.

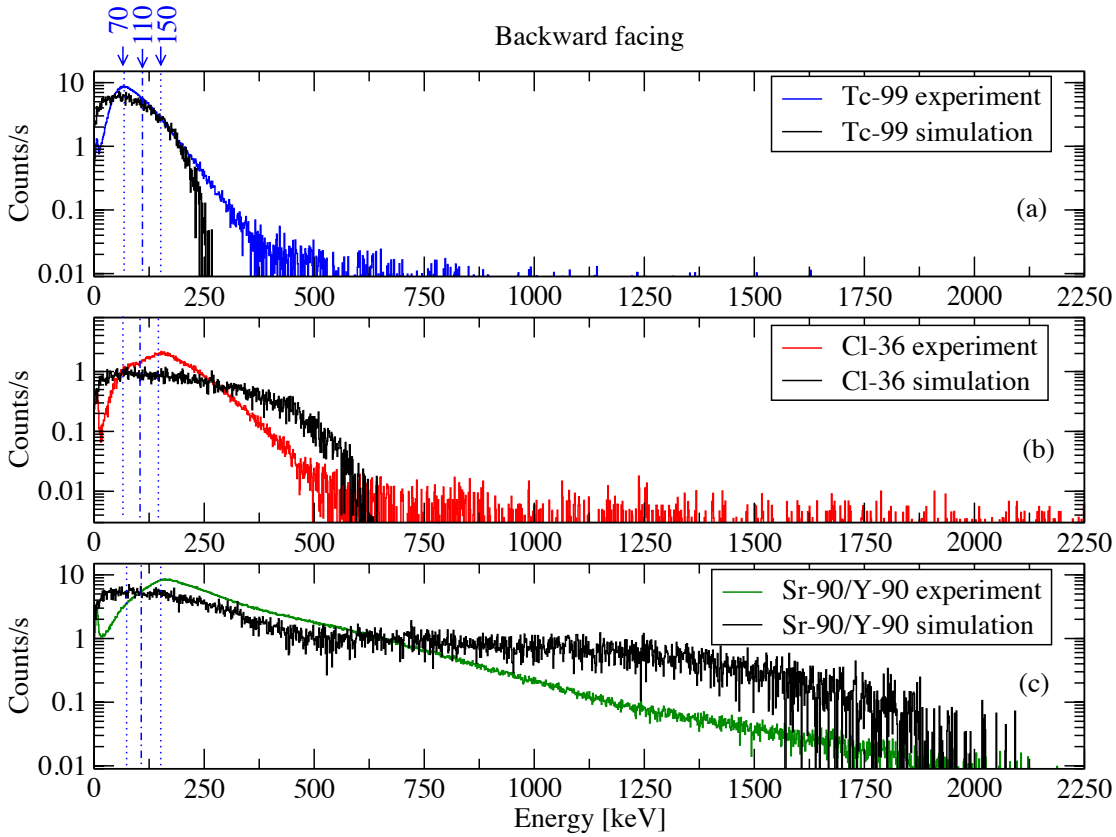

Figure 8.12: SATURN spectra for backward-facing sources compared to model results for ^{99}Tc, ^{36}Cl and ^{90}Sr β^- particle sources.

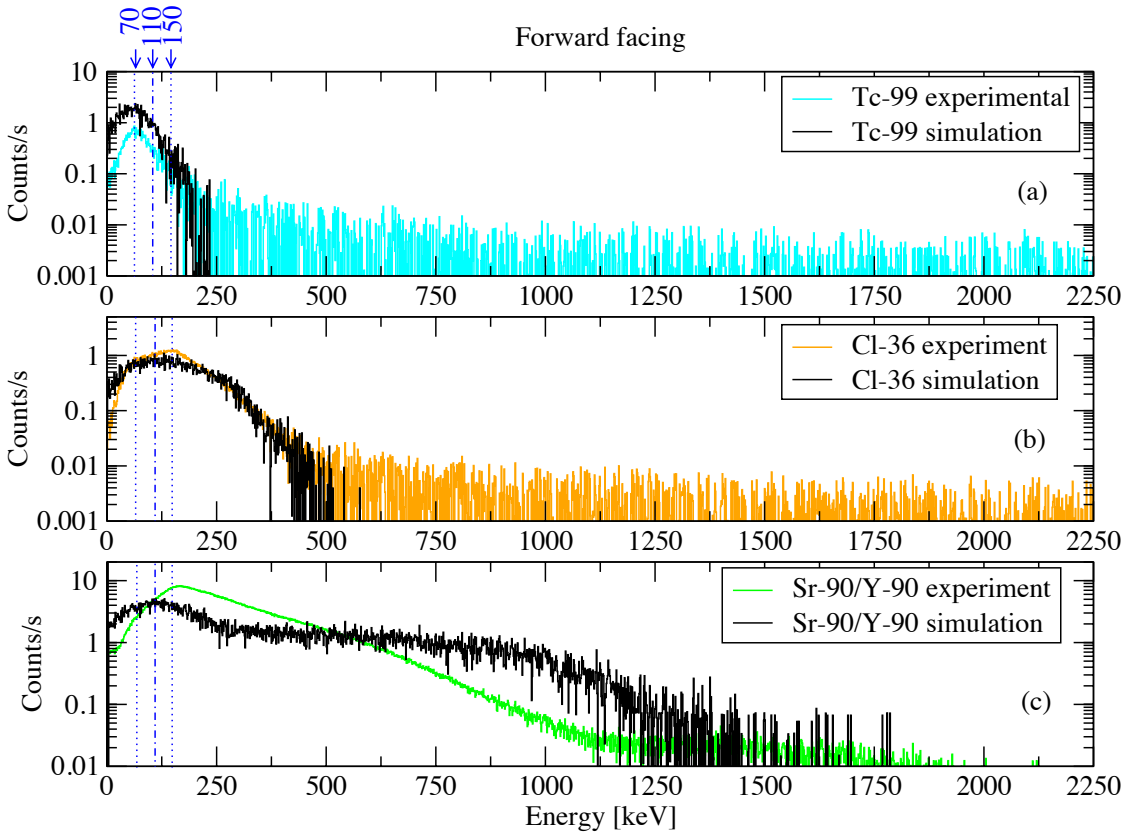

Figure 8.13: SATURN spectra for forward-facing sources compared to model results for ^{99}Tc, ^{36}Cl and ^{90}Sr β^- particle sources.

There is good overall agreement with the model roughly reproducing the correct end-point energies for all three cases (Figure 8.12 and 8.13). There is a small discrepancy between the model and experiment for the end points of the ^{99}Tc and ^{36}Cl (Figure 8.12a and b). This suggests that there is an aspect of the source enclosure for one or both sources that is not fully understood. The shape of the ^{90}Sr+^{90}Y source in the model over estimates the shape of the higher energies for both directions. The model was based on the assumption of secular equilibrium in the source and relies on the β^- particle spectra for each separate component produced by LLNL-BD. Similar results were found using the RDM-produced decay instead of LLNL-BD.

Table 8.1 compares the ratio of the integral above a threshold of the forward-facing spectra compared to the backward-facing spectra. The table compares the experimental ratio to the simulation, with the latter using a range of applied thresholds within the range of 70 to 150 keV (see Fig. 8.9 that suggested these limits).

	Forward/Backward integral above threshold					
Source	Experiment	Simulation thresholds				
		70 keV	90 keV	110 keV	130 keV	150 keV
Tc-99	0.062	0.157	0.119	0.086	0.064	0.052
Cl-36	0.587	0.559	0.543	0.512	0.485	0.448
Sr-90		0.452	0.426	0.391	0.345	0.299
Y-90		0.900	0.899	0.895	0.890	0.884
Sr-90/Y90	0.891	0.720	0.719	0.714	0.708	0.704

Table 8.1: Optical photons detected for measurements with SATURN compared to the model. Experimental column is the ratio of counts measured in the forward and backward directions with the threshold applied. Simulation results are shown as the ratio of the sum of counts in the forward and backward spectra above various threshold values.

The ^{99}Tc source suggests the threshold value is between 130-150 keV, whereas the ^{36}Cl source suggests the threshold is less than 70 keV. The simulated ^{90}Y ratios are closer to the experimental ratio compared to the ^{90}Sr or combined ^{90}Sr/^{90}Y simulation result. This discrepancy is apparent in the miss match of the spectral shapes shown in Figures 8.12c and 8.13c as mentioned previously. There is fairly good overall agreement of the experimental and modelled F/B ratios when considering that the missing information on the source construction and materials will have major impacts on the model.

8.4 Validation of the XArray model

The overall XSAT model is described in Section 3.3. The XArray component of this model was built around the dimensions and information contained in the technical drawings supplied by the manufacturer (Canberra [Tec]). These specifications show the bulk dimensions and the main components of the detector, sometimes as approximations. It was common practice in the past for manufacturers to exclude dimensions from the schematics that are required to produce a model. The difficulty with obtaining more details comes from the reluctance of the manufacturer to divulge its intellectual property. Some of the details in the specifications provided are bulk material information that the physics community often requests for the purpose of modelling. There are also some dimensions that are not accurate due to the uniqueness of the manufacturing tolerances compared to the specifications. These parameters are best determined by direct comparison of model results with

experimental data. This section focuses on the approximation of the unknown parameters in the model by comparison with experimental data.

8.4.1 The experimental XArray γ-ray efficiency

The γ-ray detection efficiency was obtained from measurements of the XArray using point-geometry calibration sources with multiple energy emissions. There are two separate data sets for the efficiency of the XArray, collected at different times and combined here for a check of consistency. The first set consisting of ^{154}Eu and ^{182}Ta, was measured during the commissioning of the XSAT by Mitchell [Mit14]. The γ-ray efficiencies of the XArray, with and without SATURN, are available in this data; however, this work is more focused on the inclusion of the SATURN detector to match experimental conditions used for the present work. The second set consisting of ^{152}Eu, ^{133}Ba, ^{137}Cs and ^{56}Co were measured during the initial setup of the XSAT experiment at CARIBU, preceding the measurements of ^{134m}Sb/^{134}Sb and ^{92}Rb. These data were collected with the calibration source located at the implantation position of the SATURN detector.

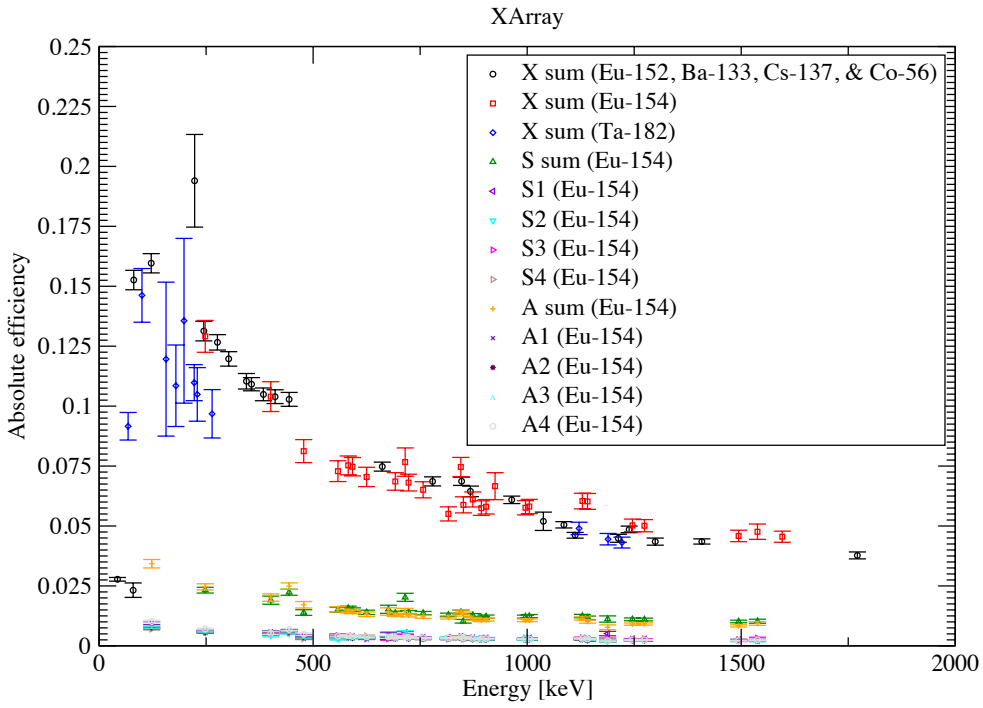

Figure 8.14: XArray Experimental γ-ray efficiency using various calibration sources. The efficiency response for the whole XArray (X_{sum}, where X_{sum} = S + A + B + C + D) is shown. The individual component efficiency results are shown for the Super clover S (where S = S1 +S2 + S3 + S4) and one of the standard clovers A (where A = A1 + A2 + A3 + A4), as examples of the two different clover geometries.

Figure 8.14 shows the γ-ray efficiency of the XArray for energies ranging from 79 keV to 2598 keV from the two measurement campaigns. The data shown are for the total XArray (sum of the clovers X= S+A+B+C+D), the S and A clovers, and some representative clover leaves for comparison. The simplified efficiency for a single γ-ray energy is

determined using Equation 8.1, where there are no complex corrections applied[‡].

$$\epsilon(E_\gamma) = \frac{c}{A\ I_\gamma\ t_{LT}} \times Corrections \tag{8.1}$$

where:

ϵ = Efficiency;
E_γ = known energy of the γ ray;
c = fitted peak counts;
A = activity of the calibration source; and
I_γ = γ ray intensity
t_{LT} = acquisition time (Live Time).

Uncertainties for each of these values are included in this data, in addition to uncertainties of the efficiency calculation values. The efficiency data are used to validate the XArray model and to approximate all of the missing parameters in the following section.

8.4.2 XArray model parameter fitting

The modelling of single crystal HPGe detectors with some unknown thickness/distance/material parameters is not uncommon in the literature [Asg15]. Some of the unknown parameters of the XArray are repeated in the model and there are others that are unique to the XArray. The key dimensions in question for the XArray are:

- a - Central contact dimensions;
- b - The HV contact thickness or dead layer;
- c - Detector crystal face to aluminium can gap;
- d - The SATURN detector to clover gap;
- e - The relative position of the XArray and SATURN detectors; and
- f - The thermal block thickness.

Figure 8.15 shows these parameters using a schematic diagram. A number of key dimensions from the experimental setup were not recorded but a range of distances were supplied. These relate to the gaps between the XArray and SATURN detector for the experiment.

An efficiency response of the model is produced by simulating mono-energetic γ rays in 10 keV steps for the range 30 keV to 250 keV and 250 keV steps for the range 250 keV to 8.25 MeV. The γ rays are emitted in an isotropic distribution as a point source located at the target position of SATURN. A basic model of the SATURN detector including all of the relevant materials was produced prior to this work, more details on that model are found in Section 8.3.

[‡]Efficiency corrections that are not applied here include count rate effects, cascade summing correction, and source decay during measurement.

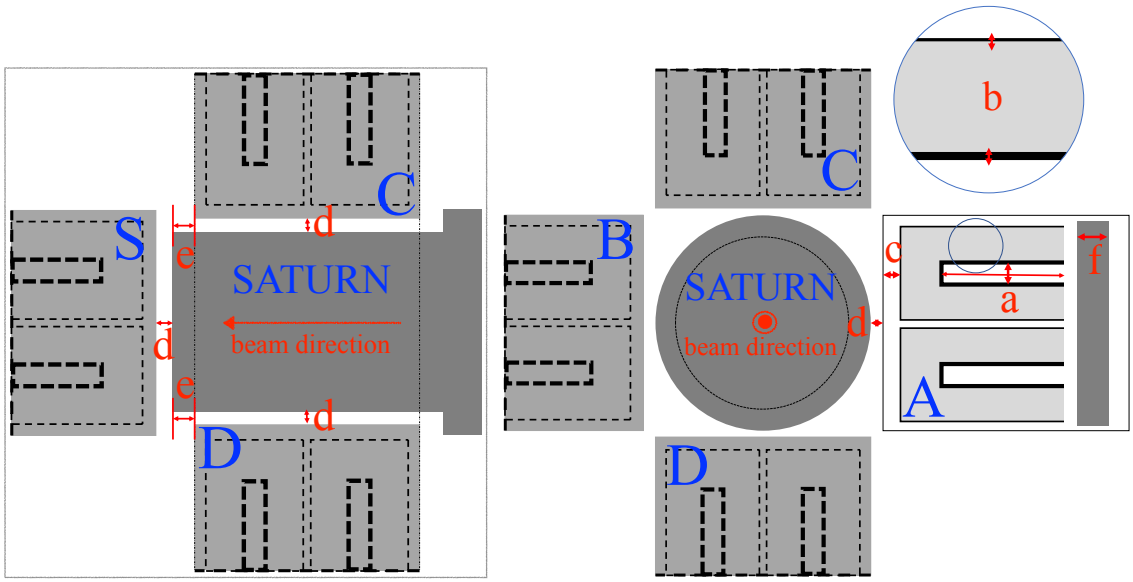

(a) Side view (b) End on

Figure 8.15: Schematic diagram of the XArray clovers showing the modelled parameters of the XArray clovers and the SATURN detector (a) from the side and (b) end on. These model parameters need to be adjusted in the GEANT4 model by comparison with experimental data. The standard Clover A is used to show the parameters of the internal dimensions, which are assumed to be the same for each of the standard clovers (A, B, C, D). The super clover (S) uses these same parameters but they may be defined as a percentage of the dimension to allow the larger crystals to be related to the smaller crystals. A zoomed in section shows the individual crystal contact variables.

The methodology used to fit the large number of model parameters to this experimental data was based upon fixing them in a logical sequence, starting with the parameters that have the largest influence or the most well-known information. This would be a difficult task given a single set of experimental data to compare against. However, Figure 8.14 shows a number of experimental sub-sets of data ranging from the individual clovers of the XArray (only S and A shown in the diagram), down to the individual response for the clover leaves (S1, S2,...,A1, A2,...). This gives 26 total sets of data available for comparison. Specifications from other single HPGe detectors are utilised to help refine the boundaries of each of these parameters when they are available.

a - Central contact dimensions

The clover detectors use coaxial-shaped crystals to maximise the volume of the interacting germanium material whilst maintaining an equal thickness across the sensitive volume. The design aim is two fold: to produce an even charge collection when biased, minimising the energy resolution; and to not exceed an unreasonable thickness between contacts, allowing full depletion of the material without exceeding a break-down bias. The crystal central contacts in these detectors are also used for physically mounting the detector onto the body of the thermal mounting; details of this design are protected by intellectual property.

The two parameters in question are the void length and diameter, shown in Figure 8.15b as parameter 'a'. These parameters are assumed to be the same for all of the clover leaves in the standard clover detectors. To make these dimensions applicable to the super clover, the parameters are given in relation to the overall crystal dimension (i.e. as a percentage). To gauge the size of these contacts, initially the specifications of other single crystal HPGe detector specifications were investigated. Only recently have the manufacturers started to provide these details to satisfy the community need for modelling; unfortunately the clover detectors pre-date this process. Using these alternative detector specifications, it was found that thevoid length is approximately 87.5% of the overall crystal length. A similar trend for the void diameter could not be found.

Starting with the length of the void as 87.5% of the length of the crystal (52.5 mm for the clovers and 61.25 mm for the super), the diameter of the void was varied between 16% to 64% of the overall diameter of the crystal. Figure 8.16 shows the comparison of the XArray total sum for the variation in central void diameter. The effect of varying the central contact diameter is to change the overall active volume of the detector, resulting in a change of the efficiency across all energies.

The value of 32% of the overall diameter gives the best agreement with experimental data when comparing the absolute efficiencies from the total XArray sum and the individual super and standard clover detectors. The selected values (19.2 mm for the standard clover and 22.4 mm for the super clover), although on the upper side of expectation, are reasonable when compared to the known values of similar sized coaxial detectors.

b - The HV contact thickness or dead layer

The coaxial geometry of the clover leaves requires contacts on the inside and outside surface of the crystal to enable a bias to be applied. The high voltage between the contacts creates a uniform depletion region across the sensitive part of the detector. HPGe crystals can be p- or n-type, dependent upon the material used, which also determines the thickness of the contacts and the direction that bias is applied. There are typically two types of

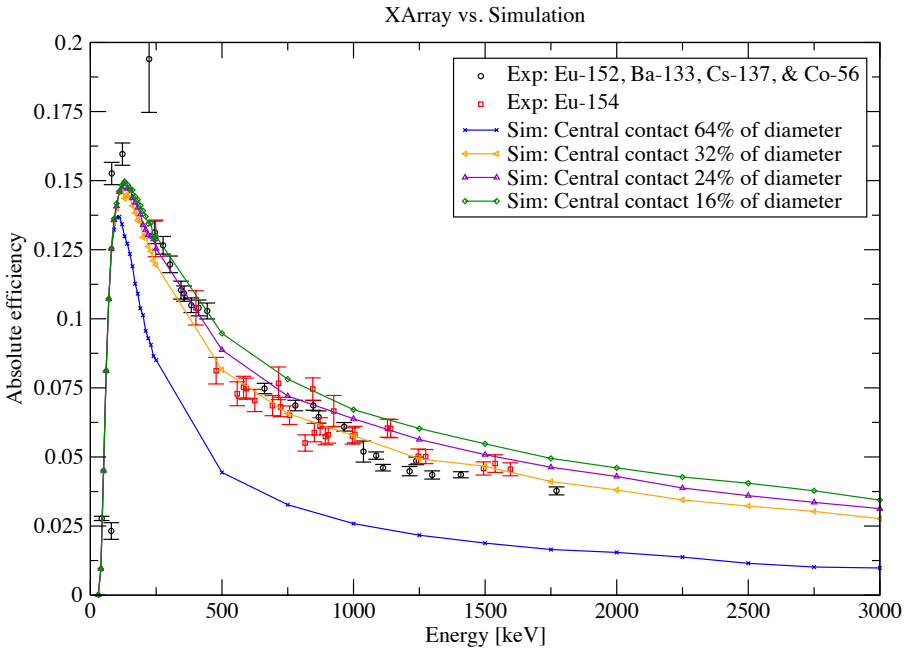

Figure 8.16: XArray model varying the diameter of a clover leaf central contact and comparing to experiment. The central contact is shown in Figure 8.15 labelled as 'a'. The diameter of the central contact cavity is given as a percentage of the overall crystal diameter. The length of this contact is fixed to 87.5% of the length of the crystal.

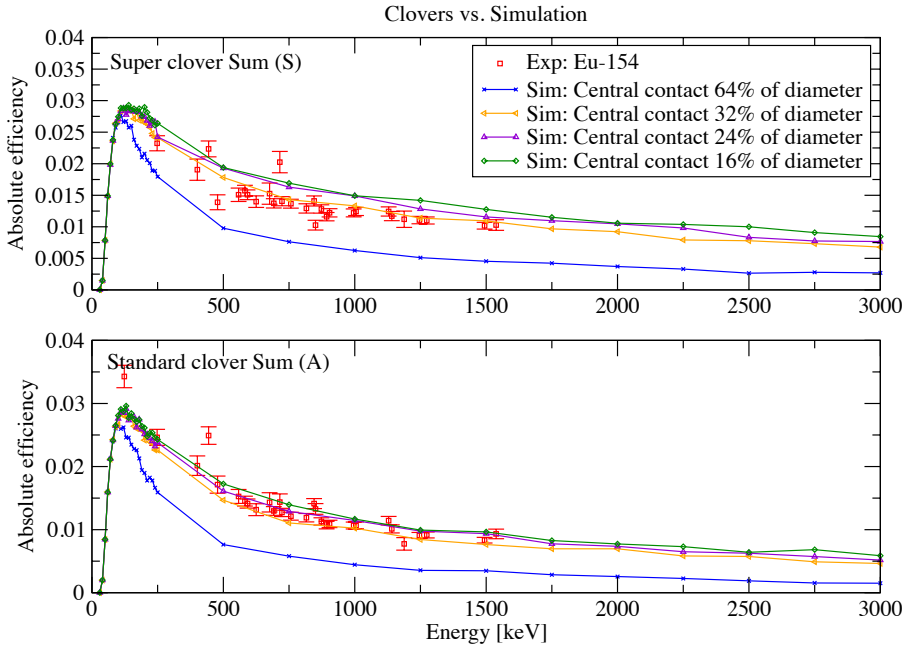

Figure 8.17: XArray model varying the diameter of a clover leaf central contact for S and A. The central contact is shown in Figure 8.15 labelled as 'a'. The diameter of the central contact cavity is given as a percentage of the overall crystal diameter. The length of this contact is fixed to 87.5% of the length of the crystal (see text).

contacts: a thick one made from lithium on one side and a thin ion-implanted contact on the other. The specific details of contacts and thicknesses are dependant upon the detector design, with little information available in detail due to commercial competition. In general terms, the thick contact can be a several hundred micron up to 800 μm thick drifted region on the surface. The result is an inactive layer of material (or dead layer) in terms of sensitivity to γ rays that can cause significant attenuation for low-energy photons and hence sets the low-energy detection threshold of a detector. For p-type detectors, this thicker contact is located on the outside surface of the detector whilst n-type detectors have the thick contact in the middle of the crystal. The thin contact can be an order of magnitude smaller in thickness, giving a preference for using n-type detectors where there is interest in observing low energy γ rays and X rays (down to 3 keV).

With respect to the model, these contacts act as a thin dead layer adding attenuating material to the active region, as shown in Figure 8.15b and marked as 'b' in the zoomed in section. The dead layers are modelled by removing a component of the active region but maintaining the same material. The influence of the contact thickness is to change the shape of the efficiency at low energies around the turning point of the curve. The front or outside contact thickness can have a significant effect compared to the back or inside contact; the latter has still been added to the model for completeness with a fixed value of 700 μm. Clovers are generally manufactured with the more expensive n-type material as their applications with accelerators bring them into neutron fields and the n-type design is less prone to damage from neutrons.

Figure 8.18 shows the influence of this outside dead layer on the efficiency at low energies for a 2 μm thick dead layer compared to a 700 μ thick dead layer, overlaid with the experimental data. The relative shapes are compared here, not the overall magnitudes, as the other parameters are not yet fitted, but are fixed for this comparison. The 2 μm and 10 μm contacts give little attenuation to the low energy component so that there is a significant deviation from the expected turn-over to the efficiency function at low energy. Although there are few experimental points at the efficiency turn over, there is a better match of the response for a much thicker rather than thinner contact.

The value chosen for this parameter is 700 μm, which is consistent with the front contact thickness of other p-type detectors, even though it is believed the clovers are of n-type. This can be explained by considering the other attenuating materials required for packing and supporting four clover detectors in a compact arrangement whilst maintaining cryogenic temperatures and insulating the clover leaves to hold the 4.5 kV applied bias.

c - Detector crystal face to aluminium can gap

The distance between the clover crystal face and the inside of the detector enclosure was not available in the original specifications. This is shown in Figure 8.15b marked as 'c'. The distance can vary between clover leaves and can only be approximated, as provided by the manufacturer. The values can be measured by using X-ray radiographic imaging of the complete detector, often at the risk of damaging the electronics, which was not done here.

The gap distance was given by Canberra upon request as nominally 7 mm. This gap is in-line with similar sized gaps documented in newer single crystal detectors where the information is provided. As this was a nominal value, simulations were undertaken for gap sizes of 5 mm to 15 mm to look at the sensitivity of this parameter. Results showed no change in the efficiency shape with respect to energy, but it did show a shift in the value

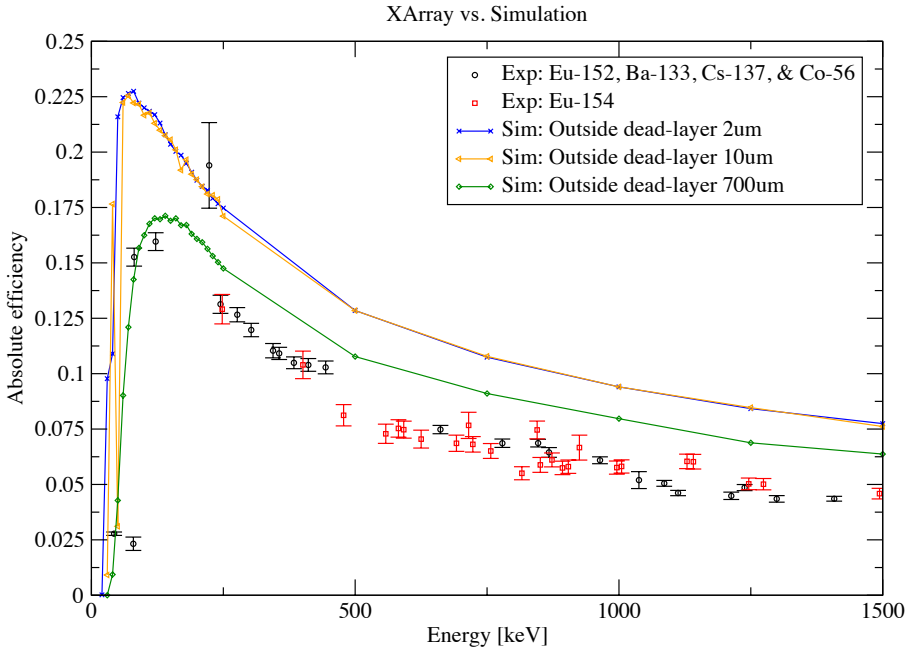

Figure 8.18: XArray variation of outside dead layer (front-contact thickness), comparing the shape of the efficiency curve as a function of the dead layer thickness.

to higher efficiencies with a smaller gap. This is a geometry effect caused by increasing the solid angle of the detector active volume by virtue of being closer to the source. The magnitude of the change is about 2% change in efficiency for the total XArray sum across the 10 mm change in gap. This parameter change is equivalent to changing the relative distance of the clover detectors, i.e. parameter d discussed in Section 8.4.2, but this value cannot be seen or altered. This model does not take into account the small variation due to the proximity of the aluminium shielding at small energies.

To reduce the number of combinations possible with the two competing free parameters c and d, the nominal 7 mm gap is accepted for both the super and standard clovers. Although this may vary from clover to clover, it is believed that the average value would take into account small variations in the manufacturing. This parameter has the same overall affect on the efficiency as the SATURN detector to clover gap (Section 8.4.2). It was more preferable to fix the current parameter first, as this value is better bound by physical constraints and the manufacturers nominal value.

d - The SATURN detector to clover gap

The SATURN detector to clover gap is the smallest separation distance of the clover enclosure to the can of the SATURN detector, marked as 'd' in Figure 8.15. Each time the XArray is removed to allow access to the SATURN detector, the clovers have to be individually re-adjusted back into position by the experimenters. This variable was estimated to have a maximum value of 30 mm from the experimental notes, the lower limit is physically restricted by the dimensions of the adjacent clover outer cans. As the position of each clover pair can be adjusted independently with respect to SATURN, for the simplicity of the model we assume this clover gap parameter is the same for all of the

clovers. Variation of this parameter has the same effect on the overall efficiency response as the internal gap between the clover leaves and is discussed in Section 8.4.2 (labelled as parameter c). The former value was first fixed to 7 mm for this comparison, as described above.

Figure 8.19 shows the effect of changing the SATURN detector to clover gap in the model. The solid angle subtended by the detectors to the source position is increased as the gap is reduced, resulting in the overall increase in the magnitude of the efficiency curve across the energy spectrum.

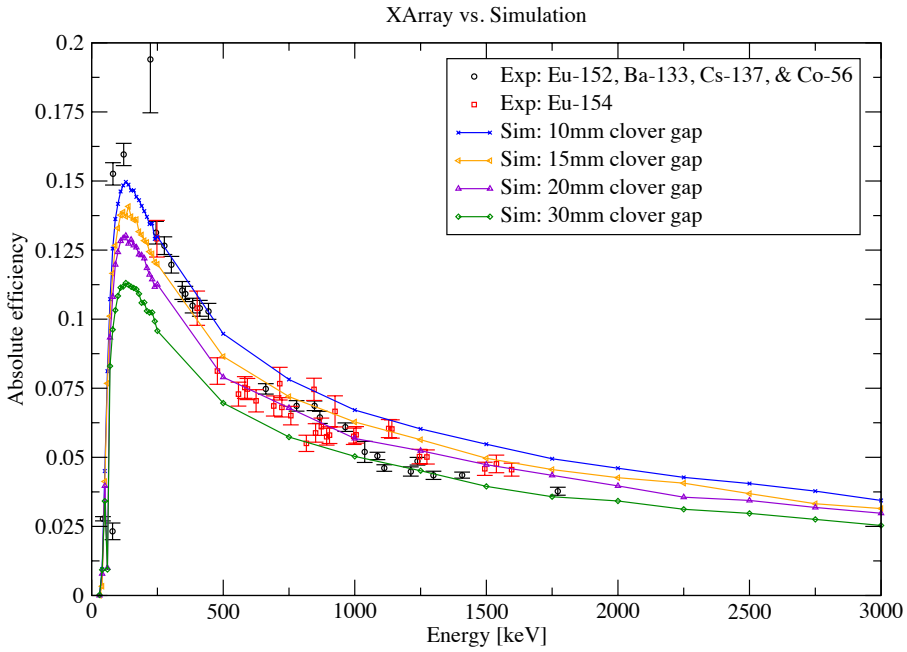

Figure 8.19: XArray model varying the SATURN detector to clover gap, d, and comparing to experiment. This parameter (shown as in Figure 8.15 labelled as 'd') is the separation distance between the outer enclosure of SATURN and the outer closure of a clover, at the closest point. The variable is varied here between 10 mm and 30 mm.

The 15 mm gap size was chosen as the most comparable to the experimental data on average across all of the energies.

e - The relative position of the XArray trolley to the SATURN detector

The XArray is mounted on a trolley with wheels allowing it to be moved between experiments and for access for filling and maintenance. For the case of these experiments, the trolley was often moved between measurements to allow access to the SATURN detector for the purpose of feeding in tape or changing calibration sources. For a measurement including the XArray, the trolley was wheeled back into an approximately reproducible position and the wheels chocked. The variable being fitted is the trolley relative position to the SATURN detector. Figure 8.15a shows the side view schematic of the XArray surrounding the SATURN detector. The trolley position fixes the plane consisting of standard clovers (A,B,C, and D) relative to the fixed position of the SATURN top-hat, i.e. labelled as dimension e. This dimension is representative of the position and a guide

to reproducibility, optimal efficiency is achieved when the centre of this XArray plane is aligned with the source position located inside of SATURN.

f - The thermal block thickness

A large thermal mass is required to maintain the liquid nitrogen temperature of 77°K to all of the clover leaves during operation. This is achieved in design by a thick piece of metal that has thermal coupling to the detectors on one side and to the cryogenically cooled copper cold finger on the other; it is shown in Figure 8.15b marked as f. In terms of the simulation, this large amount of material can cause increased scattering from γ-ray events that exit the back of the germanium crystals, predominantly for high energies. Initially this dimension was being modelled but it was unclear as to the possible thicknesses or material type without opening up the clover detector to get an appreciation of the size. This was not done due to requiring a clean-room environment, the potential damage risk and the associated voiding of the warranty of the detector.

A basic schematic of the mounting materials, thicknesses and relative positions to the crystals was provided by Canberra, which has intellectual property restrictions. The thickness of the now identified aluminium block was estimated to be 10 mm based on the drawing. The effects on the model for thickness variations either side of this value was not very clearly seen in the model and there is an absence of high-energy experimental data with which to compare the model results to.

The inclusion of this component results in a small effect on the overall efficiency response of the model; it would contribute more when dealing with higher-energy photons. The 10 mm value for all of the detectors is accepted as the best information known to hand.

8.4.3 The validation result

The final values of the parameter fitting are summarised in Table 8.2. These values are implemented in the model and used to generate the final comparison of the total XArray efficiency curve with the γ-ray calibration sources, shown in Figure 8.20. There is good overall agreement between the shape of the efficiency with experimental results, although there is a relatively large uncertainty associated with the ^{154}Eu experimental data points. These uncertainties are highly dependant upon the accuracy of relative positions of the clovers and setup of the SATURN detector at the time, experimental details which were not available. It is likely that some changes in some of these parameters could cause variations greater than the uncertainties of the experimental results, particularly parameters d and e, which would be the most sensitive to change between measurement setups.

parameter	description	value
a	Central contact dimensions	19.2 mm (Super 22.4 mm)
b	The HV contact thickness or dead layer	700 μm
c	Detector crystal face to aluminium can gap	7 mm
d	The SATURN detector to clover gap	15 mm
e	Relative position of XArray to SAT	centre-to-centre
f	The thermal block thickness	10 mm

Table 8.2: Summary of the XArray model parameters fitted in this work.

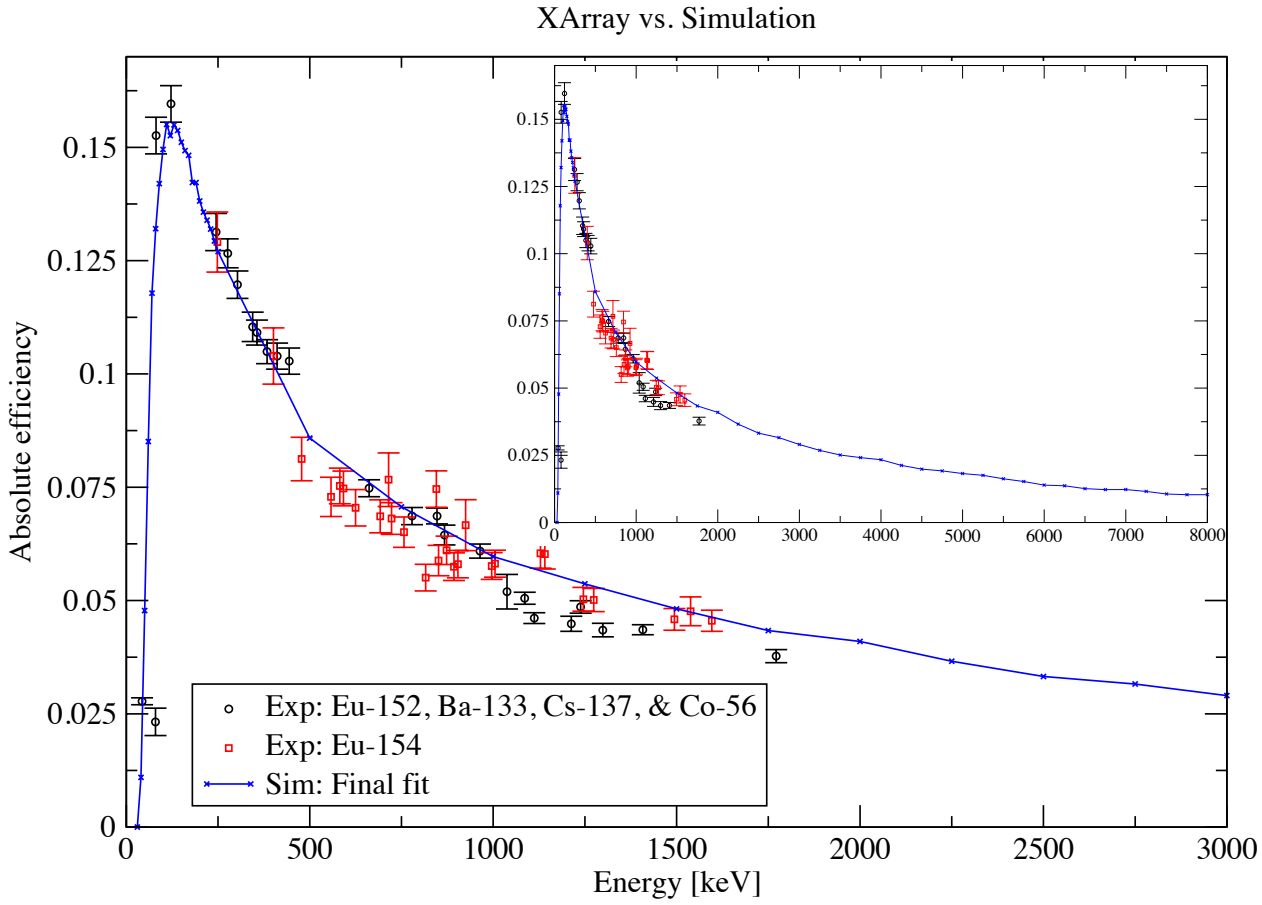

Figure 8.20: XArray efficiency simulation with final parameters, compared to experiment. The efficiency response is shown for 0 to 3 MeV in the main figure and up to 8 MeV in the inset.

8.5 Application of the validated model to XSAT results

8.5.1 ^{134}Sb results

The SATURN model was applied to inform a correction to the experimentally obtained ^{134m}Sb/^{134}Sb ratio as published by Siegl *et al.* [Sie18]. The earlier validation of this model given in Section 8.3, provides the understanding of the experimental detector and optical energy calibrations that are applied here in the form of thresholds. The β-particle spectral shapes for both of the ^{134}Sb and ^{134m}Sb cases were calculated by the LLNL-BD program, modelling 1x10^6 events; these were input into the model via macro files. The length of time to run these simulations that incorporate optical photons is significant. To reduce this time, a sub-sample was simulated using 1x10^5 events of the LLNL-BD data. The events were selected equally across the entire input file to remove the biasing from the iterative LLNL-BD data. Figure 8.21 shows the results of these optical simulations with and without γ rays. The overall shape and efficiency for ^{134}Sb does not change significantly with the inclusion of γ rays as 97.6% of decays go directly to the ground-state of ^{134}Te. Inclusion of γ rays in the case of ^{134m}Sb results in an increase of the efficiency by approximately 2%. This is due to the possibility of one of the γ rays still triggering SATURN, even if the β-particle escapes without interaction. There is also an overall shift in the spectral shape to higher energy.

The simulated response functions are integrated above the nominal threshold of 110 keV to derive the relative response. The efficiency ratio for detecting ^{134m}Sb/^{134}Sb in SATURN was evaluated using threshold variations to the same data sets for β-particle emissions only, resulting in a value of 0.998(1). When both γ rays and β-particles are included in the emitted particles for each possible decay, this ratio becomes 1.022(4). If the decay model is wrong, then there is potential systematic error that has been ignored, but is perhaps of the order of a few percent.

The original relative β-efficiency value reported by Siegl *et al.* was 1.00(1), based upon earlier simulations of β-particle emissions that used an incorrect experimental threshold value. Since the publication, modelling of the calibration sources has allowed a better understanding of the detector response and has allowed a to more accurate determination of the energy calibration and the experimental threshold value that was actually used. The result of this recent work shows a slight increase to the correction applied to the ratio, of $2.2 \pm 0.4\%$. The discrepancy will have less than a 1σ effect on the overall result, since the correction for the isomer to ground-state ratio was determined with a precision of 2.5%.

8.5.2 ^{92}Rb results

The model was applied to determine the β-particle efficiency of SATURN up to the ^{92}Rb Q value of 8095 keV. This information will contribute to the interpretation of the experimental results that are still undergoing analysis at this time by collaborators. Figure 8.22 shows the modelled SATURN efficiency, where the x-axis is the β^--particle maximum energy calculated for each level ($E_\beta max = Q_\beta - E_{level}$), with the energy thresholds of 0 keV, 70 keV, 110 keV and 150 keV applied. As the main ^{92}Rb β-particle decay intensity is approximately 91% directly to the ground state of ^{92}Sr, γ rays were excluded in this analysis. The LLNL-BD program was used to generate the β-particle energies for feeding to particular levels following decay of ^{92}Rb, with no γ-ray contributions.

The modelled efficiency at low β-particle maximum energy calculated for each level is dominated by the attenuation of the outer non-scintillating layers of SATURN. The effi-

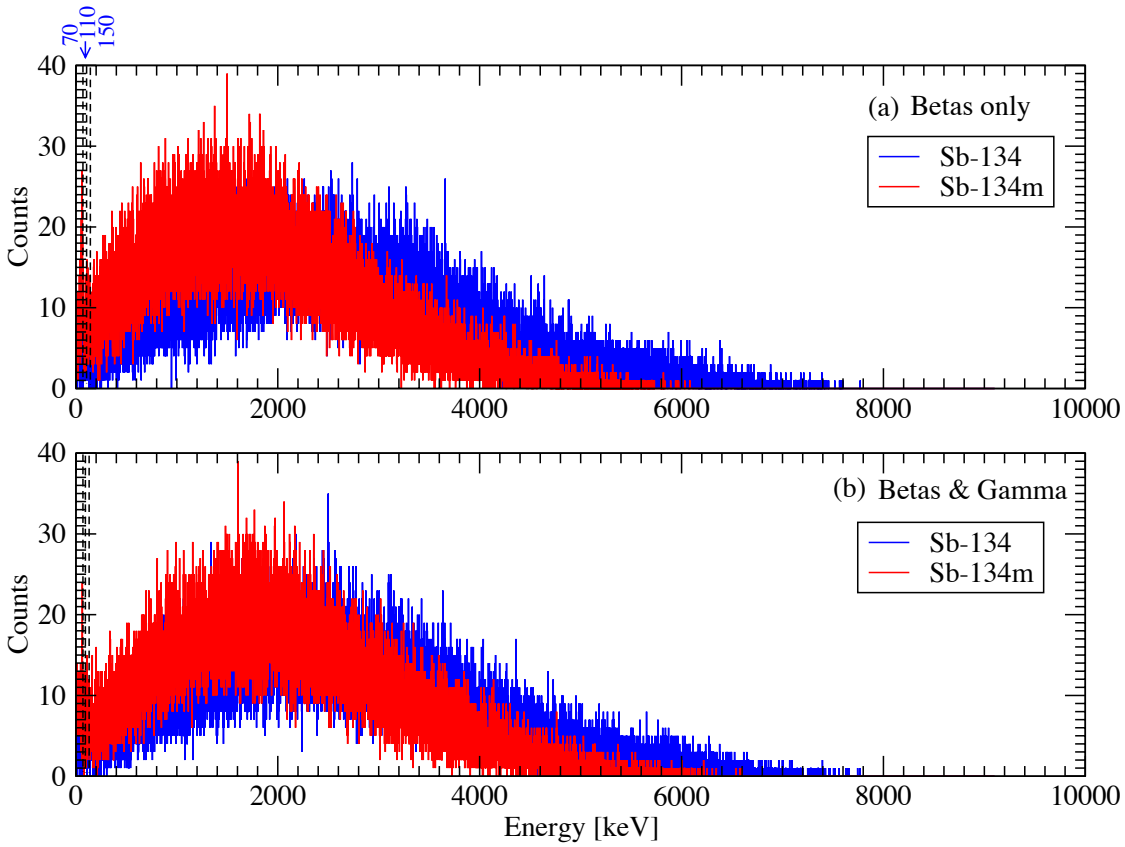

Figure 8.21: ^{134}Sb and ^{134m}Sb results using the model of SATURN for 1x10^5 events. The LLNL-BD program was used to generate the $^{134/134m}$Sb emissions for (a) only β-particles and (b) for β-particles and γ rays. Nominal energy thresholds are shown as the dashed lines at 70 keV, 110 keV and 140 keV.

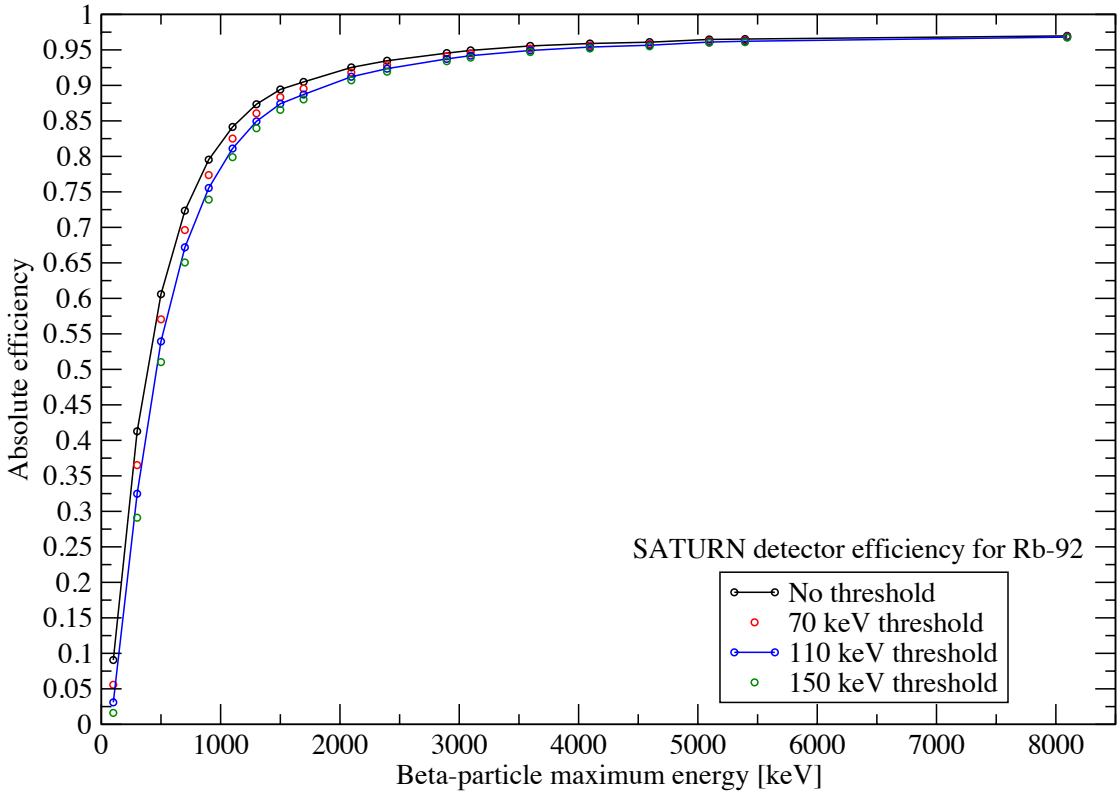

Figure 8.22: SATURN β-particle efficiency for a simulated ^{92}Rb source with energy thresholds of 0 keV, 70 keV, 110 keV and 150 keV. The x-axis is the maximum β^- particle energy calculated for each level ($E_\beta max = Q_\beta - E_{level}$). The connected lines are used as a visual guide of the efficiency shape.

ciency approaches the maximum geometrical efficiency of 98% as the energy is increased. The range of the influence of the applied energy thresholds to the efficiency is more significant at low energy (7.5% at 100 keV) than at higher energies (<2% at 1500 keV) as the majority of decay events fall above the threshold values. Figure 8.23 shows the comparison of the SATURN responses for 500 keV and 4095 keV energies demonstrating this influence. The highest energy level from the decay of ^{92}Rb (approximately 6.4 MeV), corresponds to a β-particle maximum energy of approximately 1.7 MeV. Therefore, the SATURN efficiency as calculated in this work will range from 88% to 98% across the range in which it will most likely be applied for ^{92}Rb.

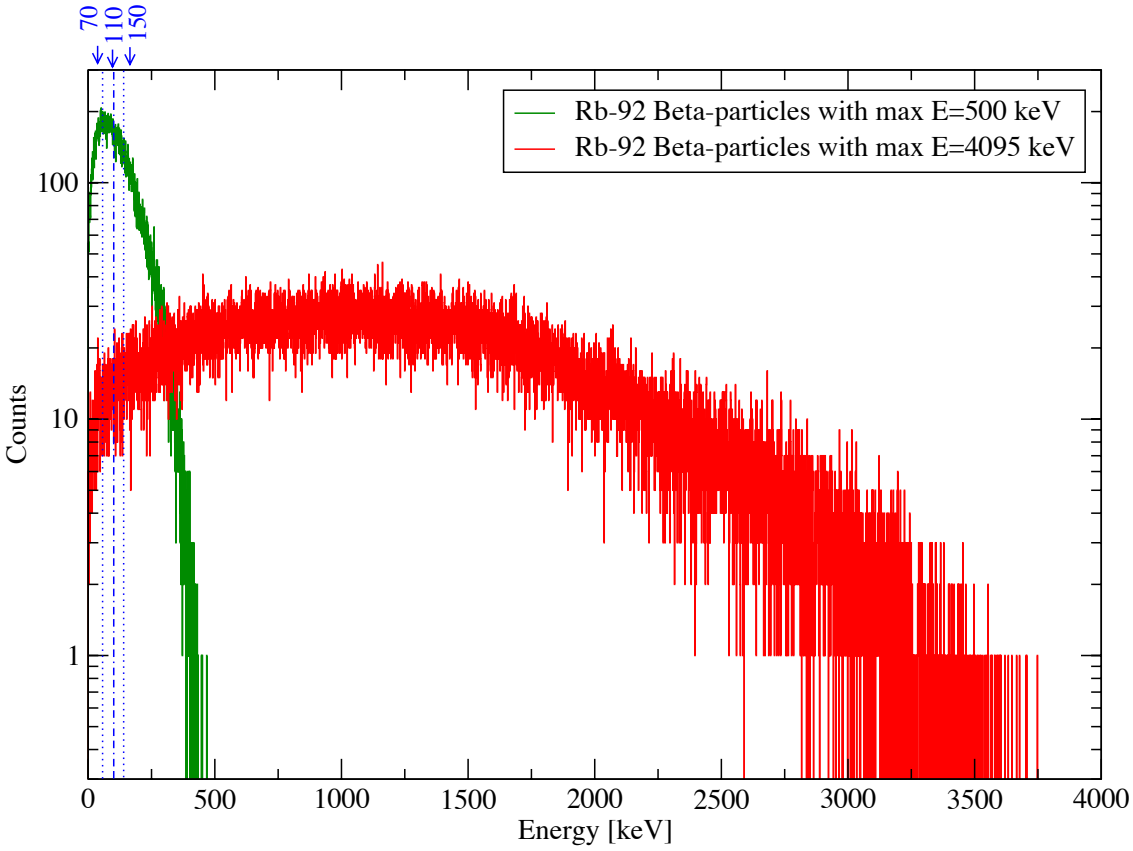

Figure 8.23: SATURN response to β-decay from ^{92}Rb into two levels with maximum β^- energies of 500 keV and 4095 keV. They are compared to the energy thresholds of 70 keV, 110 keV and 140 keV.

8.5.3 Results of ^{104,106}Nb to ^{104,106}Mo decay

The XSAT model will be used to help interpret experimental results by understanding the γ-ray sensitivity of the SATURN detector. To achieve this, mono-energetic γ rays were simulated inside the SATURN model across an energy range up to 9 MeV. Figure 8.24 shows the total efficiency of SATURN to γ rays, which is compared to the XArray total efficiency and the XArray full energy photo peak efficiency. Each point was determined by modelling 1x10^5 events.

The SATURN detection efficiency to low-energy γ rays is significant with values >50%

for energies below 150 keV. This function decreases to a value of 10% at 9 MeV. The spectral response to these γ rays is broad with no discernible full-energy peaks as shown in Figure 8.25. The total efficiency[§] of the XArray (green in Figure 8.24) is used to compare the total detected counts in each detector as a function of energy. The XArray total efficiency has a slight upward trend at high energy due to the increasing probability of the pair-production.

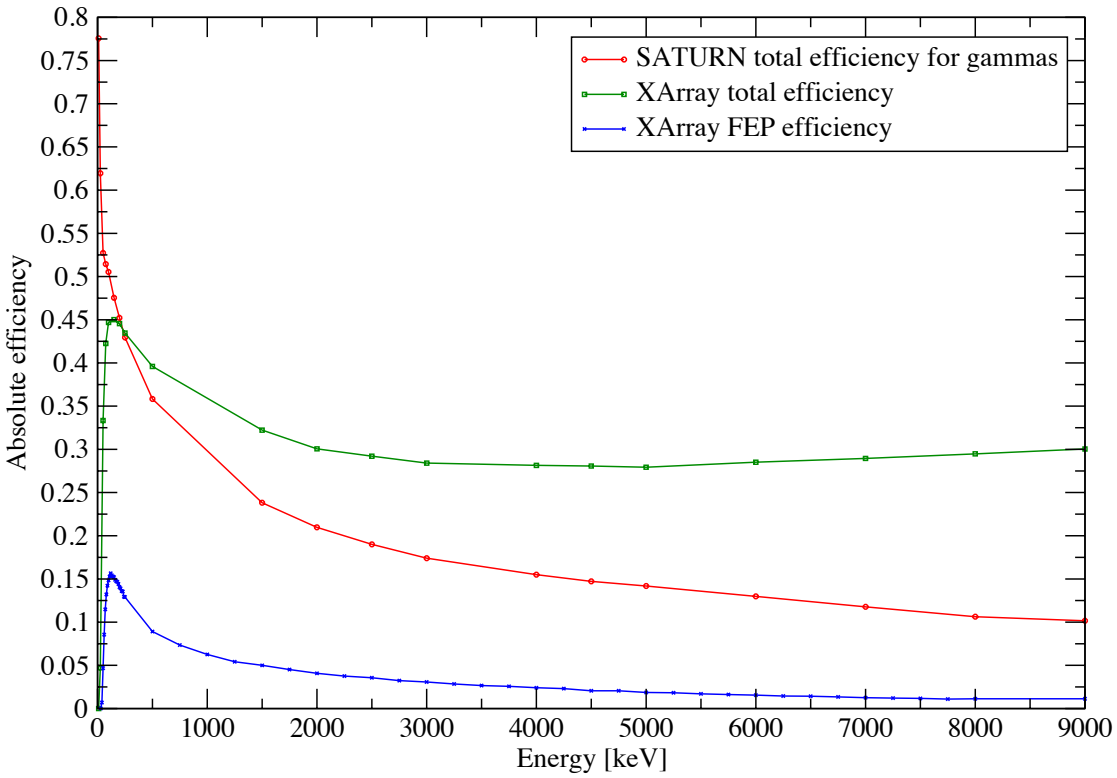

Figure 8.24: Model of the SATURN response to mono-energetic γ rays compared to the XArray total and Full Energy Photopeak (FEP) efficiencies. In the case of SATURN, the efficiency for observing any registered energy above threshold is determined.

Application to the cases of ^{104,106}Nb will entail modelling the β-particle and γ-ray energies specific to particular energy levels as the decay scheme is being developed. The decay schemes for ^{104}Mo and ^{106}Mo are not yet finalised.

8.6 Discussion

The SATURN and XArray models developed in this work are complicated by virtue of the many unknown parameters that are required for accuracy. Most of these parameters were determined by validating aspects of the model to experiment, although they are also often dependent upon each other. There are, however, some parameters that will vary for each measurement depending upon the experimenters - an example is the relative positions of clovers in the case of the XArray model. These reproducibility issues could be solved with

[§]Total efficiency is the result of all interactions, not just full-energy photo peak (FEP) detection.

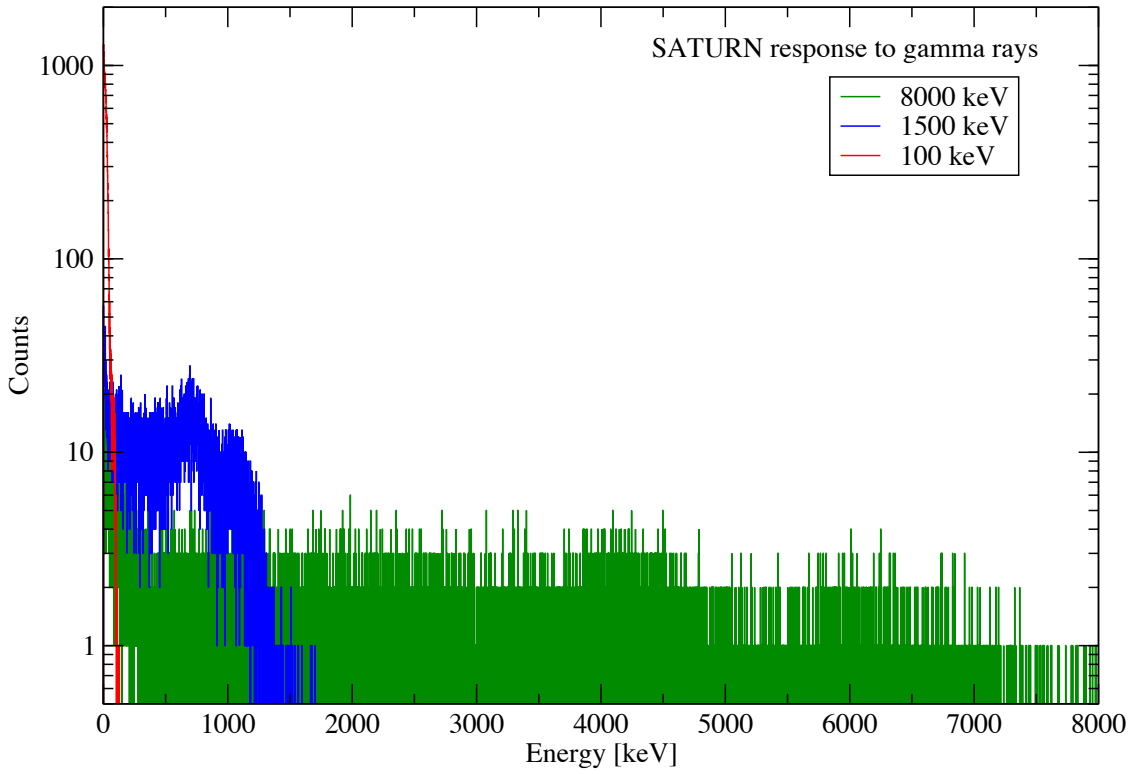

Figure 8.25: SATURN spectral response to mono-energetic γ rays.

the addition of physical stops and more controlled positioning via engineering. In lieu of these steps, the model will have to incorporate variability into the results.

Understanding the SATURN detector responses from the experimental calibrations was difficult owing to the complicated optical pathways within the plastic scintillator and unknown physical properties of the β^- calibration sources. Although SATURN was never designed as a spectrometer, the majority of the response characteristics are successfully reproduced by the model. The modelling is closely tied to the accuracy of producing the correct beta spectral shapes, generated in this work using the LLNL-BD program. This program did a good job of reproducing the expected β-decay distributions for most sources and was in good agreement with the GEANT4 RDM produced shapes in most cases. The detailed model agreement will have a dependence on the approximations, energy production cuts, and physics used in the Monte Carlo model, full information about these details can be found in Section 3.1.2.

The validated model allowed the understanding of the complicated SATURN response to β-particles and refined the experimental threshold value used for the ^{134m}Sb/^{134}Sb yield ratio experiment. An updated correction to the ratio was found to be broadly consistent with the value determined using less accurate prior simulations. The model was then applied to ^{92}Rb to contribute to the understanding and analysis of experimental data which is still being evaluated. The complicated interaction of γ rays with the XArray and SATURN was modelled to help in the interpretation of the experimental results for β-γ spectroscopy in ^{104,106}Mo.

The SATURN model can be improved by additional calibration measurements with better known source geometries. The XSAT model in its present state, is a useful tool for interpreting the complex radiation interactions within XArray and SATURN. Both models are available for the interpretation of additional experiments if required.

Chapter 9

Conclusions

The original thesis undertaking was to re-commission a large NaI(Tl) detector (ATAGS) and implement TAGS measurements for neutron-rich radioactive ions produced from CARIBU, with a focus on measuring decay data where there were gaps in knowledge. This required an accurate Monte Carlo model to interpret the complicated spectra produced by the TAGS method, characterisation of the ATAGS detector, and understanding the physical properties of, and interactions within, NaI(Tl), that can influence a TAGS measurement. A Monte Carlo model of ATAGS was developed using GEANT4 (Chapter 3) and aspects of this model were tested against these characteristics. In lieu of access to ATAGS that was located in Chicago, detection properties were investigated by using several NaI(Tl) detectors with different physical characteristics (Chapter 4). Deconvolution and analysis tools were developed in preparation for the experimental measurements

A campaign of measurements at CARIBU was undertaken in 2015 to re-commission ATAGS and measure the decays of ^{141}Cs, ^{140}Cs, ^{140}Xe, and ^{104}Nb/^{104}Nb (Chapter 5). The ATAGS with a tape station was re-commissioned at ANL but was found to have a degraded energy resolution when compared to previous work when ATAGS was operated at INEL. Nevertheless, measurements of ^{141}Cs, ^{140}Cs, and ^{140}Xe were undertaken, requiring separation of isobaric decay components (Chapter 6), before deconvolution could be applied to evaluate β-feeding intensities (Chapter 7). There is agreement for the overall spectral shape of ^{141}Cs and ^{140}Cs in this work compared to the INEL results, but deconvolution was limited because of the afore-mentioned degraded energy resolution. Xe-140 was measured using the TAGS method; to date there is no previous TAGS measurement of this nuclide and the present data is highly suggestive of considerable β-feeding intensity above 2.5 MeV was observed for the first time. For all of the nuclides studied (^{141}Cs, ^{140}Cs and ^{140}Xe) we have found discrepancies between the measured spectra and the expected results based upon modelling using evaluated data. The currently accepted evaluated data are thus shown to be incorrect or incomplete for these cases.

A second technique was added to this thesis in the form of β - γ decay spectroscopy using the XSAT detector array. The XSAT was installed and operated at CARIBU in 2015 measuring ^{134m}Sb/^{134}Sb, ^{92}Rb and ^{104,106}Mo. Each of these experiments required modelling of the XArray and SATURN detectors to interpret experimental data. A detailed and complete model of SATURN and the XArray was developed in this work, using GEANT4. The model was built using some known parameters and determining others by validation of experimental results. The model was implemented to predict key properties for the three experiments and contribute specific aspects towards the interpretation of the experimental results (Chapter 8).

In both the ATAGS and XSAT cases, it was found that inclusion of optical photon transport was necessary and/or provided important insight into the operation of the

detector. Unfortunately, such modelling requires a 100 fold or more increase in the computational time (see Section 4.6). In the case of ATAGS, the photon modelling was necessary to understand gain matching procedures and ensure the detector was understood, but once done, later modelling only required energy deposition to be recorded. In contrast, the split nature of the scintillator in SATURN meant that photon modelling is essential to truly describe the detector response.

Although the SATURN system was not meant to be used as a spectrometer, future designs could benefit from a symmetric collection of scintillator photons. The compact geometry requirements for SATURN and the need to reduce attenuating materials in the forward direction may be accomplished through the use of fibre-optic cables and waveguides. This would allow the detection of photons via PMTs or Silicon PMTs to occur at an alternative location and negate the current space restrictions.

While the delays in bringing CARIBU online have meant that only limited new experimental information on neutron-rich nuclei has been obtained as a direct result of this thesis, the extensive modelling performed has had, and will have, further impact on experimental results obtained at the CARIBU facility.

Appendix A

NaI(Tl) detectors used in this work

A direct characterisation of ATAGS by the author was limited due to it being located either in Chicago, Illinois or Lowell, Massachusetts, during the project. In lieu of access to ATAGS, the characteristics of NaI(Tl) detectors were investigated through the use of a number of smaller scintillators, each having a different size, geometry, manufacturer and/or age. The age and condition of each of the detectors varied, giving a wide range of properties for characterisation.

Four NaI(Tl) detectors used in this work were sourced from three laboratories, Argonne National Laboratory (ANL), the Australian National University (ANU) and the Australian Nuclear Science and Technology Organisation (ANSTO). The detectors were given an abbreviated name according to the owner and their size in inches (diameter x length). They are ANL3x3, ANL4x4, ANU5x5 and ANSTOwell6x5. They all share a common cylindrical shape that varies in size and they all use a single conventional PMT. The detector details are given below in order of increasing size.

ANL3x3

The ANL3x3 NaI(Tl) detector is the smallest detector used in this work and is a common geometry and design used in industry and research for γ-ray spectroscopy. Obtained from ANL, this detector has a non-detachable crystal, and is used with a Voltage Divider (VD) that is detachable and does not include an in-built Pre-Amplifier (PA). The ANL3x3 is pictured in Figure A.1a.

ANL3x3 properties:

- Crystal dimensions: 76.2 mm (3 inch) diameter x 76.2 mm (3 inch) length;
- Harshaw type 12S12/3;
- PMT: 3-inch fixed;
- separable VD, PA not included; and
- 2.3% of the volume of ATAGS.

ANL4x4

The ANL4x4 NaI(Tl) crystal was salvaged from a detector that was no longer functioning at ANL. The 127 mm PMT tube was determined to be faulty and was removed from

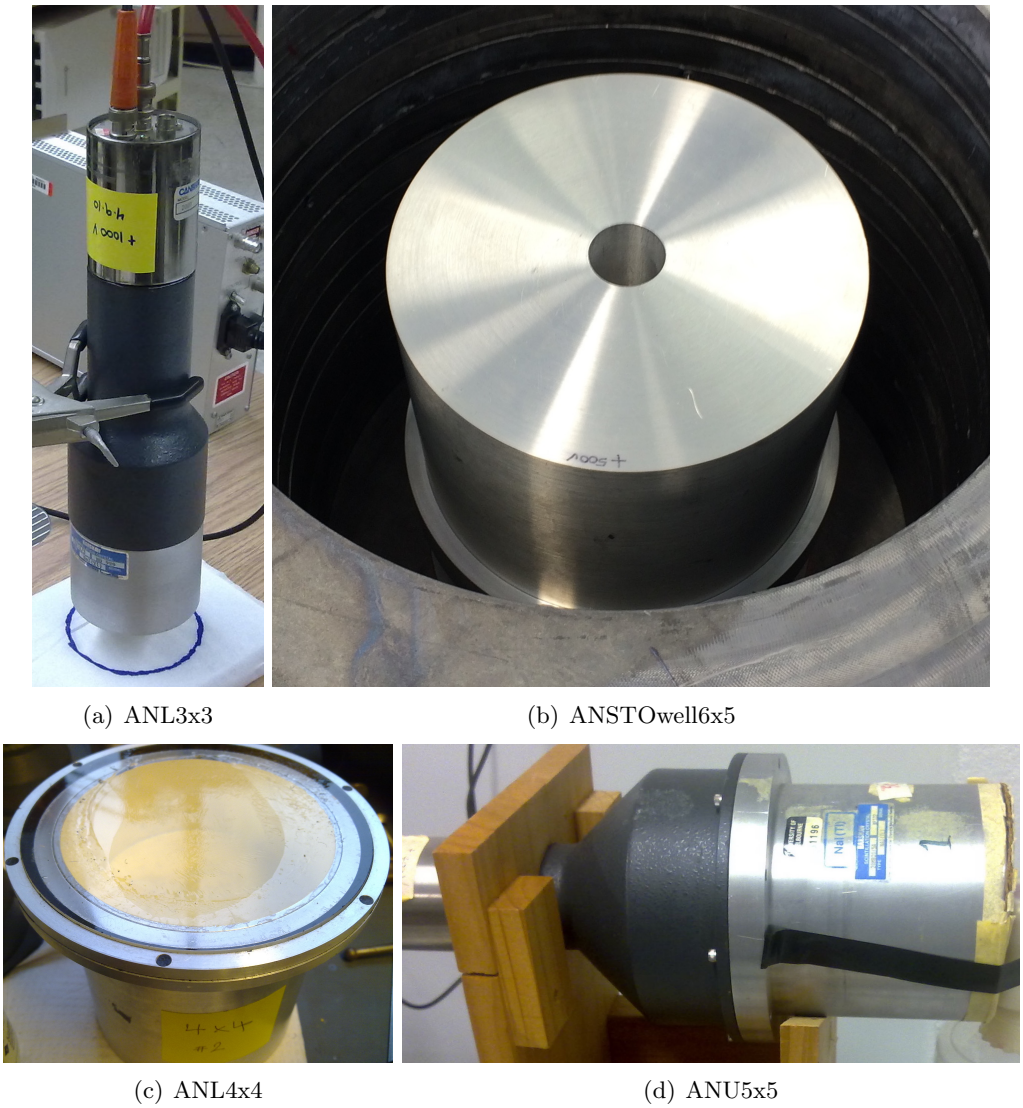

(a) ANL3x3 (b) ANSTOwell6x5

(c) ANL4x4 (d) ANU5x5

Figure A.1: NaI(Tl) detectors used in this characterisation work. (a) ANL3x3: 3 inch by 3 inch Harshaw detector at ANL, (b) ANSTOwell6x5: a 6 inch by 5 inch well type detector at ANSTO (c) ANL4x4: 4 inch by 4 inch detector used to test the PMTs at ANL (d) ANU5x5- 5 inch by 5 inch detector at the ANU.

the crystal; the crystal is shown in Figure A.1c. The NaI(Tl) was visually seen to be transparent and clear, but contained some optical de-coupling from the glass around the edges likely due to physical stress on the crystal from mounting. The crystal was used to couple to the ATAGS PMTs to compare the functioning of the tubes.

ANL4x4 properties:

- Dimensions: 127 mm (4 inch) diameter x 127 mm (4 inch) length;
- unknown manufacturer;
- PMT: detachable- not working; and
- 5.5% of the volume of ATAGS.

ANU5x5

The ANU5x5 is shown in Figure A.1d and was used to investigate the increased volume size of NaI(Tl). While the PMT was detachable, this was not required as it was found to be working.

ANU5x5 properties:

- Dimensions: 131 mm (5.2 inch) diameter x 118 mm (4.6 inch) length;
- Harshaw type 20MB20/5A;
- PMT: 5 inch single tube, detachable;
- VD detachable; and
- 10.7% of the volume of ATAGS.

ANSTOwell6x5

The ANSTOwell6x5 detector is shown in Figure A.1b. This well-type detector was used to investigate the effects of a well geometry, while maintaining the simplicity of a single PMT for light collection.

ANSTOwell6x5 properties:

- Dimensions: 159 mm (6.3 inch) diameter x 120 mm (4.7 inch) length;
- Well dimensions: 25.5 mm (1 inch) diameter x 76.6 mm (3 inch) length;
- Saint Gobain 6HW5/5;
- PMT: 5 inch single tube;
- detachable VD/PA in one unit; and
- 15.7% of the volume of ATAGS.

Appendix B

Validating the ATAGS model of energy deposition - additional examples

A number of regularly used γ-ray sources were simulated using the ATAGS model, with the resultant spectra being energy broadened using the script described in Section 4.5.2. Examples of ^{60}Co and ^{110m}Ag are compared in Section 4.5.5. This Appendix provides two additional comparisons (^{137}Cs and ^{24}Na) to evaluate the effectiveness of the ATAGS model.

B.1 ^{137}Cs

The ATAGS model of ^{137}Cs is compared to the digitisation of Figure 16 from Greenwood [Gre92b] in Figure B.1. The model and the fitting have the same details as the ^{60}Co example in the previous section. The measured spectrum shows a distinct broad shoulder extending from the nominal 662 keV γ-ray energy up to 1400 keV. The β energy for a ^{137}Cs decay is 514 keV; much of this energy is assumed to be attenuated within the dead layers before reaching the NaI(Tl). The GEANT4 simulation shows some of the contribution of this β-component adding to the γ ray, but this model does not reflect accurately the setup for ATAGS used by Greenwood *et al.* in Reference [Gre92b]. It is more reasonable to assume that the shoulder is from accidental coincidences leading to the summing of two γ-rays from separate events, noting that 2×662 keV = 1324 keV$\approx$1400 keV. The GEANT4 model appears to be a better fit to the experimental data than Greenwood's simulation, but, given the (small) inaccuracies of the digitisation method to acquire the experimental data, this may not be significant.

B.2 ^{24}Na

^{24}Na decays to ^{24}Mg via β^- decay with a Q-value of 5516 keV. Greenwood measured this radionuclide using ATAGS with different input count rates, shown in Figure B.2, which is the digitisation of Figure 2 from Reference [Gre92b]. This information is an opportunity to bench-mark the ATAGS model against a more difficult case with a larger Q-value, whilst also introducing count-rate dependent complexities.

Using the techniques as described in the previous sections, ^{24}Na decays were modelled for a source located in the bottom of the well in ATAGS. This was then fitted to each of the four experimental spectra of Figure B.2 for count rates of 63 kHz, 28 kHz, 6.8 kHz and

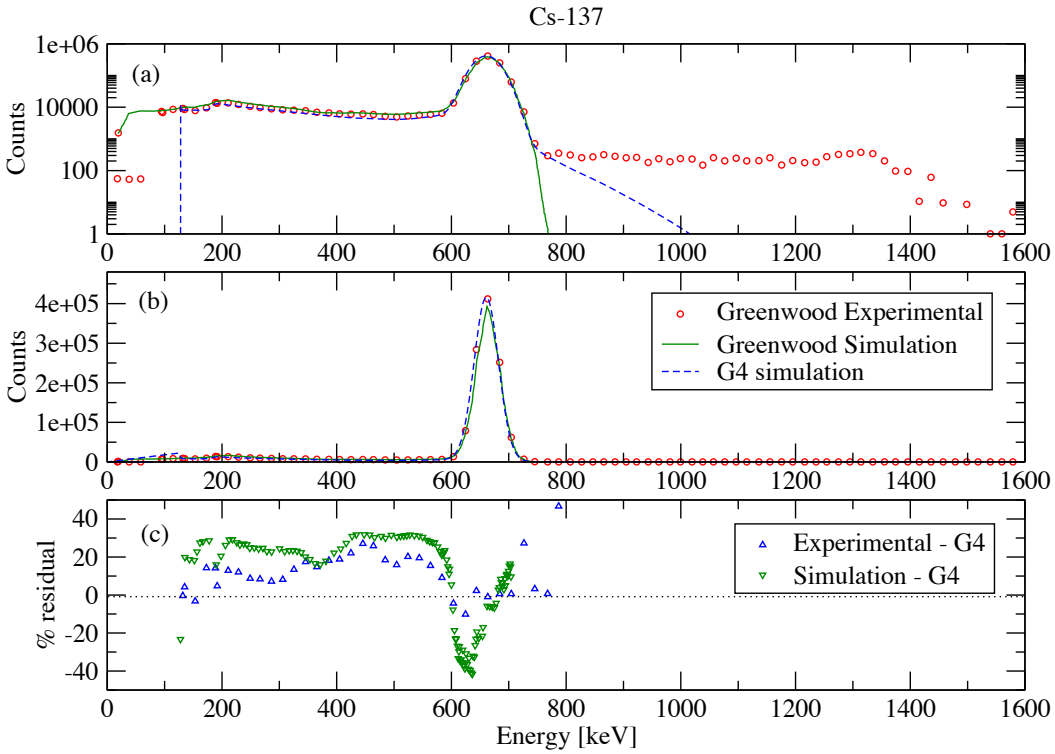

Figure B.1: Comparison of the ATAGS simulation for ^{137}Cs decay with Greenwood's 1992 measurement (taken from Figure 16 of Greenwood [Gre92b]). The GEANT4 simulation is a least squares fit of the raw simulation data to the digitised Greenwood results, varying the energy gain, FWHM and count-scaling parameters. Data is shown with the y-axis in (a) log scale, and (b) linear scale. The percentage residuals for each fit are shown in (c).

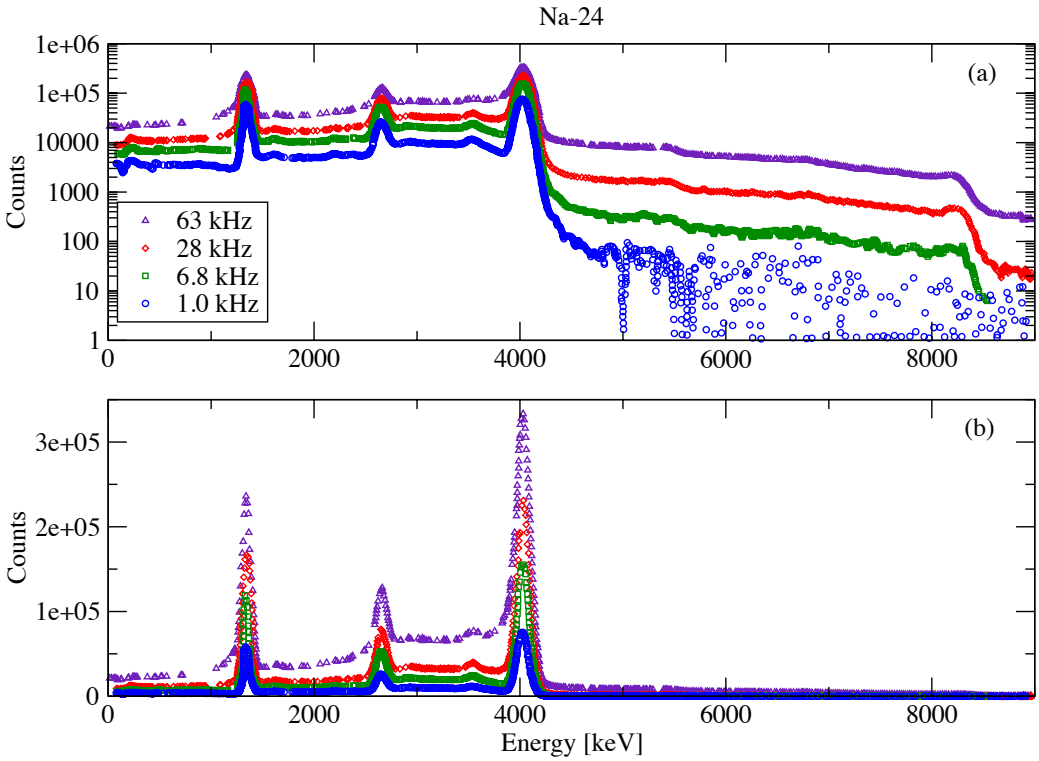

Figure B.2: Digitised results from Greenwood's Figure 2 for ^{24}Na sources at different count rates [Gre92b], shown on (a) log and (b) linear scales.

1.0 kHz, shown in Figures B.3, B.4, B.5, and B.6, respectively. The fitting routine uses the resolution broadening function described in Section 4.5.2, with FWHM parameters F_1 and F_0 (Equation 4.4). In addition, the fitting also varies the energy coefficients E_0 and E_1 of the digitised experimental data in combination with a scaling factor S. The FWHM coefficients vary as a function of count rate as seen with ATAGS FWHM coefficients extracted from publications, giving a range of values for F_1 from 2.3 to 3.2 as a function of count rate (see Figure 4.9). There are other count-rate effects that are not taken into account for the fits in this section. The fitting routine did not perform well with these data attempting to fit all three peaks at 1369 keV, 2754 keV and 4123 keV at once. The fit routine tends to remove the peak at 1369 keV as the energy resolutions get broader. In addition, the FWHM F1 coefficients range from 2.973 (63 kHz) to 6.487 (28 kHz), which are outside the expected values determined by Figure 4.9.

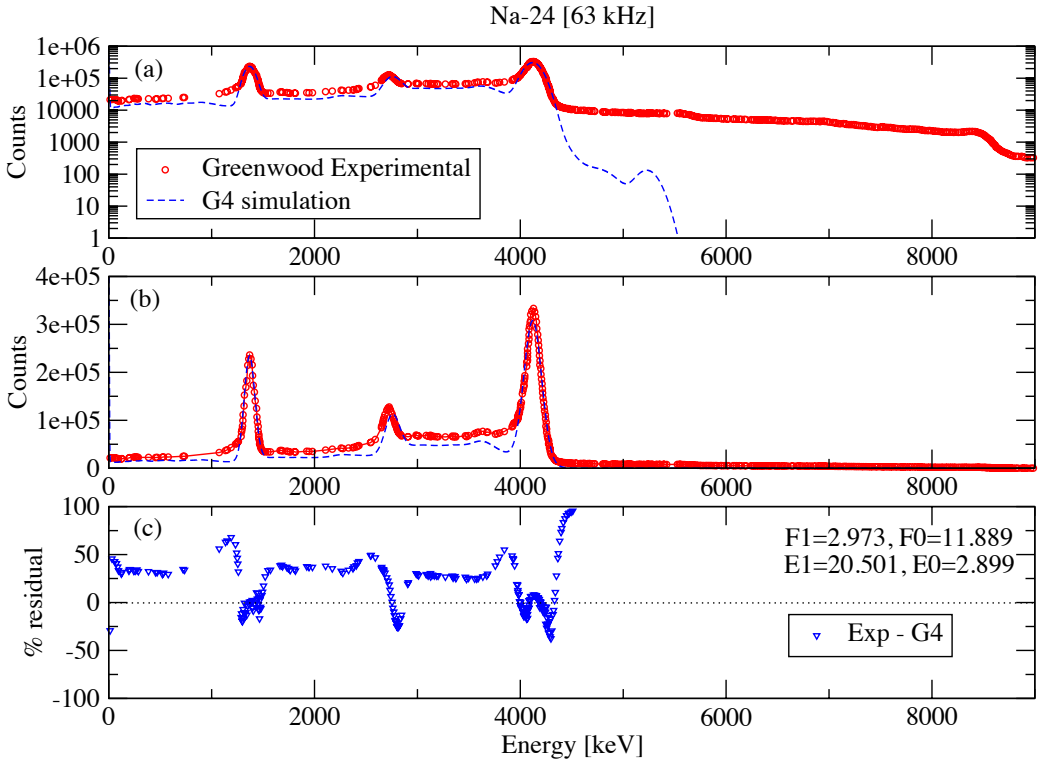

Figure B.3: Spectrum of ^{24}Na from Greenwood's Figure 2 experimental data measured at a count rate of 63 kHz vs GEANT4 simulation [Gre92b]. Data is shown with the y-axis in (a) log scale, and (b) linear scale. The percentage residuals for each fit are shown in (c).

Figure B.3 shows the only spectrum with energy resolution values falling within the nominal range. This fit however has the largest residuals due to the large count rate causing the summing shoulder for energies above the 4123 keV peak. What is also apparent is that the fitting of the centroid position of the 2754 keV peak is not well-aligned with the experiment. The fitting parameters show a distinct non-linear shift of these spectra likely due to an energy shift in the data caused by either count rate effects or non-proportionality. One can only assume that some sort of adjustment has been introduced to the data for the purposes of overlaying these graphs whilst maintaining the peak centroids in the expected positions. With the inference of this adjustment it was recognised that this data-set is not the most appropriate to benchmark the GEANT4 model.

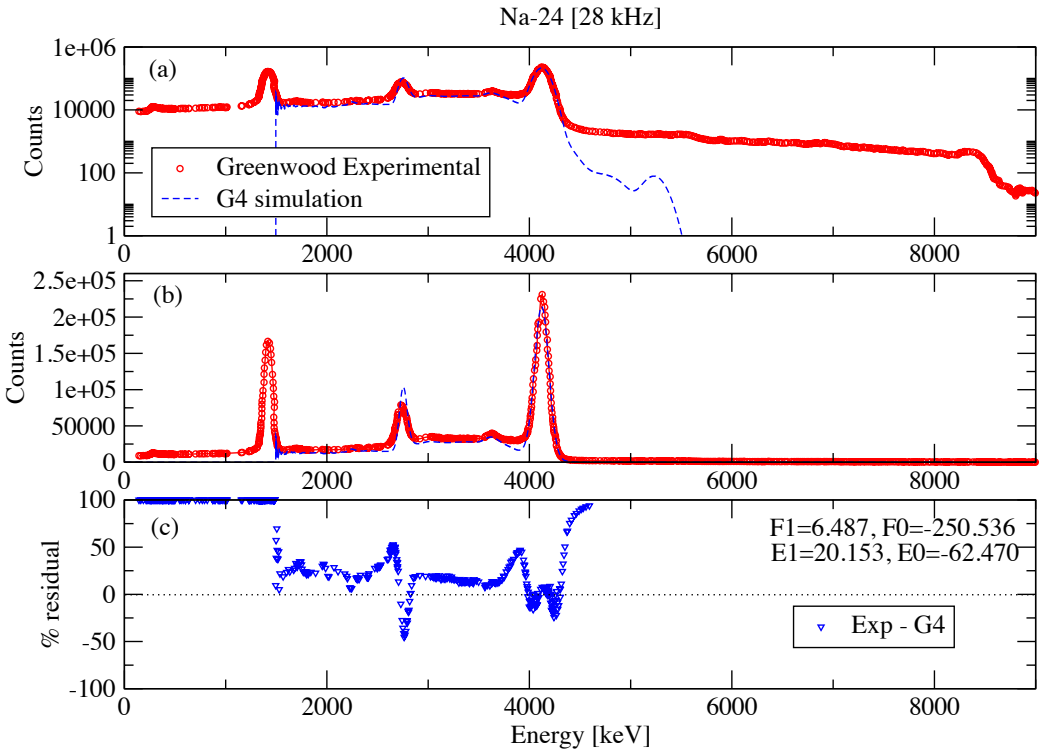

Figure B.4: Spectrum of ^{24}Na from Greenwood's Figure 2 experimental data measured at a count rate of 28 kHz vs GEANT4 simulation [Gre92b]. Data is shown with the y-axis in (a) log scale, and (b) linear scale. The percentage residuals for each fit are shown in (c).

Figure B.7 is another example of a measurement of ^{24}Na taken from Figure 17 of Greenwood [Gre92b]. This spectrum shows a similar rate to the 1 kHz example of Figure B.6, judged by the overall counts and pile-up features beyond the 4123 keV peak. The fit of the GEANT4 model to these data is qualitatively better than the digitised fit of Greenwood's simulation, and the energy coefficients of F1=2.549 and F0 = -26.621 fall within the expected values of Figure 4.9.

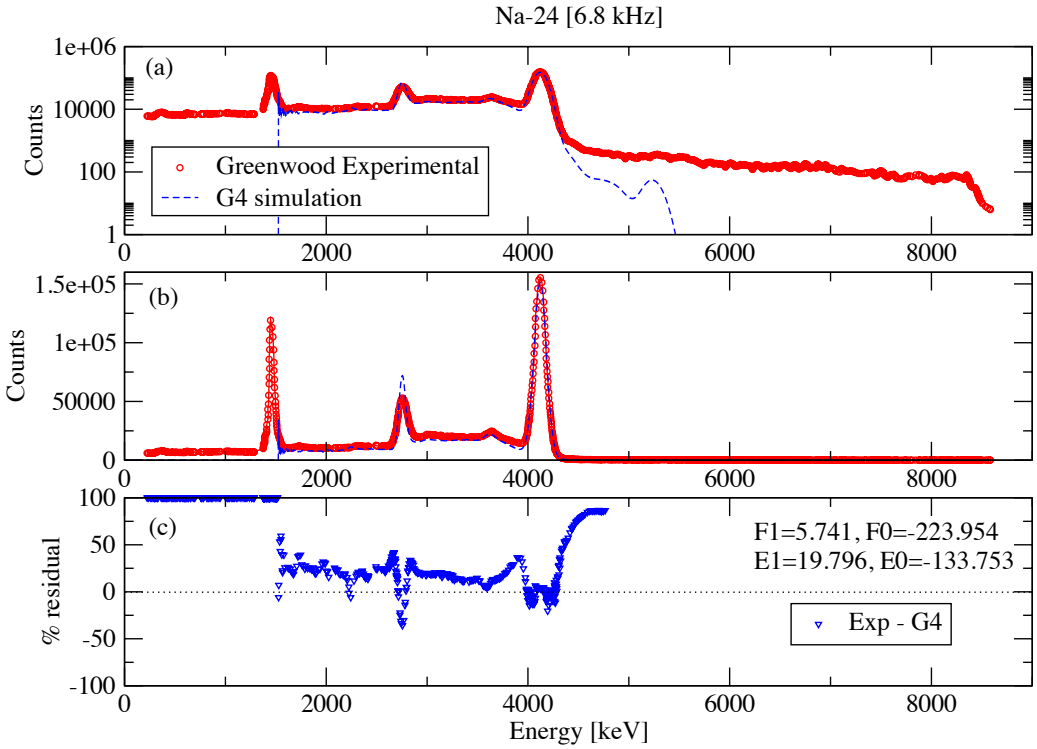

Figure B.5: Spectrum of ^{24}Na from Greenwood's Figure 2 experimental data measured at a count rate of 6.8 kHz vs GEANT4 simulation [Gre92b]. Data is shown with the y-axis in (a) log scale, and (b) linear scale. The percentage residuals for each fit are shown in (c).

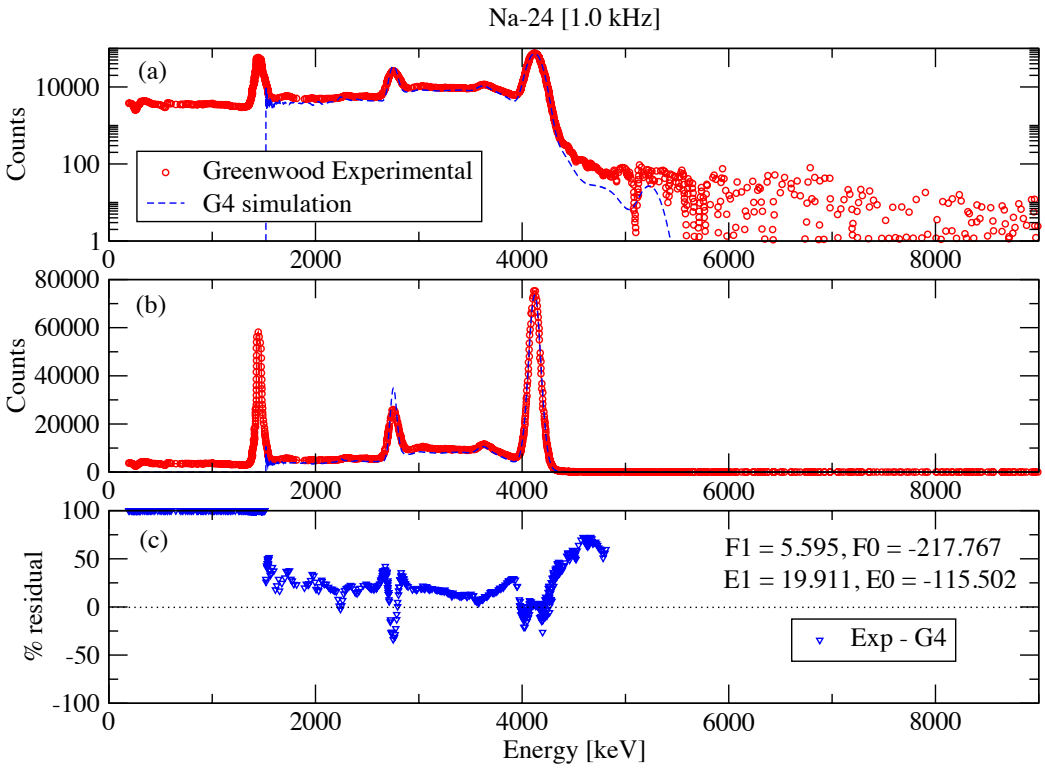

Figure B.6: Spectrum of ^{24}Na from Greenwood's Figure 2 experimental data measured at a count rate of 1.0 kHz vs GEANT4 simulation [Gre92b]. Data is shown with the y-axis in (a) log scale, and (b) linear scale. The percentage residuals for each fit are shown in (c).

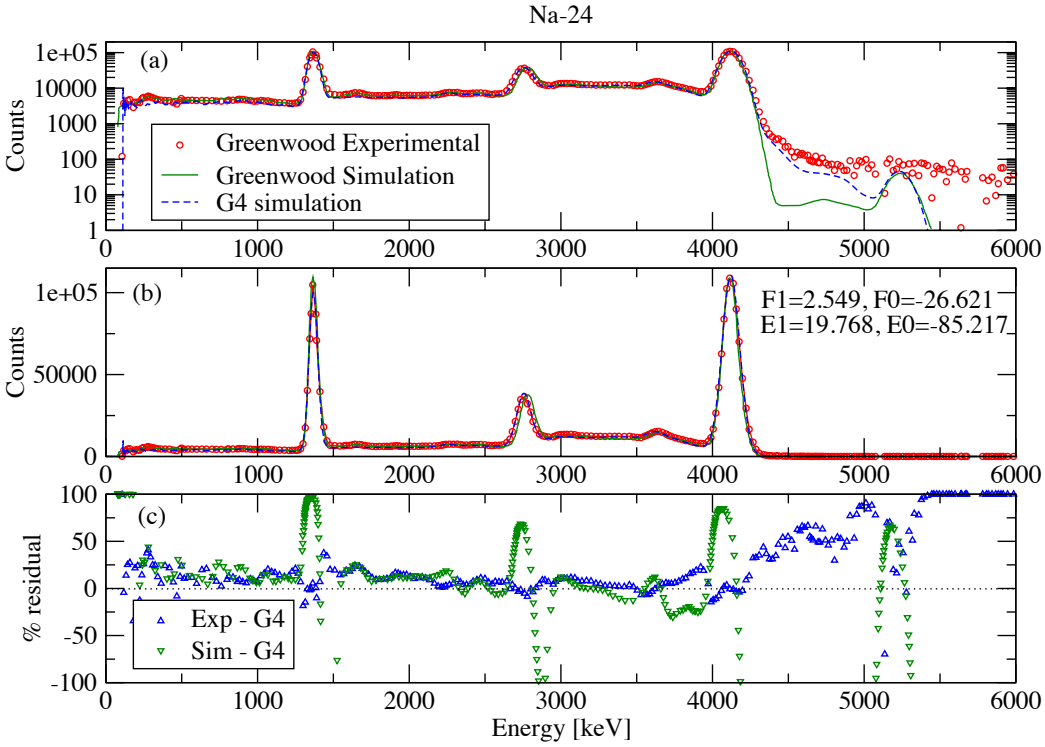

Figure B.7: Digitised results of ^{24}Na from Greenwood Figure 17 compared to GEANT4 simulation [Gre92b]. Data is shown with the y-axis in (a) log-scale, and (b) linear-scale. The percentage residuals for each fit are shown in (c).

Appendix C

High count rates - additional examples with smaller detectors

In addition to ATAGS, high-count rate affects were investigated using the ANL3x3, ANU5x5 and ANSTOwell6x5 detectors that were described in Appendix A. This appendix provides further details on these measurements which guided the characterisation of NaI(Tl) for TAGS measurements.

ANL3x3

Using the small ANL3x3 detector to look at the effects of pileup, three ^{60}Co sources of increasing activity were measured with the source placed in the same position against the detector face (fig. C.1). These measurements show a shift in the peak position to higher channels and broadening of the peaks with increasing count rate. There is a significant shift in the peak positions for the 74 kBq source activity and a very slight broadening between the 1 kBq and 11 kBq sources, with further broadening at 74 kBq.

PMTs produce significant dark current as a consequence of the amplification of electrons through the dynodes when under HV. This gives a low amplitude output corresponding to low energy γ-ray energies in a spectrum. A low-level threshold in the acquisition system typically removes these events. As the count rate is increased, the probability of a signal of interest being detected at the same time as this dark current becomes significant. The dark current increases with count rate and the intensity of the dark current can result in pileup with itself. This feature can be seen at approximately channel 50 in Figure C.1, with its intensity increasing as a function of source activity, and its shift in position correlated with the ^{60}Co peaks. It is identified as an artefact of noise pile-up, in normal circumstances at low-count rates it is excluded from a spectrum by means of setting a threshold, but at high count rates, signals gain amplitude through pile-up with other noise and dark-current signals.

The count rate dependence looks to be non-linear as can be seen from comparing the detected and expected rates. For example, the expected count rate of a 74 kBq ^{60}Co source (assuming a detector solid angle of 2π), should yield a count rate about half of the source activity. In the case of the 1 kBq source, the system dead-time was recorded to be 0.2 % giving a total count rate of 0.6 kHz for the same source position. Taking this as the approximated geometrical efficiency for the source to the ANL3x3 detector for ^{60}Co, we would expect count rates of 6.6 kHz (11 kBq source) and 44.4 kHz (74 kBq source). When these measured rates are adjusted by the recorded dead-times of 1.3 % and 6.0 %, these become 4.2 kHz (11 kBq source) and 19.0 kHz (74 kBq source). There is an increased loss of corrected counts as the system become more loaded. There are two likely causes

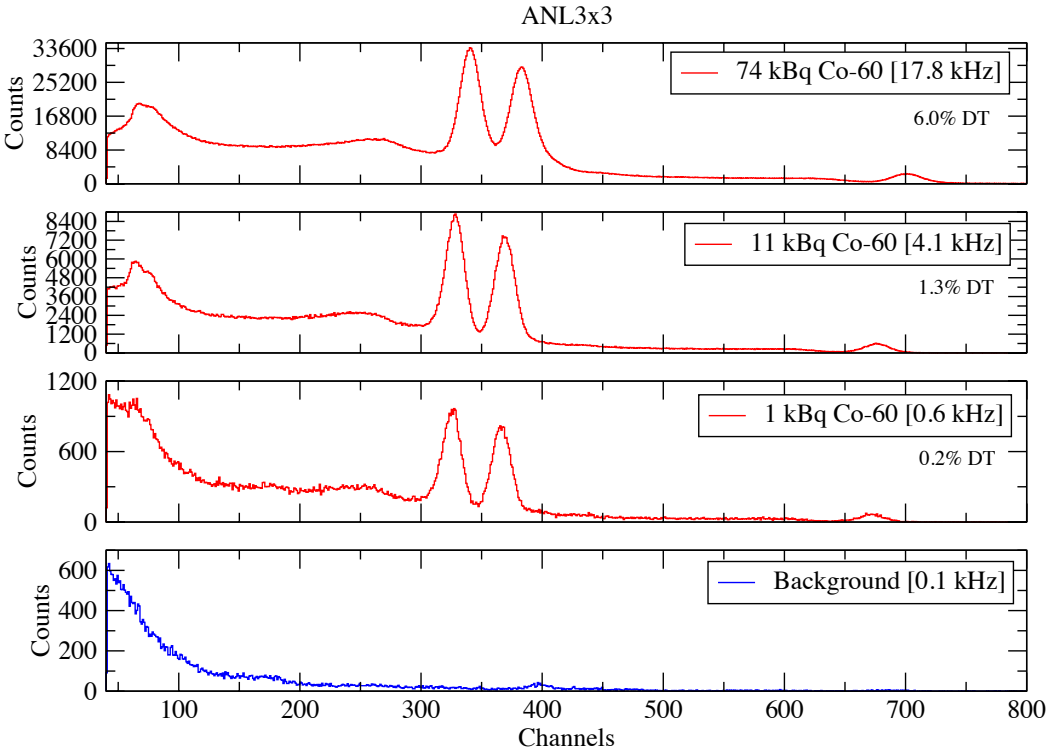

Figure C.1: Response of the ANL3x3 detector response to different activity ^{60}Co sources. The three sources were measured separately, all placed at the same position against the face of the detector. No gain adjustment or background subtraction has been applied, a background spectrum is provided for comparative purposes.

contributing to the losses: the dead-time is not accounted for in the complete acquisition system, and the dead-time accounting methods of the system have become overwhelmed.

The sum peak (2506 keV) is visible in each case of Figure C.1. The intensity of this peak is a function of detector solid angle, since γ rays emitted in different directions will have a higher probability of being simultaneously detected as the angle subtended by the detector is increased. Since the solid angle of the source subtended by the detector remains the same in each case, the relative magnitude of the sum peak compared to the individual peaks remains constant. The relative position of the sum peak compared to the single γ-ray centroids shows very little non-proportional effect for this detector (see Section 4.4.2), although there is an overall gain shift of peaks at higher rates, as already noted.

ANU5x5

Figure C.2 shows the much larger ANU5x5 detector with the ^{60}Co source count rate being varied by means of changing the source to detector distance along the detector symmetry axis. These background subtracted spectra are overlaid and show a trend of peaks shifting with count rate, similar to ANL3x3 (Figure C.1). The shift occurs for a count rate at or greater than 4.9 kHz, below which there seems to be no significant difference. This can be compared to the 4.6 times smaller ANL3x3 detector, where the shifting is seen to start at a much lower rate.

The ^{60}Co sum peak (2506 keV) is more prominent at the closest source detector position (0 cm) as expected, where the solid angle subtended is the greatest. The approximate energy calibration was performed using the lowest count rate spectrum using only the 1173 keV and 1332 keV γ-ray peaks. The limited energy range means that only a relative comparison of the mono-energetic peaks can be made and the positions of the sum-peak should not be compared.

A similar pileup energy shift with count rate is seen for two different activity ^{137}Cs sources at a distance of 10 cm from the detector (Fig. C.3). An additional high count rate feature is shown in the spectrum in the form of a sum peak. The high count rate with the increased detector volume increases the probability of uncorrelated γ rays from a source being measured simultaneously. In this case, two 662 keV (channel 1900) γ rays can be detected at the same time in the scintillator to produce a sum peak at 1324 keV (channel 3800) and a continuum up to this point. The sum peak of a ^{60}Co spectrum is due to the correlated γ rays of different energies being emitted simultaneously in a single decay and acts as a signature of that decay in the TAGS method (see Section 2.3). Figure C.2 demonstrated that one of the effects of high count rates can be to produce a summing event that is an artefact of the high event rate and detector volume; this could be confused as the signature of β^- decay level feeding and must be avoided for the TAGS method to succeed.

Figure C.4 shows the ANU5x5 detector response to the more complicated source ^{56}Co, as a function of count rate. In the first spectrum (Fig. C.4a), the ^{56}Co source is in a fixed position while another source (^{60}Co), is used to increase the total count rate by variation of source to detector distance. The peaks due to ^{60}Co at around channel 3000 are clearly dominant at 15.1 kHz total count rate. There is a slight broadening in the ^{56}Co peaks with count rates below 6.3 kHz and significant broadening above this number. Of note is a discernible shift of peak positions to lower energies for the higher count rate, against the trend seen so far. This observation is believed to be a characteristic of certain PMT designs in which the electric current due to the high rate exceeds the supply, resulting in

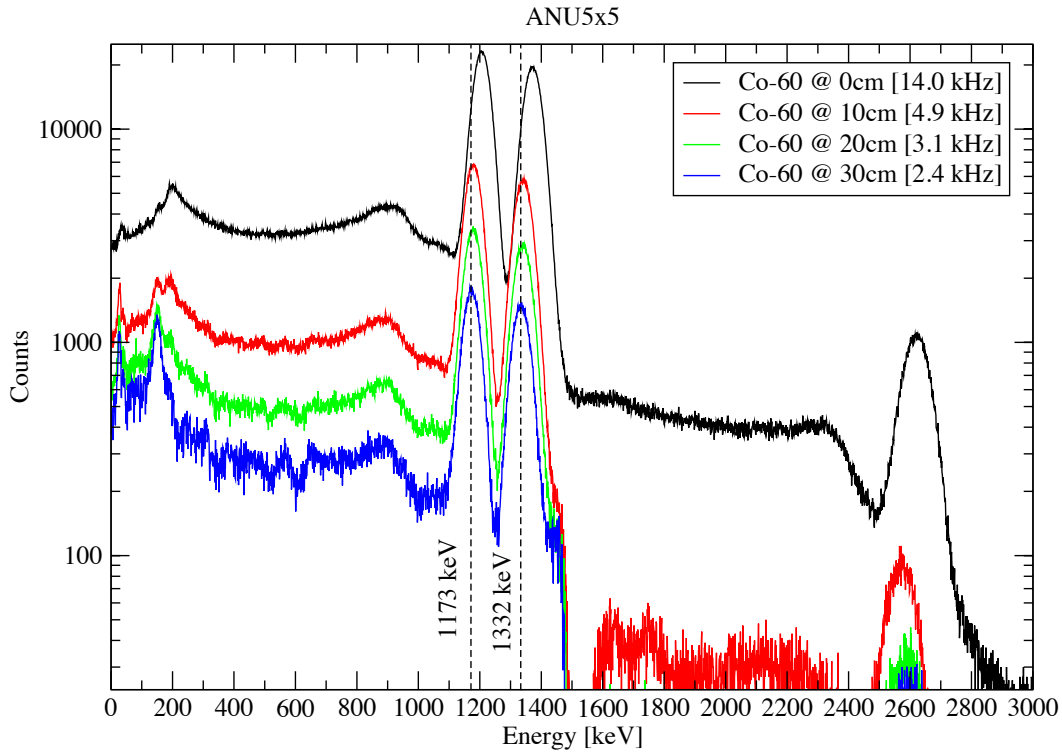

Figure C.2: Response of the ANU5x5 detector to count-rate variations measured with a ^{60}Co source. Compared to Figure C.3, in this case the ^{60}Co source is measured at different distances from the front of the detector so as to vary the count rate. A shift in peak positions is apparent. An energy calibration performed using the spectrum with the lowest count rate and then the same gain is applied to all spectra. A background spectrum has been subtracted.

lowering of the dynode voltage in the tube [San84].

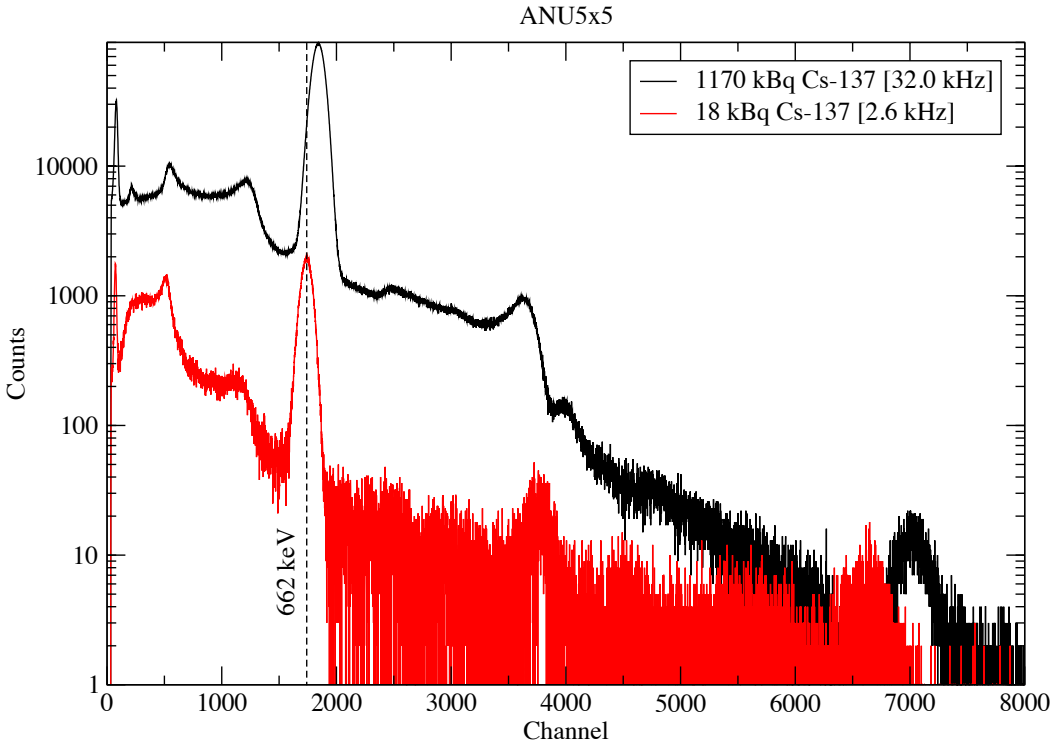

Figure C.3: Response of the ANU5x5 detector to two ^{137}Cs sources with different activities. Compared to Figure C.2, in this case the position of the ^{137}Cs source is the same 10 cm from the detector face for two sources with different activities. Background-subtracted spectra are shown.

This effect is exaggerated in Figure C.4b, showing the variation of count rate of a very active ^{56}Co source attained by changing the source to detector distance. It is believed that the resolution broadening in this case is also a result of the voltage drain due to high PMT currents. The effects of current drain with a PMT are outlined by Sandorfi *et al.* [San84] as being from 3 sources, charging of the internal structures, gain shifts due to a change in the work function of the dynode surfaces and current flow through the dynode chain at high rates. This work done at Brookhaven National Laboratory (BNL) to identify and limit count rate gain changes led to the re-design of the original ATAGS PMTs by the company RCA (type RCA S83021E).

ANSTOwell6x5

Moving to a large well-type detector (ANSTOwell6x5 has 6.8 times the active detector volume of ANL3x3), measurements were made with a different set of sources placed at the bottom of the well and at the top of the well for ^{137}Cs (fig. C.5) and ^{60}Co (fig. C.6). The broadening and shift of the peak is shown for the reasonable count rates in ^{60}Co and more pronounced for the very high count rates in ^{137}Cs. The source position at the top of the well shown in Figure C.5, results in approximately 3.6% of the total count rate being due to uncorrelated summing (energies above the 662 keV peak [>channel 1300]). This fraction increases to 8.7% when the count rate is increased by a factor of 1.5. The high count rate of the ^{137}Cs source is only used here for gauging the contribution of the

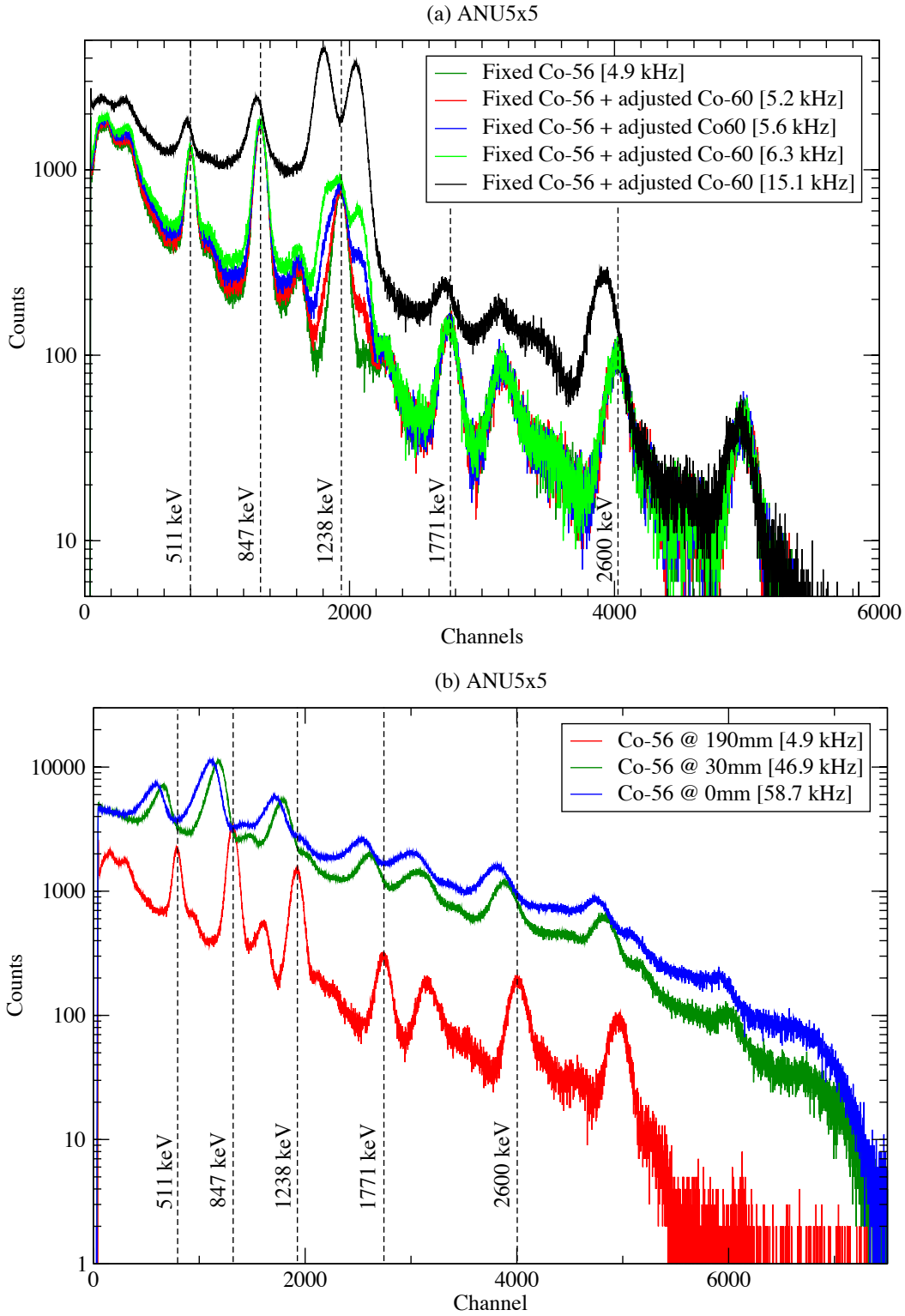

Figure C.4: Response of the ANU5x5 detector to count-rate variations measured with a ^{56}Co source. These figures show the shift of peak positions of ^{56}Co as the overall count rate is varied by (a) changing the distance of an additional ^{60}Co source whilst the position of ^{56}Co is fixed and, (b) changing the distance of the ^{56}Co source. In contrast to Figures C.2 and C.3, the count-rate load causes a shift of the peak positions to lower energies, probably caused by PMT current drain (see text).

uncorrelated summing; it is unreasonable to operate these detectors with high dead times, in this case >65%. The increased noise contribution resulting from the higher count rate is easily identifiable in this spectrum as the low energy spike.

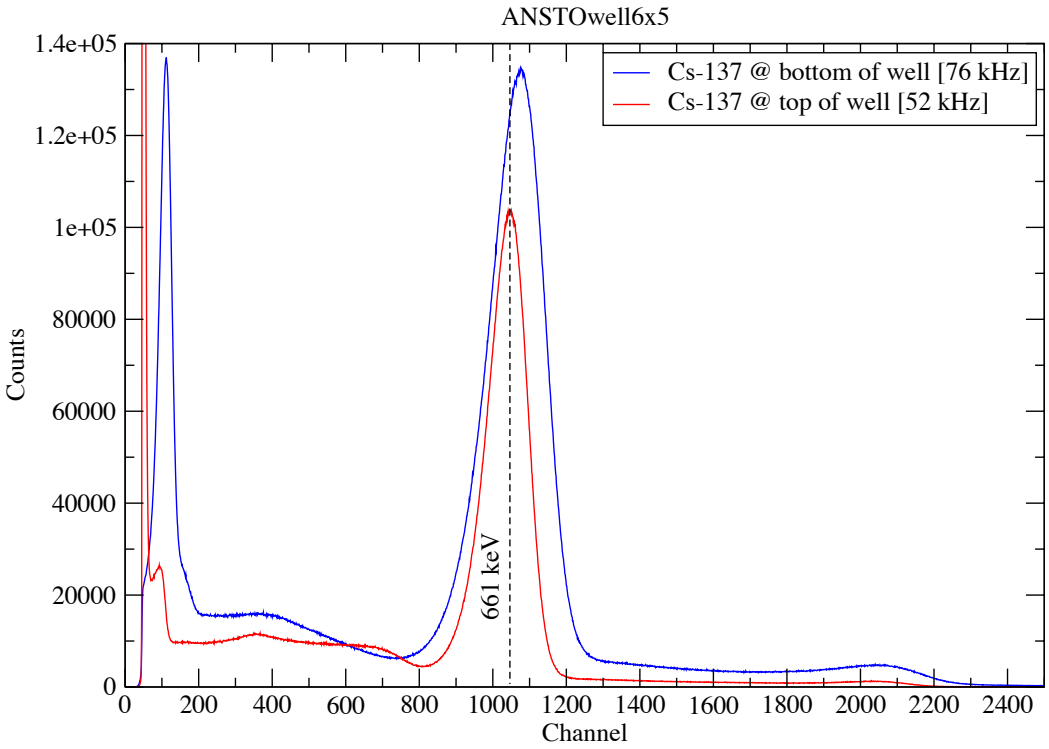

Figure C.5: Spectra from the ANSTOwell6x5 detector with a ^{137}Cs source measured at the top (blue) and bottom (red) of the well. Very high count rates show the increased relative contribution (8.7% Vs. 3.6% of the total count rate) of the uncorrelated summing (>662 keV peak).

Figure C.6 indicates the increase in the correlated summing peak (2506 keV) of ^{60}Co for source positions in and out of the well of the ANSTOwell6x5 detector. The increase of the total counts in the sum peaks (5% to 18%) with the position change for this detector is due mostly to the increased solid angle subtended by the source for correlated events but would include a smaller component due to uncorrelated summing as seen in the previous figure. Of note is the increase in the summing continuum between the 1173 keV and the 2506 keV peaks, which looks to also contribute to the resolution broadening (high-energy tail at higher rates).

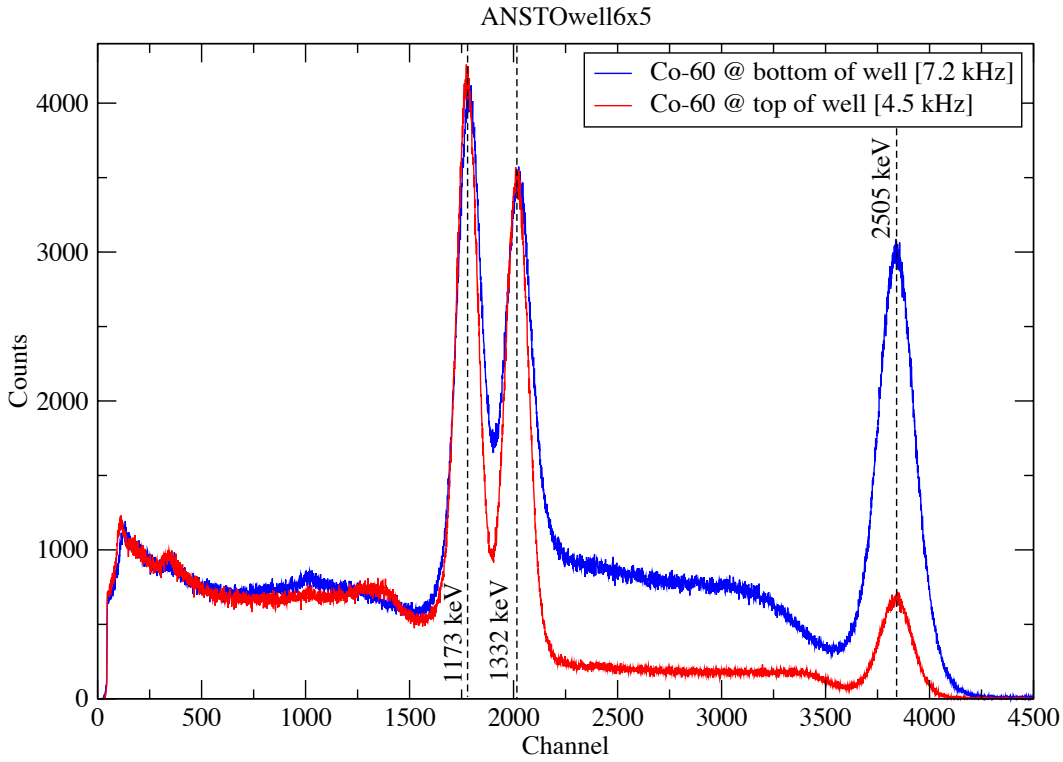

Figure C.6: Spectra from a ANSTOwell6x5 detector with a ^{60}Co source measured at the top (blue) and bottom (red) of the well. A broadening of the peaks on the high energy side is seen at low count rates. There is an increase in the correlated summing contribution due to the source detector geometry; plateau between the 1332 keV peak and 2506 keV sum peak.

Appendix D

Compton coincidence technique measurements

This appendix is a summary of measurements performed as part of this work in collaboration with Gabriel Collin. They are described in more details in the Honours thesis [Col11].

The Compton Coincidence Technique (CCT), introduced in Section 4.4.2, was applied using the ANU5x5 and ANSTOwell6x5 detectors (Section A) in conjunction with a HPGe detector in an attempt to measure the non-proportionality of NaI(Tl) (see Section 4.4.2). The method leverages the Compton interaction process to single out electrons depositing energy in a NaI(Tl) detector, achieved by measuring the corresponding photon energy and emission angle in coincidence with a high-resolution HPGe detector. The objective of the measurement was to directly measure the NaI(Tl) detector optical response to low energy electron interactions in the scintillator with the aim of eventually applying this method to a direct measurement of the scintillator non-proportionality of ATAGS.

Figure D.1 shows examples of the arrangements of the shielding and detectors used in the CCT technique, the ANU5x5 detector and a 25% relative efficiency coaxial HPGe detector. The lead shielding provided a 90% reduction in the background counts in the NaI(Tl) detector. Multiple arrangements were trialed with variations of angle, collimation and source activity, measurements 'TAGS6' and 'TAGS13' are shown in Figures D.1b and D.1c respectively.

Figure D.2 shows the results of three representative measurements all involving a ^{60}Co source with no collimation (Figures D.2a, and D.2b), and two variations of collimated measurement at different angles (Figures D.2c, D.2d, D.2e, and D.2f)). The resulting relative light yields are compared with the Cano-Ott parameterisation (see Section 4.4.2).

The statistics of the measured results were found to be poor compared to the techniques that use dedicated equipment with higher activity sources and longer acquisition times, such as the Scintillation Light Yield Non-proportionality Characterisation Instrument (SLYNCI) [Hul09]. The experiment could be improved by increasing the activity of the illuminating collimated source up to the count-rate limit of the detector, or by counting for very long periods of time. Safety and time limitations for the project constrained both options. Apart from the low statistics, it was concluded that there is a possible offset making it difficult to anchor the response to a definite energy [Col11].

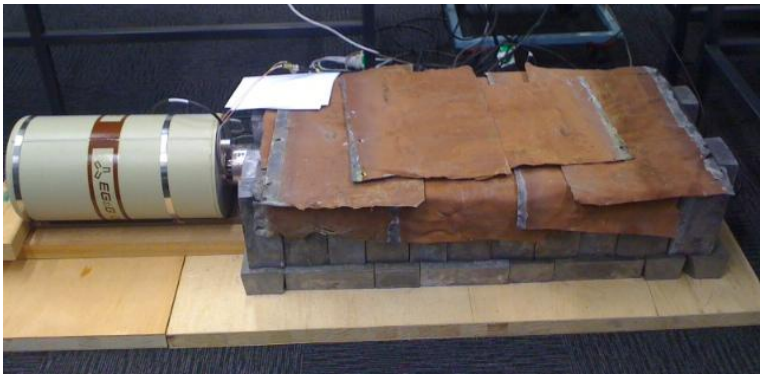

(a)

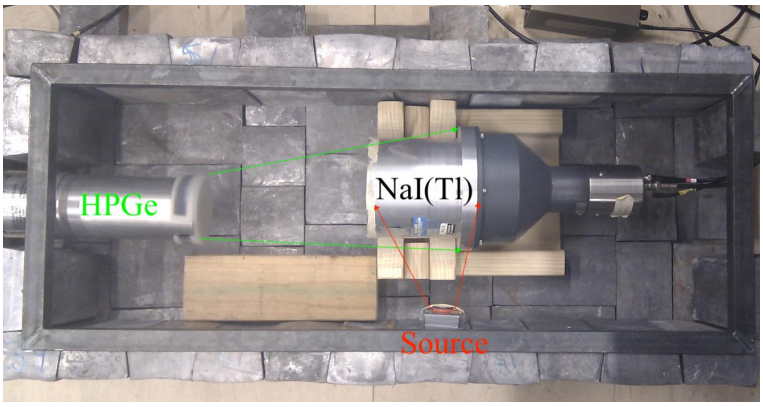

(b)

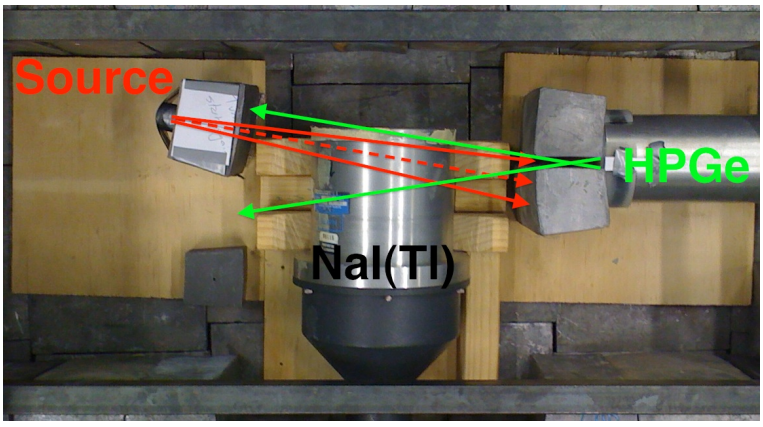

(c)

Figure D.1: Experimental arrangement of the CCT apparatus showing: (a) the lead shielding; (b) TAGS6 measurement geometry consisting of a source, HPGe detector and the ANU5x5 NaI(Tl); and (c) TAGS19 measurement geometry using collimation of the source and detector.

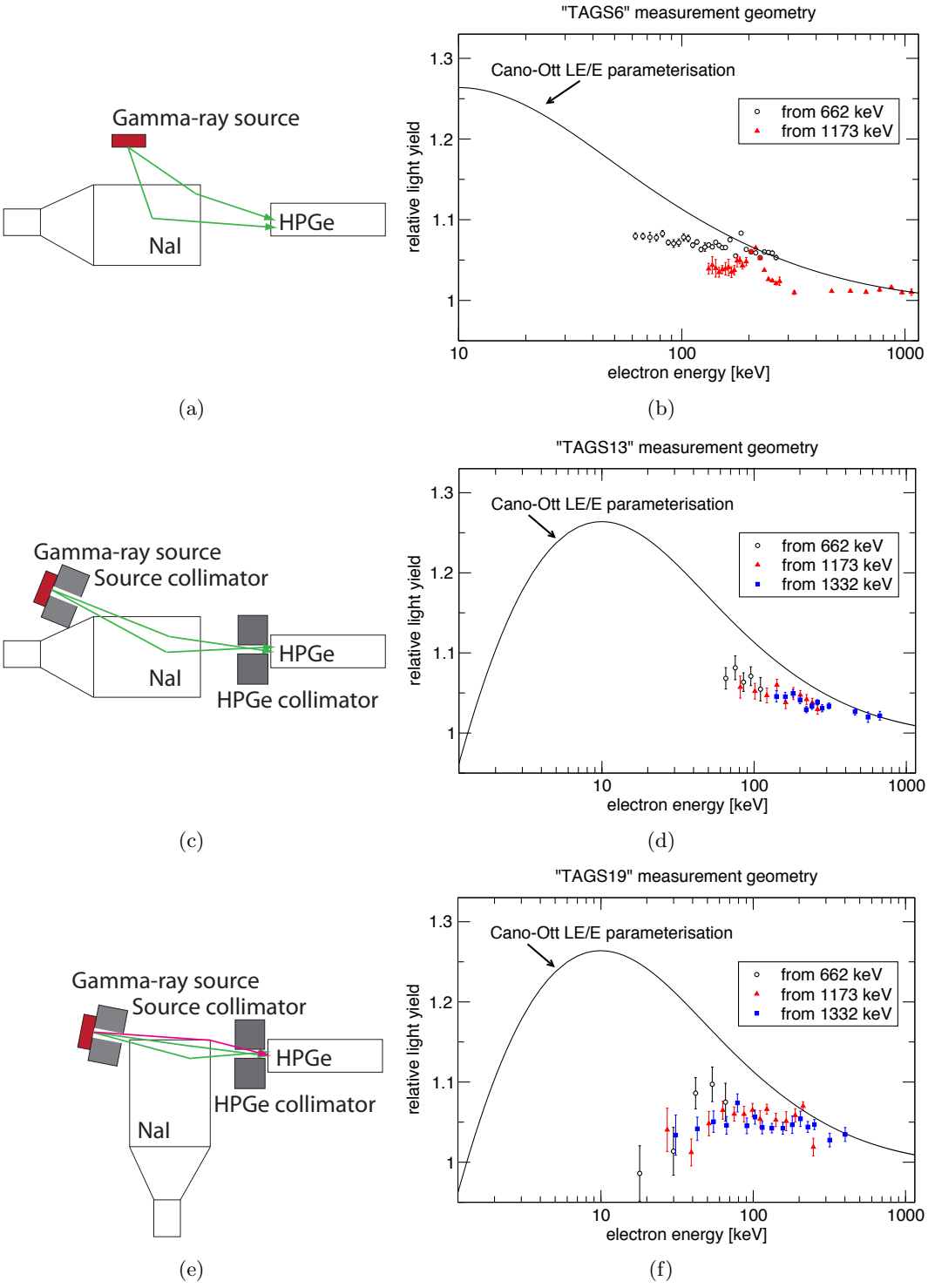

Figure D.2: CCT results for three example arrangements, data taken from [Col11].

Appendix E

Gammasphere as a calorimeter

Gammasphere (GS) [ANLe] is a large detector array consisting of 110 detector elements, each consisting of a BGO* Compton-suppressed, n-type HPGe detector. The elements are arranged in a sphere around a central target position and can be used in conjunction with ATLAS† and the FMA‡ for measurements of nuclear structure. Originally developed at Lawrence Berekely National Laboratory (LBNL), it currently resides at ANL.

It was suggested that GS, modified by the removal of the heavy-metal collimators, could be used as a calorimeter for TAGS-type measurements. The collimators are used to shield the BGO Compton suppressors from direct γ rays from the target. A model was being developed as part of this concept testing, specifically to look at using the BGO/HPGe combination as a spectrometer. The model was largely developed by the time this project was abandoned. The work that was undertaken to that point, is presented here.

The dimensions of an individual element were taken from Figure 5 of Lee [Lee92]. Figure E.1a is a replication of Figure 5 from Lee [Lee92] and shows the design of the BGO suppressor and BGO back-plug around the HPGe crystal. The individual BGO suppressor elements can be seen in the alternating blue and green colours, while the back-plug is in yellow. Optical photons had been included in the model, as were rudimentary photo-cathodes for the detection of the produced light in each of the 7 BGO components.

There are three slightly different shapes used to complete the spherical enclosure. Before creating the other two variants, the ability to combine multiple detectors was added to the model, using the original detector shape replicated. To accomodate the 110 detectors each with 7 BGO components and 1 HPGe, the collection method used in the model was updated. The individual detector angles were input using the 'Gammasphere detector angles' data available from the GS website [ANLe]. The result of the 110 detectors with different angles is shown in the openGL rendering of Figure E.2. The radius of the array was increased in this instance due to the use of the single shape type that doesn't perfectly tile a sphere. Then, a couple of the overlapping detector elements were removed, to allow the testing of event hits with this scale-up. The implementation of the scale up was found to be successful.

The completion of the model would require templates of the 2 element types that remain and the addition of the materials approximating the cold-fingers. Unfortunately the experiment idea was abandoned at this point, but the model as it stands is available and could be useful in the future.

*BGO: Bismuth Germanate, a high density scintillator material

†ATLAS - Argonne Tandem Linac Accelerator System

‡FMA: Fragment Mass Analyzer

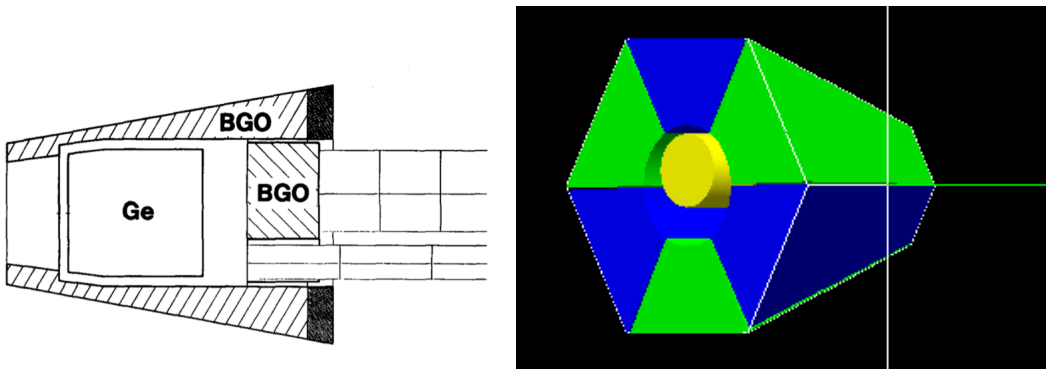

(a) (b)

Figure E.1: A single Gammasphere detector element showing: (a) the schematic reproduced from Figure 5 of Lee [Lee92], and (b) the openGL rendering of the detector in this model.

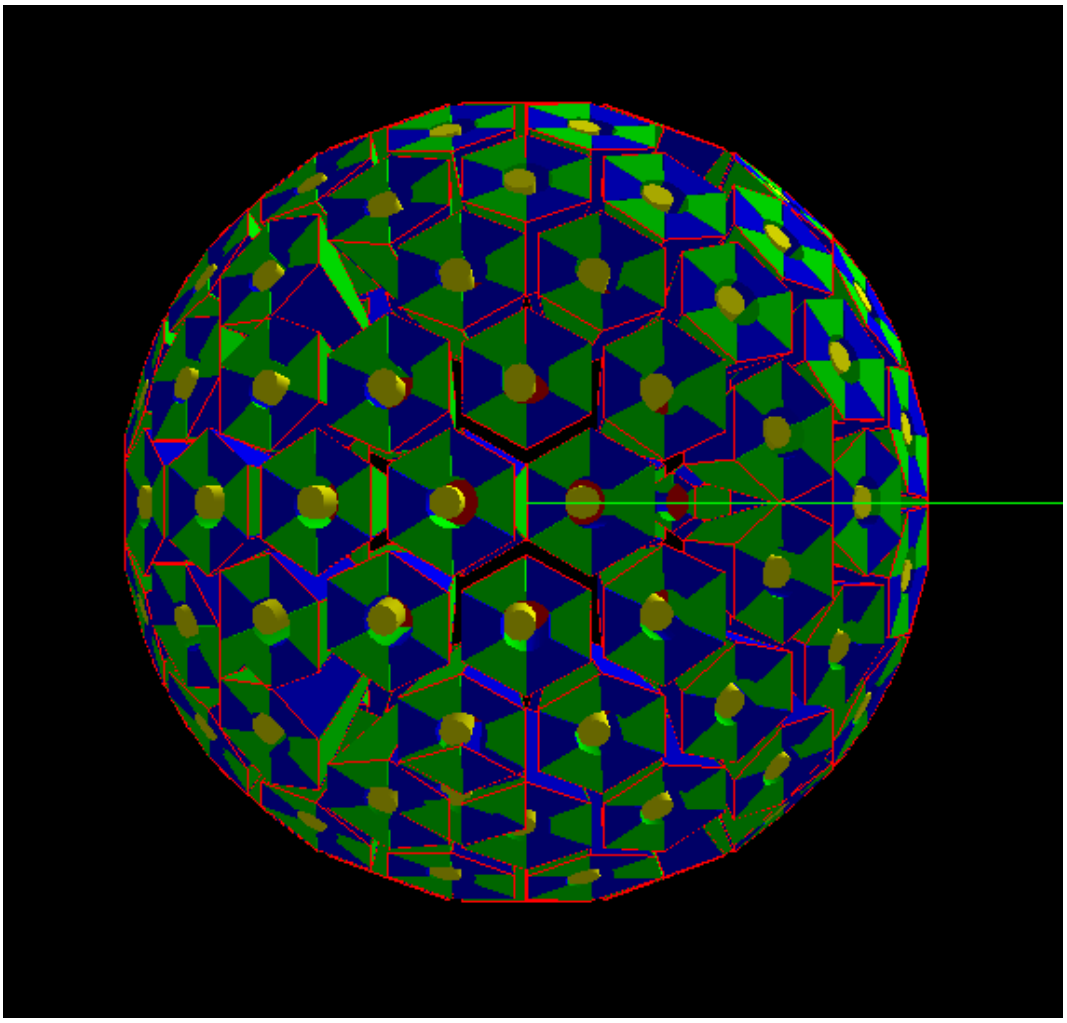

Figure E.2: Detectors at all Gammasphere angles implemented by replicating a single element model.

Bibliography

[Abb17] Abbott, B.P., et al. GW170817: Observation of Gravitational Waves from a Binary Neutron Star Inspiral. *Phys. Rev. Lett.*, 119:161101, 2017.

[Abe12] Abe, Y., et al. Indication of Reactor $\overline{\nu}_e$ Disappearance in the Double Chooz Experiment. *Phys. Rev. Lett.*, 108:131801, 2012.

[Ada73] Adams, J.P., et al. Decay energies of gaseous fission products and their daughters for $A = 138$to142. *Phys. Rev. C*, 8:767–774, 1973.

[Ada74] Adams, J.P., et al. Internal conversion coefficient measurements for transitions in ^{140}Cs from the decay of ^{140}Xe. *Phys. Rev. C*, 10:1467–1474, 1974.

[AGA] Advanced GAmma Tracking Array (AGATA). http://www.agata.org.

[Ago03] Agostinelli, S. et al. GEANT4 - a simulation toolkit. *Nuclear Instruments and Methods in Physics Research Section A: Accelerators, Spectrometers, Detectors and Associated Equipment*, 506(3):250 – 303, 2003.

[Ahn12] Ahn, J.K., et al. Observation of Reactor Electron Antineutrinos Disappearance in the RENO Experiment. *Phys. Rev. Lett.*, 108:191802, 2012.

[Ait67] Aitken, D.W., et al. The Fluorescent Response of NaI(Tl), CsI(Tl), CsI(Na) and CaF2(Eu) to X-Rays and Low Energy Gamma Rays. *IEEE Transactions on Nuclear Science*, 14(1):468–477, 1967.

[AK70] A. Kjelberg, G.R. The ISOLDE isotope seperator on-line facility at CERN. Tech. rep., CERN, 1970.

[Alg99] Algora, A., et al. The GT resonance revealed in β^+- decay using new experimental techniques. *Nuclear Physics A*, 654:727c– 730c, 1999.

[Alg04a] Algora, A., et al. β decay of ^{148}Dy: Study of the Gamow-Teller giant state by means of total absorption spectroscopy. *Physical Review C*, 70(064301), 2004.

[Alg04b] Algora, A., et al. Beta-decay studies using Total Absorption Spectrscopy. *The European Physical Journal A*, 20:199 – 202, 2004.

[Alg10] Algora, A., et al. Reactor deay heat in ^{239}Pu: Solving the γ discrepancy in the 4-3000-s cooling period. *Physical Review Letters*, 105(202501), 2010.

[Alk85] Alkhazov, G., et al. Experimental test of the ^{145}Gd decay scheme and the decay of pandemonium. *Physics Letters B*, 157:350 – 352, 1985.

[All06] Allison, J., et al. GEANT4 developments and applications. *IEEE Transactions on Nuclear Science*, 53(1):270–278, 2006.

[All16] Allison, J. et al. Recent developments in GEANT4. *Nuclear Instruments and Methods in Physics Research Section A: Accelerators, Spectrometers, Detectors and Associated Equipment*, 835:186 – 225, 2016.

[Alq76] Alquist, L., et al. On-line $\gamma - \gamma$ angular correlations of transitions in ^{140}Ba. *Physical Review C*, 13(3):1277 – 1287, 1976.

[Alv68] Alväger, T., et al. On-Line Studies of Mass-Separated Xenon Fission Products. *Phys. Rev.*, 167:1105–1116, 1968.

[An16] An, F.P., et al. Measurement of the Reactor Antineutrino Flux and Spectrum at Daya Bay. *Phys. Rev. Lett.*, 116:061801, 2016.

[And87] Anderl, R., Cole, J., and Greenwood, R. Ion-source development at the ^{252}Cf ISOL facility. *Nuclear Instruments and Methods in Physics Research Section B: Beam Interactions with Materials and Atoms*, 26:333 – 340, 1987.

[And09] Anderson, J., et al. Data Acquisition and Trigger System of the Gamma Ray Energy Tracking In-Beam Nuclear Array (GRETINA). *IEEE Transactions on Nuclear Science*, 56(1):258–265, 2009.

[And12] Anderson, J., et al. A digitial data acquisition system for the detectors at gammasphere. *IEEE Nuclear Science Symposium and Medical Imaging Conference Record*, N20-2:1536 – 1540, 2012.

[ANLa] ANL. Argonne Tandem Linac Accelerator System (ATLAS). https://www.phy.anl.gov/atlas/ATLAS-flyer.pdf.

[ANLb] ANL. CARIBU intensities. http://www.phy.anl.gov/atlas/facility/ExpectedCARIBUBeamIntensitiesForOctober2016PACCycle.pdf.

[ANLc] ANL. DGS-DAQ wiki. https://wiki.anl.gov/gsdaq.

[ANLd] ANL. Fragment Mass Analyzer. https://www.phy.anl.gov/fma/.

[ANLe] ANL. Gammasphere. https://www.phy.anl.gov/gammasphere/.

[ANLf] ANL. The X-Array. https://www.phy.anl.gov/fma/X-array.html.

[Asg15] Asgar, M.A., et al. GEANT4 simulation of a large volume segmented clover detector. *Proceedings of the DAE-BRNS symposium on Nuclear Physics*, 60:960 – 961, 2015.

[Aud03] Audi, G., Wapstra, A., and Thibault, C. The AME2003 atomic mass evaluation (ii) tables graphs and references. *Nuclear Physics A*, 729(1):337 – 676, 2003.

[Be08] Be, M., et al. Table of Radionuclides (A = 133 to 252). 4, 2008.

[Beh69] Behrens, H. and Jänecke, J. *Numerical Tables for Beta-Decay and Electron Capture*. Springer-Verlag, 1969.

[Ber11] Bertone, P., et al. Commissioning of a tape transport system for decay studies and beam diagnostics at CARIBU. *Proceedings APS Division of Nuclear Physics Meeting Abstracts*, 2011.

[BII90] BURLE INDUSTRIES INC., T.P.D. *S83021E, S83021EM1, S83021EM2 Photomultipliers*. 1000 New Holland Ave., Lancaster, PA, 1990.

[Bla07] Blachot, J. Nuclear data sheets for A = 104. *Nuclear Data Sheets*, 108(10):2035 – 2172, 2007.

[Bor71] Borg, S., et al. On-line separation of isotopes at a reactor in Studsvik (OSIRIS). *Nuclear Instruments and Methods*, pp. 109 – 116, 1971.

[Bor79] Borner, H., et al. High precision gamma-ray energy measurements of fission products. *Nuclear Instruments and Methods*, 164:579 – 586, 1979.

[Bro97] Browne, E. Nuclear Data Sheets for A = 90. *Nuclear Data Sheets*, 82(3):379 – 546, 1997.

[Bro17] Browne, E. and Tuli, J. Nuclear Data Sheets for A=99. *Nuclear Data Sheets*, 145:25 – 340, 2017.

[bur89] *Photomultiplier Handbook*, vol. TP-136. Burle Industries, Inc., 1989.

[Cas12] Casanovas, R., Morant, J., and Salvadó, M. Temperature peak-shift correction methods for NaI(Tl) and LaBr3(Ce) gamma-ray spectrum stabilisation. *Radiation Measurements*, 47(8):588 – 595, 2012.

[CERa] CERN. GEANT4 - a simulation toolkit. http://geant4.cern.ch/.

[CERb] CERN. ROOT - data analysis framework. https://root.cern.ch.

[Chi08] Chiara, C., et al. Development of a Total Absorption γ-ray Spectrometer (TAGS) for β-decay studies at ANL. In *2008 Annual Meeting of the division of Nuclear Physics, American Physical Society*. 2008.

[CO99a] Cano-Ott, D., et al. Monte carlo simulation of the response of a large NaI(Tl) total absorption spectrometer for β-decay studies. *Nuclear Instruments and Methods in Physics Research Section A: Accelerators, Spectrometers, Detectors and Associated Equipment*, 430(2-3):333 – 347, 1999.

[CO99b] Cano-Ott, D., et al. Pulse pileup correction of large NaI(Tl) total absorption spectra using the true pulse shape. *Nuclear Instruments and Methods in Physics Research Section A: Accelerators, Spectrometers, Detectors and Associated Equipment*, 430:488 – 497, 1999.

[Col11] Collin, G. Honours thesis: Methodologies for the application of TAGS, 2011.

[Cro08] Cromaz, M., et al. A digital signal processing module for gamma-ray tracking detectors. *Nuclear Instruments and Methods in Physics Research Section A: Accelerators, Spectrometers, Detectors and Associated Equipment*, 597(2):233 – 237, 2008.

[Dav08] Davids, C. and Peterson, D. A compact high-resolution isobar separator for the CARIBU project. *Nuclear Instruments and Methods in Physics Research Section B: Beam Interactions with Materials and Atoms*, 266:4449 – 4453, 2008.

[Dav09] Davids, C. and Peterson, D. A compact high-resolution isobar separator for the CARIBU project. *Proceedings of the 23rd Particle Accelerator Conference*, (FR5REP116), 2009.

[Dec81] Decker, R., et al. PräziseQ β -Wert-Messungen mit einem Intrinsic-Germanium-Detektor an schweren, neutronenreichen Spaltprodukten. *Zeitschrift für Physik A Atoms and Nuclei*, 301(2):165–175, 1981.

[DES] DESPEC https://fair-center.eu/for-users/experiments/nustar/experiments/hispecdespec.html.

[Dig] Digitizer, E. http://markummitchell.github.io/engauge-digitizer.

[Dim15] Dimitriou, P. and Nichols, A.L. Total Absorption Gamma-ray spectroscopy for decay heat calculations and other applications. *International Nuclear Data Committee IAEA*, INDC(NDS)-0676, 2015.

[Duk70] Duke, C.L., et al. Strength-function phenomena in electron-capture beta decay. *Nuclear Physics A*, 151(3):609–633, 1970.

[Eng56] Engelkemeir, D. Nonlinear response of NaI(Tl) to photons. *Review of Scientific Instruments*, 27(8):589–591, 1956.

[ens] ENSDF. https://www.nndc.bnl.gov/ensdf/.

[Erd72] Erdal, B. and Rudstam, G. Response function of a good-geometry detector for a γ-ray cascade. *Nuclear Instruments and Methods*, 104(2):263–283, 1972.

[FAI] FAIR- Facility for Antiproton and Ion Research. http://www.gsi.de/fair/index_e.html.

[Fal12] Fallot, M., et al. New antineutrino energy spectra predictions from the summation of beta decay branches of the fission products. *Phys. Rev. Lett.*, 109:202504, 2012.

[Fal17] Fallot, M., et al. Total absorption spectroscopy of fission fragments relevant for reactor antineutrino spectra. *EPJ Web Conf.*, 146:10002, 2017.

[Fir82] Firestone, R. Complex beta-decay schemes: Pandemonium lost and paradise regained. *Physics Letters B*, 113(2):129 – 131, 1982.

[Fog90] Fogelberg, B., et al. Decays of ^{134}Sn and 0^- ^{134}Sb. *Phys. Rev. C*, 41:R1890–R1894, 1990.

[FRI] FRIB- Facility for Rare Isotope Beams. http://www.frib.msu.edu.

[GREa] Gamma-Ray Energy Tracking Array (GRETA). http://grfs1.lbl.gov.

[GREb] Gamma-Ray Energy Tracking In-beam Nuclear Array (GRETINA). http://gretina.lbl.gov.

[Gre92a] Greenwood, R.C., Struttmann, D.A., and Watts, K.D. Use of a total absorption γ-ray spectrometer to measure ground-state β^--branching intensities. *Nuclear Instruments and Methods in Physics Research Section A: Accelerators, Spectrometers, Detectors and Associated Equipment*, 317(1-2):175 – 184, 1992.

[Gre92b] Greenwood, R.C., et al. Total absorption gamma-ray spectrometer for measurement of β-decay intensity distributions for fission product radionuclides. *Nuclear Instruments and Methods in Physics Research Section A: Accelerators, Spectrometers, Detectors and Associated Equipment*, 314(3):514 – 540, 1992.

[Gre95] Greenwood, R.C., Putnam, M.H., and Watts, K.D. Measurement of ground-state β^--branching intensities of deformed rare-earth nuclides using a total absorption γ-ray spectrometer. *Nuclear Instruments and Methods in Physics Research Section A: Accelerators, Spectrometers, Detectors and Associated Equipment*, 356(2-3):385 – 389, 1995.

[Gre96] Greenwood, R.C., Putnam, M.H., and Watts, K.D. Ground-state β^--branching intensities of several fission-product isotopes measured using a total absorption γ-ray spectrometer. *Nuclear Instruments and Methods in Physics Research Section A: Accelerators, Spectrometers, Detectors and Associated Equipment*, 378(1-2):312 – 320, 1996.

[Gre97] Greenwood, R., et al. Measurement of β^--decay intensity distributions of several fission-product isotopes using a total absorption γ-ray spectrometer. *Nuclear Instruments and Methods in Physics Research Section A: Accelerators, Spectrometers, Detectors and Associated Equipment*, 390(1-2):95 – 154, 1997.

[Ham06] Hamamatsu. *Photomultipler Tubes- Basics and Applications*. Hamamatsu Photonics K.K., 3rd edn., 2006.

[Ham07] Hamamatsu. *Photomultiplier Tubes*. Hamamatsu Photonics K.K., electron Tube Division, 3a edn., 2007.

[Har77] Hardy, J.C., et al. The essential decay of pandemonium: A demonstration of errors in complex β-decay schemes. *Physics Letters B*, 71(2):307 – 310, 1977.

[Har78] Hardy, J., Jonson, B., and Hansen, P.G. The essential decay of pandemonium: β-delayed neutrons. *Nuclear Physics A*, 305:15 – 28, 1978.

[Har84] Hardy, J., Jonson, B., and Hansen, P. A comment on pandemonium. *Physics Letters B*, 136:331 – 333, 1984.

[Hay15] Hayes, A.C., et al. Possible origins and implications of the shoulder in reactor neutrino spectra. *Phys. Rev. D*, 92:033015, 2015.

[Hel94a] Helmer, R., et al. Beta-decay intensity distributions for the fission products ^{139}Cs and ^{140}Cs measured with a total absorption γ-ray spectrometer. *Nuclear Instruments and Methods in Physics Research Section A: Accelerators, Spectrometers, Detectors and Associated Equipment*, 353:222 – 228, 1994.

[Hel94b] Helmer, R., et al. Methodology for the measurement of β^-- decay intensity distributions from the analysis of total absorption γ-ray spectra. *Nuclear Instruments and Methods in Physics Research Section A: Accelerators, Spectrometers, Detectors and Associated Equipment*, 351(2-3):406 – 422, 1994.

[Hel94c] Helmer, R.G., et al. Beta-particle feeding distributions for $^{138-141}$Cs from Total Absorption Gamma-ray Spectrometer (TAGS). *Nuclear Instruments and Methods in Physics Research Section A: Accelerators, Spectrometers, Detectors and Associated Equipment*, 339(1-2):189 – 199, 1994.

[Hir16] Hirsh, T.Y., et al. First operation and mass separation with the CARIBU MR-TOF. *Nuclear Instruments and Methods in Physics Research Section B: Beam Interactions with Materials and Atoms*, 376:229 – 232, 2016.

[Hof48] Hofstadter, R. Alkali halide scintillation counters. *Physical Review Letters*, 74:100, 1948.

[Hor75] Hornshøj, P., et al. Beta-strength functions of neutron-deficient isotopes in the xenon and mercury regions. *Nuclear Physics A*, 239(1):15–28, 1975.

[Hul09] Hull, G., et al. Measurements of NaI(Tl) Electron Response: Comparison of Different Samples. *IEEE Transactions on Nuclear Science*, 56(1):331–336, 2009.

[Ian07] Ianakiev, K., et al. Temperature dependence of nonlinearity and pulse shape in a doped NaI(Tl) scintillator. *Nuclear Instruments and Methods in Physics Research Section A: Accelerators, Spectrometers, Detectors and Associated Equipment*, 579(1):34 – 37, 2007. Proceedings of the 11th Symposium on Radiation Measurements and Applications.

[JAE] JAEA. http://wwwndc.jaea.go.jp/cgi-bin/FPYfig.

[Kan61] Kantele, J. and Fink, R. Coincidence summing and non-linearity studies with a two-crystal scintillation gamma spectrometer. *Nuclear Instruments and Methods*, 13:141 – 146, 1961.

[Kar97] Karny, M., et al. Coupling a total absorption spectrometer to the GSI on-line mass separator. *Nuclear Instruments and Methods in Physics Research Section B: Beam Interactions with Materials and Atoms*, 126(1-4):411 – 415, 1997.

[Kar98] Karny, M., et al. Beta decay of ^{103}In: evidence for the Gamow-Teller resonance near ^{100}Sn. *Nuclear Physics A*, 640:3 – 23, 1998.

[Kar01] Karny, M., et al. Determination of the Gamow-Teller strength function for the neutron-deficient isotopes $^{104-107}$In. *Nuclear Physics A*, 690:367 – 381, 2001.

[Kar16] Karny, M., et al. Modular total absorption spectrometer. *Nuclear Instruments and Methods in Physics Research Section A: Accelerators, Spectrometers, Detectors and Associated Equipment*, 836:83 – 90, 2016.

[Kas17] Kasen, D., et al. Origin of the heavy elements in binary neutron-star mergers from a gravitational-wave event. *Nature*, 551:80 EP –, 2017.

[Kno99] Knoll, G. *Radiation Detection and Measurement*. John Wiley and Sons, Inc., 3rd edn., 1999.

[Kra88] Krane, K.S. *Intorductory Nuclear Physics*. John Wiley and Sons, Inc., 1988.

[LC] LNHB-CEA. DDEP. http://www.lnhb.fr/nuclear-data/nuclear-data-table/.

[Lee92] Lee, I.Y. The gammasphere. *Progress in Particle and Nuclear Physics*, 28:473 – 485, 1992.

[Lic13] Licciulli, F., Indiveri, I., and Marzocca, C. A novel technique for the stabilization of SiPM gain against temperature variations. *IEEE Transactions on Nuclear Science*, 60(2):606–611, 2013.

[Lic15] Licciulli, F. and Marzocca, C. An active compensation system for the temperature dependence of SiPM gain. *IEEE Transactions on Nuclear Science*, 62(1):228–235, 2015.

[Lin99] Lindroth, A., et al. Octupole vibration and influence of shell effects on the $E1$ transition rates in ^{140}Xe. *Phys. Rev. Lett.*, 82:4783–4786, 1999.

[Lun76] Lund, E. and Rudstam, G. Spectrometer for measuring total beta decay energies. *The Swedish Research Councils' Laboratory- Research Report*, LF-66, 1976.

[Mac89] Mach, H., Gill, R., and Moszynski, M. A method for picosecond lifetime measurements for neutron-rich nuclei. *Nuclear Instruments and Methods in Physics Research Section A: Accelerators, Spectrometers, Detectors and Associated Equipment*, 280(1):49 – 72, 1989.

[Mel88] Melcher, C.L. and Schweitzer, J.S. Gamma-ray detector properties for hostile environments. *IEEE Transactions on Nuclear Science*, 35(1):876–878, 1988.

[Men02] Mengesha, W. and Valentine, J.D. Benchmarking NaI(Tl) electron energy resolution measurements. *IEEE Transactions on Nuclear Science*, 49(5):2420–2426, 2002.

[Men11] Mention, G., et al. Reactor antineutrino anomaly. *Phys. Rev. D*, 83:073006, 2011.

[Met49] Metropolis, N. and Ulam, S. The Monte Carlo Method. *Journal of the American Statistical Association*, 44(247):335 – 341, 1949.

[Mit] Mitchell, A. J. Private communication.

[Mit14] Mitchell, A., et al. The X-Array and SATURN: a new decay-spectrsocopy station for CARIBU. *Nuclear Instruments and Methods in Physics Research Section A: Accelerators, Spectrometers, Detectors and Associated Equipment*, 763:232 – 239, 2014.

[Mit16a] Mitchell, A. J., et al. Recent advances in β-decay spectroscopy at CARIBU. *EPJ Web Conf.*, 123:04006, 2016.

[Mit16b] Mitra, P., et al. Application of spectrum shifting methodology to restore NaI(Tl)-recorded gamma spectra, shifted due to temperature variations in the environment. *Applied Radiation and Isotopes*, 107:133 – 137, 2016.

[Mle81] Mlekodaj, R., Zganjar, E., and Cole, J. A new concept for a compact tape transport system. *Nuclear Instruments and Methods*, 186:239 – 241, 1981.

[Mor75] Morman, J.A., Schick, W.C., and Talbert, W.L. Lifetimes of levels in ^{136}Xe, ^{140}Cs, and ^{141}Cs populated in the decays of mass-separated ^{136}I, ^{140}Xe, and ^{141}Xe. *Phys. Rev. C*, 11:913–919, 1975.

[Mos06] Moszyński, M., et al. Temperature dependences of LaBr3(Ce), LaCl3(Ce) and NaI(Tl) scintillators. *Nuclear Instruments and Methods in Physics Research Section A: Accelerators, Spectrometers, Detectors and Associated Equipment*, 568(2):739 – 751, 2006.

[Mos08] Moses, W., et al. Scintillator non-proportionality: Present understanding and future challenges. *Nuclear Science, IEEE Transactions on*, 55(3):1049 –1053, 2008.

[NEA] NEA. Assessment of fission product decay data for decay heat calculations. http://www.nea.fr/science/wpec.

[Nic07] Nica, N. Nuclear Data Sheets for A = 140. *Nuclear Data Sheets*, 108(7):1287 – 1470, 2007.

[Nic12] Nica, N., Cameron, J., and Singh, B. Nuclear Data Sheets for A = 36. *Nuclear Data Sheets*, 113(1):1 – 155, 2012.

[Nic14] Nica, N. Nuclear Data Sheets for A = 141. *Nuclear Data Sheets*, 122(Supplement C):1 – 204, 2014.

[Nic18] Nica, N. Nuclear Data Sheets for A=140. *Nuclear Data Sheets*, 154:1 – 403, 2018.

[Nit95] Nitschke, J., et al. The Total Absorption Spectrometer (TAS) at the on-line mass separator. *GSI Annual Report 1994*, 1:285, 1995.

[ORN] ORNL. High Flux Isotope Reactor (HFIR). https://neutrons.ornl.gov/hfir.

[Ote76] Otero, D., Proto, N., and Iglesias, F. Levels of ^{141}Cs and ^{141}Ba from the decays of ^{141}Xe and ^{141}Cs. *Physical Review C*, 13(5):1996 – 2010, 1976.

[Ote81] Otero, D., et al. Level scheme of ^{140}Cs. *Phys. Rev. C*, 23:2691–2699, 1981.

[Par16] Pardo, R., Savard, G., and Janssens, R. ATLAS with CARIBU: A laboratory portrait. *Nuclear Physics News*, 26:5, 2016.

[Pee60] Peelle, R.W. and Love, T.A. Method for detecting nonproportionality of response for gamma-ray scintillators. *Review of Scientific Instruments*, 31(2):205 – 206, 1960.

[Por66] Porter, F., et al. Response of NaI, anthracene and plastic scintillators to electrons and the problems of detecting low energy electrons with scintillation counters. *Nuclear Instruments and Methods*, 39(1):35 – 44, 1966.

[Pri50] Pringle, R.W. and Standil, S. The gamma-rays from neutron-activated gold. *Phys. Rev.*, 80(4):762 – 763, 1950.

[RCA] RCA. *Photomultipler Manual Technical Series PT-61*. RCA Solid State Division, Electro Optics and Devices, Lancaster, PA.

[Reu07] Reutter, B.W., et al. Experimental and Monte Carlo investigation of intrinsic limits of scintillator energy resolution. In *2007 IEEE Nuclear Science Symposium Conference Record*, vol. 2, pp. 1447–1451. 2007.

[Rob86] Robinson, S., et al. Levels and transitions in ^{140}Ba populated following the β decay of ^{140}Cs. *Journal of Physics G*, 12:903 – 933, 1986.

[Roo96] Rooney, B.D. and Valentine, J.D. Benchmarking the compton coincidence technique for measuring electron response nonproportionality in inorganic scintillators. *IEEE Transactions on Nuclear Science*, 43(3):1271–1276, 1996.

[Roo97] Rooney, B.D. and Valentine, J.D. Scintillator light yield nonproportionality: calculating photon response using measured electron response. *IEEE Transactions on Nuclear Science*, 44(3):509–516, 1997.

[Rub05] Rubio, B., et al. Beta decay studies with the total absorption technique: past, present and future. *Journal of Physics G*, pp. S1477 – S1483, 2005.

[Rub07] Rubio, B. and Gelletly, W. Total absorption spectroscopy. *Romanian Reports in Physics*, 59(2):635 – 654, 2007.

[San84] Sandorfi, A. and Collins, M. The new BNL high-energy gamma-ray spectrometers. *Nuclear Instruments and Methods in Physics Research*, 222:479 – 495, 1984.

[Sav03] Savard, G., et al. Development and operation of gas catchers to thermalize fusion-evaporation and fragmentation products. *Nuclear Instruments and Methods in Physics Research Section B: Beam Interactions with Materials and Atoms*, 204:582 – 586, 2003.

[Sav05] Savard, G. and Pardo, R. Proposal for the ^{252}Cf source upgrade to the ATLAS facility. Tech. rep., Physics Division, Argonne National Laboratory, 2005.

[Sav08] Savard, G., et al. Radioactive beams from gas catchers: the CARIBU facility. *Nuclear Instruments and Methods in Physics Research Section B: Beam Interactions with Materials and Atoms*, 266:4086 – 4091, 2008.

[Sav16] Savard, G., Levand, A., and Zabransky, B. The CARIBU gas catcher. *Nuclear Instruments and Methods in Physics Research Section B: Beam Interactions with Materials and Atoms*, 376:246 – 250, 2016.

[Sch71] Schick, W.C., Talbert, W.L., and McConnell, J.R. Ge(Li)-Ge(Li) Study of the Decay of 14- sec ^{140}Xe. *Phys. Rev. C*, 4:507–516, 1971.

[Sch73] Schussler, F., et al. Desintegration de ^{140}Cs ($T_{1/2}$). *Nuclear Physics A*, 209:589 – 603, 1973.

[Sch74] Schick, W. and Talbert, W. Levels in ^{140}Ba populated in the decay of 64-sec ^{140}Cs. *Physical Review C*, 9(6):2328 – 2339, 1974.

[Sch83] Schweitzer, J.S. and Ziehl, W. Temperature Dependence of NaI(Tl) Decay Constant. *IEEE Transactions on Nuclear Science*, 30(1):380–382, 1983.

[Sci] Scielzo, N. Beta decay program.

[Sci04] Scielzo, N.D., et al. Measurement of the $\beta-\nu$ correlation using magneto-optically trapped ^{21}Na. *Phys. Rev. Lett.*, 93:102501, 2004.

[SG] Saint-Gobain. https://www.saint-gobain.com/en.

[Sie18] Siegl, K., et al. β-decay half-lives of ^{134,134m}Sb and their isomeric yield ratio produced by the spontaneous fission of ^{252}Cf. *Phys. Rev. C*, 98:054307, 2018.

[Sim13] Simon, A., et al. SuN: Summing NaI(Tl) gamma-ray detector for capture reaction measurements. *Nuclear Instruments and Methods in Physics Research Section A: Accelerators, Spectrometers, Detectors and Associated Equipment*, 703:16 – 21, 2013.

[Smi10] Smith, M.L. TAGS Simulations with GEANT4. *Argonne National Laboratory-Nuclear Data and Measurement Series*, ANL/NDM-167, 2010.

[Son17] Sonzogni, A.A., McCutchan, E.A., and Hayes, A.C. Dissecting reactor antineutrino flux calculations. *Phys. Rev. Lett.*, 119:112501, 2017.

[Son18] Sonzogni, A.A., Nino, M., and McCutchan, E.A. Revealing fine structure in the antineutrino spectra from a nuclear reactor. *Phys. Rev. C*, 98:014323, 2018.

[Ste13] Stetcu, I., et al. Isomer production ratios and the angular momentum distribution of fission fragments. *Phys. Rev. C*, 88:044603, 2013.

[Tai07] Tain, J. and Cano-Ott, D. Algorithms for the analysis of β-decay total absorption spectra. *Nuclear Instruments and Methods in Physics Research Section A: Accelerators, Spectrometers, Detectors and Associated Equipment*, 571(3):728 – 738, 2007.

[Tai15] Tain, J., et al. A decay total absorption spectrometer for DESPEC at FAIR. *Nuclear Instruments and Methods in Physics Research Section A: Accelerators, Spectrometers, Detectors and Associated Equipment*, 803:36 – 46, 2015.

[Tec] Technologies, C.M. https://www.canberra.com.

[Ten84] Tenney, F.H. Idealized pulse pileup effects on energy spectra. *Nuclear Instruments and Methods in Physics Research*, 219(1):165 – 172, 1984.

[Val94] Valentine, J.D. and Rooney, B.D. Design of a compton spectrometer experiment for studying scintillator non-linearity and intrinsic energy resolution. *Nuclear Instruments and Methods in Physics Research Section A: Accelerators, Spectrometers, Detectors and Associated Equipment*, 353(1):37 – 40, 1994.

[Val98] Valentine, J.D., Rooney, B.D., and Li, J. The light yield nonproportionality component of scintillator energy resolution. *IEEE Transactions on Nuclear Science*, 45(3):512–517, 1998.

[WC14] Wolińska-Cichocka, M., et al. Modular Total Absorption Spectrometer at the HRIBF (ORNL, Oak Ridge). *Nuclear Data Sheets*, 120:22 – 25, 2014.

[Wis90] Wisshak, K., et al. The Karlsruhe 4π Barium Fluoride detector. *Nuclear Instruments and Methods in Physics Research Section A: Accelerators, Spectrometers, Detectors and Associated Equipment*, 292(595 - 618), 1990.

[Wuo07] Wuosmaa, A., et al. A solenoidal spectrometer for reactions in inverse kinematics. *Nuclear Instruments and Methods in Physics Research Section A: Accelerators, Spectrometers, Detectors and Associated Equipment*, 580(3):1290 – 1300, 2007.

[Yam82] Yamamoto, H., et al. Decay of mass-seperated ^{141}Cs to ^{141}Ba and systematics of N = 85 isotones. *Physical Review C*, 26(3):1215 – 1236, 1982.

[Yee13] Yee, R.M., et al. β-delayed neutron spectroscopy using trapped radioactive ions. *Phys. Rev. Lett.*, 110:092501, 2013.

[Zer61] Zerby, C., Meyer, A., and Murray, R. Intrinsic line broadening in NaI(Tl) gamma-ray spectrometers. *Nuclear Instruments and Methods*, 12:115 – 123, 1961.

[Zim11] Zimmermann, S., et al. Implementation and performance of the electronics and computing system of the Gamma Ray Energy Tracking In-Beam Nuclear Array (GRETINA). In *2011 IEEE Nuclear Science Symposium Conference Record*, pp. 596–601. 2011.